Novel Turbomachinery Concepts for Highly Integrated Airframe/Propulsion Systems

by

Parthiv Narendra Shah

B.S. Aerospace Engineering, University of Virginia (1994)
M.S. Mechanical Engineering, Rutgers University (1998)

Submitted to the Department of Mechanical Engineering
in partial fulfillment of the requirements for the degree of

Doctor of Philosophy

at the

MASSACHUSETTS INSTITUTE OF TECHNOLOGY

February 2007

Author .....
Department of Mechanical Engineering
October 4, 2006

Certified by .....
Zoltan Spakovszky
Associate Professor
Thesis Supervisor

Certified by .....
Choon Sooi Tan
Senior Research Engineer
Thesis Supervisor

Certified by .....
John Brisson II
Associate Professor
Doctoral Committee Chair

Accepted by .....
Lallit Anand
Chairman, Department Committee on Graduate Students

Novel Turbomachinery Concepts for Highly Integrated Airframe/Propulsion Systems

by

Parthiv Narendra Shah

Submitted to the Department of Mechanical Engineering on October 4, 2006,
in partial fulfillment of the requirements for the degree of Doctor of Philosophy

Abstract

Two novel turbomachinery concepts are presented as enablers to advanced flight missions requiring integrated airframe/propulsion systems. The first concept is motivated by thermal management challenges in low-to-high Mach number (4+) aircraft. The idea of compressor cooling combines the compressor and heat exchanger function to stretch turbopropulsion system operational limits. Axial compressor performance with blade passage heat extraction is assessed with computational experiments and meanline modeling. A cooled multistage compressor with adiabatic design point is found to achieve higher pressure ratio, choking mass flow, and efficiency (referenced to an adiabatic, reversible process) at fixed corrected speed, with greatest benefit occurring through front-stage cooling. Heat removal equal to one percent of inlet stagnation enthalpy flux in each of the first four blade rows suggests pressure ratio, efficiency, and choked flow improvements of 23%, 12%, and 5% relative to a baseline, eight-stage compressor with pressure ratio of 5. Cooling is also found to unchoke rear stages at low corrected speed. Heat transfer estimations indicate that surface area limitations and temperature differences favor rear-stage cooling and suggest the existence of an optimal cooling distribution.

The second concept is a quiet drag device to enable slow and steep approach profiles for functionally quiet civil aircraft. Deployment of such devices in clean airframe configuration reduces aircraft source noise and noise propagation to the ground. The generation of swirling outflow from a duct, such as an aircraft engine, is conceived to have high drag and low noise. The simplest configuration is a ram pressure driven duct with non-rotating swirl vanes, a so-called swirl tube. A device aerodynamic design is performed using first principles and CFD. The swirl-drag-noise relationship is quantified through scale-model aerodynamic and aeroacoustic wind tunnel tests. The maximum measured stable flow drag coefficient is 0.83 at exit swirl angles close to 50°. The acoustic signature, extrapolated to full-scale, is found to be well below the background noise of a well populated area, demonstrating swirl tube conceptual feasibility. Vortex breakdown is found to be the aerodynamically and acoustically limiting physical phenomenon, generating a white-noise signature that is ~ 15 dB louder than a stable swirling flow.

Thesis Supervisor: Zoltan Spakovszky
Title: Associate Professor

Thesis Supervisor: Choon Sooi Tan
Title: Senior Research Engineer

Acknowledgments

Between July 6 and July 14, 2006, I took a thesis writing retreat at the Sheraton in terminal 3 of Toronto Pearson International Airport. Writing began in earnest there, and this unconventional vacation gave me perspective on why my research was relevant to aviation. It also reminded me that I got into this field because I like airplanes. From my hotel window, like a kid, I watched the big planes come and go, and on Airport Road I accidentally found the place where the locals knew you could see (and hear) 747s and A340s land right over your head. So my first acknowledgement goes to the manager of the Sheraton at YYZ, for heeding my complaints for a room with a view.

Being a graduate student in the MIT Gas Turbine Laboratory has been a great adventure from the beginning, and for this I'd like to first thank my two thesis supervisors, Professor Zoltan Spakovszky and Dr. Choon Tan, for their technical support and their friendship. Zolti has shown great enthusiasm for my work, and his approach really allowed our meetings to be forums for new ideas and thinking to emerge. Choon has also been a great advisor and mentor who has taught me how to communicate my thoughts clearly and effectively.

Professor John Brisson has spent many hours with me in his office discussing my research. His friendly manner, guidance and positivity have always been encouraging. Professor Ed Greitzer has asked probing questions that have helped me to understand my own work better, both in classes and in the Silent Aircraft Initiative engine team meetings. Professor Frank Marble was kind enough to meet with me and give feedback on the compressor cooling project. Professor Nick Cumpsty also gave excellent feedback. Professor Jack Kerrebrock gave us the original inspiration to look into swirling flows, and discussed vane design with me. Professor Mark Drela helped me with MTFLOW, a key design tool for the swirl tube. Dr. Yifang Gong has often provided me with ideas to resolve CFD issues.

At NASA Glenn, the compressor cooling work was supported under grant NAG3-2767, and I gratefully acknowledge the oversight of Dr. Ken Suder and Dr. Arun Sehra. Also, Dr. John Adamczyk gave input and encouraged me to dig deeper into the definition of non-adiabatic compressor efficiency, Dr. Louis Larosilier provided good discussion on loss

modeling, and Dr. Rod Chima provided me a grid for the Stage 35 compressor.

At NASA Langley, the swirl tube work was supported under contract NAS1-02044, and I am grateful to our contract monitors Dr. Russell Thomas and Dr. Henry Haskins. In addition, Dr. Tom Brooks and Tony Humphreys provided great technical guidance at the world class Quiet Flow Facility (QFF). The crew of the QFF was also a pleasure to work with, including Dan Stead, Larry Becker, Dennis Kuchta, Jaye Moen, and of course, Ronnie Geouge, who is in a league by himself in terms of test support and sense of humor.

At Pratt and Whitney and UTRC, I am thankful for the support of Dr. Wes Lord, Dr. Jinzhang Feng, Dr. Jayant Sabnis, Sanjay Hingorani, Dr. Bob Schlinker, and Prof. Thomas Barber. Also during my time at Rutgers, Professor Timothy Wei taught me a lot about being an engineer.

The infinite support of Leslie Regan and Joan Kravit of the Mechanical Engineering graduate office is appreciated. I would also like to acknowledge the support of the Mechanical Engineering department head, Professor Rohan Abeyaratne, for helping me to secure the last six weeks of my funding at MIT. Dean Blanche Staton was also very helpful in this matter.

The GTL staff has been super-supportive over the years. Special thanks go to Lori Martinez and Holly Anderson for their all around know-how within the lab.

GTL students have been great sources of friendship. Big thanks go to Darius Mobed, my swirl tube colleague. The model fabrication and experiments would not have been a success without his talents. Other students and post-docs that I have shared good times with, both at GTL and beyond, and in no particular order, include Alexi, Sean, Justin, Adrian, Jessica, Boris, Vai-man, Ryan, Anya, Jim, Angelique, Barbara, Francois, Alphonso, Trevor, Juan, Caitlyn, Joe, Keen Ian, and Josep.

To my parents, Naren and Neeta Shah, goes my heartfelt love and appreciation for their support. Their unconditional love and dedication got me to this stage in my life.

Finally, to my partner, soul mate, fiancée, and best friend, Amy... thanks for all your support during the highs and lows, quals, thesis writing, long hours, and all the joys of completing this endeavor... I love you.

Contents

Acknowledgements **5**

List of Figures **10**

List of Tables **22**

1 Introduction **31**

1.1 Background 31

1.2 Thesis Contributions 32

1.3 Synopsis of Thesis Chapters 33

2 Mission 1: Low-to-High Mach Number Flight **37**

2.1 Overview 38

2.2 Previous Work 40

2.3 Mission Profile 42

2.4 Pre-cooled Turbojet (PCTJ) 46

2.4.1 Modification of Ideal SSTJ Cycle for Compressor Pre-cooling 46

2.4.2 Specific Thrust Requirements 50

2.5 Compressor Cooling: The Idea 56

2.5.1 Compressor Cooling vs. Pre-Cooling 56

2.5.2 Diffusing Passage Heat Extraction 60

2.5.3 Research Questions 62

2.5.4 Challenges and Unknowns 62

2.6 Chapter Summary 63

3 Compressor Cooling: A Novel Turbomachinery Concept for Mission 1 65

3.1 Objectives 66

3.2 Technical Approach 67

3.3 Blade Passage Flows with Heat Extraction 69

3.3.1 Cascade Cases 69

3.3.2 Bulk Performance 72

3.3.3 Entropy Generation 77

3.3.4 Generic Rules for Blade Passage Loss and Deviation 81

3.4 On- and Off- Design Meanline Analysis 85

3.4.1 Single Stage Fan 87

3.4.2 Eight Stage Compressor 90

3.5 Three Dimensional Flow Computations 96

3.6 Heat Transfer Considerations 100

3.7 Efficiency Metrics for Non-adiabatic Compressors 103

3.8 Summary of Major Findings 106

4 Mission 2: Quiet Civil Aircraft 107

4.1 Mission Overview and Previous Work 108

4.2 Quiet Approach Trajectory 113

4.3 Swirl Tube: The Idea 119

4.3.1 Research Questions 123

4.3.2 Challenges and Unknowns 123

4.4 Preliminary Model of Ducted Drag Generator 124

4.4.1 Control Volume Analysis of Ducted Drag Generator 126

4.4.2 Drag Generating Axial Exhaust Flow Devices 129

4.4.3 Swirling Flow Dynamics 134

4.4.4 Drag Generating Swirling Exhaust Flow Devices 142

4.5 Chapter Summary 155

5 Swirl Tube: A Novel Turbomachinery Concept for Mission 2 159

5.1 Objectives 160

5.2 Technical Approach 160

5.3 Swirl Tube Aerodynamics 163

5.3.1 Two Dimensional Axisymmetric Computations 164

5.3.2 3D Vane Design Methodology 172

5.3.3 Three Dimensional CFD Computations 175

5.3.4 Model Scale Wind Tunnel Testing 183

5.4 Swirl Tube Acoustics 199

5.4.1 Swirl Mixing Noise Models based on Lighthill's Acoustic Analogy . . 201

5.4.2 Model Scale Acoustic Testing 208

5.5 Swirl Tube System Integration 228

5.5.1 Upstream Fan Stage Interaction 228

5.5.2 Comparison to Thrust Reverser 234

5.6 Summary of Major Findings 241

6 Summary and Conclusions of the Thesis 243

6.1 Compressor Cooling 243

6.1.1 Summary of Research 243

6.1.2 Summary of Contributions 245

6.1.3 Recommendations for Future Work 245

6.2 Swirl Tube 247

6.2.1 Summary of Research 247

6.2.2 Summary of Contributions 248

6.2.3 Recommendations for Future Work 249

List of Figures

2-1 Standard atmosphere model showing temperature, pressure, density, vs. altitude, and contours of Mach number in the altitude-velocity plane. Symbol indicates design point of $M = 4, h = 25$ km. 43

2-2 Selected flight path. Heavy, broken line represents low Mach number trajectory. Heavy, solid line is $\rho V^2/2 = 28.4$ kPa, representing high Mach number trajectory. Faint broken lines are lines of constant $\rho V^2/2$ in kPa. Faint dash-dot lines are lines of constant specific energy, in km. 44

2-3 Stagnation properties along flight path. 45

2-4 PCTJ schematic. Indicated stations are: 1) Inlet/pre-cooler inlet, 2) pre-cooler exit/compressor inlet, 3) compressor exit/burner inlet, 4) burner exit/turbine inlet, 5) turbine exit/nozzle inlet, 7) nozzle exit. 46

2-5 Specific thrust for ideal SSTJ (solid line) and ideal SSTJ with pre-cooling (broken line) for given mission. 49

2-6 Mach number dependence of drag model used in mission analysis, based on a typical supersonic jet aircraft [59, p. 86]. 51

2-7 Uncooled available (solid line), uncooled required (broken line), and pre-cooled (dash-dot line) specific thrust vs. Mach number for chosen vehicle in steady, level flight on selected trajectory. 53

2-8 Pre-cooling temperature ratio for chosen vehicle in steady, level flight on selected trajectory. 54

2-9 Pre-cooler requirements along selected trajectory. 55

2-10 CCTJ and HCTJ schematics. Indicated stations are: 1) Inlet/pre-cooler inlet, 2) pre-cooler exit/compressor inlet, 3) compressor exit/burner inlet, 4) burner exit/turbine inlet, 5) turbine exit/nozzle inlet, 7) nozzle exit. 55

2-11 Temperature-entropy diagram for for standard compression (A-B), compression with pre-cooling (A-C-D), and interspersed cooling and compression in N steps (A-E-...-F). 56

2-12 Same as Fig 2-11 with real precooled compression process (A-C′-D′) and compression followed by constant pressure post-cooling (A-B-B′). 58

2-13 Critical pre-cooling stagnation pressure recovery vs. cooling load. Operation above the line favors real pre-cooled compression, while operation below the line favors a lossless post-cooled compressor (a limiting case of cooled compressor with no new loss generating gas path surfaces). Plot is made on an equal work, equal cooling basis for pressure ratios of 2, 5, and 8. 59

2-14 Control volume of a diffusing blade passage with heat extraction. Upstream and downstream flow angles, α_u and α_d, respectively, are assumed fixed. . . . 60

2-15 Cooled stator passage control volume model. 61

3-1 Compressor cooling technical road map. 67

3-2 Computational grids for cascades 1 and 2. 70

3-3 Total pressure reduction coefficient, ω, vs. flow inlet angle, β_{in}, at low (0.4) and high (0.8) inlet Mach number, for cascades 1 and 2. 73

3-4 Non-dimensional cooling, q^*, vs. flow inlet angle, β_{in}, at low (0.4) and high (0.8) inlet Mach number, for cascade 2 with $T_{wall}/T_{t,in} = 0.5$ cooling boundary condition. 74

3-5 CFD estimated (solid, Equation 3.4) vs. analytical one dimensional channel flow sensitivity coefficient (dashed, Equation 3.5). Data normalized to $q^* = q/h_{t,in} = -0.001$. 75

3-6 Adiabatic vs. cooled exit Mach number, M_{out}, for cascade 2. Solid line with circles represents adiabatic boundary conditions; dashed line with triangles represents blade surface cooling. Wall temperature BC is $T_{wall}/T_{t,in} = 0.5$. . 77

3-7 Cascade 2, computed entropy generation vs. incidence at low (0.4) and high (0.8) inlet Mach number using net entropy flux method (solid lines given by Equation 3.7) and direct volume integration(dashed lines given by Equation 3.8). Adiabatic (red) and cooled (blue, $T_{wall}/T_{t,in} = 0.5$) cases shown. . 79

3-8 Cascade 2, viscous (black), and thermal (gray) dissipation vs. incidence at low (0.4) and high (0.8) inlet Mach number. Plots on left are adiabatic wall BC; plots on right are $T_{wall}/T_{t,in} = 0.5$. 80

3-9 Generic adiabatic vs. cooled loss buckets derived from cascade 1 performance. Solid line with circles represents adiabatic boundary conditions; dashed line with triangles represents blade surface cooling. Non-dimensional cooling rate is $q^* = \frac{q}{h_{t,in}} = -0.001$. 83

3-10 Adiabatic change in deviation, $\Delta\delta_a$, (relative to Carter's rule) for cascade 1. 84

3-11 Additional flow turning from cooling, $\Delta\beta_{cool} = -\Delta\delta_{cool}$, for cascade 1, $q^* = -0.001$. Dotted lines with symbols are CFD results. Heavy solid lines are average values (used in meanline analysis) for given inlet Mach numbers. . . 85

3-12 Eight stage compressor meridional layout. First stage also analyzed as a single stage fan. 86

3-13 Single stage compressor map, with and without cooling. Solid line is adiabatic; Dashed line is $q^* = -0.0025$. 100%, 80%, and 60% N_c lines are shown. 88

3-14 Single stage compressor map, with and without different effects from cooled cascade performance. Solid red line is adiabatic; Solid green line shows effect of change in deviation due to cooling; Dashed black line shows effect of change in ω due to cooling; Dashed blue line shows both effects. 100%, 80%, and 60% N_c lines are shown. In cooled cases, $q^* = -0.0025$. 90

3-15 Cooling schemes studied in eight stage compressor meanline model. 91

3-16 Eight stage efficiency map, with and without cooling. Dash-dot line is adiabatic; solid line is $q^* = -0.01$ in last two stages; dashed line is $q^* = -0.0025$ in all stages; solid line with circles is $q^* = -0.01$ in first two stages. 100%, 80%, and 60% N_c lines are shown. 92

3-17 Eight stage compressor map, with and without cooling. Solid red line is adiabatic; Dashed-dot green line is $q^* = -0.01$ in last two stages; Dashed blue line is $q^* = -0.0025$ in all stages; Solid black line is $q^* = -0.01$ in first two stages. 100%, 80%, and 60% N_c lines are shown. 93

3-18 Rotor 35 geometry and boundary conditions (single passage periodic) for non-adiabatic case. Filled static temperature contours on wall boundaries (hub, casing, and blade surfaces) show BC of 100 K on blade and middle portion of outer casing surface. Positive x-axis is downstream axial direction. 97

3-19 Rotor 35 pressure ratio map. 98

3-20 Rotor 35 efficiency map. 100

3-21 Blade surface non-dimensional heat transfer per unit solidity vs. wall temperature at various turbulent Reynolds numbers, generated using Reynolds analogy over a flat plate. 102

4-1 Comparison between Cambridge-MIT Silent Aircraft conceptual design with embedded engines, a blended wing body (BWB) aircraft with podded engines, and a conventional tube and wing aircraft. 109

4-2 Polar directivity plot of Lockheed L-1011 overall sound pressure level (OASPL) for two different flap angle settings, suggesting a strong correlation between noise and drag. Figure adopted from Smith [81]. 111

4-3 Aircraft force balance on approach. 115

4-4 Iso-contours of quiet drag coefficient, $C_{D,\text{quiet}}$ (black) and estimated noise reduction (red) as a function of velocity ratio and approach angle for $C_{D,0} = 0.01$, $\theta_{\text{ref}} = 3°$, and $V_{ref} = 1.23 \cdot V_{stall} = 60.8$ m/s, per Equation 4.10. SAX landing weight is 125,000 kg, wing area is 836 m^2, and k for the drag polar is 0.064. Blue arrows indicate three different means to achieve 5 dB noise reduction. 117

4-5 Drag-generating swirling flow concepts. 121

4-6 Propulsion system integrated swirl tube concept with deployable swirl vanes, having functionality to actuate to a closed position to serve as a thrust reverser blocker door. 122

4-7 Control volume of cross sectional area, A, around ducted quiet drag device containing an actuator disk. Pylon holds device in static equilibrium relative to freestream flow. Stations u and d are far upstream of device and at the duct exit, respectively. Stations 1 and 2 are just upstream and downstream of actuator disk, respectively. A_f and A_d are actuator disk face area and duct exit area, respectively. 127

4-8 Drag coefficient as a function of throttling parameters $V_{z,d}/V_\infty$ and ω for purely axial exhaust flow for different area ratios. Peak drag coefficient equals 0.5 times area ratio, implying an exit area increase leads to higher maximum drag. 131

4-9 Drag coefficient breakdown for purely axial exhaust flow devices indicates that total drag is comprised of a drag force on the actuator disk and a thrust force on the nacelle. Shaded area indicates likely region of vortex shedding instability, as suggested by Figure 4-10. 132

4-10 Instantaneous unsteady contours of dimensionless entropy, $T_{t,\infty}s/V_\infty^2$, on 2D CFD of deficit flow with varying velocity ratio at device scale Reynolds number. Nozzle height is 2.16 meters. Computations indicate that vortex shedding instability develops at velocity ratios $\lesssim 0.25$. 133

4-11 Types of vortex breakdown, adopted from Leibovich [48]. 137

4-12 Types of vortex breakdown from low to high swirl, adopted from Hall [28] based on the photographs of Sarpkaya [74]. 138

4-13 Profiles of axial velocity, circumferential velocity, pressure coefficient, and swirl parameter for analytical swirl tube model with Burger vortex exit flow parameters of $\omega = -\Delta p_t/q_\infty = 0.08$, $r^*_{crit} = 0.50$, and $K^*_c = 0.77$, yielding drag coefficient of $C_D = 0.8$. 146

4-14 Contours of predicted total drag coefficient (C_D, dashed red) and swirl parameter at $r = r_{crit}$ (S, solid black) in (K^*_c, r^*_{crit}) space for ram pressure driven swirl tube having $\omega = 0.08$. Triangle indicates point with $C_D = 0.8$ and $r_{crit} = 0.5$, whose radial profiles are presented in Figure 4-13. Heavy, dashed blue line indicates $(K^*_c)_{\max}$ threshold. 148

4-15 Contours of predicted total drag coefficient (C_D, dashed red) and capture streamtube to actuator disk area ratio (A_{capt}/A_f, solid black) in (K^*_c, r^*_{crit}) space for ram pressure driven swirl tube having $\omega = 0.08$. Triangle indicates point with $C_D = 0.8$ and $r_{crit} = 0.5$. Heavy, dashed blue line indicates $(K^*_c)_{\max}$ threshold. 149

4-16 Contours of predicted drag coefficients from pressure defect ($C_{D,\text{press.}}$, solid black) and net axial momentum flux ($C_{D,\text{ax. mom.}}$, dashed red) in (K^*_c, r^*_{crit}) space for ram pressure driven swirl tube having $\omega = 0.08$. Triangle indicates point with $C_D = 0.8$ and $r_{crit} = 0.5$. Heavy, dashed blue line indicates $(K^*_c)_{\max}$ threshold. 150

4-17 Contours of predicted total drag coefficient (C_D) in (S, ω) space for ram pressure driven swirl tube having $r/r_{crit} = 0.5$. 151

4-18 Contours of predicted total drag coefficient, C_D (dashed red), and swirl parameter, S (solid black), in $(K^*_c, \Delta p_t/q_\infty)$ space for pumped or throttled swirl tube with $r/r_{crit} = 0.5$. Dashed blue line indicates $(K^*_c)_{\max}$ threshold. 152

4-19 Comparison between conventional fan engine at approach idle plus stand alone, ram pressure driven swirl tube versus pumped swirl tube, for $\pi_{fan} = 1.06$, $M_\infty = 0.17$, $A_d/A_f = 1$, suggests that pumping of swirl vanes generates greater effective drag in the form of thrust reduction. 153

4-20 Contours of predicted total drag coefficient, C_D (dashed red), and capture streamtube to actuator disk area ratio, A_{capt}/A_f (solid black), in $(K_c^*, \Delta p_t/q_\infty)$ space for pumped or throttled swirl tube with $r/r_{crit} = 0.5$. Dashed blue line indicates $(K_c^*)_{\max}$ threshold. 154

5-1 Swirl tube technical roadmap. 161

5-2 Nacelle and centerbody geometry. Dotted red line shows cross-sectional area variation normalized to annulus area at $z/r_f = 0$ (actuator disk position). . . 165

5-3 MTFlow pressure coefficient (C_p) distributions for supercritical and subcritical (vortex breakdown) swirling flow. 167

5-4 Contours of MTFLOW computed total drag coefficient (C_D, dashed red) and duct exit swirl parameter at $\psi = \psi_{crit}$ (S, solid black) in (K_c^*, r_{crit}^*) space for ram pressure driven swirl tube having $\omega = 0.08$. Triangular and circular symbols represent converged ($K_c^* = 0.77, r_{crit}^* = 0.7$) and unconverged ($K_c^* = 1.10, r_{crit}^* = 0.7$) cases shown in Figure 5-3. Dashed blue line demarcates boundary between converged and unconverged solutions. 169

5-5 Example of sectional vane design for inlet (upstream) angle, θ_u, of 0°, exit (downstream) angle, θ_d, of 60° and solidity, σ, of 3. The pressure side (red), is defined using a Bezier spline. Suction side (green) is defined by the area distribution of circles. Leading (black) and trailing (magenta) edges are 3:1 half-ellipses. 173

5-6 Examples of sectional vane design. 174

5-7 Loss factor and Zweifel coefficient as a function of axial chord to spacing for two types of turbine vanes. Design range is shaded. The plot suggests that a turbine vane with inlet and exit angles of 0° and 60°, respectively, and axial chord-to-spacing ratios of 2.6 to 4 has sufficient Zweifel coefficient and reasonably low losses. Figure adopted from Kerrebrock [47] 174

5-8 Typical CFD domain replicated to show ten periodic passages. 176

5-9 Mach number on periodic boundary of CFD cases. 178

5-10 Swirl parameter on periodic boundary of CFD cases. 179

5-11 Pressure coefficient on periodic boundary of CFD cases. 179

5-12 Pressure coefficient, C_p, on surfaces of swirl tube with 47° vane angle show low pressure at vane hub and aft centerbody. Radial extent of pressure defect is seen in plane 0.5 duct diameters downstream of exit. Maximum pressure defect in downstream plane is $C_p \approx -3.5$. 180

5-13 MTFlow vs CFD comparisons for case with 47° swirl vanes. 181

5-14 WBWT wind tunnel experimental set-up. 184

5-15 Flow visualization close to the centerline axis identifies a coherent vortex core within a steady swirling flow for the stable flow cases (34°, 41°, and 47° swirl vanes) and a large unsteady core for the cases with vortex breakdown (57° and 64° swirl vanes). 185

5-16 Flow visualization at the outer radius identifies a tightly spiraling, steady swirling flow for stable cases (34°, 41°, and 47° swirl vanes) and indirectly infers an outer coherent swirling flow for vortex breakdown cases (57° and 64° swirl vanes). 186

5-17 Hot-wire traverse locations for steady and unsteady measurements. All measurements are taken in the vertical plane that passes through the swirl tube centerline. 188

5-18 Axial velocity, circumferential velocity, and computed swirl parameter (S) vs. radial location for case with 34° swirl vanes. Top row, $z/D = 0.5$, bottom row $z/D = 1.0$. 189

5-19 Axial velocity, circumferential velocity, and computed swirl parameter (S) vs. radial location for case with 47° swirl vanes. Top row, $z/D = 0.5$, bottom row $z/D = 1.0$. 190

5-20 Axial velocity, circumferential velocity, and computed swirl parameter (S) vs. radial location for case with 57° swirl vanes. Top row, $z/D = 0.5$, bottom row $z/D = 1.0$. 191

5-21 Power spectra of unsteady axial and tangential velocity in core region, $r^* = 0$, at axial location one diameter downstream of nozzle exit, $z/D = 1.0$. Data is presented at constant bandwidth of 2.44 Hz. 192

5-22 Power spectra of unsteady axial and tangential velocity in shear layer region, $r^* = 1$, at axial location one diameter downstream of nozzle exit, $z/D = 1.0$. 193

5-23 Model-scale drag coefficient vs. swirl vane angle shows measured drag coefficient of 0.83 for highest stable flow swirl vane angle (47°). CFD drag coefficient adjusted for model-scale is shown for converged, stable flow cases (34°, 47°, and 53° swirl vane angles). 198

5-24 Comparison between computed jet noise spectra using Tam's fine scale turbulence noise source, Morris-Farassat source term, and Stone and SAE round single jet empirical models. Jet diameter is 1 meter. Spectra scaled to $r = 1$ m, for an observer angle of $\theta = 90°$. 205

5-25 Hybrid Tam + Tanna model prediction of stable swirling flow noise using 2D CFD computation of swirl tube aft geometry. QFF facility background included for reference. One-third octave band spectra corrected to 1 meter observer distance at 90° observer location. 208

5-26 Spectral density integrand (at predicted peak noise frequency) for two-dimensional CFD of swirl tube exit flowfield for case of 47° swirl vanes. Freestream Mach number is set to 0.17. Axis units are in meters, based on full-scale CFD geometry of 2.16 m swirl vane outer diameter. 209

5-27 Photographs of NASA LaRC QFF setup. 210

5-28 QFF directional array polar arc variation capabilities, adopted from [9]. Medium Aperture Directional Array (MADA) is depicted relative to the free jet with swirl tube model installed. Vertical free jet flow is from bottom to top. In this thesis, all data are presented with array in $\theta = -90°$ position. 211

5-29 Full-scale (1.2 m diameter) drag coefficient (C_D) and overall sound pressure level (OASPL) vs. swirl angle suggests that a high-drag, low-noise configuration exists at swirl vane angle of 47°. Freestream Mach number for OASPL is 0.17. Observer location is 120 m from the source, at sideline angle of $\theta = -90°$ (see Figure 5-28). 213

5-30 Model-scale spectra at 47° and 57°, Mach=0.17, $\theta = -90°$. 215

5-31 Overall spectral comparison of all swirl tube configurations, constant 17.44 Hz bandwidth, Mach=0.17, $\theta = -90°$. 216

5-32 Full-scale third-octave band autospectra at 47° and 57°, Mach=0.17, $\theta = -90°$. 219

5-33 Mach number scaling of 47° spectra assuming different scaling exponents, n, per Equation 5.18. All spectra are presented non-dimensionally in a dB/St basis basis. 220

5-34 Mach number scaling of 57° spectra assuming $n = 7.5$ power law, per Equation 5.18. All spectra are presented non-dimensionally in a dB/St basis. Good collapse is suggested for $15 < St < 100$. 221

5-35 DAMAS integration zones. Zones 1, 2, and 3 correspond to aft, fore, and pylon regions, respectively. 223

5-36 DAMAS zone-integrated spectra and source maps, 47° swirl vane angle case, $M = 0.17$, $\theta = -90°$. 224

5-37 DAMAS zone-integrated spectra and source maps, 57° swirl vane angle case, $M = 0.17$, $\theta = -90°$. 225
5-38 Iso-contours of the thrust coefficient (C_T) and captured streamtube area ratio, for various approach idle pressure ratios and assumed fan stage efficiencies. Approach Mach number is 0.17. 229
5-39 Thrust reduction comparison between engine and stand alone, ram pressure-driven swirl tube (configuration 1) versus propulsion system-integrated swirl vanes (pumped swirl tube, configuration 2). 230
5-40 Swirl parameter on periodic boundary of ram pressure driven and pumped swirl tube CFD cases, $\pi = 1.08$. 231
5-41 Mach number on periodic boundary of ram pressure driven and pumped swirl tube CFD cases, $\pi = 1.08$. 231
5-42 Graphical depiction showing that the effective drag coefficient from a pumped swirl tube is approximately the difference between the total drag coefficient and the actuator disk drag coefficient on the fan stage. Negative numbers indicate net forces in the thrust direction. Freestream Mach number is 0.17. 233
5-43 SAX landing roll velocity vs. distance. 240

List of Tables

3.1 Average effect of $q^* = -0.001$ on flow turning for cascade 1, across a range of incidences. 72

3.2 Key single stage fan map parameters at points a through h, as shown in Figure 3-13. The variables M, i, $\Delta\delta$, and ω are Mach number, incidence, deviation change, and total pressure reduction coefficient, respectively. The subscripts *in* and *out* correspond to the inlet and outlet, respectively. The subscripts R and S correspond to the rotor and stator, respectively 89

3.3 Key eight stage compressor map parameters at adiabatic points i through n, as shown in Figure 3-17. From top to bottom, sub-tables show rotor incidence, stator incidence, rotor inlet Mach number, and stator inlet Mach number, respectively. 94

3.4 Eight stage compressor cooling scheme summary for design corrected speed line (100% N_c) and design corrected mass flow. 95

4.1 Silent drag similarity across several aircraft types. The two right most columns show drag coefficient required to change conventional 3° glideslope to 6°, in terms of wing area and propulsion system fan area. Fan area includes fan spinner. All numbers are approximate. 120

5.1 Maximum vane turning angle (rounded to nearest degree) associated with drag coefficient computed by MTFLOW. 172

5.2 MTFLOW vs. CFD drag coefficient comparison. Total drag coefficient is given by C_D. Pressure and viscous drag coefficients are given as $C_{D,\text{press.}}$ and $C_{D,\text{visc.}}$, respectively. 182
5.3 WBWT test matrix. 184
5.4 Table of measured and CFD computed drag coefficients for model-scale geometry. All C_D values are referenced to the axially projected swirl vane annulus area. CFD values of viscous drag coefficient, $C_{D,\text{visc.}}$, are corrected to model-scale using Reynolds number correction of Equation 5.4. Pylon drag is shown for reference only, and is subtracted out of all other cases. 196
5.5 Pumped swirl tube drag coefficient comparison and breakdown. 233
5.6 Braking coefficient summary reproduced from Raymer [70], assuming the conservative scenario of worn brakes. 236
5.7 Landing roll lengths in meters for various scenarios. Published values from Jane's [44] included for comparison. 239

Nomenclature

Roman

a	Speed of sound
A	Area
c	Chord length; convective speed; speed of sound
c_ℓ	Length scale constant in Tam et al. fine-scale turbulence jet-noise model
c_p	Specific heat at constant pressure
c_τ	Time scale constant in Tam et al. fine-scale turbulence jet-noise model
C_D	Drag coefficient
C_f	Skin friction coefficient
C_L	Lift coefficient
C_p	Pressure coefficient
C_T	Thrust coefficient
C_W	Weight coefficient
D	Drag; diameter
f	Frequency
F	Thrust; force; function
g	Gravitational acceleration constant
h	Specific enthalpy; altitude
i	Incidence angle; Einstein summation convention index
k	Induced drag constant; Turbulence kinetic energy; coefficient

K	Induced drag constant; Circulation (rV_θ)
ℓ	Length scale
L	Lift
m	Mass
$\dot{m}$	Mass flow
M	Mach Number
n	Power law exponent
$\vec{n}$	Unit normal vector
N	Number of blades/vanes
N_c	Corrected rotor speed
p	Pressure
p_t	Stagnation pressure
q	Dynamic pressure; heat transfer per unit mass
q^*	Non-dimensional heat transfer rate
$\overline{q}_w$	Average wall heat flux (heat transfer rate per unit surface area)
$\dot{Q}$	Heat transfer rate
r	radius, radial coordinate; distance from sound source
R	Ideal gas constant (per unit mass)
Re	Reynolds number
s	Specific entropy
S	Swirl parameter; area; wetted area; spectral density
St	Stanton number
T	Temperature; thrust
T_0	Ambient temperature
T_{ij}	Lighthill stress tensor
T_t	Stagnation temperature
$\mathcal{T}_x$	Axial torque
u	Velocity

V	Velocity
w_{sh}	Shaft work
W	Weight
$\vec{x}$	Observer location
z	Axial coordinate

Greek

α	Swirl angle; angle of attack; Tanna noise modeling parameter
β	Flow angle
γ	Ratio of specific heats
Γ	Circulation
δ	Deviation angle
δ_{ij}	Kronecker delta
Δ	Difference or change in
ϵ	Small perturbation; Dissipation rate ($k-\epsilon$ turbulence model)
η	Efficiency, induced drag exponent
θ	Temperature ratio; circumferential coordinate; polar angle; glideslope angle
μ	Density
ν	Radian frequency
π	Pressure ratio
ρ	Density
σ	Solidity
τ	Temperature ratio; viscous stress; time scale
ϕ	Equivalence ratio
χ	Metal angle
ψ	Streamfunction; observer angle

Ψ	Streamfunction for quasi-cylindrical flow
Ω	Total pressure reduction coefficient; rotational frequency
ω	Rotational shaft speed

Subscripts

$_0$	Ambient condition
$_a$	Adiabatic; adjoint Greens function
$_{a.d.}$	Actuator disk
$_b$	Blade row
$_c$	Compressor face; based on chord length
$_{capt}$	Captured streamtube
$_{comp}$	Compressor face
$_{cool}$	Cooling
$_{crit}$	Critical value
$_d$	Downstream; discharge (duct exit)
$_D$	Drag
$_f$	Fan or actuator disk face
$_{gen}$	(Entropy) generation
$_H$	Hub
$_{in}$	Inlet, inflow
$_{lam}$	Laminar
$_{max}$	Maximum
$_{na}$	Non-adiabatic
$_{out}$	Outlet, outflow
$_{\text{press.}}$	Pressure component
$_{\text{quiet}}$	Used with C_D for quiet drag

$_r$	Radial direction
$_{ref}$	Reference condition
$_{rev}$	Reversible
$_R$	Rotor
$_S$	Stator
$_T$	Tip
$_{turb}$	Turbulent
$_u$	Upstream
$_{\text{visc.}}$	Viscous component
$_w$	Wing
$_{wall}$	Wall value
$_z$	Axial direction
$_\theta$	Circumferential direction

Superscripts

*	Non-dimensional quantity

Acronyms

BC	Boundary Condition
BWB	Blended Wing Body Aircraft
CCTJ	Compressor-cooled Turbojet
CFD	Computational Fluid Dynamics
CMI	Cambridge-MIT Institute
HCTJ	Hybrid-cooled Turbojet
LHS	Left Hand Side

MADA	Medium Aperture Directional Array
OASPL	Overall Sound Pressure Level
PCTJ	Pre-cooled Turbojet
QFF	NASA Langley Quiet Flow Facility
RANS	Reynolds Averaged Navier-Stokes Equations
RHS	Right Hand Side
SAE/ARP	Society of Automotive Engineers/Aerospace Recommended Practice
SAI	Silent Aircraft Initiative
SAX	Silent Aircraft eXperimental Design
SPL	Sound Pressure Level
SSTJ	Single Spool Turbojet
WBWT	Wright Brothers Wind Tunnel

Symbols

∇	Del operator
∞	Freestream value

Chapter 1

Introduction

1.1 Background

Aircraft design is driven by mission requirements. The mission profile, i.e. the position-time history through the flight envelope, may depend on myriad requirements such as (i) payload capacity, (ii) fuel economy, (iii) time to achieve a certain objective, (iv) structural loading, (v) maximum flight speed, and (vi) maneuverability. In addition to these, noise and emissions are now at the forefront of technology efforts to minimize adverse environmental impacts. All aircraft missions, military or commercial, involve a compromise of these and other requirements.

Conventional aircraft design largely separates the airframe design from the powerplant. This occurs in part because conventional tube and wing designs have relatively little interference between airframe and engine air flows. Today, however, there is increased demand for unconventional missions, for which vehicle design must be heavily integrated at the system level.

This thesis presents novel turbomachinery design concepts for two such missions: 1) a low-to-high Mach number (4+) flight vehicle and 2) a functionally silent[1] aircraft. The first mission addresses the need for the next generation of space-access and high speed interceptor

[1]Here, the term functionally silent means quieter than the background noise of a well populated urban area.

vehicles, while the second mission addresses the need for sustained or increased commercial passenger capacity in the face of increasing population densities near airports and associated community noise complaints.

For the low-to-high flight Mach number mission, the concept of blade passage surface heat extraction, so-called compressor cooling, is conceived and assessed as a means to improve fan/compressor performance, operability, and durability. The idea of compressor cooling is conceived as a means to sustain the production of specific thrust at high Mach number, because it can both improve the compressor's performance as well as reduce compressor exit temperatures, allowing heat addition without violating engine hot section temperature limits.

For the functionally silent aircraft mission, a quiet drag device utilizing ducted swirl vanes, a so-called swirl tube, is conceived, designed, and validated as a means to achieve the drag necessary for a next-generation aircraft to fly a slower and steeper approach profile in clean airframe configuration. Flying such a trajectory potentially reduces noise source strength and increases the attenuation during propagation to the ground. This device is a key enabler to reducing the need to generate drag on approach through conventional devices such as flaps, slats, and landing gear, which generally have a strong correlation between drag and noise.

1.2 Thesis Contributions

The primary contributions of the thesis are:

Compressor Cooling

1. Assessment of the effects of heat extraction on blade passage performance metrics.

2. Development of a first-of-its-kind compressor meanline modeling framework with heat extraction to assess the on- and off-design behavior of a cooled axial compressor.

3. Explanation of the causality between performance implications of heat extraction in blade passage flows and the behavior of an axial compressor, including a CFD simulation of a three-dimensional rotor passage of practical interest.

4. Establishment of new efficiency metrics for compressors with heat extraction, substantiated by a bookkeeping of entropy generation from viscous and thermal dissipation.

Swirl Tube

1. Successful demonstration of quiet drag coefficient of 0.8 with overall A-weighted sound pressure level (OASPL) of 42 dBA from a full-scale swirl tube.

2. Quantification of the relationship between swirl angle, drag, and noise for a family of swirl tube designs.

3. Identification and quantification of acoustic sources associated with the swirling outflow of a ram pressure driven swirl tube.

4. Identification of the limitations imposed by the vortex breakdown phenomenon on swirl tube aerodynamic and acoustic performance.

5. Preliminary description of the propulsion-system integrated effect of a fan driven swirl drag device for slow, steep approaches to reduce aircraft approach noise.

6. Recommendation to integrate swirl vanes into a thrust reverser system to achieve the dual functionality of drag on approach and thrust reverser blocker doors during landing.

1.3 Synopsis of Thesis Chapters

The thesis is comprised of two major bodies of work, each presented in two chapters. Chapters 2 and 3 present the ideas and outcomes of the compressor cooling project. Chapters 4 and 5 present the ideas and outcomes of the swirl tube project. A description of the remaining chapters is provided below for the reader's guidance.

Compressor Cooling

Chapter 2. This chapter presents background and preliminary analysis of low-to-high flight Mach number propulsion system configurations to motivate the concept of compressor cooling. A selected literature review of combined cycle powerplant concepts indicates that heat extraction, in the form of compression pre-cooling, has been recommended by numerous authors to extend the vehicle operational Mach number envelope. Compressor cooling, i.e., heat extraction within compressor blade passages is thus proposed as a means to achieve the benefits associated with pre-cooling, without introducing new loss-generating surfaces within the engine gas path. Analysis indicates that scenarios may exist that favor compressor cooling or hybrid compressor/pre-cooling, over simple pre-cooling, suggesting benefits in aero-thermodynamic performance, operability, and durability. This motivates a detailed component level performance study to quantify these benefits.

Chapter 3. This chapter assesses the performance of a cooled compressor through computational experiments and meanline modeling. Computational fluid dynamics (CFD) experiments on two prismatic cascade geometries provide blade passage performance figures of merit with and without cooling. Conventional figures of merit, loss and deviation, are quantified along with the two sources of entropy generation, viscous and thermal dissipation. The performance metrics form the basis of a generic set of performance rules that are applied to the on- and off-design analysis of an axial compressor with heat extraction. Pressure ratio and efficiency maps are presented for a single- and eight-stage axial compressor. A three-dimensional rotor computation on a geometry of practical interest is then presented to demonstrate that the meanline modeled results are in accord with high-fidelity computations. A heat transfer study quantifies the opportunity for blade passage heat exchange and elucidates the practical challenges that must be overcome in cooled compressor design. The chapter ends with a discussion of appropriate efficiency metrics for cooled compressors.

Swirl Tube

Chapter 4. This chapter presents the issues and challenges associated with the design of a functionally silent aircraft, i.e., one whose noise signature is well below the background noise of a well populated urban environment. A slow and steep approach profile in clean airframe configuration is identified as a means to achieve a step reduction in noise, but requires the introduction of devices that generate quiet drag. A ram pressure or fan driven ducted device that creates high drag by generating a steady swirling outflow is proposed. The ram pressure driven device is referred to as a swirl tube, while the fan driven device is referred to as a pumped swirl tube. A first principles control volume analysis suggests that the swirl tube generates drag coefficients comparable to bluff bodies by swirling the flow close to but not in excess of the vortex breakdown instability criterion. This motivates a detailed aerodynamic design and aerodynamic and acoustic validation of a model-scale swirl tube in Chapter 5.

Chapter 5. This chapter presents the detailed aerodynamic design of the swirl tube, and the scale model validation through aerodynamic and acoustic testing. In addition, propulsion-system integration is explored for a pumped swirl tube that is incorporated into the bypass or mixing duct of a high bypass ratio turbofan engine. The aerodynamic design begins with an axisymmetric, inviscid streamline curvature based tool that provides swirl vane exit angles for a range of drag levels. This output leads to three-dimensional vane designs for a family of swirl tubes. Three-dimensional viscous RANS CFD computations are then performed to predict the onset of vortex breakdown and the exit flow profiles. Model-scale wind tunnel tests validate the aerodynamic design, using flow visualization, drag measurements, and exit velocity profile mapping. The swirl tube noise signature is then quantified at the state-of-the-art Quiet Flow Facility (QFF) at NASA Langley Research Center. The swirl tube is found to be a viable quiet drag device with full-scale approach noise signature below the background noise of a well-populated urban area. The chapter finishes with a study of propulsion system-integration effects. A recommendation is put forth to incorporate swirl vanes into a turbofan bypass duct, with the dual function of quiet drag generation

on approach and thrust reverser blocker door capability on the landing roll.

Chapter 6.

Chapter 6 summarizes the thesis, lists the research contributions, and provides recommendations for future work.

Chapter 2

Mission 1: Low-to-High Mach Number Flight

This chapter presents an overview of the challenges associated with low-to-high Mach number (4+) flight vehicles, in order to motivate the idea of compressor cooling, a novel turbomachinery concept to potentially extend the maximum operational flight Mach number of turbomachinery-based propulsion systems. For air-breathing turbomachinery-based propulsion systems, the ram temperature increase with increasing flight Mach number is shown to limit production of specific thrust because material temperature limits prevent addition of fuel in the combustion process. A review of combined cycle concepts to address these challenges includes an analysis of the pre-cooled turbojet (PCTJ), a concept that extracts heat upstream of the compression process, usually with an on-board heat sink or by mass-injection, to increase the cycle operating envelope. The PCTJ motivates the idea of compressor cooling, i.e., heat extraction within the blade passages of the compressor itself. Improvements in compressor and overall cycle performance are hypothesized, suggesting the opportunity to improve on the PCTJ concept by compressor cooling alone or in tandem with pre-cooling. The component-level assessment of axial compressor performance with blade surface heat extraction in Chapter 3 is thus motivated.

2.1 Overview

A large portion of turbomachinery research has focused on aircraft turbine engine applications. The resulting scientific body of knowledge has enabled the design and development of aircraft engine turbomachinery components with improved performance, at lower cost, and in reduced time. Turbomachinery for wide flight Mach number applications such as those needed to access space, however, must operate under very different conditions of temperature, pressure and mass flow. Specifically, this type of turbomachinery must meet performance requirements along an ever changing set of flight Mach numbers, and hence, inlet stagnation temperatures and pressures. This stands in direct contrast to the fixed design point cruise-type missions for which most aircraft engine turbomachinery components are optimized. For example, in order to operate a compressor adiabatically at a fixed compressor map condition throughout the mission, the compressor would need both: (1) a robust inlet airflow delivery system and (2) performance capability at a wide range of mechanical speeds. This research effort is thus motivated by the need to determine the potential of turbomachinery for operation across wide flight Mach number ranges; specifically, its role in a hypothetical two-stage-to-orbit (TSTO), horizontal take-off-propulsion system, as well as in a high-speed interceptor.

While work has been pursued on various aspects of propulsion systems for high Mach number flight, to the author's knowledge relatively little effort has been devoted to exploring the utility of high flight Mach number turbomachinery within the context of integrated vehicle-propulsion systems. The drivers that set the performance and operability of compressors for high Mach number flight (1.5 to 5) are very different from those of compressors for subsonic and transonic flow regimes. The large change in inlet temperature as the flight Mach number increases poses several key challenges that must be addressed adequately if the turbomachinery components are to maintain acceptable levels of performance along the mission profile.

This research thus requires a preliminary analysis of integrated airframe/propulsion system performance to motivate a component level analysis of a novel turbomachinery concept

aimed at cycle performance improvements to increase the mission operational Mach number. This involves first examining a specific propulsion system configuration to assess the system benefits of turbomachinery for flight from earth through the upper atmosphere. This serves to identify the challenges, design issues and constraints that must be overcome and addressed to meet the operational requirements, and to define the critical elements of a propulsion system that uses turbomachinery. A potential enabler that emerges from the analysis is the idea of compressor cooling. Heat extraction in the blade passages is hypothesized to improve aero-thermodynamic performance, operability, and durability. The focus of Chapter 3 is thus the component level performance of a cooled compressor.

The remainder of this chapter is organized as follows. Section 2.2 presents a selected literature review of combined cycle powerplant concepts that have been applied to the challenge of high-speed flight. The pre-cooled turbojet (PCTJ) is a particular cycle that has received attention because it takes advantage of an on-board heat sink, such as the fuel, to increase the heat addition capability within the combustion process and therby increase specific thrust. Section 2.3 then defines a constant dynamic pressure mission trajectory based on vehicle structural requirements, as a baseline to quantify the PCTJ cycle benefits. The PCTJ cycle is analyzed along the mission profile in Section 2.4. Anticipated benefits include an increase in available specific thrust and a reduction in required specific thrust, enabling a potential increase of the flight envelope to Mach 4+.

Section 2.5 introduces the idea of compressor cooling, a novel turbomachinery concept to enable high speed flight. It is hypothesized that heat extraction within the compressor blade passages provides aerodynamic and thermodynamic cycle benefits, independently or in tandem with pre-cooling. Two cycle concepts are proposed: 1) a compressor cooled turbojet (CCTJ) that exclusively extracts heat within the compressor, and 2) a hybrid cooled turbojet (HCTJ), that has tandem pre-cooling and compressor cooling. A comparison of 1) non-ideal pre-cooling followed by isentropic compression versus 2) isentropic compression followed by lossless post-cooling suggests that scenarios may exist that favor the CCTJ or HCTJ over the PCTJ. A one dimensional control volume model suggests that heat extraction within

a diffusing blade passage will increase the pressure rise across the passage, as well as the total pressure. This is consistent with quasi-one dimensional compressible flow analysis, the so-called Rayleigh line. Research questions to determine the feasibility of compressor cooling are thus posed. This motivates the computational experiments and meanline modeling in Chapter 3 to assess what effect heat extraction has on axial compressor performance.

2.2 Previous Work

A selected literature review is presented in this section to survey the progress made in the area of high-speed vehicle propulsion systems. The sources referred to in this literature review are not exhaustive, but do represent a good cross-sectional sample of work to date on this topic. Much ingenuity over the past decades has resulted in a broad range of conceptual designs. The focus in this review will be on designs that incorporate heat extraction as a means to enhance compressive processes and push the operational limits of turbomachinery-based propulsion systems.

Some variable cycle turbomachinery-based propulsion systems from takeoff to high-speed flight are reviewed and described in Heiser[31] and Johnson[46]. Many concepts that are described fall under the heading of combined cycle engines, i.e., engines that integrate multiple propulsion concepts within the same internal flowpath. Different combined cycle concepts include the combination of turbojets and ramjets (turboramjet), or the former plus a rocket motor (turboramjet rocket). Another concept that is commonly found in the literature is the liquid air cycle engine (LACE), which uses cryogenic liquid hydrogen fuel to produce liquid air (oxidizer) via a heat exchanger, and then reacts the fuel and oxidizer inside a rocket engine to produce thrust. Another concept, the inverse cycle engine (ICE) also appears in various studies. This concept is unique in that the inlet airflow is first expanded through a turbine and then passed through a heat exchanger (cooler) before being compressed, burned and expanded through a nozzle. Both the turbine expansion and heat exchange processes serve to lower the compressor inlet temperature. Although theoretically capable of producing thrust at high Mach numbers, the ICE's main drawback is that it can not produce adequate

subsonic thrust, thereby preventing it from being a stand-alone system.

Yet another concept that has potential as a stand-alone low-to-high Mach number propulsion system is the pre-cooled turbojet (PCTJ), or the pre-cooled turbojet with reheat (afterburning). The use of pre-cooling to stretch the SSTJ operating envelope to Mach 5 or 6 is not new, and is discussed in several sources[32, 43, 66, 73, 84, 86]. As it may involve straightforward modifications to existing turbojet engines, it is an attractive concept in its own right. A brief review of the finding of some of the studies of cycles utilizing compressor pre-cooling is presented below.

Hewitt and Johnson [32] cite potential compressor inlet temperature reductions from pre-cooling to be about 300 K, for a stoichiometric fuel flow of LH_2 used as coolant on a turbojet with 16:1 pressure ratio and 2000 K turbine inlet temperature. This effectively reduces Mach 4 compressor inlet temperatures to Mach 3 values, and increases the operating envelope. Overfueling (equivalence ratio, $\phi > 1$) is cited as a means to get to Mach 5.

Rudakov [73] also mentions "relatively insignificant air cooling", with turbojet pre-cooler air temperature reductions of $40 - 100K$ ($\phi = 1$), to achieve cruise Mach numbers from 3 to 5, with slightly improved specific impulse.

Powell and Glickstein [66] report a Mach number operating range increase through pre-cooling. Their study is focused on the turbojet with afterburning. They conclude that pre-cooling can increase the operating Mach number from 4 to 5, at the expense of system weight penalties. The potential for cooling in their study is also linked to fuel flow (LH_2). Overfueling is also considered. The overfueled cases ($\phi = 2, 3$) show significantly less specific impulse than the pre-cooled turbojet with stoichiometric fuel consumption or even the simple turbojet.

Sreenath [84] presents a mission analysis for the pre-cooled turbojet (with and without afterburning) and the ICE. Two fuel/coolant concepts are considered for the pre-cooled engines: (1) liquid hydrogen (LH_2) as both fuel and coolant, and (2) kerosene fuel with water as coolant. In the case of the water cooled cycle, the heated water is used to generate additional thrust after passing through the pre-cooler. Therefore, it figures into the fuel

flow rate, and the pre-cooled cycles produce less specific impulse than the simple cycle counterparts. Both the pre-cooled turbojet and the ICE are found to greatly increase the maximum Mach number capability of a hypothetical flight vehicle. At Mach 6, the ICE is found to be superior to the pre-cooled, afterburning turbojet, while at Mach 4 the opposite is true. In general, it is concluded that the pre-cooled, afterburning turbojet can operate successfully over the speed range of Mach 0 to 6.

Most recently, researchers at the Institute of Space and Astronautical Science (ISAS) in Japan have engaged in a systematic development and design of an air-turbo ramjet (ATREX) engine [43, 75, 86, 93] for a TSTO space access vehicle [60, 76]. A key technology of this engine is a pre-cooler [29], with much development effort focused on the challenges of total pressure loss and adequate heat transfer. These practical considerations suggest that technology readiness for pre-cooled turbojet applications has advanced significantly through this effort.

The examples of pre-cooled compression cycles provide a good starting point for studying the potential cycle benefits associated with enhancing compressive shaft work through cooling. To the author's knowledge, there exist no examples in the literature of cooling within the compressor itself, i.e., across the blade passage surfaces. Combining the compression and heat transfer function is attractive because loss generating surfaces from a pre-cooler may be reduced or eliminated. Hence it is the focus of this thesis research. In Section 2.3 a representative mission is used as the basis for establishing requirements for a hypothetical PCTJ mission that is discussed in Section 2.4. These requirements establish a logical framework to introduce the idea of compressor cooling in Section 2.5.

2.3 Mission Profile

The first step in a vehicle analysis is to define a mission profile. Here, the term mission profile corresponds to the vehicle trajectory definition in the Mach number-altitude plane. The trajectory for a low-to-high Mach number aircraft depends on the vehicle's intended mission. Several types of mission profiles could be considered for a wide flight Mach number vehicle: (1) a minimum fuel to climb mission may be appropriate for a two-stage-to-orbit

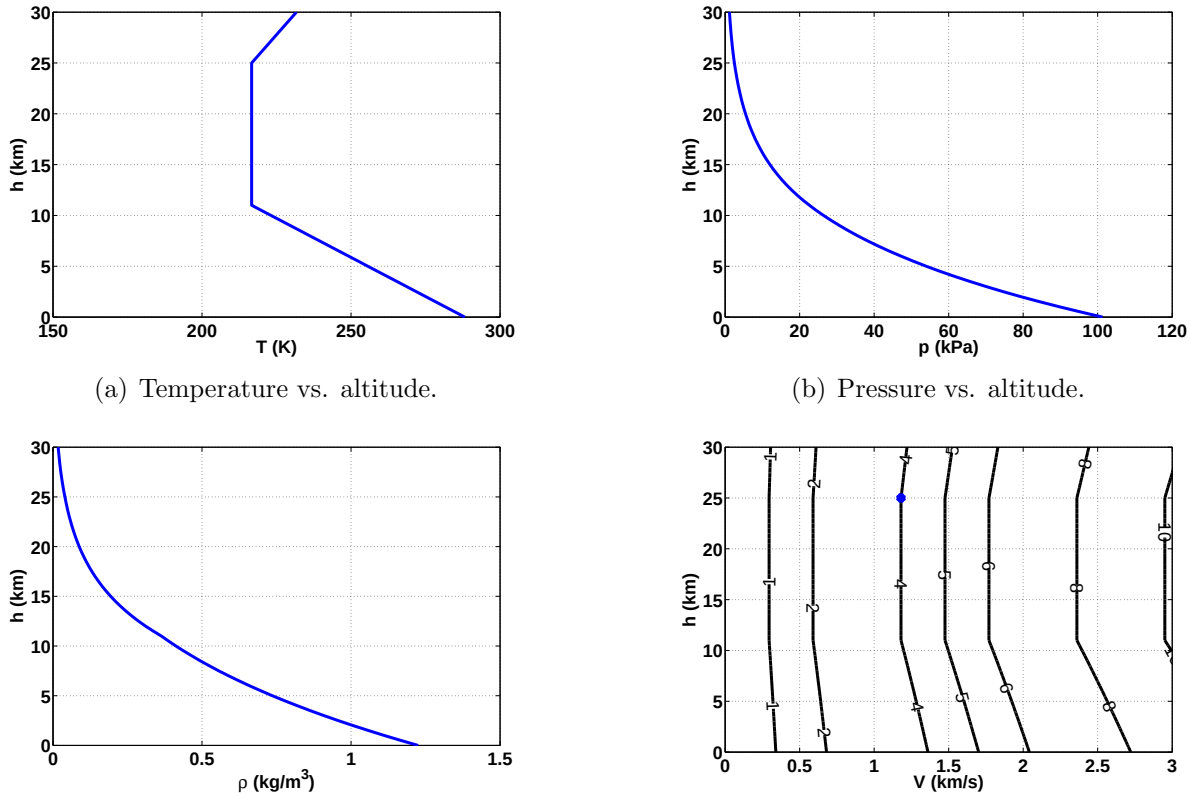

(a) Temperature vs. altitude.

(b) Pressure vs. altitude.

(c) Density vs. altitude.

(d) Mach contours in velocity-altitude plane.

Figure 2-1: Standard atmosphere model showing temperature, pressure, density, vs. altitude, and contours of Mach number in the altitude-velocity plane. Symbol indicates design point of $M = 4, h = 25$ km.

(TSTO) vehicle, since minimizing fuel would permit the second stage to maximize payload; (2) a minimum time to climb mission may be appropriate for an advanced fighter aircraft; (3) a constant dynamic pressure mission may be appropriate for structural reasons. These different mission profiles imply different propulsion system operating conditions.

A standard atmosphere model defines the ambient air properties along the flight path [2, p. 74-79]. Figure 2-1 shows the temperature, pressure, and density as functions of altitude, as well as contours of constant Mach number in the altitude-velocity plane.

For simplicity, a baseline mission profile is established by examining a flight vehicle climbing along a nearly constant dynamic pressure ($\rho V^2/2$) trajectory of 0.28 atmospheres, from Mach number zero to "high" Mach numbers of 4 or 5. Figure 2-2 depicts the trajectory

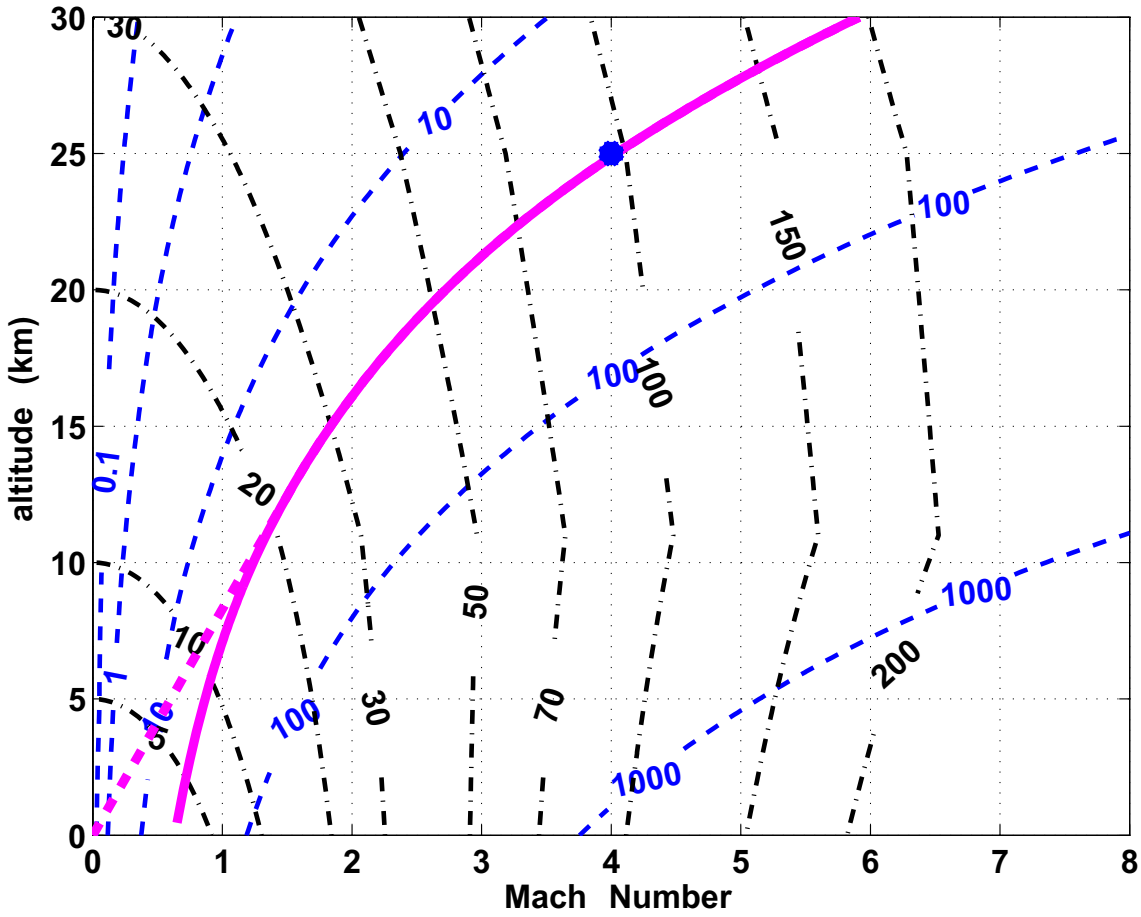

Figure 2-2: Selected flight path. Heavy, broken line represents low Mach number trajectory. Heavy, solid line is $\rho V^2/2 = 28.4$ kPa, representing high Mach number trajectory. Faint broken lines are lines of constant $\rho V^2/2$ in kPa. Faint dash-dot lines are lines of constant specific energy, in km.

in the Mach number-altitude plane. At "lower" Mach numbers the trajectory is defined by the broken line, while at "high" Mach numbers the trajectory follows a line of constant $\rho V^2/2$. The dynamic pressure selected for the high Mach number portion of the trajectory corresponds to M=4 at an altitude of 25 km, and falls within design ranges typically given in the literature [46, p. 148]. It is comparable to the vehicle structural limitations of the Space Shuttle [45].

As the aircraft climbs, its Mach number increases, leading to increasing freestream total temperature (T_t) and total pressure (p_t) along the flight path, as shown in Fig. 2-3.

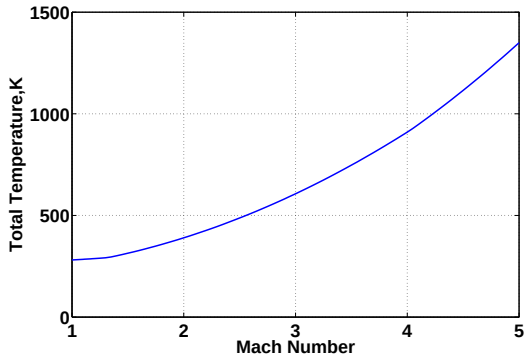

(a) Total temperature vs. Mach number along selected flight path.

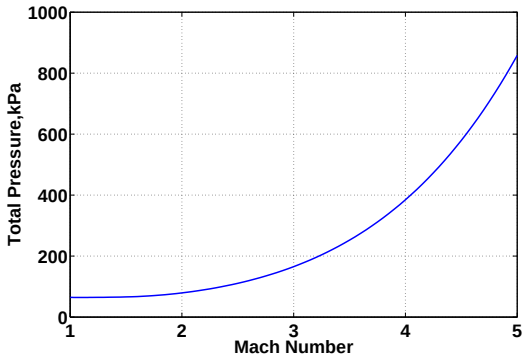

(b) Total pressure vs. Mach number along selected flight path.

Figure 2-3: Stagnation properties along flight path.

Freestream total temperatures at Mach 3, 4, and 5, are approximately 600, 900, and 1350 degrees Kelvin, respectively. The rapid increase in T_t with Mach number is the primary reason that a single-spool turbojet (SSTJ) cycle fails to produce thrust at high Mach numbers. Current material temperature limits in both the compressor, and especially the turbine limit the production of thrust by reducing the heat addition capability of the fuel in the combustor. Cooling the air entering the compressor is a means to regain this heat addition capability, and leads to a cycle concept called the pre-cooled turbojet (PCTJ). Typically, pre-cooling of the inlet air would be achieved using a heat sink, e.g., a cryogenic fuel, or via mass injection e.g., water or liquid oxygen. Variants of PCTJ cycles, both with and without afterburning, have been studied by several authors [29, 32, 43, 66, 73, 84, 86]. The authors cite practical hurdles that must still be overcome in order to introduce this concept into an engine, such as weight penalties associated with pre-cooler hardware, robust variable capture inlets, and mitigation of frost formation in the troposphere. Despite these challenges, the general conclusion in the literature is that cooling of the order of several tens of degrees to a few hundred degrees Kelvin can theoretically result in enough specific thrust enhancement to push conventional turbomachinery out to flight Mach numbers of 4 to 6. The next section gives a quantitative example of the cycle benefits from using a pre-cooler upstream of the compressor in a single spool turbojet cycle.

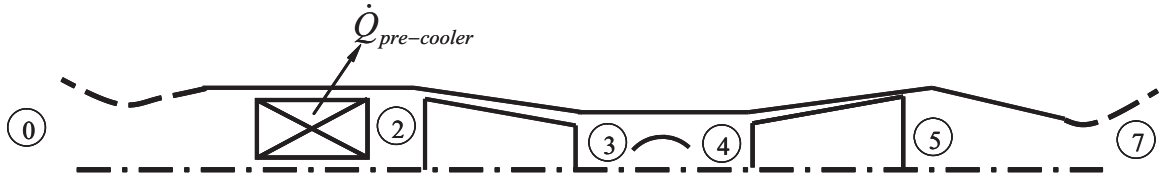

Figure 2-4: PCTJ schematic. Indicated stations are: 1) Inlet/pre-cooler inlet, 2) pre-cooler exit/compressor inlet, 3) compressor exit/burner inlet, 4) burner exit/turbine inlet, 5) turbine exit/nozzle inlet, 7) nozzle exit.

2.4 Pre-cooled Turbojet (PCTJ)

This section presents a mission analysis using an ideal pre-cooled turbojet (PCTJ) cycle to illustrate the effect of heat extraction on thrust production at high flight Mach numbers. By modifying the specific thrust expression of an ideal single-spool turbojet (SSTJ) to allow lossless heat extraction upstream of the compressor, the following benefits and requirements are suggested:

1. A maximum flight Mach number increase resulting from greater heat addition capability in the combustor.

2. An increase in ingested mass flow, resulting in a reduction of the required specific thrust to maintain level flight during the mission.

3. Required temperature changes within the pre-cooler of several tens to several hundreds of degrees Kelvin.

4. Tens of megawatts of cooling for a typical vehicle on a two-stage to orbit (TSTO) space access mission.

2.4.1 Modification of Ideal SSTJ Cycle for Compressor Pre-cooling

A schematic of the ideal PCTJ is depicted in Figure 2-4. Station 0 represents the engine inlet. Because stagnation properties are assumed not to change within an ideal inlet, station 0 is also the pre-cooler entrance. Station 2 is the pre-cooler exit/compressor inlet. Station 3

is the compressor exit/combustor inlet. Station 4 is the combustor exit/turbine inlet, Station 5 is the turbine exit. Station 7 is the nozzle exit.

An expression for the specific thrust of the ideal PCTJ is derived by performing an ideal design point cycle analysis. This is written in terms of the controlling non-dimensional parameters M_0, θ_t, θ_0, τ_c and τ_x as shown in Equation 2.1, following the SSTJ convention of Kerrebrock [47, p. 38],

$$\left(\frac{F}{\dot{m}a_0}\right)_{available} = \sqrt{\frac{2\theta_0}{\gamma-1}\left(\frac{\theta_t}{\theta_0\tau_c}-\tau_x\right)(\tau_c-1)+\frac{\theta_t {M_0}^2}{\theta_0\tau_c}} - M_0, \tag{2.1}$$

where the specific thrust, $\left(\frac{F}{\dot{m}a_0}\right)$, consists of:

- F, the thrust.
- $\dot{m}$, the airflow through the engine.
- a_0, the local speed of sound.

The right hand side of Equation 2.1 consists of:

- M_0, the vehicle's flight Mach number.
- $\theta_t = T_{t4}/T_0$, the turbine inlet temperature, T_{t4}, normalized by the ambient temperature, T_0.
- $\theta_0 = T_{t0}/T_0 = 1 + \frac{\gamma-1}{2}{M_0}^2$, the ram temperature rise coefficient.
- $\tau_c = T_{t3}/T_{t2}$, the compressor temperature ratio.
- $\tau_x = T_{t2}/T_{t0}$, the pre-cooler temperature ratio.

Equation 2.1 has been derived assuming:

1. Airflow through the engine can be modeled as a perfect gas (c_p =constant, $\gamma = 1.4$)

2. All conventional SSTJ components are lossless: inlet, compressor, combustor, turbine, nozzle. (Note that under the lossless compressor assumption, cycle compressor pressure ratio is related to the cycle temperature ratio by the isentropic relation $\tau_c = \pi_c^{(\gamma-1)/\gamma}$).

3. An ideal pre-cooler consisting of a lossless, constant-pressure heat exchanger is located upstream of the compressor.

4. Fuel flow is small compared to mass flow ($\dot{m}_{fuel} \ll \dot{m}_{air} \approx \dot{m}$).

5. Flow through the nozzle is isentropically expanded to ambient pressure.

6. The engine inlet and nozzle are "rubber," so as to change inlet and exit area as needed to maintain an "on-design" engine condition.

Typically, a cycle is defined by the turbine inlet temperature, T_{t4}, the compressor pressure ratio, π_c, and the vehicle trajectory. Along with the trajectory defined in Section 2.3, the value of T_{t4} is chosen as 2300 K to represent a next generation technology level for a high performance aircraft [47, p. 296]. The value of π_c is chosen as 5, a compromise between the high optimal pressure ratio at low flight Mach number and low optimal pressure ratio at high flight Mach number [47, p. 41].

The pre-cooler exit to inlet temperature ratio, $\tau_x = T_{t2}/T_{t0}$, characterizes the heat transfer. Setting $\tau_x = 1$ (i.e., no pre-cooling) simplifies Equation 2.1 to the standard ideal SSTJ cycle specific thrust, given by Kerrebrock [47, p. 38]. For cooling, this ratio is less than unity. The lower the value of τ_x, the greater the increase in specific thrust.

Figure 2-5 compares the specific thrust, $F/(\dot{m}a_0)$, of an uncooled ($\tau_x = 1$) vs. pre-cooled ($\tau_x = 0.8$) SSTJ having the given T_{t4}, π_c, and the trajectory described in Section 2.3. Specific thrust falls off as flight Mach number increases and becomes zero at a critical Mach number. This is directly attributable to the increase in compressor inlet stagnation temperature, T_{t2}, which correspondingly results in increased compressor exit temperature, T_{t3}. Since the turbine inlet temperature, T_{t4}, is fixed by material temperature limits, higher flight Mach numbers further reduce the combustor heat addition potential, $T_{t4} - T_{t3}$, and thus reduce the

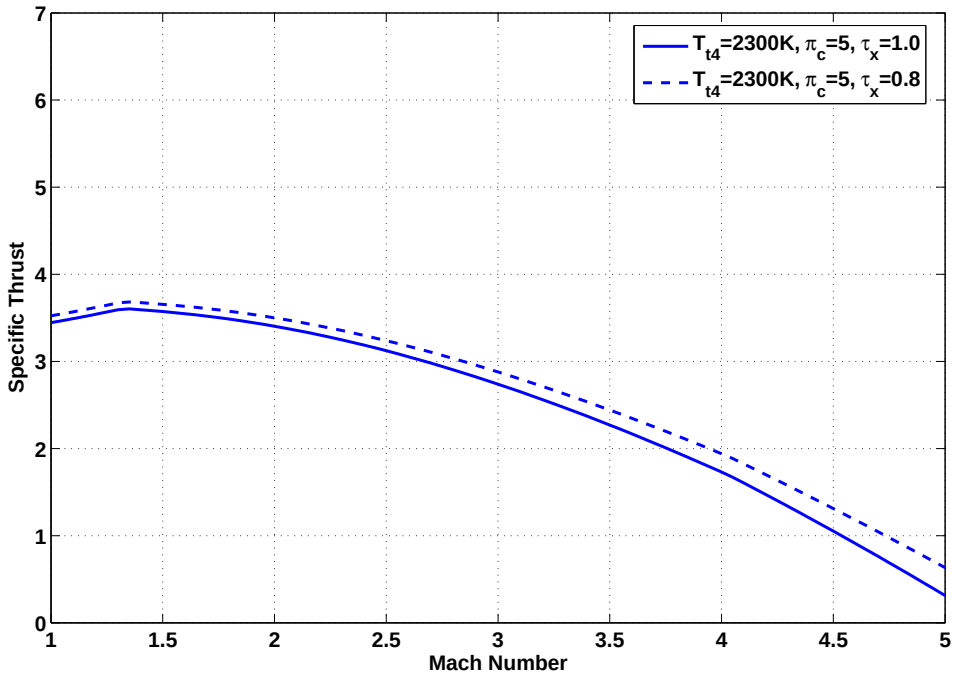

Figure 2-5: Specific thrust for ideal SSTJ (solid line) and ideal SSTJ with pre-cooling (broken line) for given mission.

the specific thrust. Pre-cooling increases the specific thrust by recovering the heat addition capability. This results in an increase in the maximum operational Mach number.

The dimensionless heat transfer, q^*, is defined as the stagnation temperature drop across the pre-cooler normalized by the pre-cooler inlet stagnation temperature, $\Delta T_t/T_{t0}$,

$$q^* = \frac{\dot{Q}}{\dot{m}c_p T_{t0}} = \frac{\dot{q}}{c_p T_{t0}} = \frac{\Delta T_t}{T_{t0}} = \tau_x - 1, \tag{2.2}$$

where q^* is negative for cooling. Besides the specific thrust, the specific impulse, $I_{sp} = F/\left(\dot{m}_{fuel}g\right)$, i.e., the cycle's ability to convert fuel into thrust, is also of interest. Other studies on pre-cooling have generally focused on balancing the cooling requirement with the fuel available as coolant [32, 66, 73, 84]. In the SSTJ with afterburning, pre-cooling is often achieved by overfueling (fuel equivalence ratio, $\phi > 1$), with the excess fuel dumped into the afterburner. One author [84] suggests carrying water on board for cooling and then eventually

recovering a small amount of thrust from it. Depending upon the equivalence ratio and the fuel/coolant selection, the specific impulse of pre-cooled turbojets ranges from hundreds to thousands of seconds in the literature. As vehicle thermal management, including heat exchanger design, is not discussed in this research, a further discussion of specific impulse is not presented here.

2.4.2 Specific Thrust Requirements

For a typical TSTO vehicle, the propulsion system may be required to generate thrust levels that enable the vehicle to climb from Mach zero at sea level to Mach 4 to 6 at an altitude of 25 km. The minimum required thrust is estimated by considering a vehicle in steady, level flight everywhere along the selected trajectory shown in Figure 2-2. Under these conditions, the vehicle weight, W, must equal the lift, L, and the thrust, F, must equal the drag, D,

$$W = L = C_L q_\infty S, \tag{2.3}$$

$$F = D = C_D q_\infty S, \tag{2.4}$$

so that

$$C_L = \frac{W/S}{q_\infty}. \tag{2.5}$$

In equations 2.3, 2.4 and 2.5, q_∞ is the dynamic pressure and is given by

$$q_\infty = \frac{\rho_0 {V_0}^2}{2} = \frac{\gamma p_0 {M_0}^2}{2}. \tag{2.6}$$

W/S is the wing loading. The vehicle drag consists of the zero-lift drag coefficient, C_{D_0}, and the drag due to lift, i.e., induced drag,

$$C_D = C_{D_0} + K \left(\frac{W/S}{q_\infty} \right)^\eta. \tag{2.7}$$

Along the flight path, the coefficients, C_{D_0}, K and η in Equation 2.7 are functions of the flight Mach number only. The definition of vehicle reference area, S, is chosen by the designer, and

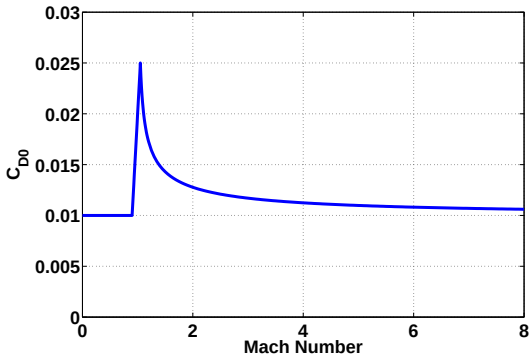

(a) Zero lift drag coefficient, $C_{d,0}$.

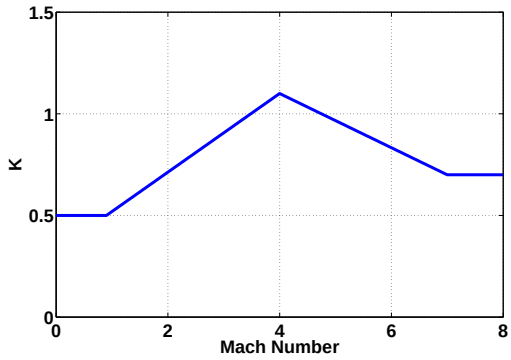

(b) Induced drag constant, K.

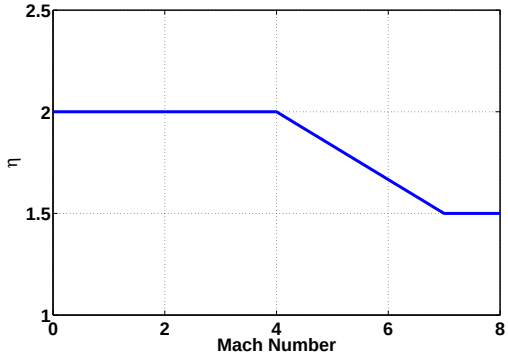

(c) Induced drag exponent, η.

Figure 2-6: Mach number dependence of drag model used in mission analysis, based on a typical supersonic jet aircraft [59, p. 86].

affects the value of the coefficients. For two vehicles having a consistent vehicle reference area definition, the vehicle drag model is scalable. When choosing these coefficients for preliminary analysis the class of vehicle is important (e.g., a high performance aircraft versus a hypervelocity glider). The drag model chosen in this analysis is based on the aerodynamic characteristics of a typical jet aircraft at supersonic speeds [59, p. 86], and is shown in Figure 2-6.

Assuming that flow into the compressor is purely axial and nowhere choked, the ideal mass flow can be determined by the vehicle trajectory variables (p_0, T_0, and M_0), the pre-cooling temperature ratio (τ_x), the compressor face Mach number (M_C), and the compressor face area (A_C). The expression for the mass flow is given as

$$\dot{m} = \sqrt{\frac{\gamma}{R}} \frac{A_c p_0}{\sqrt{T_0}} \frac{1}{\sqrt{\tau_x}} M_c \left[\frac{1 + \frac{\gamma-1}{2} {M_0}^2}{1 + \frac{\gamma-1}{2} {M_c}^2} \right]^{(\gamma+1)/2(\gamma-1)} . \tag{2.8}$$

The ideal mass flow varies inversely with the square root of the pre-cooling ratio. Hence, more pre-cooling at constant-pressure allows greater mass flow to be ingested by the engine if the other variables are held fixed. For the vehicle in this example, the trajectory variables are given by the mission profile. The total propulsion system compressor face area and compressor face Mach number are assumed to be constant and have the values

$$A_c = 1 \text{ m}^2$$

and

$$M_c = 0.6 .$$

The compressor face area, A_c, is the only engine geometric variable present in this analysis, and is estimated to be comparable to other supersonic aircraft such as the SR-71 [44]. Other than the compressor face, the engine is assumed to be "rubber", implying it is capable of changing geometry as necessary to satisfy the lossless component assumption and remain "on-design" at all points along the mission. The assumption of fixed compressor face area and Mach number fix the corrected flow on the compressor map. Selecting the cycle pressure ratio, π, to be constant effectively fixes the compressor operating point throughout the mission. With these assumptions, finally, the required specific thrust is given as

$$\left(\frac{F}{\dot{m} a_0} \right)_{required} = \frac{\left[C_{D_0} + K \left(\frac{W/S}{q_\infty} \right)^\eta \right]}{2} \left(\frac{S}{A_c} \right) \left(\frac{{M_0}^2}{M_c} \right) \sqrt{\tau_x} \left(\frac{1 + \frac{\gamma-1}{2} {M_c}^2}{1 + \frac{\gamma-1}{2} {M_0}^2} \right)^{(\gamma+1)/2(\gamma-1)} . \tag{2.9}$$

Equation 2.9 suggests that in addition to increasing the cycle available specific thrust, as shown in the previous subsection, the presence of an ideal pre-cooler reduces the required specific thrust by the square root of the pre-cooling temperature ratio, $\sqrt{\tau_x}$. This is directly attributable to the greater mass flow capability from cooling shown in Equation 2.8. The mission requirements are met when

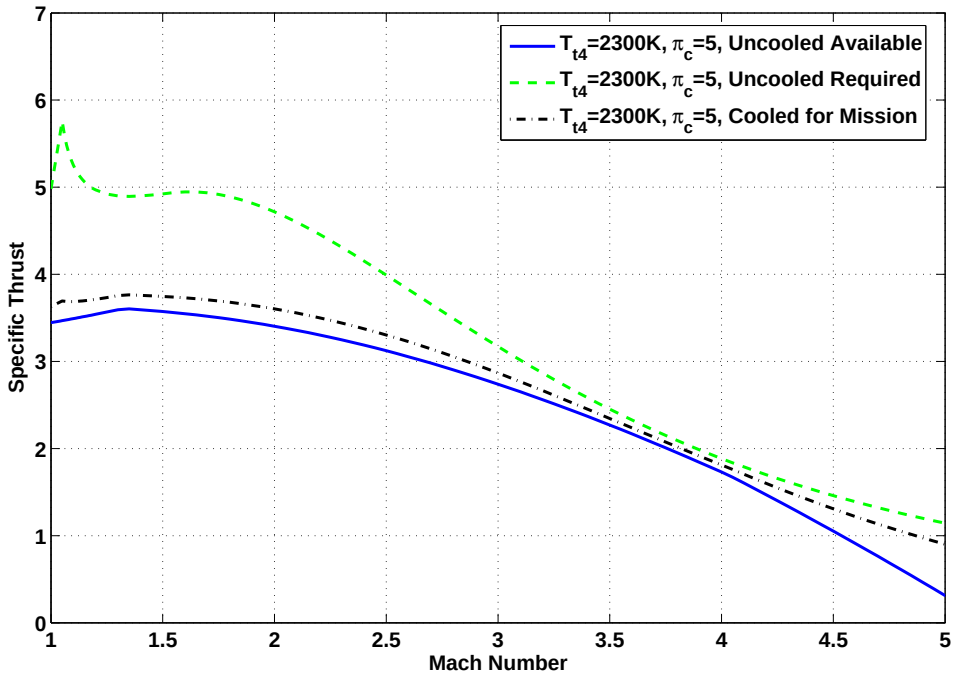

Figure 2-7: Uncooled available (solid line), uncooled required (broken line), and pre-cooled (dash-dot line) specific thrust vs. Mach number for chosen vehicle in steady, level flight on selected trajectory.

$$\left(\frac{F}{\dot{m}a_0}\right)_{available} \geq \left(\frac{F}{\dot{m}a_0}\right)_{required}. \tag{2.10}$$

Figure 2-7 compares 1) available specific thrust without pre-cooling, 2) required specific thrust without pre-cooling, and 3) specific thrust with sufficient pre-cooling to maintain steady, level flight, for a vehicle having $W = 980,000\ N$ and $S = 217\ m^2$, along the given trajectory. The chosen wing loading, (W/S) is estimated to be comparable to an SR-71 ($W \sim 756,000N$, $S \sim 167m^2$) [44] in steady, level flight at maximum takeoff weight. For simplicity, the vehicle mass is assumed constant at all points along the trajectory[1]. The

[1]Fuel consumption causes the vehicle weight to decrease as the chosen mission progresses, thereby reducing the required specific thrust at higher Mach numbers. Accounting for fuel consumption increases the vehicle's Mach envelope. As this simplified example is designed by the author to illustrate the theoretical effect of an ideal pre-cooler, the effect is neglected for convenience.

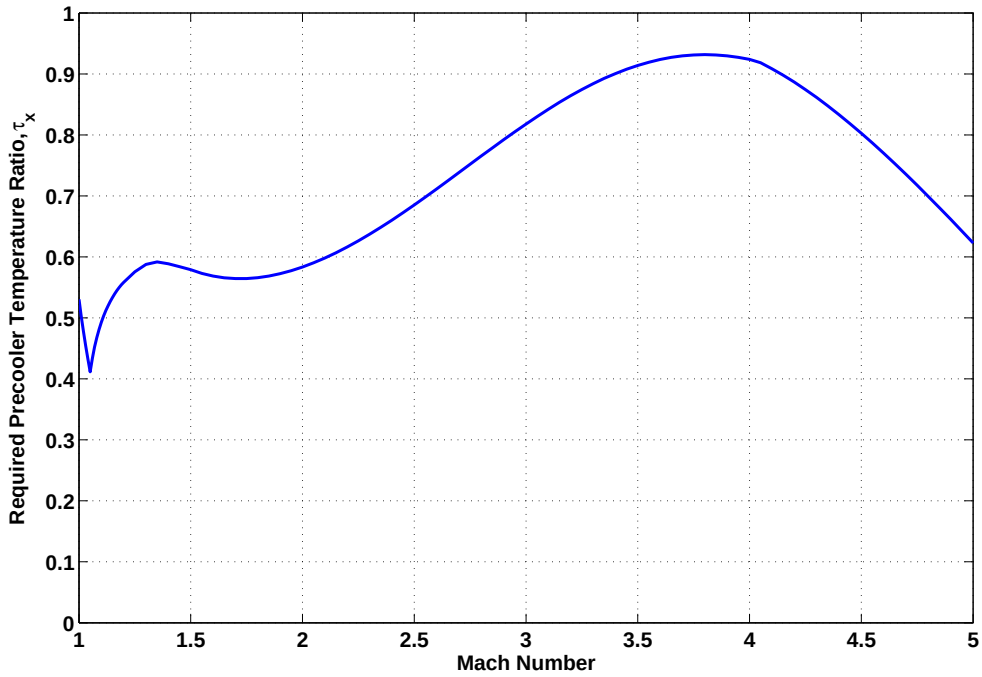

Figure 2-8: Pre-cooling temperature ratio for chosen vehicle in steady, level flight on selected trajectory.

dynamic pressure-to-wing loading ratio, a quantity which appears in equations 2.7 and 2.9, is:

$$\left(\frac{q_\infty}{W/S}\right) \approx 6.3$$

Without cooling, the required cycle specific thrust (dashed line) is greater than the available cycle specific thrust (solid line). The gap between required and available is eliminated by the correct amount of pre-cooling (dash-dot line). The dash-dot curve is the locus of points that matches required specific thrust and the cycle available thrust through sufficient pre-cooling. From this figure, it is clear that pre-cooling both augments specific thrust to satisfy mission requirements, and expands the Mach number operational range for a given engine cycle.

The value of the pre-cooler temperature ratio, τ_x, required to match the available and required specific thrusts roughly varies from 0.4 to 0.9 in the range of Mach 1 to 5, as

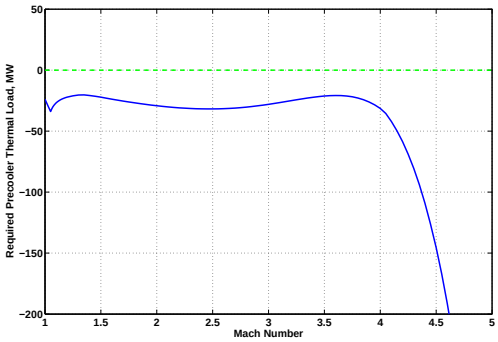

(a) Pre-cooling load (MW) for chosen vehicle in steady, level flight on selected trajectory.

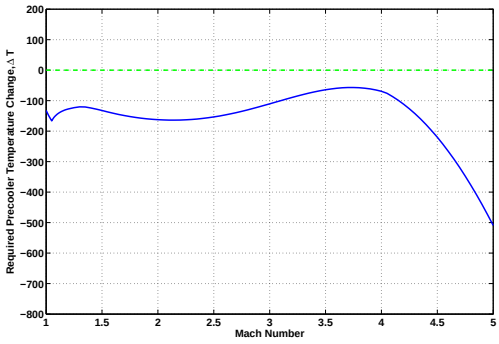

(b) Pre-cooler temperature change (K) for chosen vehicle in steady, level flight on selected trajectory.

Figure 2-9: Pre-cooler requirements along selected trajectory.

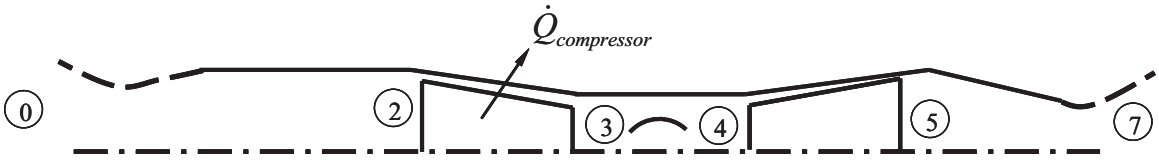

(a) Compressor cooled turbojet cycle (CCTJ).

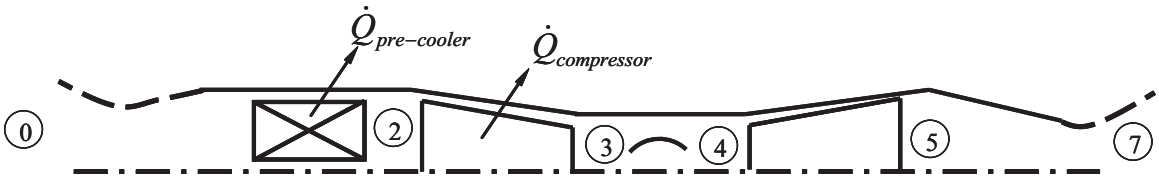

(b) Hybrid-cooling turbojet cycle (HCTJ).

Figure 2-10: CCTJ and HCTJ schematics. Indicated stations are: 1) Inlet/pre-cooler inlet, 2) pre-cooler exit/compressor inlet, 3) compressor exit/burner inlet, 4) burner exit/turbine inlet, 5) turbine exit/nozzle inlet, 7) nozzle exit.

presented in Fig. 2-8. The required pre-cooling in terms of energy transfer rate and temperature change, ΔT, is given in Figure 2-9. The required temperature change is on the order of $\sim 100K$, and the required heat transfer is on the order of tens of megawatts, up to a Mach number of ~ 4, beyond which the cooling requirement increases rapidly.

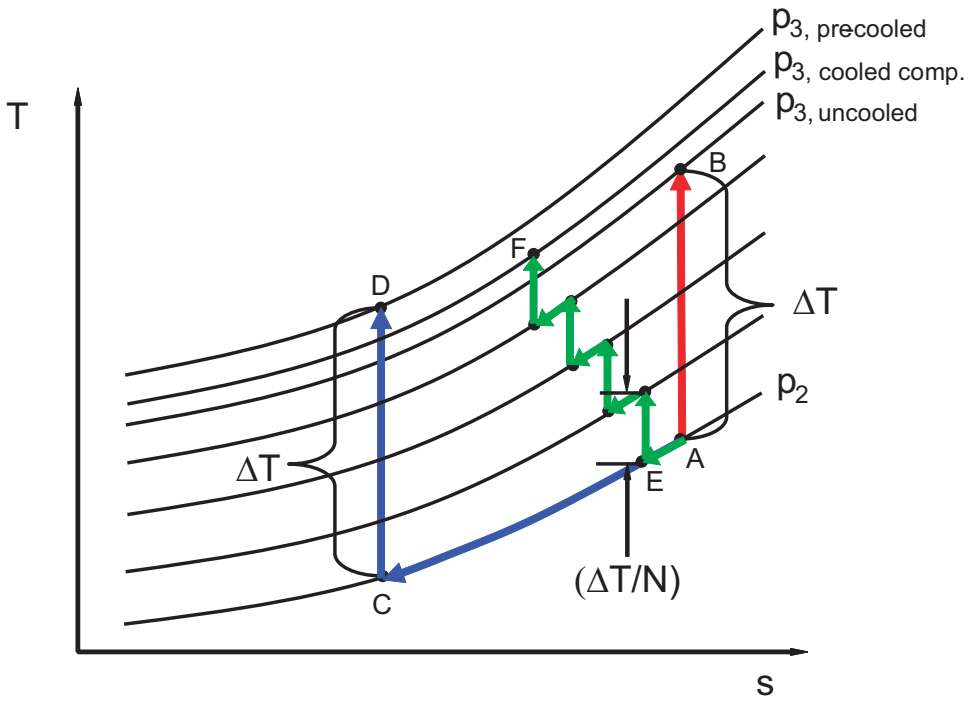

Figure 2-11: Temperature-entropy diagram for for standard compression (A-B), compression with pre-cooling (A-C-D), and interspersed cooling and compression in N steps (A-E-...-F).

2.5 Compressor Cooling: The Idea

In Section 2.3 and 2.4 a representative mission profile is established and used to model the PCTJ. It is shown that one to several hundreds of degrees of cooling generate enough specific thrust to achieve Mach 4+ flight. This section extends the concept to compressor cooling, where heat extraction inside the compressor blade passages may be used alone in a compressor cooled turbojet cycle (CCTJ), or in addition to pre-cooling in a hybrid-cooling turbojet cycle (HCTJ), as depicted in fig 2-10.

2.5.1 Compressor Cooling vs. Pre-Cooling

Despite practical challenges associated with the PCTJ, this propulsion concept provides a starting point for studying the potential cycle benefits of compressor cooling. To the author's knowledge, there exist no examples in the literature of cooling within the compressor via

blade passage surface heat extraction. It is first necessary, then, to compare the concept of the PCTJ to compressor cooling. The temperature-entropy diagram in Fig. 2-11 compares standard ideal compression (A-B) to constant pressure pre-cooling (A-C) followed by isentropic compression (C-D). The comparison is made on an equal work basis, meaning ΔT is the same for the isentropic compression process in both cases (a perfect gas is assumed). Process (A-E-...-F) superimposes a third conceptualization, the case of N constant-pressure cooling steps interspersed with N equal work steps. It is implied by the temperature rise of $\Delta T/N$ that the total compression work for all three processes (A-B), (A-C-D), (A-E-...-F) is equal. It is argued by the author that process (A-E-...-F) could represent: (1) an N stage compressor with constant-pressure cooling in an inlet guide vane and the first N-1 stators, or (2) perhaps, in the limit as N approaches infinity, a single stage device with a continuous cooling scheme. Both descriptions are generally referred to as cooled compressors.

Under the perfect gas assumption, two lines of constant-pressure diverge on a T-s diagram with increasing temperature or entropy. The implication of this fact on the three processes shown is that the theoretical pressure rise capability of the pre-cooled compressor is greatest, followed by the cooled compressor (schematically similar to intercooling), and finally the standard (adiabatic) compressor, because compression work done at a lower temperature results in greater pressure rise. This idealized model fails, however, to account for the fact that a real pre-cooler may create significant loss of stagnation pressure [29, 66], and that cooling within blade passage surfaces may have additional aerodynamic benefit. Assuming that a cooled compressor introduces no new gas path geometry, and hence no new loss generating solid boundaries, the cooled compressor underperformance may be mitigated or even reversed when compared to a real pre-cooler[2].

The natural point of departure from this conceptual example is to determine in what situations a cooled compressor has comparable effect to a pre-cooled compressor with real pressure loss. Figure 2-12 depicts two additional processes superimposed on the previous

[2]In addition to the loss penalties associated with a real pre-cooler, significant system weight penalties from heat exchanger hardware are also seen as a technological challenge, requiring lightweight heat exchanger materials to be surmounted [66]. This thesis does not address the modeling of system weight. It would be necessary in any vehicle-system level study.

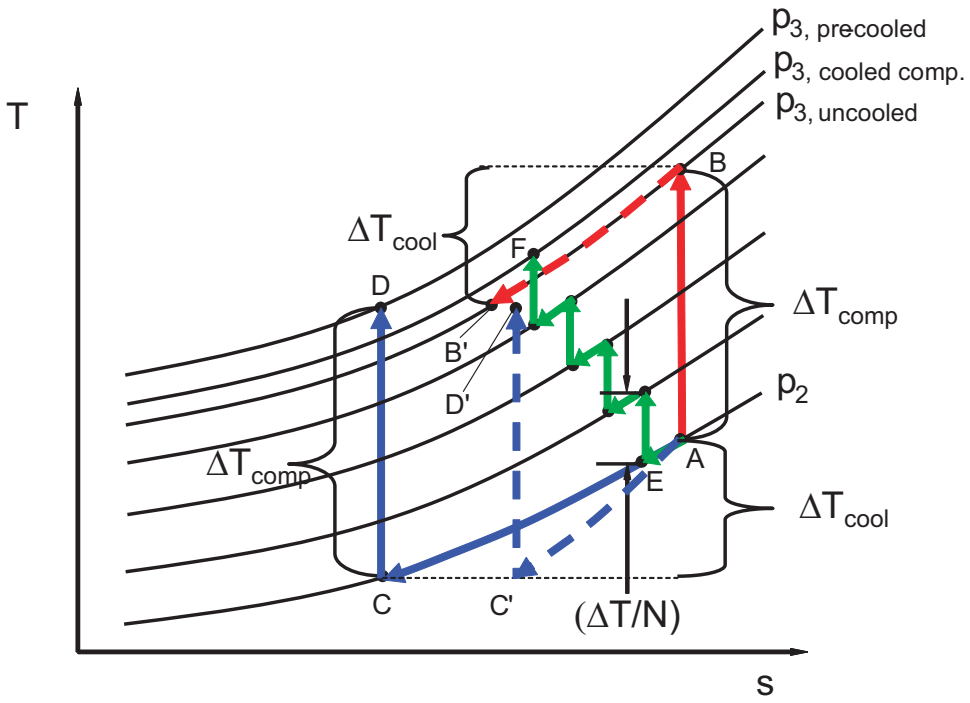

Figure 2-12: Same as Fig 2-11 with real precooled compression process (A-C′-D′) and compression followed by constant pressure post-cooling (A-B-B′).

temperature-entropy diagram. Process (A-C′-D′) represents a pre-cooling with loss of pressure followed by an isentropic compression with the same work input as process (A-C-D). Compared to this is an isentropic compression followed by constant pressure cooling, a so-called post-cooling process (A-B-B′). It is argued by the author that the constant pressure post-cooling is a conservative limiting case of a cooled compressor that assumes no additional total pressure losses because no new gas path geometry is introduced.

One source suggests typical pre-cooler stagnation pressure loss ($\Delta p_t/p_t$) of one to eight percent, with loss being a function of pre-cooler temperature drop [66]. Figure 2-13 shows the critical pre-cooler recovery factor versus non-dimensional heat addition for the comparison of two isentropic compressors with pressure ratios of 2, 5, and 8. The first device follows process (A-C′-D′) in Fig. 2-12, i.e., isentropic compression preceded by a real pre-cooler with stagnation pressure recovery of π_x, while the second device follows process (A-B-B′), i.e. isentropic compression followed by a constant pressure cooling process that represents a

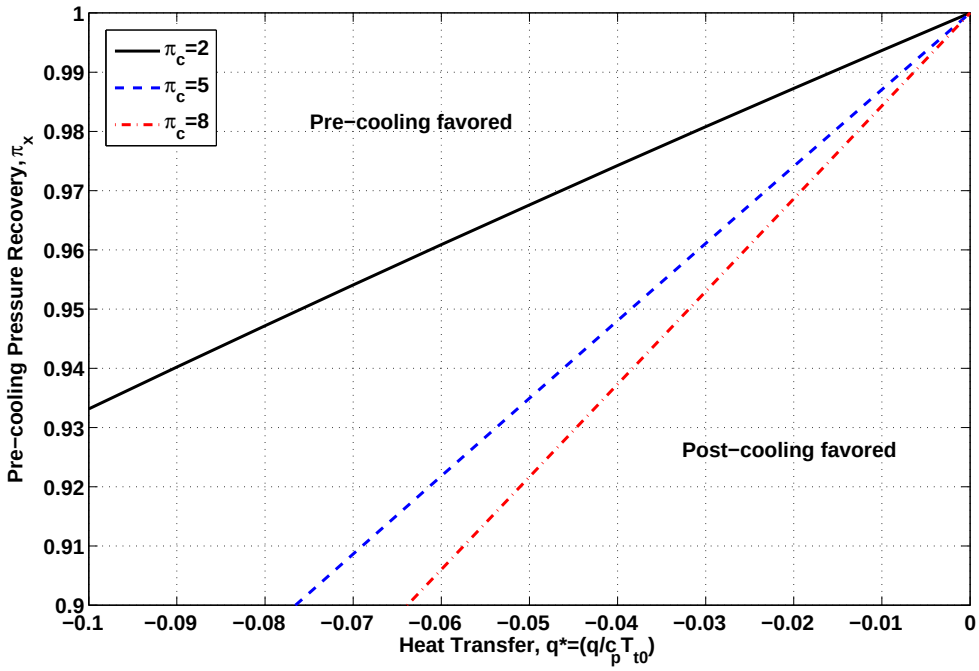

Figure 2-13: Critical pre-cooling stagnation pressure recovery vs. cooling load. Operation above the line favors real pre-cooled compression, while operation below the line favors a lossless post-cooled compressor (a limiting case of cooled compressor with no new loss generating gas path surfaces). Plot is made on an equal work, equal cooling basis for pressure ratios of 2, 5, and 8.

conservative limiting case of a cooled compressor. To first order, the presence of compressor cooling is assumed to introduce no new loss mechanisms. The interpretation of this plot is that for a given level of cooling, q^*, the pre-cooled compressor is favorable if π_x is above the line, while the post-cooled compressor is favorable if π_x is below the line. As the absolute value of cooling increases, the acceptable pressure recovery for the pre-cooler decreases. For an inlet total temperature of $\sim$ 1000K, found near the high speed flight point of $M = 4$ and 25km altitude, $q^* = -0.1$ corresponds to $\sim$ 100K of cooling, comparable to PCTJ requirements presented in the analysis of Section 2.4. Thus this simple and conservative analysis suggests that scenarios may exist for which compressor cooling either in CCTJ or HCTJ operation is favorable to the PCTJ. In Section 3.6 a heat transfer analysis indicates

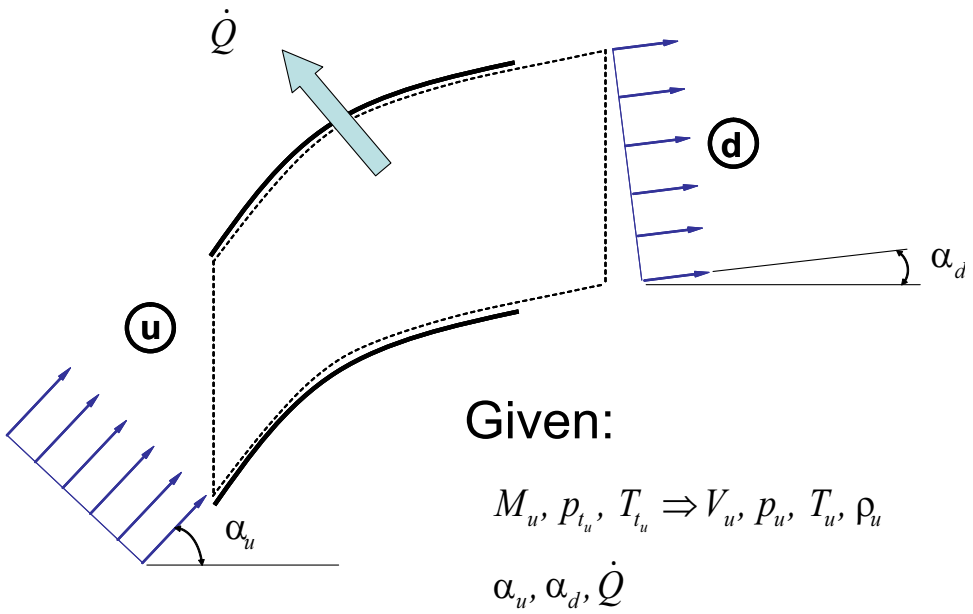

Figure 2-14: Control volume of a diffusing blade passage with heat extraction. Upstream and downstream flow angles, α_u and α_d, respectively, are assumed fixed.

that individual blade rows are capable of providing heat transfer rates roughly an order of magnitude smaller than $q^* = -0.1$, suggesting that high-solidity, multistage compressors with low pressure ratio having cooling in multiple blade rows may be able to achieve heat transfer rates for similar application as a pre-cooler.

2.5.2 Diffusing Passage Heat Extraction

A one-dimensional, steady control volume (CV) model of a cascade passage with cooling, as depicted in Fig. 2-14, is performed to study how cooling affects the loading capability of the blade row. The passage is treated as a subsonic stator, with uniform inflow and outflow conditions. The upstream Mach number, stagnation pressure, and stagnation temperature are assumed known. The upstream and downstream flow angles, α_u and α_d, respectively, are assumed constant. The dimensionless cooling, q^*, is defined per Equation 2.2. Mass conservation, axial and circumferential momentum conservation and energy conservation expressions are applied, along with the ideal gas law. Further, entropy generation is neglected,

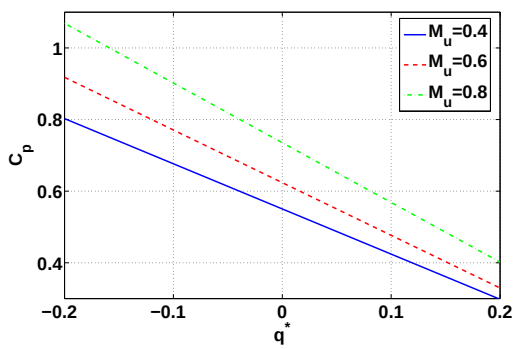

(a) Pressure Coefficient, C_p, vs. heating/cooling, $\pm q^*$ in selected stator passage, at various upstream Mach numbers.

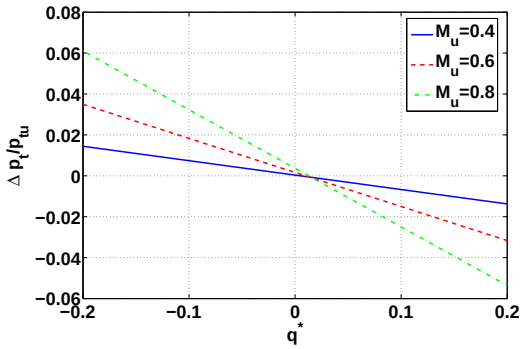

(b) Fractional change in stagnation pressure, $\frac{p_{td}-p_{tu}}{p_{tu}}$, vs. heating/cooling, $\pm q^*$ in selected stator passage, at various upstream Mach numbers.

Figure 2-15: Cooled stator passage control volume model.

and the specific entropy transfer associated with heat extraction is estimated to occur at a temperature that is the average of the upstream and downstream static temperatures:

$$s_{trans} = s_d - s_u = \frac{q}{\frac{1}{2}\left(T_u + T_d\right)} \tag{2.11}$$

Solution of the governing equations at three subsonic inlet Mach numbers, with upstream and downstream flow angles set to $\alpha_u = 50°$ and $\alpha_d = 25°$, respectively, suggests that cooling increases the dimensionless static pressure rise in the passage, $C_p = 2\left(p_d - p_u\right)/\rho_u V_u^2$, as shown in Figure 2-15(a). As M_u increases, the effect of cooling is greater, as seen by the relative slopes of the three lines. This result is consistent with the Mach number dependence of the static pressure sensitivity coefficient in quasi one-dimensional flow with heat transfer [27, 80]. Figure 2-15(b) shows that cooling also increases the passage stagnation pressure, with heating producing the opposite effect. This is also consistent with the quasi 1-D result, the so-called Rayleigh line. This CV analysis suggests that the loading and total pressure change benefit from a given amount of heat extraction is an aero-thermodynamic effect, i.e., it is Mach number dependent. In addition, the CV analysis shows that exit Mach number and stagnation temperature are lowered by heat extraction. It may be hypothesized that these effects will provide favorable inlet conditions to downstream blade passages in a multi-stage compressor.

2.5.3 Research Questions

Two high-level research questions may now be posed in the study of compressor cooling:

- What is the aerodynamic/thermodynamic performance effect of heat extraction within the blade passages?
- How should the presence of cooling affect the design of a new compressor?

In this thesis the latter question is not directly addressed. The focus remains on the first question, i.e., the aerodynamic and thermodynamic benefits of compressor cooling on a device with an adiabatic design point. The following detailed research questions are thus addressed in Chapter 3:

- What is the effect of surface heat extraction on blade-to-blade performance within the compressor?
- How does cooling change the generation of entropy within the blade passage?
- How does cooling affect the performance of a multi-stage axial compressor in terms of conventional metrics of pressure ratio, π, corrected mass flow, $\dot{m}_c$, and efficiency, η?
- What are the best efficiency metrics for this type of device?

2.5.4 Challenges and Unknowns

A key challenge in the assessment of compressor cooling is the development of a new modeling framework to account for the level of heat extraction. Blade passage performance with heat extraction must be defined in terms of conventional parameters, plus a new cooling parameter. In addition, conventional efficiency metrics and figures of merit must be reconsidered in light of the new cooling variables.

The unknowns associated with compressor cooling include the effect of heat extraction on the bulk flow through blade passages, and the subsequent effect at the multistage compressor level. The effect of location of heat extraction within the multistage compressor is also an important unknown that this research must address.

2.6 Chapter Summary

This chapter provides a review of the challenges associated with versatile turbopropulsion systems for low-to-high Mach number flight, to motivate the idea of compressor cooling. Inlet stagnation temperature rise with increasing flight Mach number along a mission trajectory limits the production of thrust by limiting heat addition capability in the combustor. Compressor cooling, like pre-cooling, is expected to improve cycle performance and hardware durability. Preliminary analysis suggests that compressor cooling, in exclusive operation or in hybrid operation with a pre-cooler may be favorable to the pre-cooled turbojet in certain scenarios. The hypothesized benefits of compressor cooling are summarized below:

- Thermodynamic benefit of compression at colder temperatures.
- Operability benefit associated with greater mass flow ingestion.
- Aerodynamic benefit associated with increased loading across compressor blade passages, potentially enabling a more compact design.
- An efficiency benefit versus a pre-cooler, as no new gas path surface geometry is introduced. In hybrid operation compressor cooling may reduce the surface area requirements of a pre-cooler.
- Improved durability, especially in the rear of the compressor, through material temperature reduction.

The next chapter explores the component performance aspects of compressor cooling in greater detail, using computational experiments and meanline modeling. Emphasis is placed on blade passage flows with heat extraction and the cooled compressor as a component alone.

Chapter 3

Compressor Cooling: A Novel Turbomachinery Concept for Mission 1

Chapter 2 introduces the concept of compressor cooling, a novel approach to improving axial compressor performance and extending the flight envelope of a high speed propulsion system. A mission analysis of a pre-cooled turbojet (PCTJ) cycle suggests that several tens to hundreds of degrees Kelvin of pre-cooling can stretch the operating envelope of a conventional turbopropulsion system to Mach 4+. Compressor cooling in a turbojet cycle is an offshoot of the PCTJ concept, that may be an enabler to high speed flight–independently or in tandem with pre-cooling.

This chapter presents the first description of the expected performance of a single and a multistage cooled axial compressor, through computational experiments and meanline modeling. Results suggest that for an axial compressor with an adiabatic design point, compressor cooling would: 1) raise the overall pressure ratio (at a given corrected flow), 2) raise the maximum mass flow capability, 3) raise the efficiency, defined as the ratio of isentropic work for a given pressure ratio to actual shaft work, and 4) provide rear stage choking relief at low corrected speed. In addition, a given amount of cooling is found to have

more impact in the front stages versus the rear stages. This is primarily a thermodynamic effect that results from the fact that, for a given gas, the compression work required to achieve a given pressure ratio decreases as the gas becomes colder. For an eight-stage compressor with an adiabatic design pressure ratio of 5, heat extraction equal to 1% of inlet stagnation enthalpy flux in the first four blade rows is found to improve pressure ratio and efficiency by 23% and 12%, respectively, at design values of corrected speed and corrected mass flow. Choking mass flow at design speed is also found to improve by 5%.

The end of the chapter discusses heat transfer considerations that set performance limits, and discusses the appropriate selection of efficiency metrics for non-adiabatic compressors. The heat transfer considerations indicate that the engineering challenges lie in achieving high enough heat transfer rates to provide significant impact to the compressor's performance.

3.1 Objectives

The research question that must be answered is how blade passage cooling affects the performance of a multistage compressor. It is hypothesized that blade passage cooling has both thermodynamic and aerodynamic benefits that lead to improvements in multistage axial compressor performance and operability. Testing this hypothesis requires meeting the following objectives:

1. Describing the bulk effect of surface heat extraction on the performance of diffusing blade passages typical of axial compressors.

2. Characterizing the on- and off-design performance and operability of a single- or multistage compressor with cooled blade passages utilizing different cooling schemes.

3. Estimating the available heat transfer potential in axial compressors.

4. Quantifying the relative importance of the thermal and viscous dissipation loss mechanisms and defining an appropriate cooled compressor efficiency metric at the component and system level.

3.2 Technical Approach

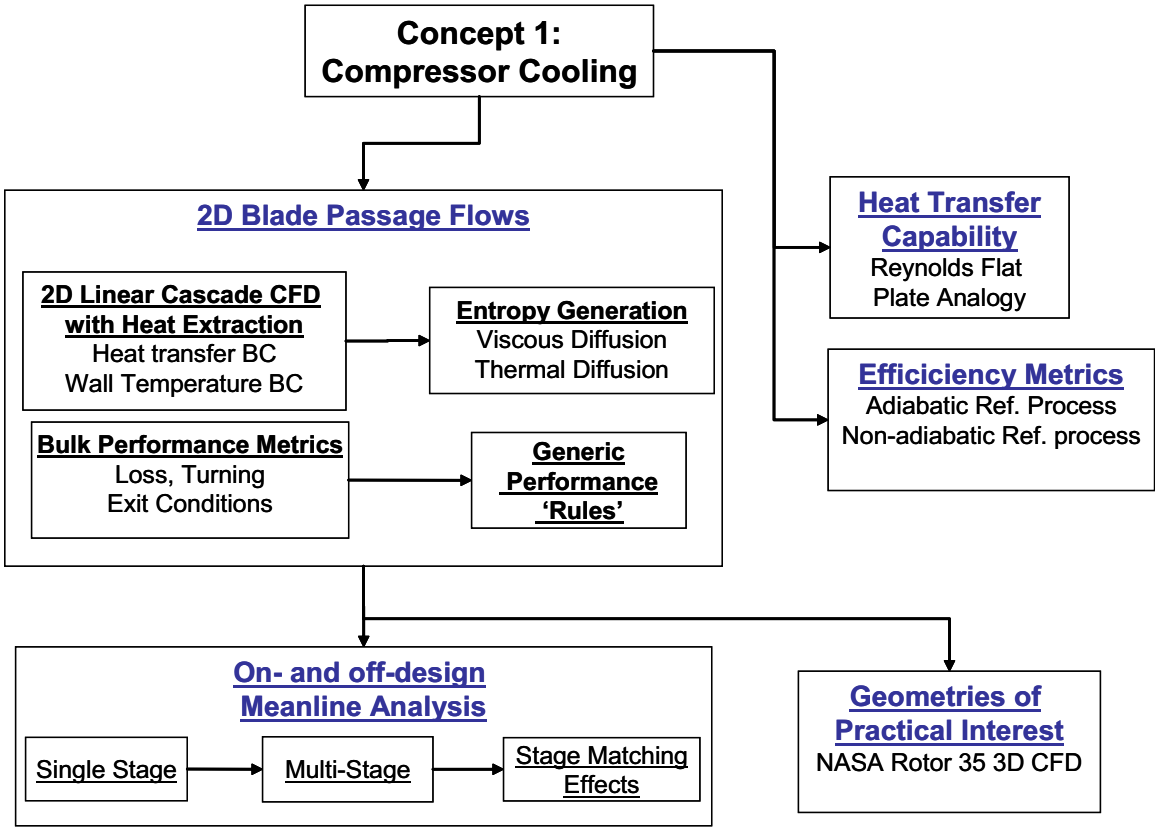

Figure 3-1: Compressor cooling technical road map.

The research objectives are met through computational experiments on blade passage flows with heat extraction, coupled with on- and off-design cooled compressor meanline analysis. The final step involves estimating the limits imposed by the heat transfer capability of blade passages. A technical road map of the compressor cooling study is shown in Figure 3-1. The technical approach is executed sequentially in the remaining sections, as described here.

Results from computational fluid dynamics (CFD) modeling of typical two-dimensional diffusing blade passages (linear cascades) with heat extraction are presented in section 3.3. The heat transfer-incidence design space of two representative cascade geometries is mapped in terms of typical bulk performance metrics in Section 3.3.2. The two entropy generation

mechanisms, viscous and thermal diffusion, are also quantified in Section 3.3.3. The bulk performance figures of merit lead to generic rules for cooled blade passages, presented in Section 3.3.4.

In section 3.4, these rules are applied to the on- and off-design meanline analyses of a single- and eight-stage compressor with low pressure ratio and an adiabatic design point. Pressure ratio and efficiency maps are thus generated, and the off-design behavior is described in terms of incidences and losses in individual stages. The meanline analysis shows improvements in pressure ratio, mass flow, and efficiency, and indicates that cooling produces rear stage choking relief. In addition, it is found that a given amount of cooling has the greatest effect if implemented in the front of the device.

In section 3.5, a CFD computation on a three dimensional rotor with and without cooling is presented. Cooling improvements are shown to be in accord with meanline predictions, suggesting compressor cooling as a concept is applicable to geometries of practical interest. It is indirectly inferred that the pressure rise from cooling is primarily an aero-thermodynamic effect, whereas the mass flow increase is a purely thermodynamic effect.

In section 3.6 heat transfer considerations are taken up. A simple model using Reynolds analogy on a flat plate is invoked to demonstrate that the limitations to cooled compressor performance come from available heat transfer areas. It is also pointed out that available heat transfer would be greatest in the rear of a compressor, which competes with the finding that the greatest effect comes from cooling in the front.

In section 3.7, two efficiency metrics for non-adiabatic compressors are discussed. The first metric, used throughout the thesis, compares the actual performance to an adiabatic reference process. The second metric compares the actual performance to a non-adiabatic reference process. It is argued that the first metric is appropriate for comparing the output between adiabatic and non-adiabatic compressors at the component level, while the second metric may be more appropriate as part of a system level analysis.

3.3 Blade Passage Flows with Heat Extraction

Computational experiments of two representative cascade geometries with and without cooling are presented in this section. Results given in terms of bulk aerodynamic performance metrics show that cooling improves cascade performance by reducing total pressure drop and by increasing turning. Bookkeeping of entropy generation and entropy flux in the computations reveals that the total pressure reduction coefficient is driven by both viscous and thermal diffusion. Viscous diffusion is found to have strong Mach number dependency and weak dependency upon heat transfer boundary conditions, whereas the opposite is found to be true of thermal diffusion.

3.3.1 Cascade Cases

Two-dimensional CFD experiments using Fluent are performed on two different cascade geometries in order to produce bulk aerodynamic performance figures of merit. The two selected geometries are representative of airfoils used in multistage compressors. Cascade 1 is based on a NACA 65 airfoil series blade definition, with an inlet and exit metal angle of $\chi_{in} = 38°$ and $\chi_{out} = 0°$, respectively, and a cascade solidity of 0.75. Cascade 2 has $\chi_{in} = 51°$, $\chi_{out} = 14°$, and solidity of 1.0, similar to the mid span metal angles of the NASA/GE E^3 compressor.

Geometry and Computational Domain

Figure 3-2 shows the gridded computational domains, as well as enlarged airfoil region views, for cascades 1 and 2. Cascade 1 has ~ 6000 grid cells. Grid y^+ is $\sim 5-10$ in the wall adjacent cells, with Reynolds number based on chord (Re_c) in the range of $100,000$ to $200,000$. The computational domain extends one axial chordlength upstream of the leading edge and two axial chordlengths downstream of the trailing edge. Cascade 2 has ~ 26000 grid cells. Grid y^+ is $\sim 1-3$ in the wall adjacent cells, with Re_c in the range of $300,000$ to $500,000$. The computational domain extends two axial chordlengths upstream of the leading edge and three axial chordlengths downstream of the trailing edge.

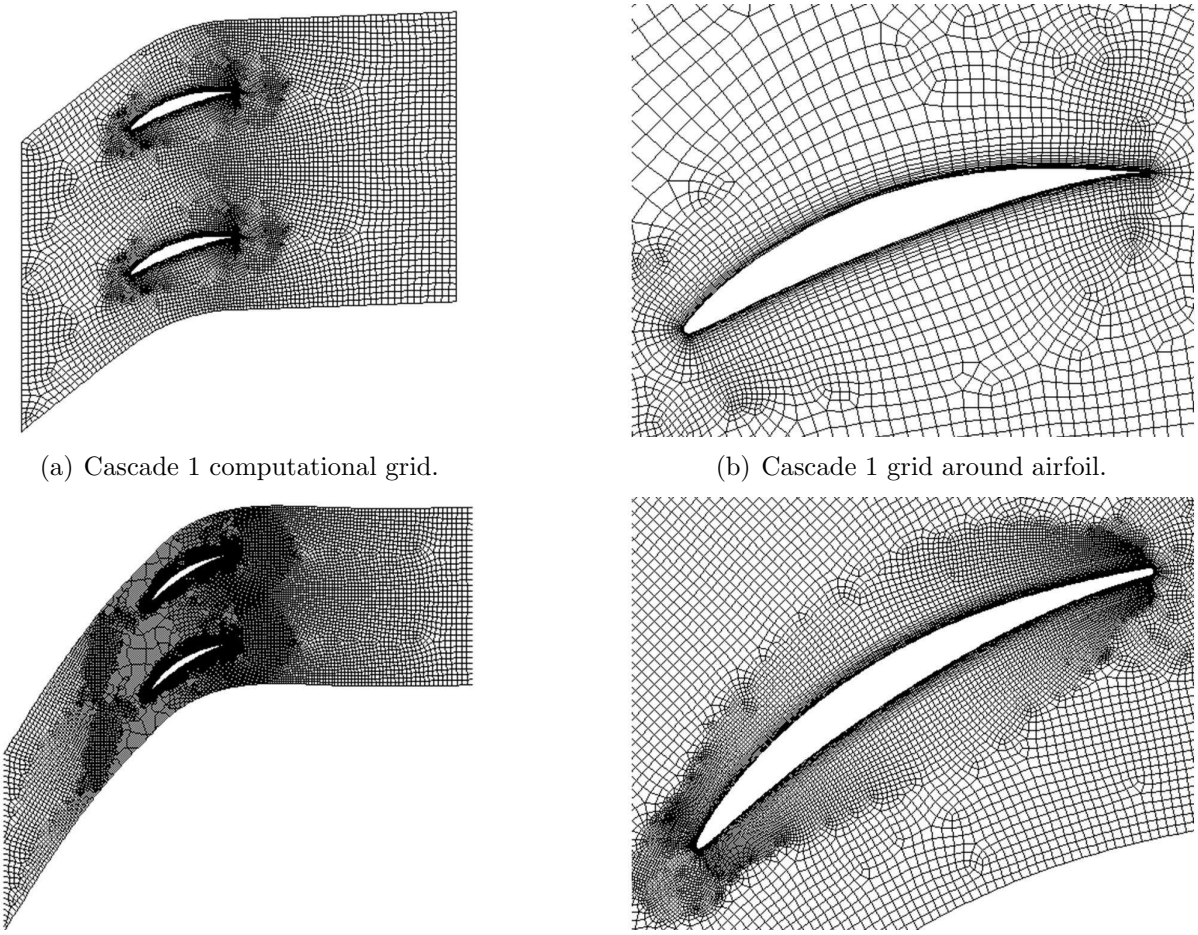

(a) Cascade 1 computational grid.

(b) Cascade 1 grid around airfoil.

(c) Cascade 2 computational grid.

(d) Cascade 2 grid around airfoil.

Figure 3-2: Computational grids for cascades 1 and 2.

Both blade passage geometries are modeled in Fluent using the $k-\epsilon$ turbulence models. The near wall region is modeled using an enhanced wall treatment, which smoothly switches between: 1) completely resolving the viscous sublayer in the near wall region and 2) a wall function that bridges the viscous sublayer and the fully turbulent region using a semi-empirical function, depending upon the value of y^+ adjacent to any solid boundaries. The enhanced wall treatment resolves the viscous sublayer when the y^+ value of the first wall adjacent cell is $\sim 4-5$ [23]. Thus the cascade 1 boundary layer is generally defined using wall functions, while cascade 2 has a generally resolved viscous sublayer[1].

[1]Although grid resolution, selection of turbulence model, and level of inlet turbulence have some effect on overall bulk performance levels, they are found to not affect trends between adiabatic and cooled bulk

For both cascades, matrices of cases are assembled by varying the flow inlet angle and the ratio of upstream total pressure to downstream static pressure. For cascade 1, cases are generated using (1) adiabatic wall and (2) constant heat flux boundary conditions (BCs). For cascade 2, cases are generated using (1) adiabatic wall and (2) cooled wall temperature BCs equal to one-half the freestream value. The non-dimensional cooling rate is defined as the heat removed from the flow normalized by the inlet stagnation enthalpy flux,

$$q^* = \frac{\dot{Q}}{\dot{m}h_{t,in}} = \frac{\Delta h_t}{h_{t,in}} = \frac{\Delta T_t}{T_{t,in}} < 0 \text{ (for cooling).} \tag{3.1}$$

Post-processing

Integrated bulk flow properties are area- or mass- averaged one chord length upstream of the airfoil leading edge (inlet) and one chord length downstream of the trailing edge (outlet). For example, velocities are mass-averaged, while pressures are area-averaged[2]. All of the results are interpolated to a given set of inlet Mach numbers in order to produce bulk performance data. The primary figures of merit used to characterize bulk blade passage performance are non-dimensional total pressure reduction (loss buckets[3]), ω, and deviation (difference between air and blade metal exit angle), δ, defined as

$$\omega = \frac{p_{t,in} - p_{t,out}}{p_{t,in} - p_{in}} \tag{3.2}$$

and

$$\delta = \beta_{out} - \chi_{out}. \tag{3.3}$$

Results in the next section are either presented at constant dimensionless cooling rate, q^*, or constant wall temperature ratio, $T_{\text{wall}}/T_{t,in}$.

performance.

[2]It is found that the differences between area-averaging and mass-averaging are not appreciable in terms of the essential conclusions of the thesis.

[3]Strictly speaking, the term loss bucket should be used with adiabatic blade-to-blade flows only, as in these flows entropy generation (lost work) is tied to loss of total pressure alone. Here, the term loss bucket is used per its conventional definition of total pressure reduction divided by inlet dynamic head.

3.3.2 Bulk Performance

The computations reveal that cooling impacts blade passage flows in the following ways:

1. For a given value of q^* at a given inlet Mach number, cooling improves performance by producing a relatively uniform reduction in ω across the loss bucket.

2. For a given value of q^* the reduction in ω increases as inlet Mach number increases.

3. The effect of reversible cooling on a one-dimensional channel flow[4] provides a reasonable first approximation to the effect of cooling on total pressure change at low inlet Mach numbers, whereas at high subsonic inlet Mach numbers (e.g., $M_{in} \sim 0.8$), cooling appears to have a more beneficial impact above and beyond the bulk cooling of the working fluid.

4. Cooling increases the flow turning (or lowers δ). Table 3.1 summarizes the average level of change of flow turning for cascade 1, for $q^* = -0.001$.

5. Cooling reduces the exit Mach number[5]. The effect of a Mach number reduction downstream (in most compressors) will be to reduce the inlet Mach number into the next blade row, thereby potentially reducing losses associated with locally supersonic regions on the blade.

6. Cooling decreases the exit stagnation temperature. This has a favorable effect on the downstream blade rows, as less work is required to compress colder air to a given pressure ratio.

[4] see Equation 3.5
[5] see Equation 3.6

M_{in}	$\Delta\beta_{na} = -\Delta\delta_{na}$
0.4	0.1°
0.8	0.25°

Table 3.1: Average effect of $q^* = -0.001$ on flow turning for cascade 1, across a range of incidences.

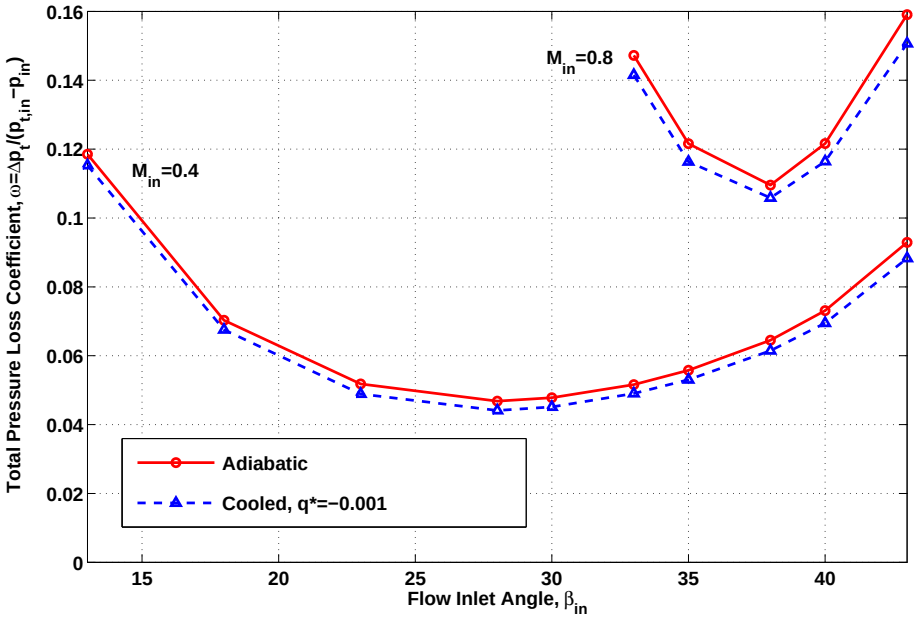

(a) Solid lines are adiabatic wall BC; dashed lines are $q^* = \frac{q}{h_{t,in}} = -0.001$.

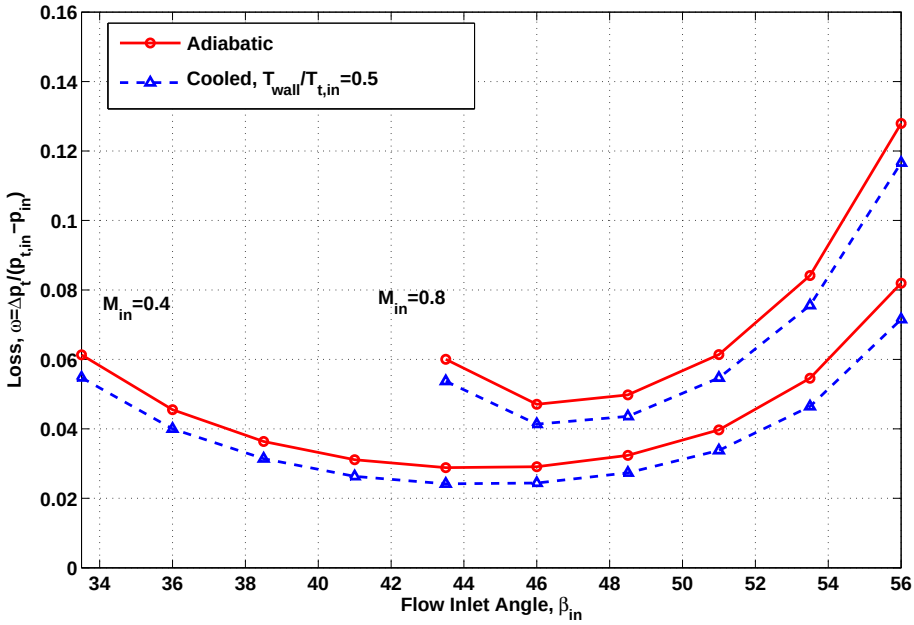

(b) Solid lines are adiabatic wall BC; dashed lines are $T_{wall}/T_{t,in} = 0.5$.

Figure 3-3: Total pressure reduction coefficient, ω, vs. flow inlet angle, β_{in}, at low (0.4) and high (0.8) inlet Mach number, for cascades 1 and 2.

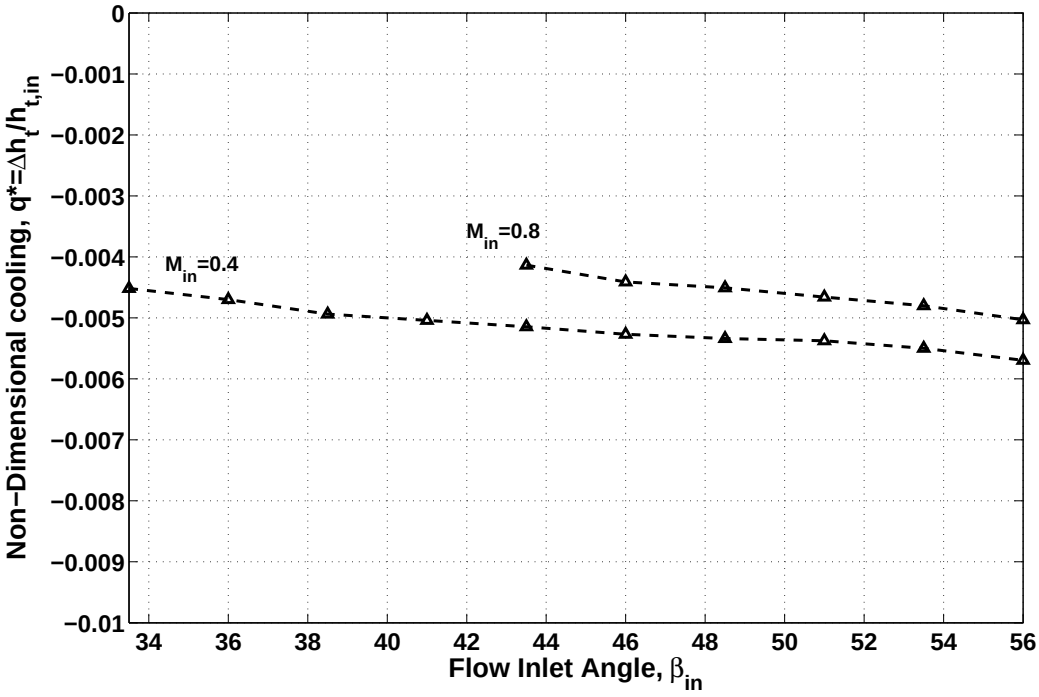

Figure 3-4: Non-dimensional cooling, q^*, vs. flow inlet angle, β_{in}, at low (0.4) and high (0.8) inlet Mach number, for cascade 2 with $T_{wall}/T_{t,in} = 0.5$ cooling boundary condition.

Figure 3-3 shows the adiabatic and cooling wall BC loss bucket for cascades 1 ($q^* = -0.001$) and 2 ($T_{wall}/T_{t,in} = 0.5$), respectively, at a low (0.4) and high (0.8) Mach number. For a given cooling wall temperature or heat flux BC at a fixed Mach number, there is a fairly uniform reduction in ω across the range of operational cascade inlet angles. Corresponding values of q^* for cascade 2 with $T_{wall}/T_{t,in} = 0.5$ are shown in Figure 3-4. As q^* shows a relatively slight variation with incidence at a given Mach number, one may conclude that this uniform ω reduction is consistent with observation 1. It is also apparent that the reduction in ω at a given wall temperature ratio or q^* increases with increasing inlet Mach number. In the fixed wall temperature case (cascade 2) absolute values of q^* are lower at the higher Mach number, implying that the benefit from cooling at a fixed q^* is further pronounced with increasing Mach number.

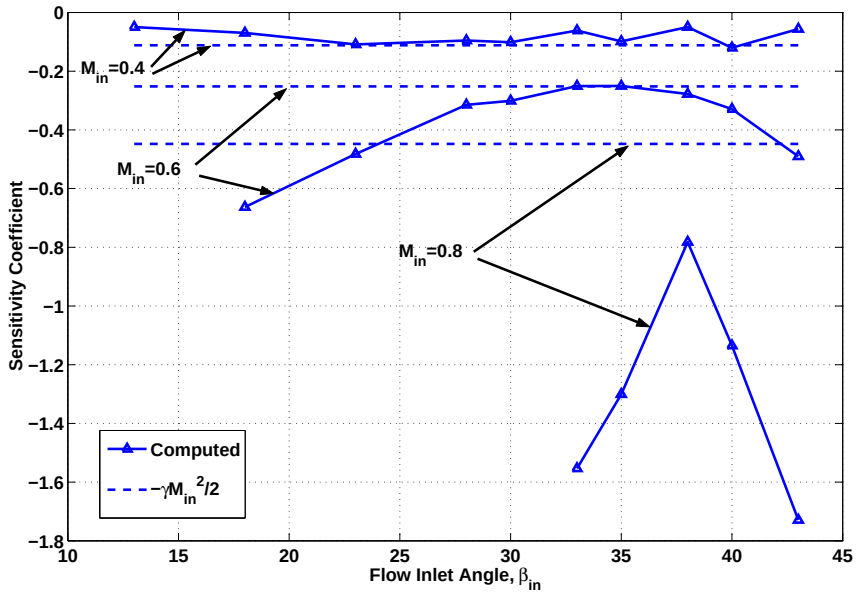

(a) Cascade 1.

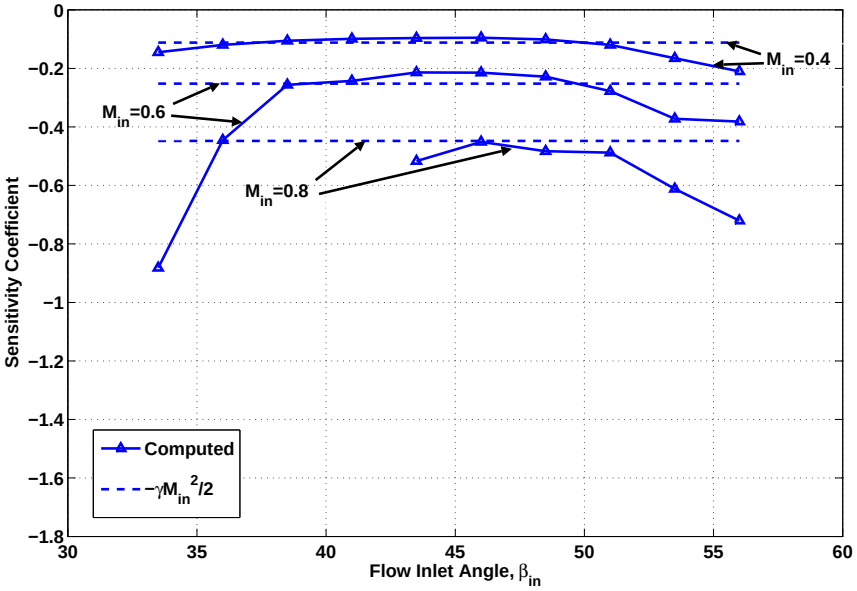

(b) Cascade 2.

Figure 3-5: CFD estimated (solid, Equation 3.4) vs. analytical one dimensional channel flow sensitivity coefficient (dashed, Equation 3.5). Data normalized to $q^* = q/h_{t,in} = -0.001$.

To elaborate on observation 3, an estimate of the fractional change in total pressure for a given amount of dimensionless cooling is obtained by comparing adiabatic and non-adiabatic CFD computations at identical inlet Mach numbers:

$$\left(\frac{\frac{\partial p_t}{p_t}}{\frac{\partial T_t}{T_t}}\right)_{M=\text{constant}} \approx \frac{\left(\frac{\Delta p_{t,cool}}{p_t} - \frac{\Delta p_{t,ad}}{p_t}\right)}{\frac{\Delta T_{t,cool}}{T_t}}. \tag{3.4}$$

The computed values given by Equation 3.4 may be compared to an analytically derived one dimensional channel flow value using the sensitivity coefficient [80] for the cooled cases, i.e.,

$$\frac{dp_t}{p_t} = -\frac{\gamma M^2}{2}\frac{dT_t}{T_t} \approx -\frac{\gamma M_{in}^2}{2} q^* \;\; (|q^*| \ll 1)\,. \tag{3.5}$$

Figure 3-5 demonstrates that at low Mach number the effect of cooling on total pressure reduction is well predicted by the analytical result given in Equation 3.5. This can be interpreted as the aero-thermodynamic benefit of heat extraction in a blade passage. At high Mach number the total pressure reduction is greater for the computed flow fields, indicating a potential additional aerodynamic benefit.

Observation 5 indicates that cooling reduces the exit Mach number of the cascade flow. This result is demonstrated by Figure 3-6. The exit Mach number reduction increases with increasing inlet Mach number, consistent with the influence coefficient from one dimensional compressible channel flow [27, 80],

$$\frac{dM^2}{M^2} = \frac{(1+\gamma M^2)(1+\frac{\gamma-1}{2}M^2)}{1-M^2}\frac{dT_t}{T_t} - \frac{2(1+\frac{\gamma-1}{2}M^2)}{1-M^2}\frac{dA}{A}. \tag{3.6}$$

From the expression in Equation 3.6, it is clear that subsonic cooling has the effect of directly reducing the Mach number (just as heating does the opposite, driving flow toward sonic conditions) by reducing the total temperature, and indirectly reducing the Mach number by an increase in effective exit flow area caused by a reduction in deviation.

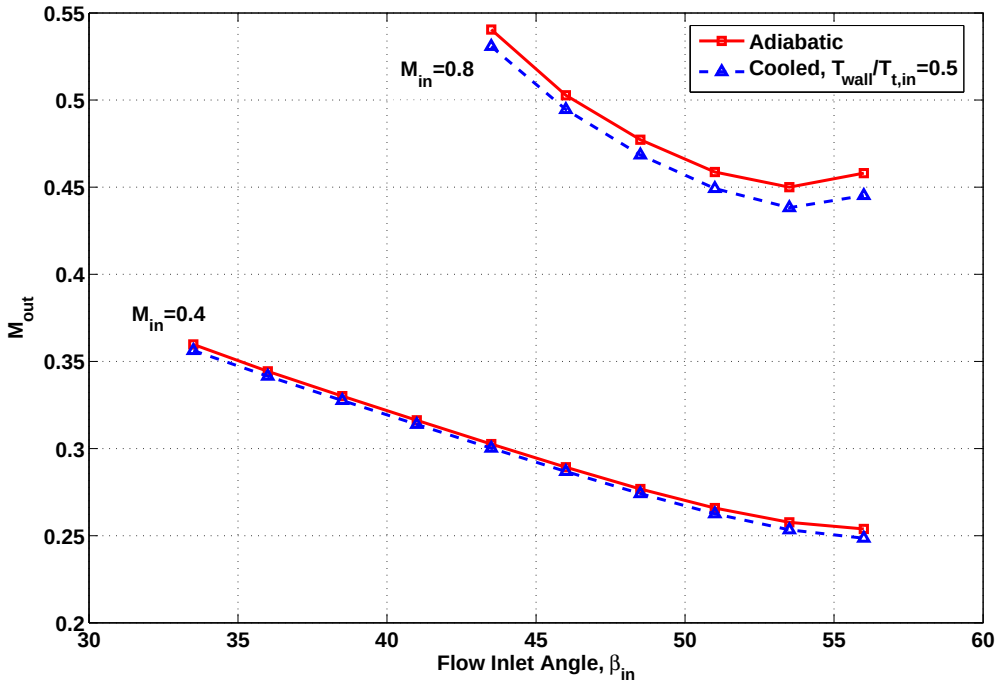

Figure 3-6: Adiabatic vs. cooled exit Mach number, M_{out}, for cascade 2. Solid line with circles represents adiabatic boundary conditions; dashed line with triangles represents blade surface cooling. Wall temperature BC is $T_{wall}/T_{t,in} = 0.5$.

3.3.3 Entropy Generation

Observation 3 in the previous subsection indicates that the reduction in ω from cooling occurs both from aero-thermodynamic compressibility effects (reversible cooling) and from the re-balancing of entropy generation (loss) inside the flow field with entropy removal across blade surfaces. The constant wall temperature BCs on the airfoil surfaces of cascade 2 allow for easy computation of the entropy flux across the blades themselves. From this, it is possible to compute the entropy generation, by considering the second law of thermodynamics over the computational domain, namely,

$$\frac{s_{gen}}{c_p} = \frac{s_{out} - s_{in}}{c_p} - q^* \frac{T_{t,in}}{T_{wall}} = \frac{s_{out} - s_{in}}{c_p} - \frac{h_{t,out} - h_{t,in}}{c_p T_{wall}}. \tag{3.7}$$

The entropy generation is comprised of two components, viscous dissipation and ther-

mal dissipation[27], which may also be computed by numerical integration over the entire computational domain,

$$\frac{s_{gen}}{c_p} = \frac{1}{\dot{m}c_p} \iiint_{\mathcal{V}} \left[\underbrace{\frac{1}{T}\tau_{ik}\left(\frac{\partial u_i}{\partial x_k}\right)}_{viscous} + \underbrace{\frac{k}{T^2}\left(\frac{\partial T}{\partial x_i}\frac{\partial T}{\partial x_i}\right)}_{thermal} \right] d\mathcal{V}, \tag{3.8}$$

where,

$$\tau_{ik} = \lambda \frac{\partial u_l}{\partial x_l}\delta_{ik} + \mu\left(\frac{\partial u_i}{\partial x_k} + \frac{\partial u_k}{\partial x_i}\right) \tag{3.9}$$

and the factor λ is assumed to be equal to $-\frac{2}{3}\mu$ [77]. It is important to note that in order to use equations 3.8 and 3.9 to calculate the specific entropy generation for turbulent flows, it is appropriate to use the effective viscosity, μ (and effective thermal conductivity, k), which is the sum of the laminar and turbulent, or eddy, viscosities (and thermal conductivities).

Figure 3-7 demonstrates that it is possible to re-construct the entropy generation using both the technique of entropy flux bookkeeping given by Equation 3.7 and the direct integration of the viscous and thermal dissipation terms given by Equation 3.8. The figure also demonstrates that entropy generation is greater for the cooled cases versus the adiabatic cases. The net decrease in ω from cooling shown in Figure 3-3 must therefore occur because the transfer of entropy across the blade surface counters additional entropy generation by thermal dissipation, such that the exit total pressure is higher in the cold wall case than for the adiabatic cascade. Specifically, the entropy constitutive relation for a perfect gas,

$$\frac{s_{out} - s_{in}}{c_p} = ln\frac{T_{t,out}}{T_{t,in}} - \frac{\gamma - 1}{\gamma} ln\frac{p_{t,out}}{p_{t,in}} = \frac{s_{gen}}{c_p} + q^*\frac{T_{t,in}}{T_{wall}}, \tag{3.10}$$

may be used to manipulate the definition of ω:

$$\omega = \frac{p_{t,in} - p_{t,out}}{p_{t,in} - p_i} = \frac{1 - \left[(1+q^*)\, exp\left(-q^*\frac{T_{t,in}}{T_{wall}} - \frac{s_{gen}}{c_p}\right)\right]^{\frac{\gamma}{\gamma-1}}}{1 - \left[1 + \frac{\gamma-1}{2}M_{in}^2\right]^{\frac{\gamma}{1-\gamma}}}. \tag{3.11}$$

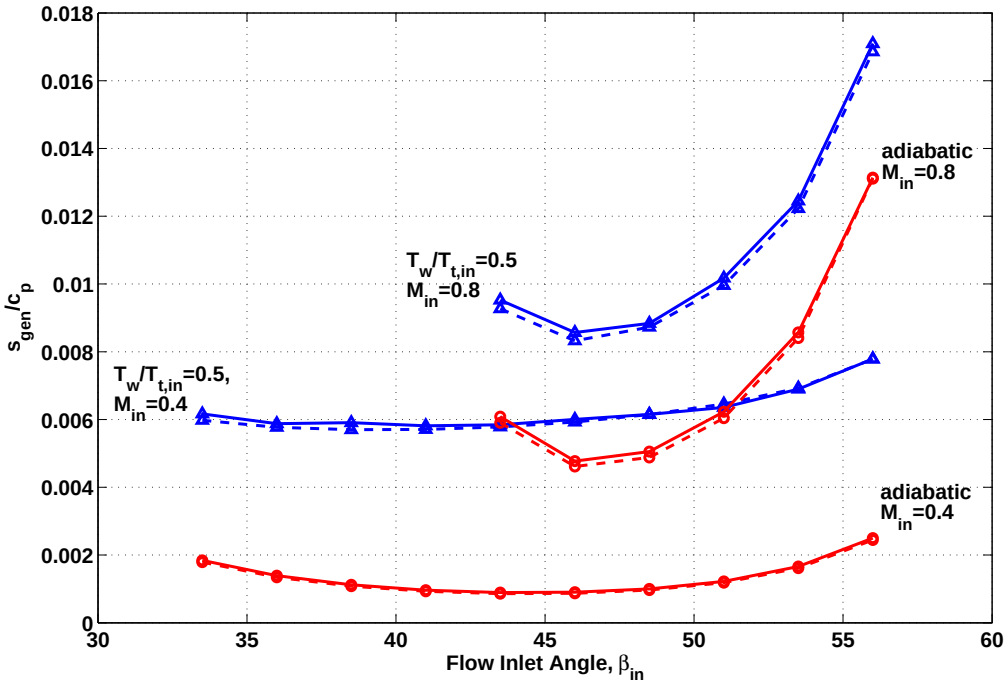

Figure 3-7: Cascade 2, computed entropy generation vs. incidence at low (0.4) and high (0.8) inlet Mach number using net entropy flux method (solid lines given by Equation 3.7) and direct volume integration(dashed lines given by Equation 3.8). Adiabatic (red) and cooled (blue, $T_{wall}/T_{t,in} = 0.5$) cases shown.

The numerator of the right hand side of Equation 3.11 shows that ω is affected both by the temperature reduction from cooling (the $1 + q^*$ term), and the competition between entropy transfer and entropy generation in the exponential ($q^* < 0$ for cooling).

Figure 3-8 presents bar charts of the viscous and thermal dissipation at a low (0.4) and high (0.8) inlet Mach number, for both the adiabatic and wall temperature boundary condition cases. From these charts several interesting observations follow. First, in the adiabatic cases virtually all of the entropy generation comes from viscous dissipation. Second, in the cases with $T_{wall}/T_{t,in} = 0.5$, the relative magnitudes of viscous and thermal dissipation are highly Mach number dependent. At low Mach numbers, thermal dissipation is the larger contributor to total entropy generation, whereas at high Mach number viscous dissipation is the larger contributor. The results show that viscous dissipation has a strong Mach number

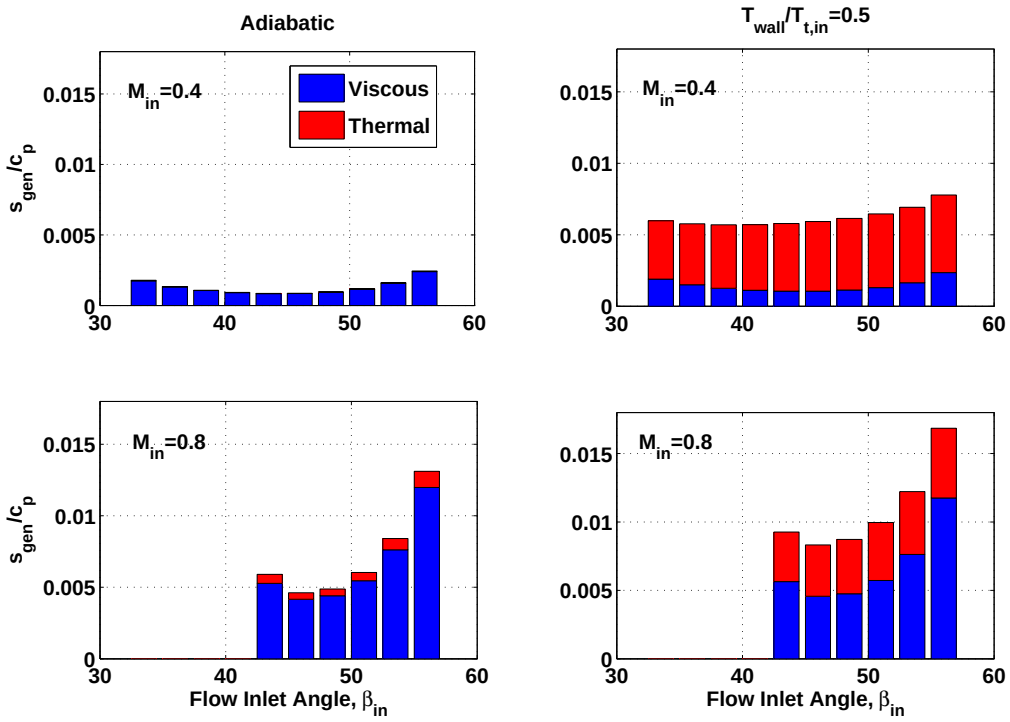

Figure 3-8: Cascade 2, viscous (black), and thermal (gray) dissipation vs. incidence at low (0.4) and high (0.8) inlet Mach number. Plots on left are adiabatic wall BC; plots on right are $T_{wall}/T_{t,in} = 0.5$.

dependency, but is virtually independent of the cooling BC, whereas thermal dissipation has weak Mach number dependency but is, of course, highly dependent upon the wall temperature BC. Since the viscous dissipation term is dependent upon local strain rates in the flow field, this may suggest that the velocity boundary layer is fairly independent of the temperature boundary layer. This implies that a simple model for the effect of blade surface heat extraction on blade passage aerodynamic performance could be constructed by building two separate models for the viscous and thermal dissipation, where the viscous dissipation could come strictly from adiabatic computations.

In summary, blade passage flows are described by traditional bulk figures of merit such as ω and δ, as well as by considering the flow from a second law of thermodynamics perspective, for two different blade passage geometries. The effect of cooling is found to decrease the value

of ω and δ, both of which favorably affect compressor performance. In addition, one would expect that the decrease in the exit stagnation temperature and exit Mach number should both favorably affect subsequent downstream blade rows, due to the increased pressure rise capability on a relatively colder fluid and the decrease in ω with decreasing Mach number. Finally, the loss generation mechanisms in the flowfield, namely viscous and thermal dissipation, are found to be relatively uncoupled, which indicates that a simple model for aerodynamic performance of non-adiabatic blade passage flows could be constructed using these components as the basis.

3.3.4 Generic Rules for Blade Passage Loss and Deviation

Generic rules for ω and δ are next created by postprocessing the CFD results shown in the previous section. The motivation for using generic rules comes from the fact that no detailed geometry information exists during the preliminary design of a compressor. These rules serve as a set of trends that can be used in a preliminary design.

By introducing cooling to the cascades, an additional performance variable is required, namely, the non dimensional cooling, q^*. For the meanline model in section 3.4, it is assumed that cooling takes place at a uniform rate over the airfoil surface. In fact, the details of the cooling distribution could also be a design variable. However, to make use of the data in a general sense, the definition is simplified to isolate the effect of each variable. The set of variables that describe the cascade performance parameters of interest are then,

$$\text{Cascade Performance} = f(\mathbf{geometry}, i, M_{in}, Re_c, q^*), \tag{3.12}$$

where,

geometry (including airfoil shape and cascade solidity, σ) is fixed for the experiment.

i is the inlet flow incidence angle.

M_{in} is the inlet Mach number.

Re_c is the inlet Reynolds Number, using airfoil chord as an appropriate length scale.

q^* is the non-dimensional cooling rate, defined as the ratio of the change in stagnation enthalpy due to cooling to the inlet stagnation enthalpy (see Equation 3.1). Because cooling involves heat removal, the adopted sign convention makes q^* a negative number for cooled cascades.

For the situation where dependence on Re_c is weak[6], and the solidity only appears in the expression for 'base' deviation (i.e., Carter's rule[7]), Equation 3.12 simplifies to

$$\omega, \Delta\delta = f(i, M_{in}, q^*), \tag{3.13}$$

where,

ω is the total pressure reduction coefficient.

$\Delta\delta$ is the change in deviation relative to the 'base' deviation.

For a low level of cooling ($|q^*| \ll 1$), the channel flow sensitivity coefficient relating a differential change in stagnation temperature of a perfect gas to the resultant differential change in stagnation pressure is linear for a given Mach number (Equation 3.5). Thus, it is assumed that to first order, it will be reasonable to scale the observed changes in ω linearly with the cooling rate.

Generic loss buckets are developed by taking each loss bucket from the CFD data for cascade 1 and referencing its minimum ω value as 'zero' incidence. Polynomial fits are used to define the bucket in the incidence range of $-15°$ to $15°$, as shown in Figure 3-9.

[6]For cascade 1, values of Re_c range from 100,000 to 200,000. For cascade 2 Re_c values range from 300,000 to 500,000. Re_c does not change appreciably between comparable adiabatic and cooled cases.

[7]Carter's rule gives the base deviation (predominantly a potential flow effect) near the minimum ω point, $\delta_{\text{base}} = m\theta\sigma^{-n}$, where m is an empirical constant which depends on geometry, θ is the camber angle (angular difference between blade metal inlet tangency and exit tangency) and n is usually taken as 0.5 for decelerating cascades [14].

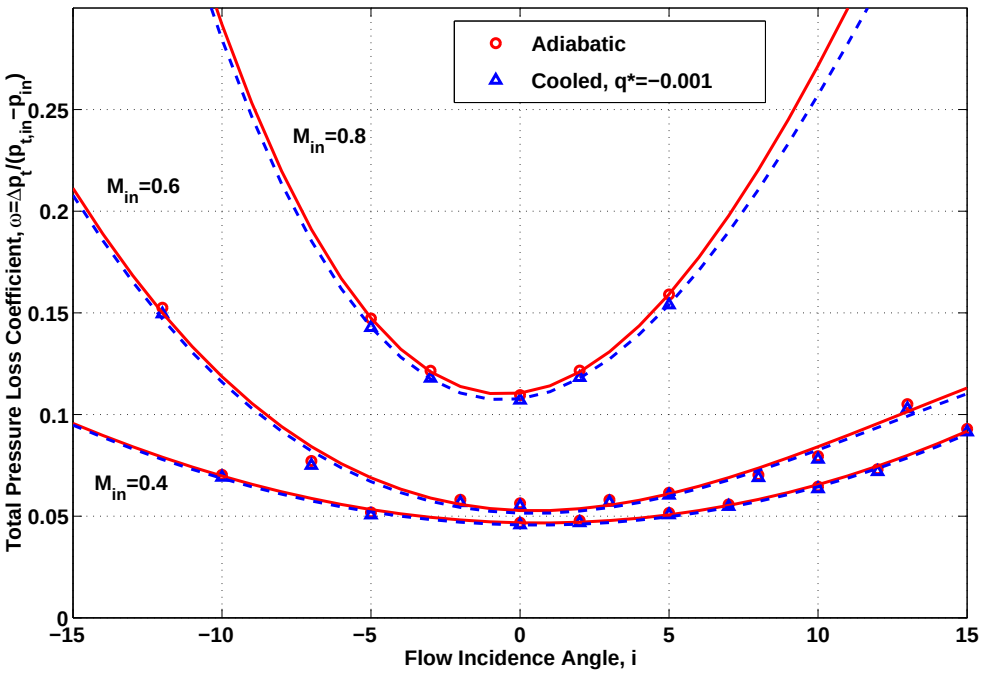

Figure 3-9: Generic adiabatic vs. cooled loss buckets derived from cascade 1 performance. Solid line with circles represents adiabatic boundary conditions; dashed line with triangles represents blade surface cooling. Non-dimensional cooling rate is $q^* = \frac{q}{h_{t,in}} = -0.001$.

Nominal deviation for adiabatic cascades at design (minimum ω) is predicted using Carter's rule. The deviation is then modified for incidence, Mach number, and cooling rate. The first deviation modification, $\Delta\delta_a$, is the increase in deviation due to 'off-design' incidence and Mach number for an adiabatic cascade. Figure 3-10 presents a smooth curve fit at three Mach numbers of $\Delta\delta_a$ used in the generic model. The figure demonstrates that the narrow operability at high Mach number occurs from a rapid deviation increase associated with flow separation and unrealized flow turning. The physical mechanism that causes the boundary layer to separate at high Mach numbers is an adverse pressure gradient created by a local normal shock on the suction side.

The second modification is reduction of deviation due to cooling, $\Delta\delta_{na}$. The generic non-adiabatic deviation reduction model is based on the cascade 1 observations summarized

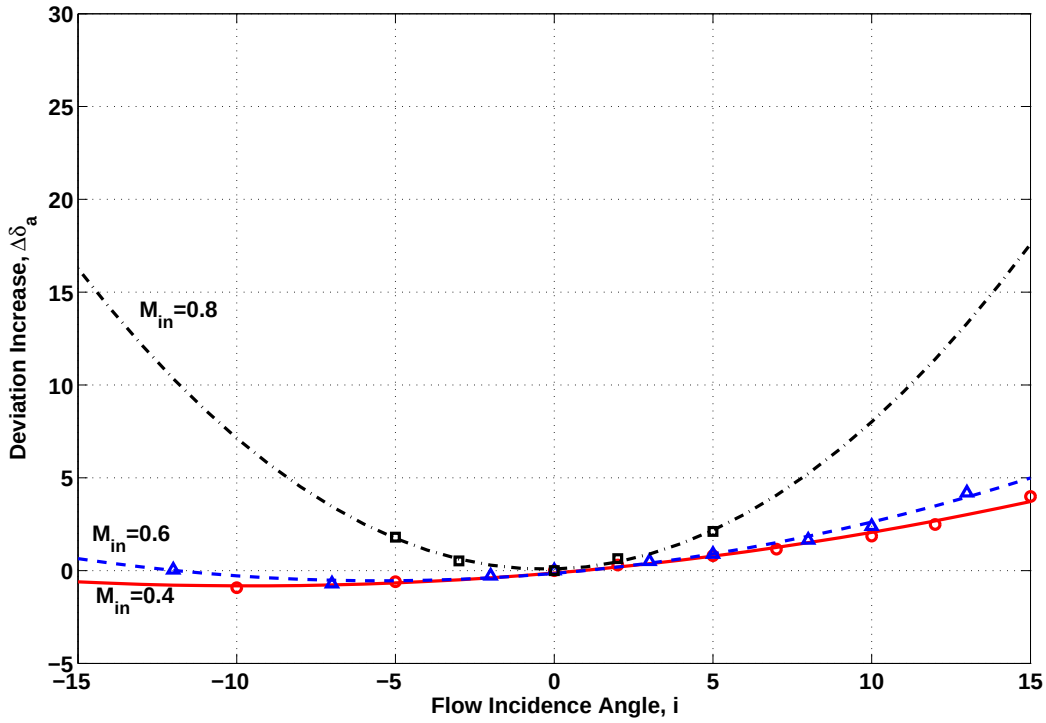

Figure 3-10: Adiabatic change in deviation, $\Delta\delta_a$, (relative to Carter's rule) for cascade 1.

earlier in Table 3.1. Figure 3-11 demonstrates that cooling reduces the deviation, and that the effect improves with inlet Mach number. The effect of inlet Mach number on $\Delta\delta_{na}$ is included in the generic model, while the effect of incidence is neglected by averaging the values of $\Delta\delta_{na}$ at each Mach number, as shown by the two solid lines.

The changes in deviation due to cooling do not have as simple an analog as changes in p_t, and hence changes in ω. In this study it is assumed that the observed changes in deviation due to cooling will scale linearly for cooling rates up to $q^* = -0.01$. This model is a significant simplification of the physical effect, but it is nonetheless valuable to include deviation effects to give a sense of the potential impact of cooling on axial compressor performance. If levels of cooling such as this are available ($q^* \sim -0.01$), the model allows for two to three degrees of deviation to be recovered from the blade rows at high subsonic Mach numbers. Two to

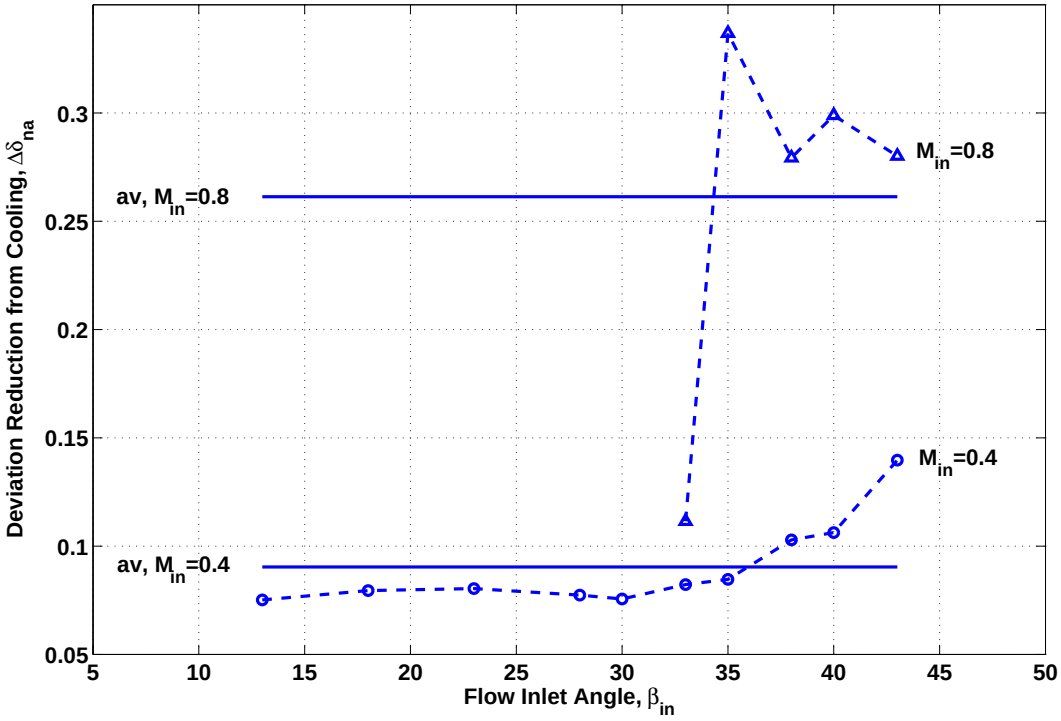

Figure 3-11: Additional flow turning from cooling, $\Delta\beta_{cool} = -\Delta\delta_{cool}$, for cascade 1, $q^* = -0.001$. Dotted lines with symbols are CFD results. Heavy solid lines are average values (used in meanline analysis) for given inlet Mach numbers.

three degrees of deviation reduction per blade row would make cooling a legitimate control variable to improve off design matching. In the meanline analysis of the next section, cooling rates up to ten times higher ($q^* = -0.01$) are selected, giving extrapolated turning values due to cooling of two to three degrees in the high Mach number stages of the compressor. The next section presents a performance map which gives an idea of the impact of the additional turning from deviation for the cooled, single stage compressor selected in this study.

3.4 On- and Off- Design Meanline Analysis

In this section, results from 2D CFD experiments are used to assess the effect of cooling on a single stage and an eight stage compressor. As the number of stages increases, off-design

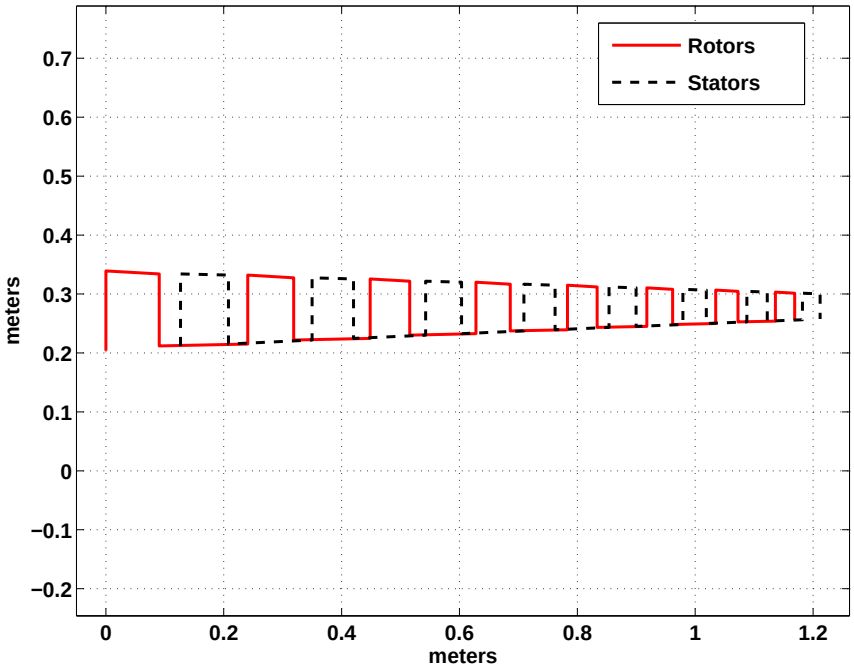

Figure 3-12: Eight stage compressor meridional layout. First stage also analyzed as a single stage fan.

matching becomes more challenging. The presence of cooling affects matching significantly, both in terms of the propagation of off-design perturbations to velocity triangles and in terms of total pressure reduction. Results show that constant corrected speed lines (constant $N_c = N/\sqrt{T_{t,in}/T_{ref}}$) on a compressor map are raised relative to their adiabatic counterparts. Qualitatively, cooling affects low N_c lines differently than high N_c lines. This is primarily due to the Mach numbers seen by the airfoils at low and high values of N_c. At high values of N_c (and hence high rotor Mach numbers), there is a very narrow range of incidences in which the airfoils may operate successfully. There is also an increase of loss with increasing Mach number. Cooling (1) increases the pressure rise, (2) increases the turning, (3) decreases the downstream stagnation temperature, and also (4) slightly decreases the downstream Mach number. Effects (2), (3), and (4) all potentially affect the flow conditions into the next blade row in a favorable manner.

The eight stage compressor is designed by specifying compressor inlet conditions based on a flight vehicle at 25 km altitude and flight Mach number of 4 (from the mission analysis of section 2.3), assuming that a lossless inlet exists upstream of the compressor. The overall pressure ratio at design is taken as 5, with each stage taken to produce the same pressure ratio, for simplicity. Air is assumed to behave as a perfect gas[8] with $\gamma = 1.4$. The compressor is sized for a 'typical' high flight Mach number vehicle by specifying an inlet corrected mass flow[9] of 51 kg/s. The hub and tip radii are chosen so as to keep the meanline radius constant from blade row to blade row. Each stage is designed to return the flow to the axial direction at the design point, so that the first stage may also be studied as a single stage fan. The meridional layout of the eight stage compressor is shown in Figure 3-12.

In order to compare various compressor cooling schemes, the local heat extraction is non-dimensionalized by the compressor face inlet stagnation enthalpy,

$$q^*_{\text{comp}} = \frac{\dot{Q}}{\dot{m} h_{t,in,\text{comp}}} = \frac{\Delta\ h_t}{h_{t,in,\text{comp}}}. \tag{3.14}$$

The subscript 'comp' is dropped in the subsequent discussion of compressor cooling, but it should be noted that the non-dimensionalization follows Equation 3.14. The results from the single stage and the eight stage compressors are presented in the next two subsections.

3.4.1 Single Stage Fan

The single stage fan map comparing an adiabatic and a cooled fan stage is shown in Figure 3-13. For a non-dimensional cooling value of $q^* = -0.0025$ in both the rotor and stator, results indicate that the constant corrected speed line on a given adiabatic compressor map moves up

[8] In general, a variable specific heat thermodynamic model may be more accurate for a high flight Mach number vehicle in which air enters the compressor at very high temperature. For consistency between the meanline analysis and the CFD computations γ is chosen to be 1.4. No qualitative difference is expected between a variable or fixed specific heat model.

[9] $\dot{m}_c = \frac{\dot{m}\sqrt{T_t/T_{ref}}}{p_t/p_{ref}}$, where T_{ref} and p_{ref} are standard day conditions.

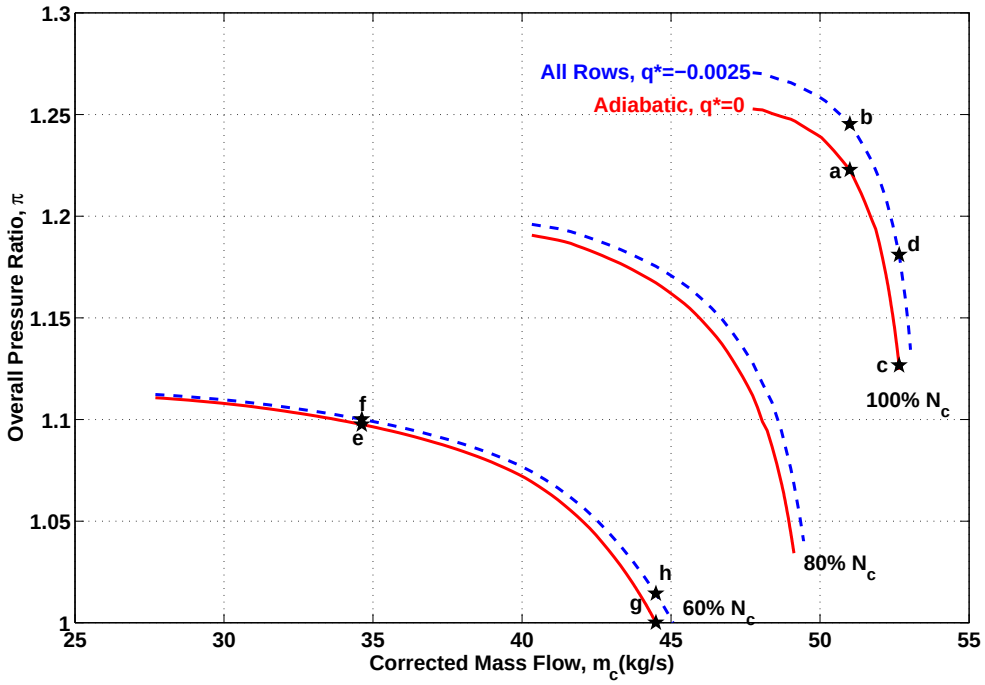

Figure 3-13: Single stage compressor map, with and without cooling. Solid line is adiabatic; Dashed line is $q^* = -0.0025$. 100%, 80%, and 60% N_c lines are shown.

in pressure ratio and in mass flow[10]. Thus, a cooled compressor produces a greater pressure rise at a given corrected mass flow and corrected speed. In addition, as $\dot{m}_c$ increases along a given constant N_c line and the line approaches vertical (i.e. choked), a cooled compressor can pass greater corrected mass flow versus an adiabatic compressor.

The increase in corrected mass flow occurs both at high and low corrected speed, but a constant value of q^* affects the corrected speed lines differently. Table 3.2 presents key blade passage parameters for points a through h in Figure 3-13. At high N_c (points a-d), the blade passages see higher inlet Mach numbers and thus have a narrower range of operable incidences, resulting in a greater sensitivity to the beneficial effects of cooling. For example, at 100% N_c the 'stall' side of the speed line shows a greater improvement in pressure ratio for the same corrected mass flow (point a vs. b), than at 60%N_c (point e vs. f). Examination of

[10]It should be noted that some of the chosen values of q^* in both the single stage and multi-stage examples lead to values of q^* which require extrapolation of the two-dimensional cascade data presented earlier.

Point	$M_{in,R}$	$M_{in,S}$	$M_{out,R}$	$M_{out,S}$	i_R	i_S	$\Delta\delta_R$	$\Delta\delta_S$	ω_R	ω_S
a	0.941	0.718	0.772	0.669	0.000	0.000	0.370	0.045	0.177	0.099
b	0.941	0.701	0.769	0.645	0.000	1.559	0.370	0.300	0.166	0.096
c	0.985	0.831	0.845	0.949	-1.919	-5.772	1.382	3.186	0.206	0.187
d	0.985	0.793	0.828	0.770	-1.919	-3.372	1.382	1.013	0.191	0.125
e	0.537	0.438	0.468	0.423	0.967	-0.704	0.000	-0.229	0.051	0.050
f	0.537	0.436	0.469	0.421	0.967	-0.311	0.000	-0.178	0.048	0.046
g	0.664	0.656	0.638	0.718	-7.963	-14.661	0.240	1.743	0.111	0.220
h	0.664	0.648	0.634	0.693	-7.963	-13.877	0.240	1.347	0.101	0.185

Table 3.2: Key single stage fan map parameters at points a through h, as shown in Figure 3-13. The variables M, i, $\Delta\delta$, and ω are Mach number, incidence, deviation change, and total pressure reduction coefficient, respectively. The subscripts *in* and *out* correspond to the inlet and outlet, respectively. The subscripts R and S correspond to the rotor and stator, respectively

the one-dimensional flow properties at the points shown explains why this is so. The 100% N_c line is in the high subsonic regime, where cooling has a more pronounced impact on ω and δ than the low subsonic regime that is encountered along the 60% N_c line. Comparison of the stator inlet and exit Mach numbers of points c (adiabatic) and d (cooled) shows that in the adiabatic case the stator behaves as a throttle, and is no longer diffusing the flow, whereas in the cooled case there is much less total pressure reduction and the stator is still diffusing the flow. The difference in stator incidence at these points varies by only 2.4 degrees, but since the inlet Mach number is in the high subsonic regime, ω in the cooled stator is 33% lower than the adiabatic stator. Comparing these two points to their low N_c counterparts, points g and h, shows that the smaller change in total pressure reduction due to cooling is a result of less incidence change and lower inlet Mach numbers. Points e and f show even less change, as their Mach numbers are closer to the low subsonic regime.

Studies on the single stage fan reveal that the improvement in pressure rise capability seen on the compressor map is attributable to both the increase in stagnation pressure from cooling (lower ω) and the increased flow turning (lower δ). Figure 3-14 shows the change in cooled speed lines when the effects on total pressure reduction and flow turning are both isolated, and when they are both included. For the selected geometry, both of these effects

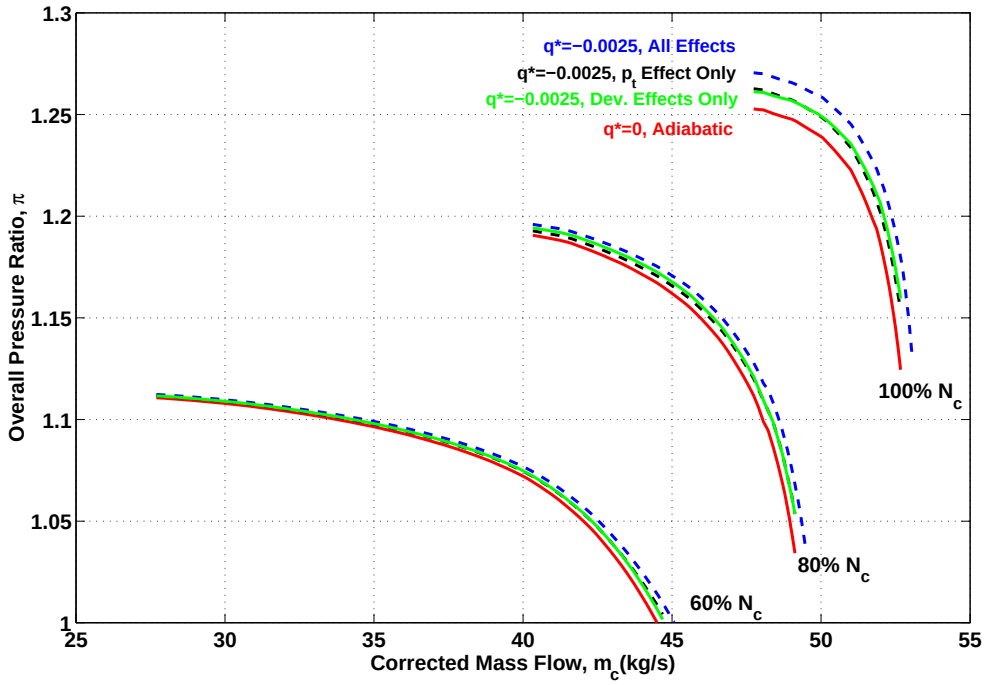

Figure 3-14: Single stage compressor map, with and without different effects from cooled cascade performance. Solid red line is adiabatic; Solid green line shows effect of change in deviation due to cooling; Dashed black line shows effect of change in ω due to cooling; Dashed blue line shows both effects. 100%, 80%, and 60% N_c lines are shown. In cooled cases, $q^* = -0.0025$.

appear comparable when isolated and applied alone. This map also indicates that if the effects of deviation are not included, the predicted benefits would be lower, but the essential conclusions would remain unchanged.

3.4.2 Eight Stage Compressor

Four different cases are analyzed on a hypothetical eight stage compressor using the meanline design framework. The cooling schemes are $q^* = -0.01$ in the first two stages (rotor and stator cooling), $q^* = -0.0025$ in all eight stages, and $q^* = -0.01$ in the last two stages, as depicted in Figure 3-15. The total cooling rates of the three schemes are non-dimensionally equal to four percent of the inlet stagnation enthalpy flux. Thus, for a given corrected mass

flow and inlet stagnation temperature, the same total cooling rate, in units of power (e.g. Watts), is extracted from each of the cooled compressors.

Efficiency, η, is defined in Equation 3.15 per the conventional adiabatic efficiency definition of isentropic work required to achieve a given pressure ratio divided by the actual shaft work. This constitutes a modification of the conventional definition to account for the effect of cooling on the change in total temperature (i.e., the temperature ratio alone is no longer an indicator of shaft work). The use of this efficiency definition allows for the comparison between the actual work inputs of an adiabatic and a cooled compressor at a given pressure ratio, because the same adiabatic reference process is assumed in both cases [11].

[11] An alternate, 'non-adiabatic' efficiency (η_{na}) definition given in section 3.7 compares the actual shaft work required to achieve given pressure ratio to a lossless, non-adiabatic reference process. The definition of η_{na} accounts for the additional theoretically extractable work between the hot gas and cold wall (via a hypothetical heat engine).

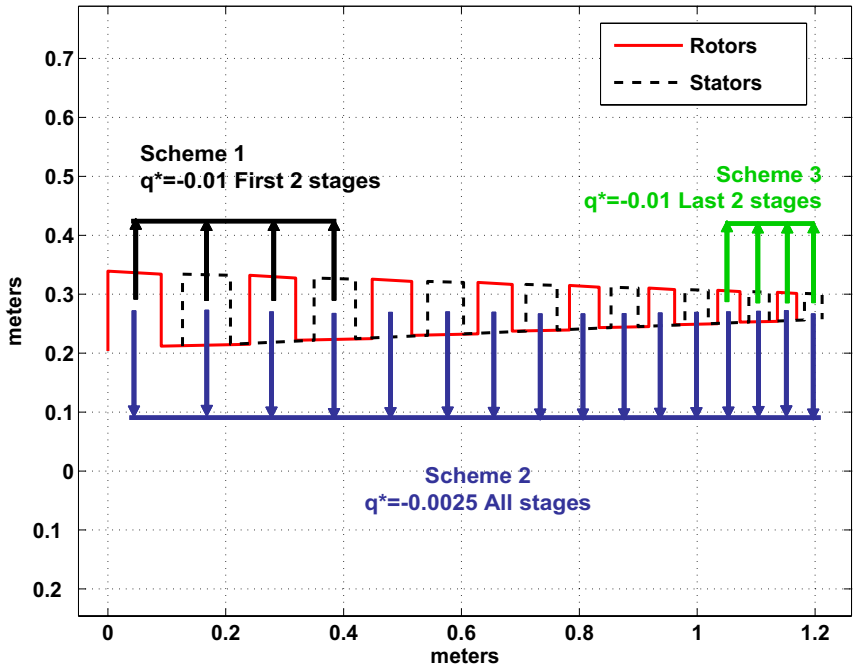

Figure 3-15: Cooling schemes studied in eight stage compressor meanline model.

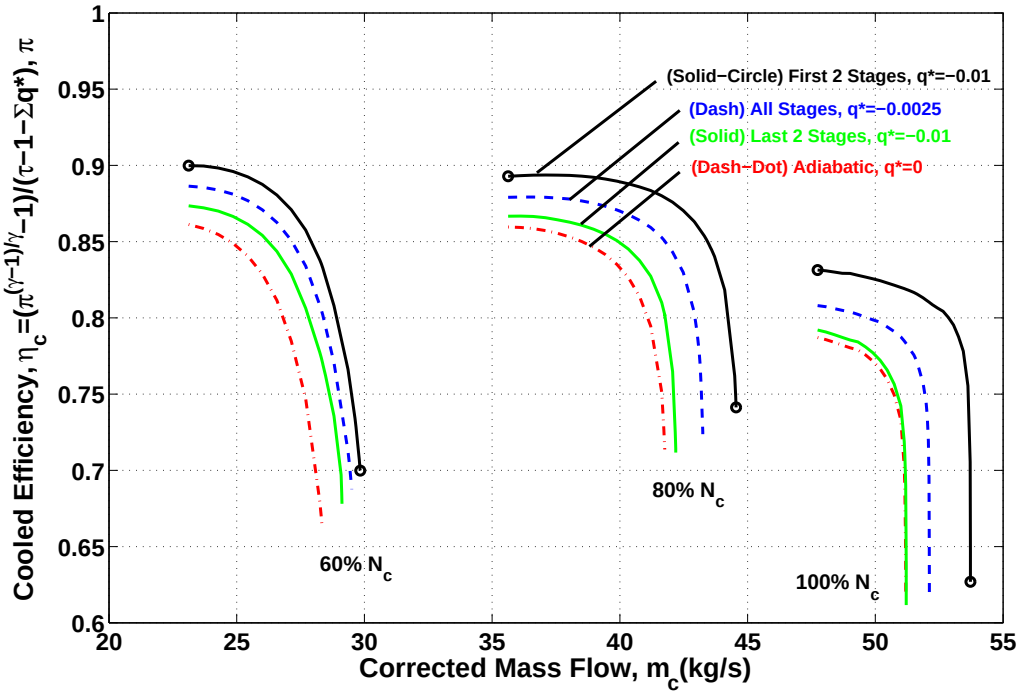

Figure 3-16: Eight stage efficiency map, with and without cooling. Dash-dot line is adiabatic; solid line is $q^* = -0.01$ in last two stages; dashed line is $q^* = -0.0025$ in all stages; solid line with circles is $q^* = -0.01$ in first two stages. 100%, 80%, and 60% N_c lines are shown.

$$\eta = \frac{\pi^{(\gamma-1)/\gamma} - 1}{\tau - 1 - q^*} \tag{3.15}$$

The efficiency map and compressor maps for an adiabatic case and three cooled cases are shown in Figures 3-16 and 3-17, respectively. The six key adiabatic points, i through n, shown on the compressor map are summarized in Table 3.3. Points i, j, and k are on the high speed (100% N_c) line, and represent the design point, a high speed stall side point and a high speed choke side point, respectively. Points l, m, and n are on the low speed (60% N_c) line, and represent a point having the same throttle characteristic as point i (i.e., a low speed throttle point), a low speed stall side point, and a low speed choke side point, respectively. The incidence angles and inlet Mach numbers into the eight rotors and stators set the levels of ω and $\Delta\delta$. The adiabatic design point, i, has zero incidence into each rotor and stator.

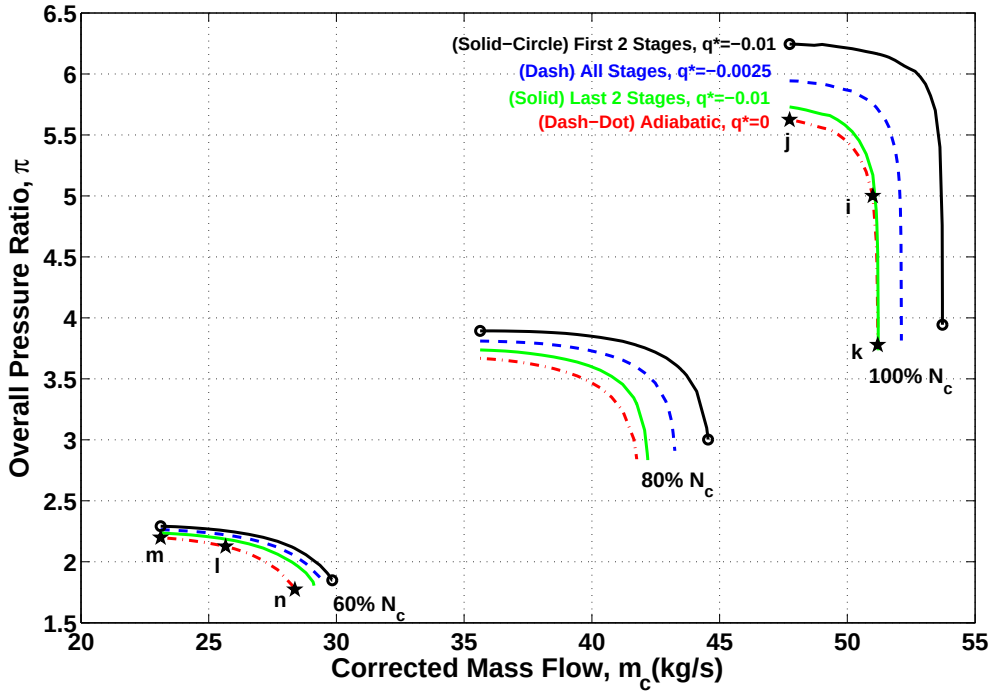

Figure 3-17: Eight stage compressor map, with and without cooling. Solid red line is adiabatic; Dashed-dot green line is $q^* = -0.01$ in last two stages; Dashed blue line is $q^* = -0.0025$ in all stages; Solid black line is $q^* = -0.01$ in first two stages. 100%, 80%, and 60% N_c lines are shown.

The Mach number into the rotors is above 0.8 in the early stages[12], i.e. in the high subsonic regime. As one moves along the speed line toward the stall side, i.e, toward point j, all of the rotor and stator incidences increase monotonically. In the opposite direction, toward point k, all of the blade row incidences decrease monotonically. At low power, the low speed throttle point, point l, shows that the front stages are all operating at positive incidence, while the rear stages all operate toward negative incidence. The change in incidence from

[12]Note that this represents an area of extrapolation in the generic loss bucket data, as $M_{in} = 0.8$ is the maximum Mach number included in the generic loss buckets and flow turning data. One would expect consistency in the cooling performance trends beyond the range of data shown (up to higher subsonic Mach numbers such as $M_{in} \sim 0.9$), because data from lower subsonic Mach numbers is used to extrapolate into a region where there is typically a strong divergence of flow properties (e.g., drag, pressure coefficient), thereby making the extrapolations conservative. One would also expect this diverging trend to apply to changes in cascade performance due to cooling. For example, Equation 3.5 shows that the incremental total pressure reduction goes up parabolically with increasing Mach number for small amounts of cooling.

Rotor Incidence, i								
Stage →	1	2	3	4	5	6	7	8
Point i	0.000	0.000	0.000	0.000	0.000	0.000	0.000	0.000
j	3.332	3.644	4.138	4.484	4.817	5.229	5.508	5.663
k	-0.210	-0.409	-0.696	-1.113	-1.691	-2.447	-3.614	-5.967
l	10.539	7.496	5.496	3.435	1.279	-0.961	-3.363	-6.030
m	13.599	10.265	8.303	6.320	4.277	2.201	0.050	-2.207
n	7.464	4.713	2.632	0.430	-1.950	-4.548	-7.596	-11.884

Stator Incidence, i								
Stage →	1	2	3	4	5	6	7	8
Point i	0.000	0.000	0.000	0.000	0.000	0.000	0.000	0.000
j	4.001	4.906	5.490	6.068	6.651	6.889	6.923	6.812
k	-0.460	-0.803	-1.273	-1.929	-2.801	-4.012	-6.014	-11.165
l	11.410	8.722	5.774	2.807	-0.127	-3.039	-5.995	9.160
m	15.344	12.740	9.797	6.845	3.939	1.123	-1.624	-4.332
n	7.503	4.698	1.688	-1.390	-4.498	-7.801	-11.720	-19.178

Rotor Inlet Mach Number, M_{in}								
Stage →	1	2	3	4	5	6	7	8
Point i	0.941	0.898	0.860	0.825	0.794	0.764	0.737	0.711
j	0.876	0.818	0.773	0.736	0.702	0.670	0.643	0.619
k	0.945	0.906	0.874	0.848	0.827	0.811	0.803	0.812
l	0.457	0.453	0.465	0.479	0.496	0.515	0.538	0.568
m	0.439	0.428	0.437	0.449	0.462	0.477	0.494	0.513
n	0.479	0.481	0.496	0.515	0.537	0.565	0.603	0.667

Stator Inlet Mach Number, M_{in}								
Stage →	1	2	3	4	5	6	7	8
Point i	0.775	0.745	0.719	0.697	0.680	0.663	0.648	0.635
j	0.708	0.672	0.642	0.617	0.598	0.580	0.566	0.555
k	0.781	0.755	0.735	0.721	0.714	0.712	0.721	0.767
l	0.383	0.394	0.408	0.424	0.446	0.471	0.502	0.543
m	0.363	0.373	0.383	0.396	0.413	0.433	0.456	0.483
n	0.406	0.420	0.438	0.460	0.489	0.526	0.579	0.689

Table 3.3: Key eight stage compressor map parameters at adiabatic points i through n, as shown in Figure 3-17. From top to bottom, sub-tables show rotor incidence, stator incidence, rotor inlet Mach number, and stator inlet Mach number, respectively.

stage to stage progresses monotonically from stall side to choke side. Again, moving along the low speed line in the direction of lower mass flow increases the incidence on all blade rows, while moving in the opposite direction has the opposite effect.

Examination of the inlet Mach numbers from stage to stage reveal an important multi-stage compressor matching feature. On the 100% N_c line Mach numbers primarily decrease from front to back, while on the 60% N_c line they increase. This is due to the fact that the annulus areas at low N_c are under-designed to pass the required mass flow, versus at high N_c. Stated another way, at low speed the front stages provide relatively less charging pressure (or density rise) to pass the required mass flow leading to greater axial (and blade relative) Mach numbers. The degree to which the annular area is under-designed on the low N_c line increases as the rear stages are reached; therefore, cooling in the last two stages alone has greater effect on the choke side of the low N_c line than on the choke side of the high N_c line.

The compressor map also clearly shows that at all corrected speeds, for the cooling schemes presented, the highest pressure ratio is achieved by (1) cooling the first two stages, followed by (2) cooling all stages, (3) cooling the last two stages, and finally (4) the adiabatic case. Table 3.4 quantifies the performance improvement of the three cooled compressors relative to the adiabatic case, along the design corrected speed line and at the design corrected mass flow. Cooling schemes (1) to (3), respectively, produce 23%, 15%, and 3% improvements in pressure ratio, relative to adiabatic case (4). Efficiency improves by 12%, 7%, and 1%, respectively. Choking mass flow of schemes (1) and (2) increase by 5% and 2%, respectively,

Case	π	π/π_{des}	η	η/η_{des}	$\dot{m}_{\text{choke}}$ (kg/s)	$\dot{m}_{\text{choke}}/\dot{m}_{\text{choke,des}}$
First 4 Stages $q^* = -0.01$	6.17	1.23	82.00%	1.12	53.72	1.05
All Stages $q^* = -0.0025$	5.76	1.15	78.75%	1.07	52.12	1.02
Last 4 Stages $q^* = -0.01$	5.17	1.03	74.23%	1.01	51.21	1.00
Adiabatic	5.00	1.00	73.31%	1.00	51.19	1.00

Table 3.4: Eight stage compressor cooling scheme summary for design corrected speed line (100% N_c) and design corrected mass flow.

while there is negligible change in the choking mass flow of scheme (3).

The results are consistent with the $T - s$ diagram shown in Figure 2-11, which says that ideally, a lossless pre-cooler is superior to cooled compression, because the fluid upon which shaft work is being done is at the lowest temperature possible, producing the highest total pressure rise. In other words, in addition to the aerodynamic benefit associated with cooling in the blade passages, there is a thermodynamic benefit associated with delivering colder, lower Mach number air to the downstream blade rows, making it most desirable to introduce a given amount of cooling, q^*, as far forward in the compressor as possible.

Finally, it is well known that at low N_c the rear of the compressor sets the mass flow capability. Moving along a low N_c speed line in the direction of increasing $\dot{m}_c$, the front stages provide lower and lower pressure (or density) rise, leading to higher and higher axial velocities in order to pass the required mass flow in the rear stages. The rearmost stator thus encounters flow at larger negative incidences, leading to higher losses, and reduced turning capability. Eventually, turning is reduced to such low amounts that throttle-like behavior occurs in the rearmost stator, increasing the compressor exit Mach number until it reaches the thermal choking limit of 1. Since putting all of the cooling in the first two stages produces the largest increase in corrected mass flow at all speeds, one may conclude that the presence of cooling in upstream blade rows relieves the adiabatic choking limit in the downstream rows. This effect arises both due to the increased pressure (or density) rise capability in the cooled upstream blade rows (aerodynamic effect), and the temperature reduction (relative to adiabatic) into the downstream blade rows (thermodynamic effect).

3.5 Three Dimensional Flow Computations

Three-dimensional CFD experiments using Fluent on the transonic NASA Rotor 35 geometry are presented in this section to demonstrate the utility of compressor cooling on a geometry of practical interest. Computations on this geometry have the advantage of readily available test data in the literature [71]. NASA Stage 35 consists of a rotor and stator that have been designed and tested for transonic operation. The design pressure ratio is 1.82 and the design

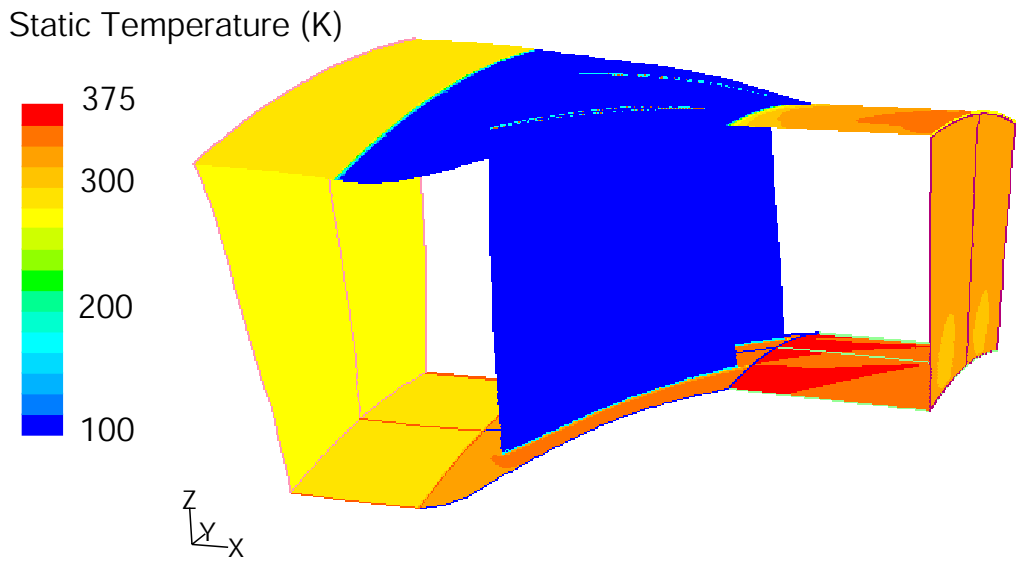

Figure 3-18: Rotor 35 geometry and boundary conditions (single passage periodic) for non-adiabatic case. Filled static temperature contours on wall boundaries (hub, casing, and blade surfaces) show BC of 100 K on blade and middle portion of outer casing surface. Positive x-axis is downstream axial direction.

rotor tip speed is 455 m/s. The stage has been tested over the stable operating range of 70%, 90%, and 100% operating speed. Results presented in this section are based on rotor-alone computations.

An adiabatic and wall temperature BC speedline is generated for the rotor alone. Figure 3-18 shows the rotor geometry and the wall temperature BCs employed in the non-adiabatic computation. The x-axis represents the positive axial direction. The inlet total temperature in both cases is 300 K. Static temperature BCs of 100 K are placed on the blade surface and on the OD rotor case wall in the non-adiabatic speedline computation. Since a real compressor is three-dimensional, the ratio of wetted surface area to annular cross sectional area is higher than in a two-dimensional cascade. Thus, it is advantageous to allow heat transfers and entropy transfers to take place across a portion of this casing surface.

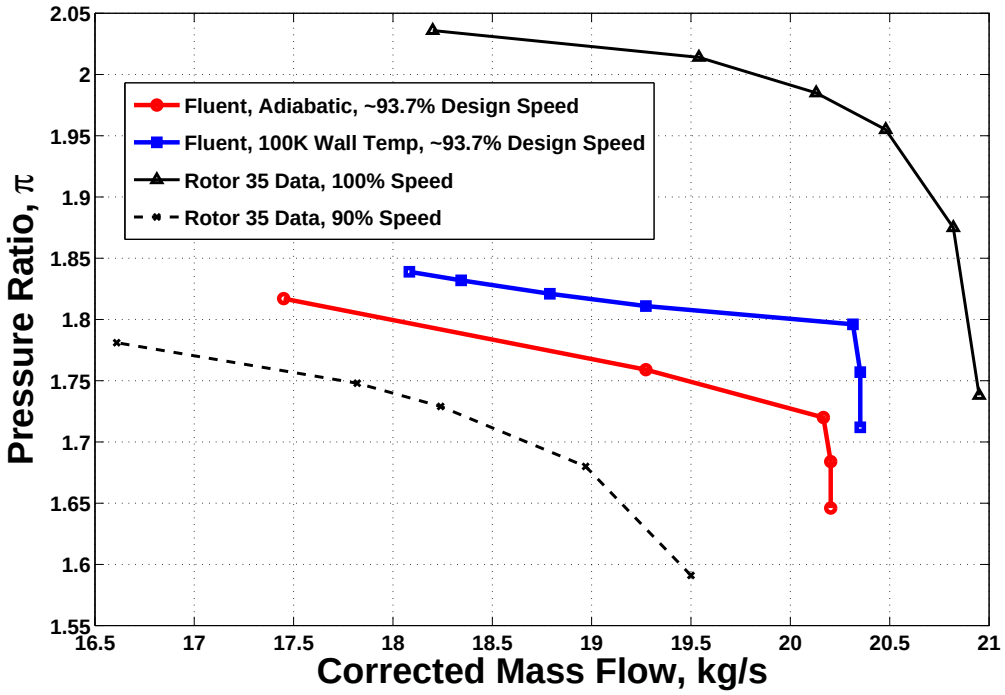

Figure 3-19: Rotor 35 pressure ratio map.

Figure 3-19 shows the compressor map for the CFD cases studied, and compares it to test data at 90% and 100% corrected speed. The CFD cases are run to a corrected speed of 93.7%[13]. The pressure ratio computed in the CFD cases is based on a mass-average of the total pressure in the absolute frame of reference at the exit plane of the computational domain. The adiabatic CFD speed line is positioned reasonably well relative to the rig data. The non-adiabatic speed line is qualitatively similar to the non-adiabatic speed lines generated in the meanline analysis, in terms of increased pressure ratio and mass flow capability. For example, at a corrected flow of 19.27 kg/s, the non-adiabatic rotor computation shows a pressure ratio of 1.81, versus a pressure ratio of 1.76 at a similar corrected flow in the adiabatic case. The maximum mass flow capability increases from 20.20

[13]The intent of these computations is to to determine whether the conclusions from the meanline analysis are relevant to higher performance geometries of practical interest. The computations have been run at a speed near the absolute design speed and have been corrected to the absolute and reference conditions given in the test report *a posteriori*, resulting in a corrected speed different from available data.

kg/s to 20.35 kg/s, or 0.7%. The value of q^* for the non-adiabatic speed line is of the order of -0.008 across the range of mass flows shown. Gong [26] presents a simple model for the purely thermodynamic effect of constant pressure heat exchange followed by compression at fixed adiabatic efficiency. The non-adiabatic pressure ratio, π_{na} is related to the adiabatic pressure ratio, π_a by,

$$\pi_{na} = \left[\frac{1}{1+q^*} \left(\pi_a{}^{\frac{\gamma-1}{\gamma}} - 1 \right) + 1 \right]^{\frac{\gamma}{\gamma-1}}, \tag{3.16}$$

and the non-adiabatic mass flow, $\dot{m}_{na}$ is related to the adiabatic mass flow, $\dot{m}_a$, by,

$$\dot{m}_{na} = \dot{m}_a \frac{1}{1+q^*}. \tag{3.17}$$

By considering the value of $q^* = -0.008$ and the adiabatic pressure ratio of 1.76, it may be shown that Equation 3.17 predicts the increased mass flow quite accurately (0.8%), whereas the increased pressure ratio is well underpredicted by Equation 3.16. Thus it may be indirectly inferred that it is primarily the aerodynamic performance improvement from blade passage surface heat extraction that provides the pressure rise shown in this computation, while the mass flow improvement is a purely thermodynamic effect. These simple models result in a similar conclusion for the compressors modeled earlier in the meanline analysis.

Figure 3-20 shows the efficiency map for the 93.7% speed line, as compared to the 90% and 100% rig test measuremnts. The efficiency definition for the transonic rotor CFD cases is consistent with that used in the meanline analyses, namely, the ratio of the isentropic work required to achieve the given pressure ratio to the actual (shaft) work done by the rotor. The actual shaft work is computed by integrating over the rotating surfaces to compute the axial torque ($\mathcal{T}_x$) and multiplying by the rotational shaft speed (Ω), as shown in Equation 3.18:

$$\eta = \frac{\pi^{(\gamma-1)/\gamma} - 1}{\frac{\mathcal{T}_x \Omega}{\dot{m} h_{t,in,comp}}}. \tag{3.18}$$

The efficiency map suggests a peak efficiency increase of approximately 2% for the case with cooling BC, and 1%-2% at lower values of corrected flow. These efficiency improvements are

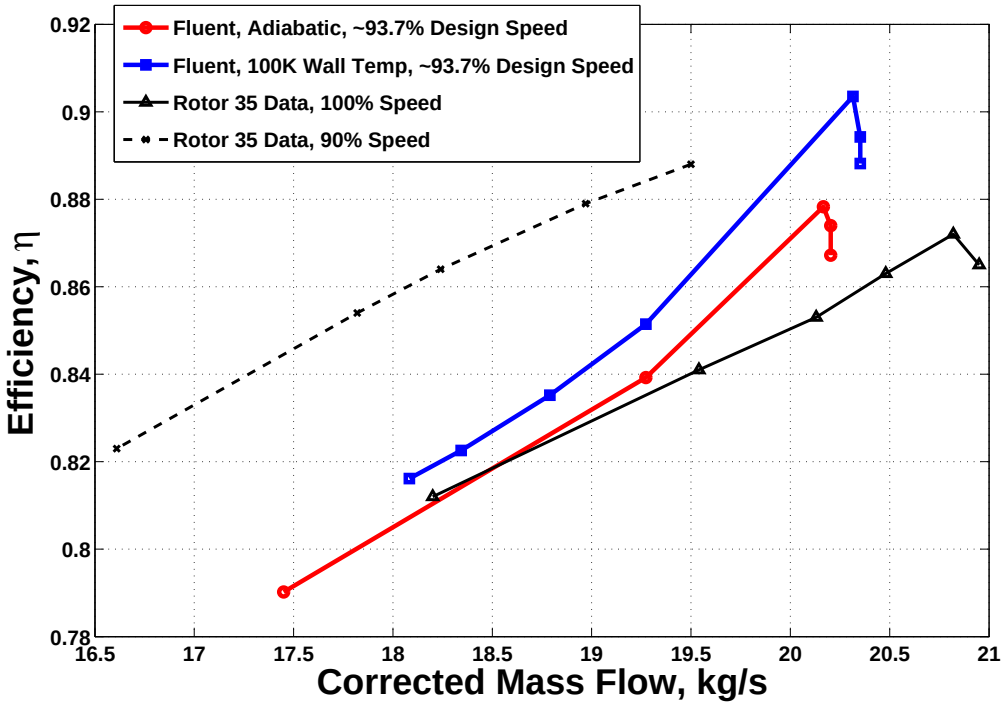

Figure 3-20: Rotor 35 efficiency map.

consistent with those seen in the meanline cases.

3.6 Heat Transfer Considerations

CFD and meanline modeling on single stage and multistage compressor geometries having adiabatic design points show potential performance improvements through the presence of blade passage heat extraction (surface cooling). The obvious follow-on question is what types of cooling rates can be achieved. Although details of a practical cooling scheme are outside the scope of this research, a first step toward identifying the answer is presented here. Results demonstrate that available heat transfer area sets the limit to performance improvements from compressor cooling. A back-of-the-envelope heat transfer analysis is presented in this section, using Reynolds analogy over a flat plate, assuming cooling on the

pressure and suction side of the blade surface[14]. The available surface area for cooling in a particular blade row, A_b, is approximated as

$$A_b \approx 2Nc\left(r_T - r_H\right), \tag{3.19}$$

where N is the number of blades, c is the blade chord, and r_T and r_H are representative values of the tip and hub radii, respectively. The heat transfer to the fluid per unit blade surface area, i.e., the heat flux, $\overline{q}_w$, is the total heat transfer, $\dot{Q}$, divided by A_b, and is also equal to a dimensionless heat transfer coefficient, the mean Stanton number, $\overline{St}$, times the rate of heat transfer per unit cross-sectional flow area:

$$\overline{q}_w = \frac{\dot{Q}}{A_b} = -\overline{St}\frac{\dot{m}}{\pi\left(r_T^2 - r_H^2\right)}c_p\left(T_{t,in} - T_{wall}\right). \tag{3.20}$$

By definition, the dimensionless cooling, q^*, equals $\dot{Q}/\dot{m}c_pT_{t,in}$. Equations. 3.19 and 3.20 may be combined, and the definition of q^* may be invoked to yield

$$\overline{St} = \frac{q^*T_{t,in}}{T_{wall} - T_{t,in}}\frac{\pi\left(r_T + r_H\right)}{2cN} = \frac{1}{\left(\frac{T_{wall}}{T_{t,in}} - 1\right)}\frac{q^*}{2\sigma}, \tag{3.21}$$

where the solidity, σ, is approximated by the chord divided by the spacing, and the mean spacing, s, approximately equals $\pi\left(r_T + r_H\right)/N$. Finally, a form of Reynolds analogy that assumes Prandtl number near unity [47] is invoked to relate the mean Stanton number to a mean skin friction coefficient, $\overline{C}_f$,

$$\overline{St} \approx \frac{\overline{C}_f}{2}. \tag{3.22}$$

Using this approach, the available non-dimensional cooling per unit solidity as a function of wall temperature ratio is found to be approximately linear:

[14]It should be noted that this analysis has an element of conservatism in that cooling levels would increase if heat transfer was available along casing walls.

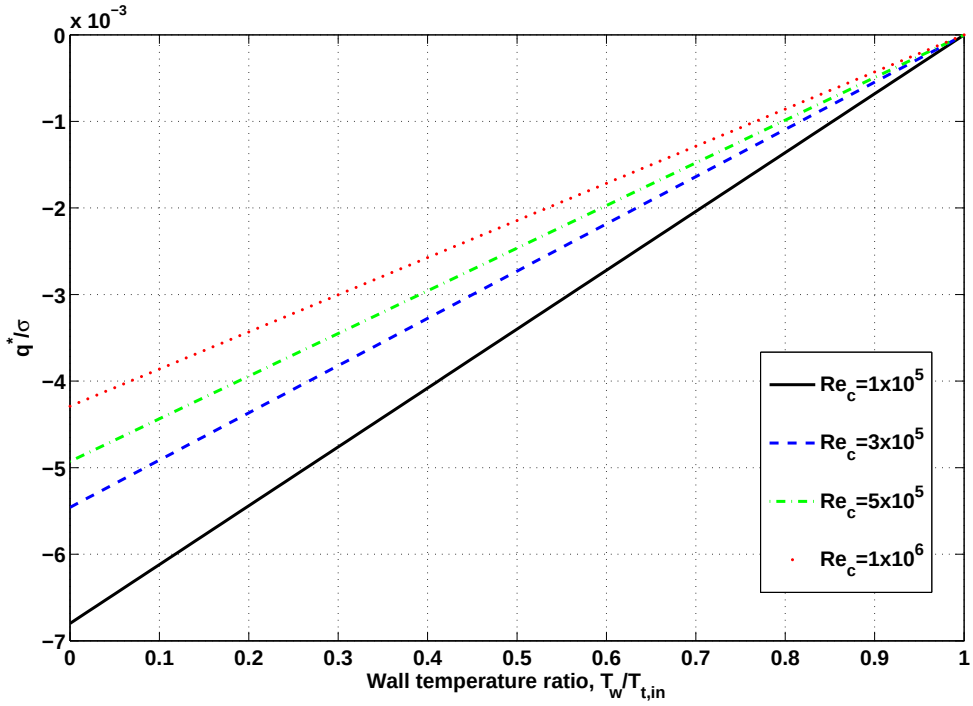

Figure 3-21: Blade surface non-dimensional heat transfer per unit solidity vs. wall temperature at various turbulent Reynolds numbers, generated using Reynolds analogy over a flat plate.

$$\frac{q^*}{\sigma} \approx \overline{C}_f \left(\frac{T_{wall}}{T_{t,in}} - 1 \right). \tag{3.23}$$

The representative mean skin friction coefficient, $\overline{C}_f$, is estimated using expressions for laminar and turbulent flat plate skin friction coefficient [47] at a mid-chord Reynolds number:

$$\overline{C}_{f,lam} = \frac{0.664}{\overline{Re_x^{1/2}}} \approx \frac{0.664}{Re_{c/2}^{1/2}} = \frac{0.933}{Re_c^{1/2}} \tag{3.24}$$

and

$$\overline{C}_{f,turb} = \frac{0.0592}{\overline{Re_x^{1/5}}} \approx \frac{0.0592}{Re_{c/2}^{1/5}} = \frac{0.068}{Re_c^{1/5}}. \tag{3.25}$$

Figure 3-21 presents the estimated heat transfer capability for several turbulent Reynolds numbers between 100,000 and 1,000,000. Solidity, σ, is nominally proportional to the ratio

of blade 'wetted' area to annular cross-sectional area. This analysis suggests that for a representative Reynolds number and a fixed wall temperature ratio, q^* can be increased only by increasing σ. Assuming a Reynolds number of $300,000$ and a solidity of unity implies that a wall temperature ratio of 0.54 is required to achieve $q^* = -0.0025$. Higher values of solidity can either increase the magnitude of the achievable q^*, or raise the required wall temperature ratio.

In a typical multistage compressor, solidities usually increase in the rear stages. In addition, the compression work leads to higher freestream temperatures ($T_{t,in\mathrm{bl}}$), which can increase heat transfer capability with a fixed temperature heat exchanger fluid. The observation that heat transfer capability may be greatest in the rear of the compressor, competes with the earlier finding that a given amount of cooling has the most impact in the front of the compressor. This opens the door to an optimization problem for future work.

3.7 Efficiency Metrics for Non-adiabatic Compressors

The compressor efficiency definition employed in the presentation of results in the thesis is given by Equation 3.15, and is interpreted as *the ratio of adiabatic, reversible work input required to achieve a given exit total pressure to the work input associated with the actual non-adiabatic, irreversible process.* The utility of this "adiabatic" efficiency definition is that it allows the work input into a real, adiabatic compressor to be compared to the corresponding work input into a real, non-adiabatic compressor, when compressing to the same exit total pressure. Stated another way, the actual work inputs of the two types of compressors may be compared to the same reference (ideal) process.

It would also be entirely reasonable to consider the efficiency of the non-adiabatic compressor on its merits alone. To do this requires that the reference, or ideal process against which the comparison is made be a non-adiabatic, reversible process. Such an efficiency definition may be interpreted as *the ratio of non-adiabatic, reversible work input required to achieve a given exit total pressure to the work input associated with the actual non-adiabatic, irreversible process.* The purpose of this section is to derive such a definition.

To begin, a control volume (CV) is defined around the entire compressor in steady operation. Mass may only cross the CV boundary at the inlet and outlet of the device, and the first law of thermodynamics is given by the steady flow energy equation as

$$h_{t,out} - h_{t,in} = q + w_{sh}, \tag{3.26}$$

where,

h_t is the specific stagnation enthalpy.

q is the specific heat transfer.

w_{sh} is the specific shaft work transfer to the working fluid.

Hence, the specific work associated with any process, is

$$w_{sh} = (h_{t,out} - h_{t,in}) - q = c_p \left(T_{t,out} - T_{t,in}\right) - q = c_p T_{t,in} \left(\tau - 1 - q^*\right). \tag{3.27}$$

The second law of thermodynamics on the CV is given by

$$s_{out} - s_{in} = \int \frac{\delta q}{T_{wall}} + s_{gen}, \tag{3.28}$$

where the domain of integration includes all walls across which heat transfers take place. The integral expression is general, such that the wall temperature may vary throughout the domain of integration.

In any reversible process, s_{gen} equals zero. The entropy constitutive relation for a perfect gas given by the leftmost equality in Equation 3.10 allows one to write

$$\begin{aligned} \frac{(s_{out} - s_{in})_{rev}}{c_p} = \int \frac{\delta q}{c_p T_{wall}} &= \left[ln \frac{T_{t,out}}{T_{t,in}} - \frac{\gamma - 1}{\gamma} ln \frac{p_{t,out}}{p_{t,in}} \right]_{rev} \\ &= \left[ln\left(\tau\right) - \frac{\gamma - 1}{\gamma} ln\left(\pi\right) \right]_{rev}. \end{aligned} \tag{3.29}$$

The non-adiabatic, reversible work transfer required to achieve a given pressure ratio, π, is then given by

$$(w_{sh})_{rev} = c_p T_{t,in} \left(\tau_{rev} - 1 - q^*\right) = c_p T_{t,in} \left(\pi^{\frac{\gamma-1}{\gamma}} \left[e^{\int \frac{T_{t,in}}{T_{wall}} \delta q^*}\right] - 1 - q^*\right). \tag{3.30}$$

The "non-adiabatic" efficiency definition is thus

$$\eta_{na} = \frac{(w_{sh})_{na,rev}}{(w_{sh})_{na,actual}} = \frac{\pi^{\frac{\gamma-1}{\gamma}} \left[e^{\int \frac{T_{t,in}}{T_{wall}} \delta q^*}\right] - 1 - q^*}{\tau - 1 - q^*}. \tag{3.31}$$

In Equation 3.31, if the ideal process in the numerator is assumed to be adiabatic ($q^* = 0$), η_{na} reduces to the definition of η given by Equation 3.15. Clearly, then, the efficiencies η and η_{na} only differ by the nature of the reference process. Each definition has its own utility. At the component level, the utility of η lies in the fact that it provides the most conventional (adiabatic, reversible) reference process against which may be compared the work inputs of an adiabatic and non-adiabatic compressor achieving the same pressure ratio. Taking the compressor as a component whose purpose is to provide a given exit pressure, the definition of η also allows comparison between the exit conditions of two compressors given the same inlet conditions, rotor speed, and work input. This provides the basis for the decision to present the results in the main text of the thesis using this efficiency, and the recommendation to employ this definition for component level comparisons.

At the system level the efficiency definition given by η_{na} allows for the bookkeeping of lost work that may be recovered in a lossless process with heat transfer. The discussion on entropy generation mechanisms in Section 3.3.3 shows that for an aggressive cooling wall temperature ($T_{wall}/T_{t,in} = 0.5$), cooling introduces additional thermal dissipation to the blade passage with little change in viscous dissipation. This implies that the amount of lost work would likely increase in the non-adiabatic compressor, and the value of η_{na} may be lower for an aggressively cooled compressor versus its adiabatic counterpart. Theoretically, one could conceive of some type of heat engine between the gas path and an on-board heat sink

to recover this lost work. A proper determination of the feasibility of a cooled compressor powerplant on a specific vehicle mission may require some type of system-level availability analysis.

3.8 Summary of Major Findings

The major findings from this chapter are:

1. For an axial compressor with an adiabatic design point, compressor cooling results in an increase in the overall pressure ratio (at a given corrected flow), an increase in the maximum mass flow capability, and an increase in the efficiency, defined as the ratio of isentropic work for a given pressure ratio to actual shaft work.

2. Compressor cooling provides rear stage choking relief at low corrected speed.

3. If available, a given amount of compressor cooling is better in the front of the compressor than in the rear. This is primarily a thermodynamic effect resulting from the downstream stages compressing the colder air to a higher pressure ratio for a given amount of work. For an adiabatically designed eight-stage compressor with $\pi = 5$, results suggest that heat extraction of 1% of inlet stagnation enthalpy flux in each of the first four blade rows improves pressure ratio and efficiency by 23% and 15%, respectively, at design corrected speed and mass flow. Choking mass flow is also found to improve by 5% at design corrected speed.

4. Heat transfer surface area sets the limit to performance improvements from compressor cooling. The fact that higher gas path temperatures and higher solidities in the rear of the compressor may produce higher heat transfer rates competes with the finding that it is thermodynamically most desirable to have cooling in the front of the compressor, and implies that an optimal cooling scheme represents a best compromise these effects.

Chapter 4

Mission 2: Quiet Civil Aircraft

The major focus of the second-half of this thesis is the conception, design, and assessment of a novel quiet drag device to enable the slow and steep approach profile of a functionally silent aircraft[1]. This chapter presents: 1) an aircraft approach trajectory analysis to quantify the noise benefits of a quiet drag device, and 2) a preliminary drag model of candidate devices, in order to introduce the idea of the swirl tube, a novel concept that is shown to generate high drag with a low noise signature. A mission overview is first presented to describe the goals of a next generation functionally silent civil airliner. Work by previous authors has recognized that clean airframe noise sets a minimum noise floor that can only be further reduced through slower, steeper approach profiles of a clean airframe, requiring additional quiet drag. Analysis of the approach requirements for a candidate aircraft, the Cambridge-MIT Institute (CMI) SAX (Silent Aircraft eXperimental) aircraft conceptual design, demonstrates that the drag required to change an approach glideslope by one degree is comparable to the clean airframe drag, and is close to the drag of a bluff body with cross-sectional area equal to the total fan area of the propulsion system. For conventional drag devices, such as flaps, slats, and landing gear struts, drag and noise are strongly correlated, implying quiet drag is a formidable challenge. Swirling outflow from a duct, such as an aircraft engine, is a hypothesized solution to this challenge, and a control volume analysis

[1]Here, the term functionally silent means quieter than the background noise of a well populated urban area.

suggests that swirl vanes creating an exit flow with maximum swirl parameter of about 1.2, or 50° swirl exit angle meets the requirements. A review of swirling flow dynamics suggests that this will be close to the stability limit for such flows, which motivates the detailed aerodynamic design, and aerodynamic and acoustic assessment in Chapter 5.

4.1 Mission Overview and Previous Work

In the modern global economy, noise from civil aircraft places a major constraint on society's ability to freely move persons and goods. Since the advent of the turbojet engine, noise around airports has resulted in increasing numbers of complaints, resulting in stricter international noise certification requirements for aircraft manufacturers, and greater local operational restrictions, regulations, and non-compliance fines for airline operators. Aircraft manufacturers have relied on technology improvements to meet certification requirements, while manufacturers, operators, and regulators have introduced operational changes to address local noise issues.

Noise at takeoff and approach are potentially annoying events in the vicinity of an airport. Takeoff is a high-power operating condition for the propulsion system, where sound generation is typically dominated by engine sources associated with jet mixing noise and turbomachinery noise, primarily from the high bypass ratio fan. Approach, however, is a low-power operating condition, where engine noise is greatly reduced, especially due to the paradigm shift from turbojets to high bypass ratio turbofan engines. For large civil aircraft, this has created a scenario where engine noise sources are comparable in strength to airframe noise sources. Airframe noise sources include acoustic scattering of turbulent boundary layer eddies past the trailing edge of the clean airframe, plus additional sources such as flaps, slats and landing gear. When several noise sources of comparable level are present, all sources must be reduced in order to achieve meaningful overall noise reduction.

Operational changes offer the potential to keep noise sources farther from the communities around airports that suffer the annoyance. An operational change that has been considered for decades, within the context of the safe operating capabilities of current aircraft is the

continuous descent approach (CDA). CDAs have proven to be successful in airport trials in the U.S. [13] and are under trial in the busy U.K. aircraft corridors around London [72]. CDAs achieve significant reductions in the overall noise exposure to a community by keeping the aircraft higher and at lower thrust, eliminating level flight segments and associated thrust transients [72]. CDAs are thus far focused on conventional approach glideslopes; however, new technologies may offer the promise to steepen conventional glideslope angles without compromising safety margins.

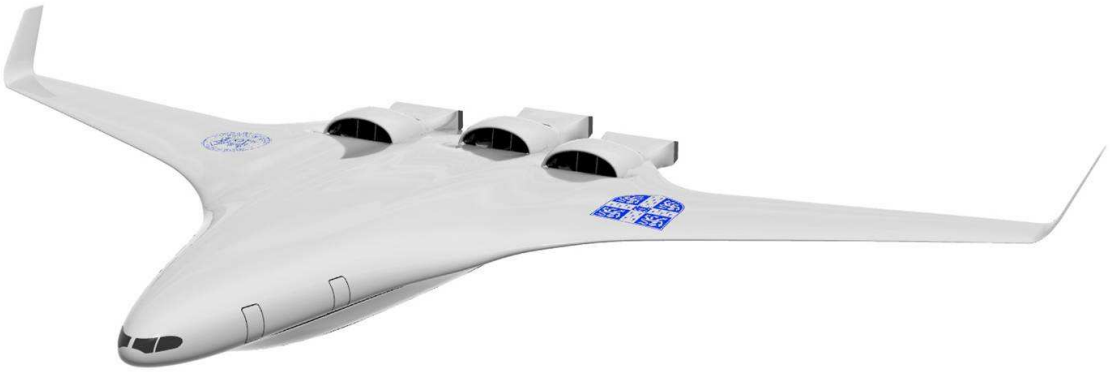

(a) Cambridge-MIT Silent Aircraft conceptual design with embedded engines

(b) Boeing blended wing body (BWB) aircraft with podded engines [36, 37])

(c) Boeing 777 - a conventional tube and wing aircraft [36]

Figure 4-1: Comparison between Cambridge-MIT Silent Aircraft conceptual design with embedded engines, a blended wing body (BWB) aircraft with podded engines, and a conventional tube and wing aircraft.

The modern noise challenge is a system-level problem, requiring simultaneous reductions in the various engine and airframe sources, while also enabling operational changes to further attenuate the propagation of sound before it reaches the ears of the people within the airport's vicinity. An example of a system-level approach to noise reduction is the Cambridge-MIT Institute's (CMI) Silent Aircraft Initiative (SAI). The SAI's conceptual aircraft, the Silent Aircraft eXperimental design (SAX), has been designed as a highly integrated airframe/propulsion system, with engines embedded within the airframe itself. The SAI has set the aggressive noise goal of designing an aircraft that is no louder than the background noise in a typical urban environment outside the airport perimeter. The SAX design incorporates several novel design features in order to achieve a step change in noise source reduction over conventional commercial aircraft [17, 33, 53, 54, 55, 65]. Its aerodynamically clean, all-lifting body configuration and embedded, ultra-high bypass ratio, boundary layer ingesting engines enables conventional approach profiles without the use of noisy auxiliary high-lift devices such as flaps and slats. High-lift configurations are achieved quietly through a deployable drooped leading edge that introduces no additional edge discontinuities into the flow around the airplane. Embedding of engines on the upper side of the aircraft provides a significant noise benefit through shielding [1]. Landing gear noise is also reduced through aerodynamic fairing [68] and late deployment [67]. This results in a step change in noise over blended wing body (BWB) aircraft with podded engines, and an additional step change over conventional tube and wing aircraft such as the Boeing 777. A comparison of these three configurations is shown in Fig.4-1.

In addition to source noise reduction through clean aerodynamics, a key enabler to meeting the aggressive SAI noise goals is airframe design for lower speed and steeper approach profiles. This introduces a requirement for additional quiet drag, to compensate for the loss of drag from the absence of conventional high-lift devices and fairing of landing gear [55]. Conventional high-drag devices such as flaps and slats may have a correlation between drag and noise, as suggested by Figure 4-2 adopted from Smith [81]. The same may be true for landing gear. A key difference of a quiet drag device, then, is a departure from this

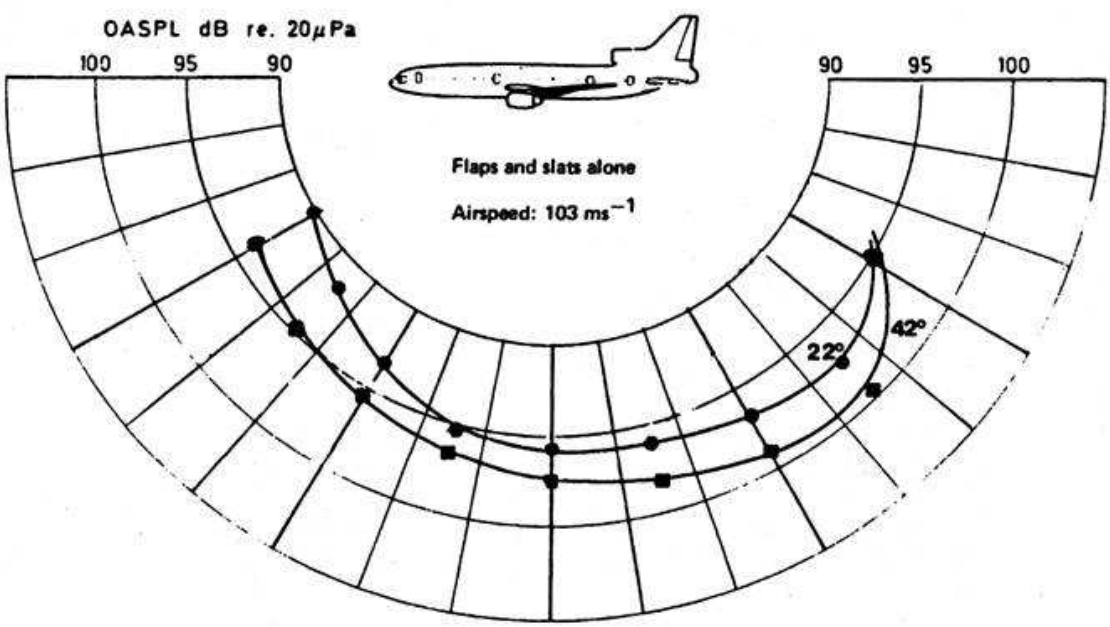

Figure 4-2: Polar directivity plot of Lockheed L-1011 overall sound pressure level (OASPL) for two different flap angle settings, suggesting a strong correlation between noise and drag. Figure adopted from Smith [81].

correlation. A device to meet this challenge is the key focus of this thesis.

For an early design variant of the SAX, the amount of additional quiet drag required for slow, steep approach at 60 m/s at 5° glideslope is found to correspond to a drag coefficient of $C_D = 0.02$ based on aircraft wing wetted area, which is comparable to or greater than the clean airframe drag itself [33]. This implies that a device that relies on skin friction would require extremely large surface area to produce the necessary drag. Instead, this thesis conceives of a compact device having a high drag coefficient (comparable to a bluff body) based on cross-sectional area. In fact, typical engine duct throughflow areas are compatible with this concept.

Pilczer [65] lays the groundwork for the SAX concept by assessing the noise reduction potential of a functionally silent BWB-type aircraft, at both takeoff and approach conditions. Her analysis considers various novel design technologies, and concludes that a BWB with a seamless trailing edge and embedded engines would be dominated by airframe trailing edge

noise on approach, i.e., clean airframe noise. A potential step change in noise reduction of 27 dB relative to a conventional approach profile is found, but the need for quiet drag is recognized. Preliminary drag estimates lead to the recommendation to consider engine air-brakes or silent spoilers as auxiliary drag devices.

Manneville [53] develops the air-brake concept further by modeling a simple one dimensional fan stage operating in turbine mode. He assumes variable pitch turbomachinery is capable of reversing the pitch of the fan blades while a clutch disengages the fan from the gas generator. Furthermore it is assumed that there exists a means of storing or dissipating the turbine work extraction. Manneville focuses on concepts with axial exit flows that generate an axial momentum defect out of the engine exhaust. His analyses on fan rotors at design suggest that a maximum drag coefficient of about 0.45 is theoretically possible and occurs at an exit velocity of 0.5 times the freestream[2]. This theoretical maximum is also consistent with models for windmilling engines in the literature [21].

Manneville [53] also lays out the basic equations of quiet drag requirements. His comparison between a conventional (A300) and a typical BWB shows that a BWB in clean configuration can land 15 m/s slower than a conventional aircraft in clean configuration due to higher wing area and higher $C_{L,max}$. Quiet drag allows the approach glideslope to become steeper for a fixed approach velocity. Today, for safety, this is at least 1.23 times stall speed [22], though more aggressive approaches are considered in Manneville's analysis. In general, Manneville [53] identifies a blended wing body aircraft as an ideal candidate for quiet approach drag devices because the all-lifting body meets lift requirements on approach without the use of high-lift devices, unlike conventional aircraft.

Clean airframe noise is sometimes referred to as the ultimate noise barrier [81]. Lilley [51] presents the challenges associated with airframe noise reduction. He shows that on modern aircraft, airframe noise begins to compete with engine noise during approach, due to the significant achievements made in engine noise reduction from high bypass ratio engine cycles.

[2]A physical explanation for the maximum limit is derived in Section 4.4.1. It is shown that pressure forces on the fan-in-turbine-mode actuator disk compete with lip suction forces from spillage around the nacelle to generate the theoretical peak drag for a device with axial outflow.

The clean airframe noise limit is thus identified as the lower limit to further airframe noise reduction.

Though quiet drag is not identified as a concept by Lockard and Lilley [52], mention is made of the "possibility of speed brakes to enable aircraft to fly a preferred flight schedule." Their noise reduction scaling law, given by Equation 4.1, shows that clean airframe noise reduction is governed by the aircraft flight velocity and distance to the observer,

$$\text{Noise Reduction (dB)} = 10 \log_{10} \left(\frac{V}{V_{ref}} \right)^5 \left(\frac{r_{ref}}{r} \right)^2 . \tag{4.1}$$

Clean airframe sound power scales with the fifth power of velocity, due to the scattering of acoustic energy from turbulent boundary layer eddies passing the airframe trailing edge [35], and scales as the square of the distance due to spherical spreading of the acoustic wavefronts. The requirement for slow and steep approach operation drives the SAX aircraft conceptual design away from conventional tube and wing aircraft with podded engines.

In summary, a key operational aspect of next generation, low-noise civil aircraft may be the clean airframe approach trajectory, where flaps are stowed, slats are replaced by a seamless, drooped leading edge, and the landing gear is faired and deployed later to reduce noise. In addition to the acoustic benefits of the clean-airframe, operational changes such as slower and steeper glideslope angles up to 6° (versus 3° for current aircraft) may be employed to reduce source noise strength and increase attenuation during sound propagation.

In the next section quiet drag requirements and noise reduction potential is quantified for a SAX-type aircraft, and more generally for other conventional aircraft, to motivate the development of a novel quiet drag device called the swirl tube which is the focus of this thesis.

4.2 Quiet Approach Trajectory

This section quantifies the influence of a quiet drag device on overall noise reduction along the approach trajectory of the conceptually designed SAX aircraft. A force balance analysis

demonstrates that there are two operational aspects to low approach noise, namely, slow and steep flight. As the acoustic power radiated from a given set of airframe sources generally scales with velocity raised to a power between 5 and 6, slower flight inherently reduces source noise, provided the aerodynamic changes to achieve the slower configuration do not require devices that introduce new noise sources (e.g., flaps, air-brakes, exposed landing gear) that are louder than the baseline airframe sources. In addition, a key safety requirement to slower flight is to maintain adequate margin relative to stall speed. The approach speed requirement is mandated by the FAA to be at least 1.23 times the aircraft's stall speed [22], and thus sets a lower limit to the noise reduction benefit from slow flight alone.

Holding the minimum approach speed fixed, the analysis of this section demonstrates that steepening the glideslope from the conventional 3° to 6° reduces noise by about 6 dB, but requires additional quiet drag approximately equal to the component of weight in the direction of the conventional glideslope trajectory. This drag requirement is suggested to be comparable to or greater than the clean airframe drag itself for a SAX-type aircraft. When the required drag coefficient to change glideslope by a given factor at fixed approach speed is normalized to propulsion system fan area, a requirement similarity emerges across several aircraft. A bluff body drag coefficient (C_D about 1) based on the propulsion system fan area is found to enable a one degree glideslope change from 3° to 4° at fixed approach speed, resulting in a 2.5 dB potential overall noise reduction if the drag generator is quiet.

A force balance diagram of an aircraft on a steady approach glideslope of θ is pictured in Figure 4-3. For simplicity, it is assumed that idle thrust is fixed[3] on approach by the requirement that in a go-around maneuver the engines must return to full power within a fixed minimum time. The natural coordinate system for the force balance is formed by the direction along the aircraft trajectory and the direction normal to it. Steady flight along the trajectory requires balancing of thrust, drag, and the component of weight along the flight path direction,

[3]The approach thrust is a weak function of aircraft speed. It is neglected to simplify the analysis in this section by assuming that the ram pressure rise at approach speeds is small in comparison the pressure rise across the turbofan propulsor.

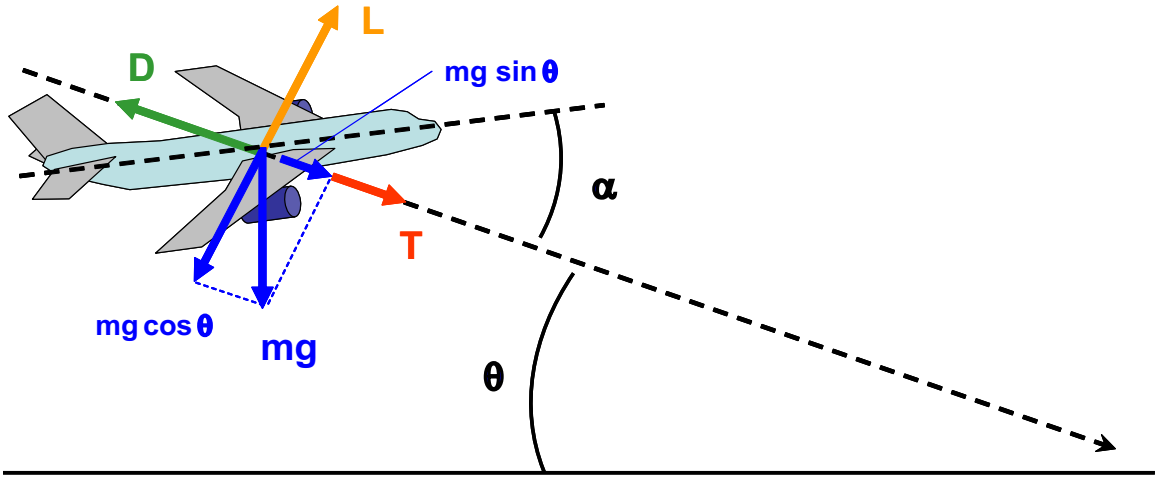

Figure 4-3: Aircraft force balance on approach.

$$T + mg\sin\theta = D, \tag{4.2}$$

where D is the total drag force of the clean airframe plus any additional quiet drag. The force balance in the direction normal to the trajectory equates the lift and the normal weight component:

$$L = mg\cos\theta. \tag{4.3}$$

The maximum lift coefficient, L, occurs at angle of attack, α, near stall, and hence constrains the minimum safe flight speed (inclusive of a safety margin) and the lift on approach. Traditionally the minimum approach speed has been 1.3 times the stall speed, though this factor has recently been relaxed to 1.23 [22]. The clean airframe drag coefficient is the sum of zero-lift drag coefficient and induced drag coefficient (drag due to lift), created by the downwash velocity induced by tip vortices on a lifting aircraft:

$$C_{D,\text{airframe}} = C_{D,0} + k\left[C_L\left(\alpha\right)\right]^{\eta}. \tag{4.4}$$

The exponent η in Equation 4.4 is typically approximated as 2 [2], because the induced drag

is the product of the lift vector and the small induced angle of attack, both of which are proportional to the lift coefficient. A more precise relationship is dependent upon knowledge of the aircraft drag polar. The total drag coefficient is the sum of the clean airframe drag and any additive quiet drag:

$$C_D = C_{D,0} + k\left[C_L\left(\alpha\right)\right]^{\eta} + C_{D,\text{quiet}}. \tag{4.5}$$

As the airframe drag is a function of the lift, Equation 4.3 may be non-dimensionalized by the dynamic pressure, $\rho V_\infty^2/2$, times the wing reference area, A_w, and substituted into Equation 4.4. The equation that must be solved to determine the glideslope-velocity relationship as a function of quiet drag is then given by the non-dimensionalization of the force balance in Equation 4.2:

$$\left(\frac{T}{\frac{1}{2}\rho_\infty V_\infty^2 A_w}\right) + \left(\frac{mg}{\frac{1}{2}\rho_\infty V_\infty^2 A_w}\right)\sin\theta = C_{D,0} + k\left[\left(\frac{mg}{\frac{1}{2}\rho_\infty V_\infty^2 A_w}\right)\cos\theta\right]^{\eta} + C_{D,\text{quiet}}. \tag{4.6}$$

A reference trajectory may next be defined using θ_{ref} and $V_{\infty,\text{ref}}$, for a clean airframe approach profile with zero quiet drag:

$$\left(\frac{T}{\frac{1}{2}\rho_\infty V_{\infty,\text{ref}}^2 A_w}\right) + \left(\frac{mg}{\frac{1}{2}\rho_\infty V_{\infty,\text{ref}}^2 A_w}\right)\sin\theta_{\text{ref}} = C_{D,0} + k\left[\left(\frac{mg}{\frac{1}{2}\rho_\infty V_{\infty,\text{ref}}^2 A_w}\right)\cos\theta_{\text{ref}}\right]^{\eta}. \tag{4.7}$$

Both V_∞ and $V_{\infty,\text{ref}}$ are constrained to be larger than the stall speed multiplied by the safety factor of 1.23, as mentioned earlier. Defining the first and second quantities in parentheses in Equation 4.7 as reference thrust and weight coefficients, $C_{T,\text{ref}}$ and $C_{W,\text{ref}}$, yields equations 4.8 and 4.9 in non-dimensional terms:

$$\frac{C_{T,\text{ref}}}{\left(\frac{V_\infty}{V_{\infty,\text{ref}}}\right)^2} + \left[\frac{C_{W,\text{ref}}}{\left(\frac{V_\infty}{V_{\infty,\text{ref}}}\right)^2}\right]\theta \approx C_{D,0} + k\left[\frac{C_{W,\text{ref}}}{\left(\frac{V_\infty}{V_{\infty,\text{ref}}}\right)^2}\right]^{\eta} + C_{D,\text{quiet}} \tag{4.8}$$

and

$$C_{T,\mathrm{ref}} + C_{W,\mathrm{ref}} \cdot \theta_{\mathrm{ref}} \approx C_{D,0} + k\left(C_{W,\mathrm{ref}}\right)^{\eta}. \tag{4.9}$$

Setting η equal to 2, and assuming θ and θ_{ref} are small, such that $(\sin\theta/\sin\theta_{\mathrm{ref}}) \approx \theta/\theta_{\mathrm{ref}}$ and $(\cos\theta/\cos\theta_{\mathrm{ref}}) \approx 1$, equations 4.8 and 4.9 may be combined to eliminate the zero-lift drag coefficient, $C_{D,0}$:

$$\frac{\theta}{\theta_{\mathrm{ref}}} \approx \frac{kC_{W,\mathrm{ref}}}{\theta_{\mathrm{ref}}} \frac{1}{\left(\frac{V_\infty}{V_{\infty,\mathrm{ref}}}\right)^2} + \left(1 + \frac{C_{D,\mathrm{quiet}} + C_{T,\mathrm{ref}}}{C_{W,\mathrm{ref}} \cdot \theta_{\mathrm{ref}}} - \frac{kC_{W,\mathrm{ref}}}{\theta_{\mathrm{ref}}}\right)\left(\frac{V_\infty}{V_{\infty,\mathrm{ref}}}\right)^2 - \frac{C_{T,\mathrm{ref}}}{C_{W,\mathrm{ref}} \cdot \theta_{\mathrm{ref}}}. \tag{4.10}$$

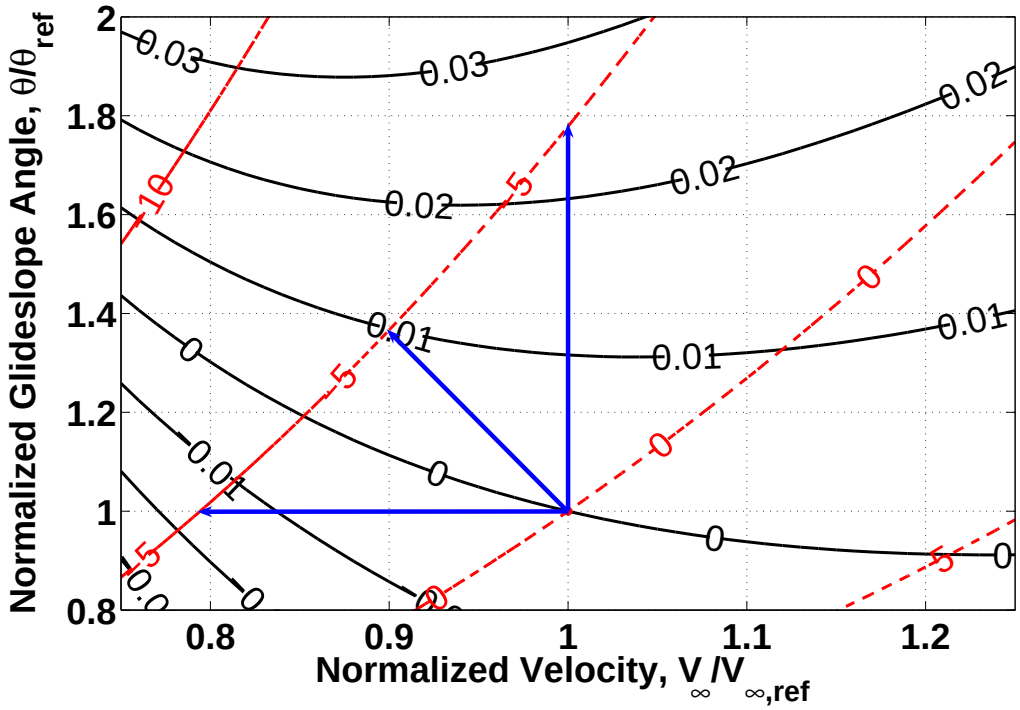

Figure 4-4: Iso-contours of quiet drag coefficient, $C_{D,\mathrm{quiet}}$ (black) and estimated noise reduction (red) as a function of velocity ratio and approach angle for $C_{D,0} = 0.01$, $\theta_{\mathrm{ref}} = 3°$, and $V_{ref} = 1.23 \cdot V_{stall} = 60.8$ m/s, per Equation 4.10. SAX landing weight is 125,000 kg, wing area is 836 m^2, and k for the drag polar is 0.064. Blue arrows indicate three different means to achieve 5 dB noise reduction.

Equation 4.10 indicates that for a fixed amount of quiet drag the aircraft approach glideslope depends both on the square of the approach speed and the inverse of the square of the approach speed. For the SAX conceptual aircraft, typical values of zero-lift drag coefficient ($C_D = 0.01$), landing weight (125,000 kg), wing area (836 m^2), and drag polar coefficient ($k = 0.064$) yield the solid iso-contours of quiet drag as a function of $V_\infty/V_{\infty,\text{ref}}$ and $\theta/\theta_{\text{ref}}$ presented in Figure 4-4. Similar plots resulting from an analysis that includes the detailed aerodynamic and propulsion characteristics of an early variant of the SAX conceptual aircraft are presented in Hileman et al. [33].

The estimated noise reduction by Lockard and Lilley [52] given in Equation 4.1 is also plotted in red in Figure 4-4. With the small angle assumption the noise reduction relationship becomes approximately:

$$\text{Noise Reduction (dB)} \approx 10 \log_{10} \left(\frac{V_\infty}{V_{\infty,\text{ref}}} \right)^5 \left(\frac{\theta_{\text{ref}}}{\theta} \right)^2 . \tag{4.11}$$

The three blue arrows in Figure 4-4 represent different strategies to achieve 5 dB overall noise reduction. The horizontal arrow pointing left shows such a reduction is possible by large reductions in safe approach speed, i.e., by flying at $\sim 80\%$ of the reference flight speed and actually decreasing the drag (increasing the thrust). This significant approach speed reduction requires either: 1) a large permissible stall margin reduction, or 2) a significant stall speed reduction, which may or may not be aerodynamically feasible without noisy devices such as flaps and slats. The diagonal arrow suggests another, more direct means to 5 dB noise reduction is to reduce approach velocity to 90% of the reference flight speed, and introduce quiet drag equivalent to an airframe drag coefficient of $C_D = 0.01$. Finally, the vertical arrow pointing upwards shows that a quiet drag increase of $C_D = 0.025$ at fixed approach velocity, and hence, the same stall margin, also leads to a potential 5 dB noise reduction. Hence, reduction of noise by several decibels can be achieved by different combinations of quiet drag, $C_{D,\text{quiet}}$, and/or airframe changes that achieve quiet high-lift to reduce the allowable approach speed.

To assess the effect of steeper approaches alone, the approach velocity is set equal to

the reference velocity in Equation 4.10, yielding a simple expression between quiet drag and approach angle (and hence noise reduction), as given by Equation 4.12. This equation shows that doubling the glideslope angle requires a quiet drag coefficient equal to the product of the reference weight coefficient and the reference glideslope angle (in radians). Physically, this says that quiet drag equal to the component of the weight in the reference trajectory direction is needed to double the glideslope from the reference value (for small angles), and yields overall noise reduction of about 6 dB,

$$\left(\frac{\theta}{\theta_{\text{ref}}}\right)_{\left(\frac{V_\infty}{V_{\infty,\text{ref}}}\right)=1} \approx 1 + \frac{C_{D,\text{quiet}}}{C_{W,\text{ref}} \cdot \theta_{\text{ref}}}. \tag{4.12}$$

Table 4.1 compares the quiet drag requirements for three different aircraft to undergo a 3° to 6° glideslope change. The two rightmost columns show the required quiet drag coefficient in terms of wing area and propulsion system fan face area. The Boeing 737-700, 777-200, and SAX have bypass ratios of about 5, 9, and > 15. Despite their differences, the table suggests that the drag requirement when referenced to the total propulsion system fan area is remarkably similar. A drag coefficient of roughly 3 based on fan area is required to change the glideslope from 3° to 6°. Bluff body drag coefficient is about 1 based on cross-sectional area, so the maximum glideslope change one would expect this type of device to passively achieve is about one degree, or steepening to 4°. This represents 2.5 dB overall noise reduction for fixed approach speed, i.e., steep flight alone, for both current and next generation aircraft. Further noise reduction may be achieved through a combination of slow and steep flight, but may require novel airframe design features such as those considered by the SAI [17, 33, 53, 54, 55, 65].

4.3 Swirl Tube: The Idea

The approach trajectory analysis of the previous section suggests that a quiet device with drag coefficient of about 1.0 based on propulsion system total fan area can provide sufficient drag to change the glideslope from 3° to 4° at fixed approach speed, resulting in the potential

Aircraft	Approach Speed (m/s)	Landing Mass (kg)	Wing Area (m^2)	Fan Area (m^2)	$C_{W,\text{ref}} \cdot \theta_{\text{ref}}$	Fan $C_{D,\text{quiet}}$
$737-700$	66.4	$58,000$	125	3.77	0.09	3.04
$777-200$	71.1	$213,000$	428	15.33	0.09	2.40
SAX	60.8	$125,000$	836	10.18	0.03	2.90

Table 4.1: Silent drag similarity across several aircraft types. The two right most columns show drag coefficient required to change conventional 3° glideslope to 6°, in terms of wing area and propulsion system fan area. Fan area includes fan spinner. All numbers are approximate.

for 2.5 dB overall noise reduction without the additional requirement to fly slower. By incorporating airframe aerodynamic changes to safely fly at a slower speed (e.g., quiet high-lift), a similarly sized quiet drag device can assist in potential overall noise reductions of 5 or more dB. A new quiet drag idea is thus proposed from this drag requirement: an on-board throughflow device with an exhaust duct, such as an aircraft engine, that turns an axial inflow into a steady swirling outflow. The simplest implementation of this is a ram pressure driven duct with embedded swirl vanes, a so-called swirl tube. The key conceptual hypotheses that summarize the expected performance of the swirl tube are:

1. The swirl tube can generate drag coefficients similar to bluff bodies (C_D about 1) with a flow that is steady on the device scale.

2. Stable swirling flow gives the swirl tube a low noise signature at full scale, enabling a slower, steeper approach for a next generation functionally silent aircraft.

3. Locally separated flow, vortex shedding instabilities, and, especially, vortex breakdown (vortex burst) are the key flow features to avoid in the successful design of a quiet swirl tube. A burst vortex near the duct exit is hypothesized to be noisier than a stable flow.

A potential additional acoustic benefit of the swirl tube is that internally generated noise sources may be shielded from the ground or attenuated with acoustic liners in practical applications.

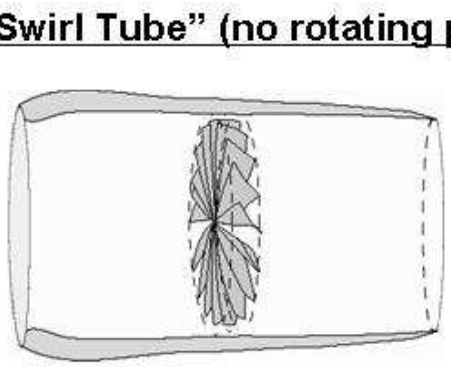

(a) Ram pressure driven, or throttled concept

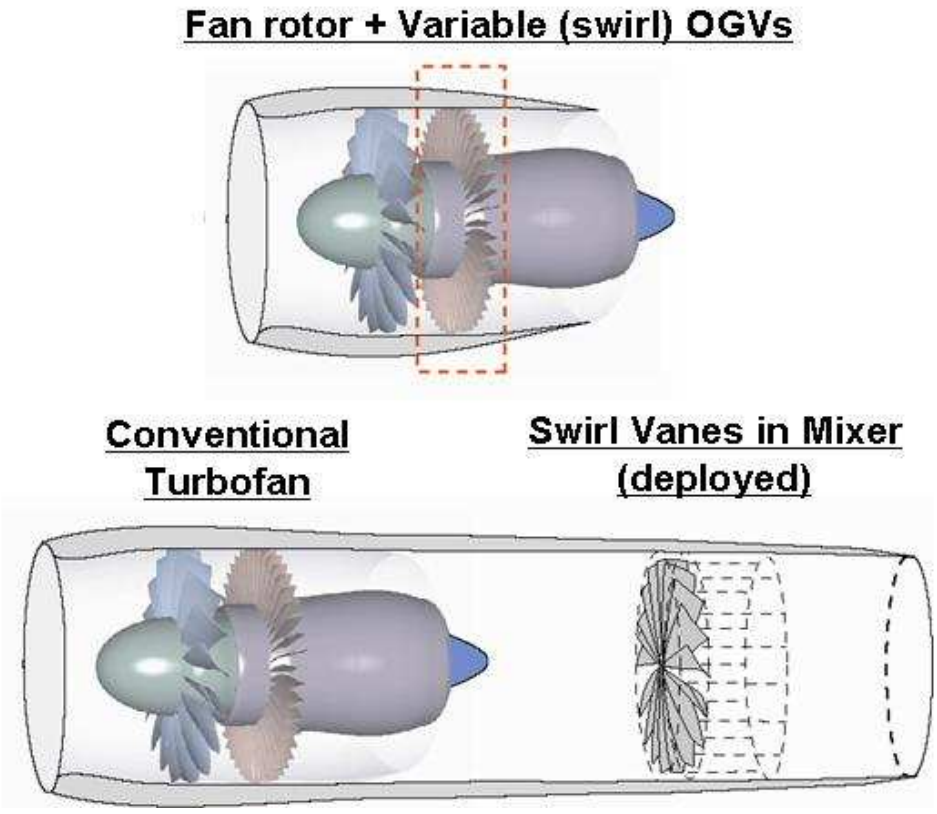

(b) Fan driven, or pumped concepts

Figure 4-5: Drag-generating swirling flow concepts.

Figure 4-5 presents two types of swirl device concepts. The upper concept, (a), is a ram pressure-driven, or throttled device without moving parts. It represents the simplest configuration to demonstrate the concept of drag from swirling flows, and is the focus of detailed analysis, design and experimentation in this thesis. The lower two concepts, (b),

require actuation of outlet guide vanes (OGVs), or deployment of stowable swirl vanes into the mixing or bypass duct of a propulsion system on approach. In this thesis, the ram pressure-driven concept will be referred to as a swirl tube, while the fan driven concept will be referred to as a pumped swirl tube.

Two types of swirl tube configurations may be envisioned. An airframe-integrated, ram air-driven configuration may include throughflow ducts with inlet and exhaust doors that remain closed in conventional operation and are actuated open on approach. In terms of implementation, this type of configuration may require dedicated additional duct area on the aircraft. A propulsion system-integrated, or pumped swirl tube configurations consist of variable OGVs or deployable vanes in the bypass or mixing duct that actuate to the desired swirl angle to generate a prescribed amount of drag. These configurations have the benefit of integrating into the existing propulsion system but have the challenge of interacting with a pumping (fan) stage located upstream. Integration challenges include fan stage operability due to the resistance applied by the vanes, and mitigation of blade row interaction noise.

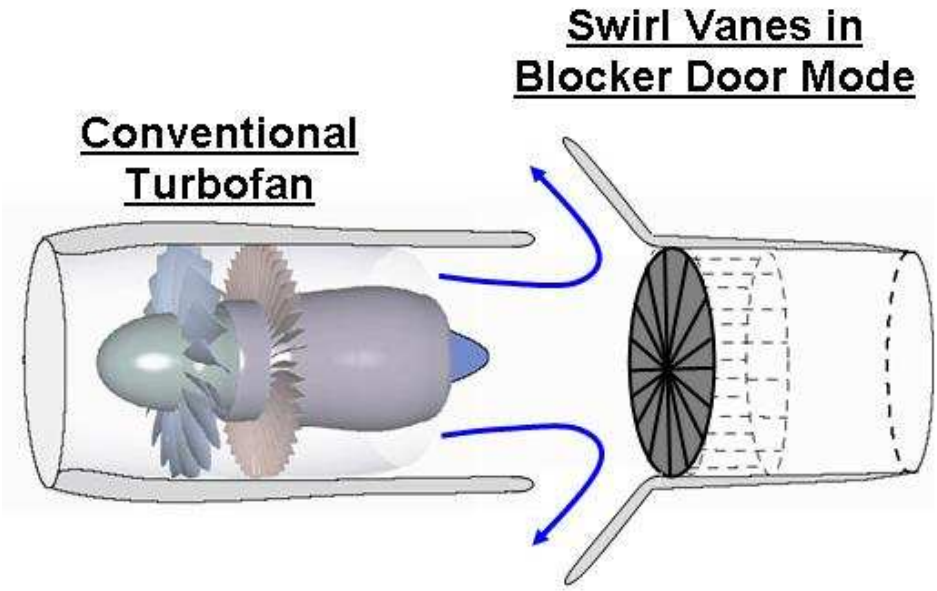

Figure 4-6: Propulsion system integrated swirl tube concept with deployable swirl vanes, having functionality to actuate to a closed position to serve as a thrust reverser blocker door.

The deployable vanes may also have the additional benefit of actuating to a fully closed position, in order to serve as blocker doors within a thrust reverser system, as depicted in Figure 4-6. This would potentially save weight when compared to stand-alone quiet drag and thrust reverse systems.

4.3.1 Research Questions

The ultimate objective of this research is to demonstrate that a ram pressure driven swirl tube is capable of producing high drag (C_D about 1.0) with quiet noise signature at device scales of practical interest for a typical aircraft on approach. Section 4.4 presents preliminary drag estimates that motivate the swirl tube design and validation presented in Chapter 5. The technical approach employs detailed design techniques and high fidelity computational fluid dynamics (CFD) simulations to ensure that the aerodynamics meets the design intent. Wind tunnel aerodynamic and acoustic tests are performed to quantify the drag and noise. This approach is chosen to answer the following key research questions:

1. What is the relationship between swirling outflow, drag, and noise for a ram pressure driven swirl tube? Does a high-drag, low-noise design exist, and if so, what are its key design features? Is a full-scale device quiet, and hence viable to implement in an aircraft application?

2. What are the stability limits associated with the swirl tube exhaust flowfields?

3. What noise source mechanisms characterize the swirl tube noise signature? How does far-field noise scale with freestream velocity?

4. What is the effect of a fan driven, or pumped, swirl tube on drag and noise?

4.3.2 Challenges and Unknowns

Major challenges center around the development of a fundamental understanding of the aerodynamics and acoustics of the proposed device, in order to identify design features

that achieve quiet drag. Secondary challenges focus on achieving a first understanding of propulsion system integration effects in order to develop practical design recommendations for a next-generation aircraft.

The unknowns associated with swirl tube aerodynamics include the drag capability as a function of swirl, and the effect of swirling flow instability, i.e., vortex breakdown, on the device performance. Preliminary models that describe the device exit flow features are required to aid in understanding the drag generation mechanism. Vortex breakdown effects must be assessed through computations and experimental drag measurements.

The unknows associated with the acoustics of a ram pressure driven swirl tube include the noise signature of a stable swirling outflow and the vortex breakdown noise. To the author's knowledge, suitable empirical and theoretical models of such noise sources are not in the literature, suggesting that the understanding may only be gained through experiments. If different noise mechanisms are present they must be identified by their spatial location and their power scaling laws as a function of velocity.

The major propulsion system integration unknown is the effect of swirl vanes downstream of a fan stage on drag, noise, and fan operability. Computational simulations are required to provide a first-order estimation of these effects and to develop practical recommendations for future work.

These challenges and unknowns are addressed systematically in the remainder of the thesis. The next section presents the preliminary drag estimations that motivate the swirl tube design and validation in Chapter 5.

4.4 Preliminary Model of Ducted Drag Generator

The objective of this section is to develop an analytical drag prediction model of candidate quiet drag device concepts. The model assumes steady, incompressible flow, but instability mechanisms associated with purely axial and swirling flows are also identified to delineate the threshold of the model's validity. An axisymmetric control volume analysis is first presented to study the drag generation capability of a throughflow device. The duct geometry is defined

by an exit to actuator disk area ratio, A_d/A_f , of unity. Flow profiles are parametrically defined for purely axial and swirling flows, by modeling the presence of an actuator disk across which there is a discontinuity in total pressure and swirl velocity. Results suggest that:

1. The maximum theoretical drag coefficient from a purely axial exhaust flow throttling device is 0.5, because excessive captured streamtube contraction leads to lip suction forces on the nacelle that counter the pressure force on the actuator disk.

2. Within the space of stable, steady solutions, maximum swirl tube drag coefficients of $C_D \gtrsim 0.8$ may be generated, a nearly two-fold increase versus the best axial flow device. A large pressure defect in the exit flowfield is found to be the dominant drag mechanism.

3. Near the maximum steady flow drag, typical swirl tube exit flow features may include: i) axial velocity excess of about 2 times freestream velocity on the centerline, ii) axial velocity defect of about 0.6 times freestream velocity at the outer radius, and iii) maximum centerline pressure defect of about 3.5 times the freestream dynamic pressure.

4. Vortex breakdown is likely to set the limitation to maximum swirl tube drag capability, near a swirl parameter of about 1.2, or 50° maximum exit flow angle, as suggested by the theory of waves on vortex cores.

5. Loss of total pressure within the duct and across the actuator disk serves to throttle the swirl tube mass flow. Loss increases drag at low levels of swirl, but has a weak effect for high-swirl, high-drag devices, suggesting that greater emphasis should be placed on proper flow turning rather than loss prediction in the swirl tube design process.

6. Swirl also throttles the device mass flow, with maximum stable swirl levels generating a ten to twenty percent reduction in device mass flow relative to a purely axial exit flow.

Swirling flow generated by turbomachinery downstream of a fan stage is also modeled. It is found for a pumped swirl tube that:

1. Relative to the ram pressure driven swirl tube, greater mass flow ingestion from pumping results in higher vane loadings and greater effective drag, or thrust reduction, for similar exit flow swirl angles.

2. Greater pumped swirl tube exit velocities suggest higher noise levels (relative to ram pressure driven devices) that may scale to an appropriate velocity ratio power law.

3. The throttling effect of swirl relative to axial exit flow suggests that a wide fan operating range or a variable area nozzle would be beneficial to swirl tube propulsion system integration.

4.4.1 Control Volume Analysis of Ducted Drag Generator

The initial design requirement for a ducted drag generator is that the exit flow be 'steady' at the scale of the device, because it is hypothesized that device-scale unsteadiness results in excess noise that is detrimental to quiet approach goals. The drag capability assessment begins with a steady control volume (CV) analysis. The CV analysis establishes a theoretical framework for throughflow device drag estimation by treating the internal duct components as actuator disks [34].

Figure 4-7 shows a sketch of a fixed control volume around an aircraft engine-like duct, or nacelle, that contains an actuator disk. A pylon force keeps the device in static equilibrium relative to the freestream flow. The duct is assumed to have smoothly faired inlet lines in order to avoid flow separation. Stations u and d represent the far upstream station and the discharge, or exit plane, respectively. Stations 1 and 2 are located just upstream and downstream of the actuator disk, respectively. The actuator disk generates total pressure and circulation discontinuities. The total pressure change can theoretically be generated from 1) a work input or extraction device, such as a fan or turbine, 2) a loss generator, such as a screen, or 3) skin friction from swirl vanes.

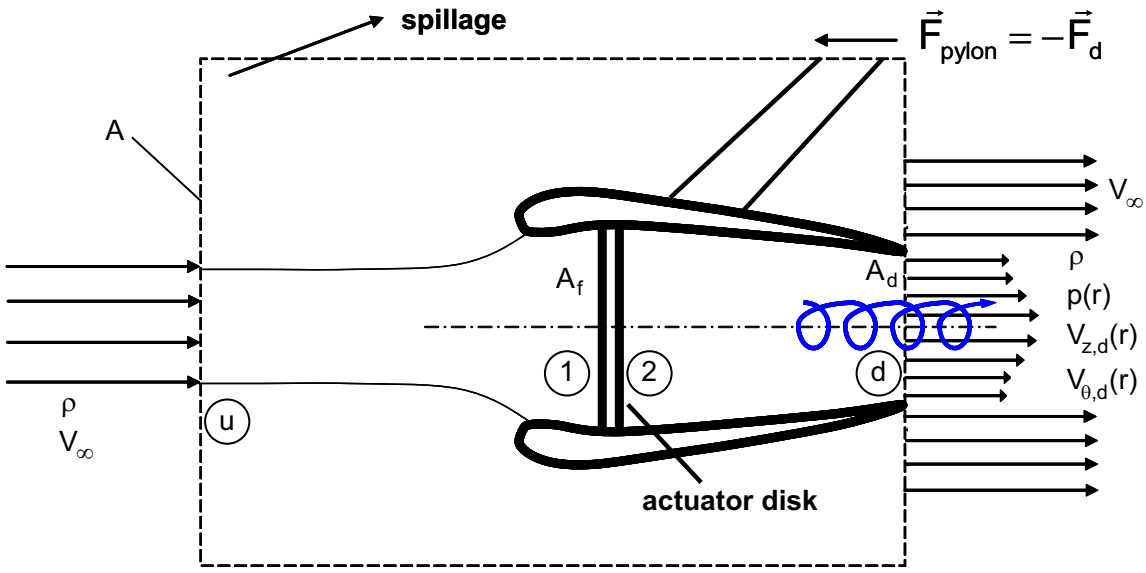

Figure 4-7: Control volume of cross sectional area, A, around ducted quiet drag device containing an actuator disk. Pylon holds device in static equilibrium relative to freestream flow. Stations u and d are far upstream of device and at the duct exit, respectively. Stations 1 and 2 are just upstream and downstream of actuator disk, respectively. A_f and A_d are actuator disk face area and duct exit area, respectively.

The following assumptions are employed in the analysis:

1. There is low Mach number flow throughout ($\rho = \rho_\infty \approx$ constant).

2. The exit flow satisfies simple radial equilibrium[4] ($V_{r,d} = 0$), with atmospheric pressure at the edge of the duct. At the exit, the axial velocity, circumferential velocity, and pressure are functions of radius only ($V_{z,d} = V_{z,d}(r)$, $V_{\theta,d} = V_{\theta,d}(r)$, and $p_d = p_d(r)$) .

3. There is uniform axial flow at stations u and 1.

4. Freestream flow that is diverted (spilled) around the duct remains attached. Near the duct trailing edge, the external flow returns to freestream velocity and direction.

5. The upper and lower CV boundaries are sufficiently far away from the device to have streamlines nearly parallel with the freestream flow. This allows for some flow having

[4]see Equation 4.29

small but finite radial velocity component to spill or entrain both mass and axial momentum across the outer CV boundary.

Under the assumption of steady flow, conservation of mass requires zero net mass flux through the fixed CV,

$$\iint_S \rho \left(V \cdot \vec{n}\right) dS = 0 = -\rho V_\infty A + \rho V_\infty \left(A - A_d\right) + \iint_{A_d} \rho V_{z,d}\left(r\right) dA + \dot{m}_{out}, \tag{4.13}$$

where $\dot{m}_{out}$ equals the mass flow (which carries axial momentum per unit mass equal to freestream velocity V_∞) exiting the outer control volume boundary. A positive value of $\dot{m}_{out}$ implies spillage, while a negative value implies entrainment. Solving for $\dot{m}_{out}$ gives:

$$\dot{m}_{out} = \rho V_\infty A_d - \iint_{A_d} \rho V_{z,d}\left(r\right) dA = \rho V_\infty \iint_{A_d} \left(1 - \frac{V_{z,d}\left(r\right)}{V_\infty}\right) dA. \tag{4.14}$$

Axial momentum conservation requires the next flux of axial momentum through the fixed CV to be balanced by the net surface and body forces acting on the CV,

$$\iint_S \rho V_z \left(V \cdot \vec{n}\right) dS = -\rho V_\infty^2 A + \rho V_\infty^2 \left(A - A_d\right) + \iint_{A_d} \rho V_{z,d}^2\left(r\right) dA + \dot{m}_{out} V_\infty = \sum \vec{F}_{cv}. \tag{4.15}$$

External surface forces acting on the CV include pressure forces and the pylon force required to maintain force equilibrium. The drag force is vectorially equal and opposite to the pylon force, as shown in Fig 4-7. Recognizing that the pressure is everywhere atmospheric except at the nozzle discharge plane, the net force term may be written as an integration of the pressure defect in this region minus the drag force

$$\sum \vec{F}_{cv} = \iint_{A_d} \left[p_\infty - p_d\left(r\right)\right] dA - F_{drag}, \tag{4.16}$$

Substitution into the momentum balance thus yields

$$-\rho V_\infty^2 A_d + \iint_{A_d} \rho V_{z,d}^2(r) dA + \dot{m}_{out} V_\infty = \iint_{A_d} \left[p_\infty - p_d(r)\right] dA - F_{drag}. \tag{4.17}$$

Substitution of Equation 4.14 into Equation 4.17, with rearrangement, yields the final expression for the drag force,

$$F_{drag} = \iint_{A_d} \left(\rho V_\infty^2 \left[\frac{V_{z,d}(r)}{V_\infty} \left(1 - \frac{V_{z,d}(r)}{V_\infty} \right) \right] + \left[p_\infty - p_d(r)\right] \right) dA. \tag{4.18}$$

The drag coefficient, normalized by the actuator disk area, A_f, may be written as the sum of an axial momentum flux drag term and a pressure drag term,

$$C_D = \frac{F_{drag}}{\frac{1}{2}\rho_\infty V_\infty^2 A_f} = \frac{1}{A_f} \int_{A_d} \left[\underbrace{2\frac{V_{z,d}(r)}{V_\infty}\left(1 - \frac{V_{z,d}(r)}{V_\infty}\right)}_{\text{axial momentum flux defect}} - \underbrace{C_p(r)}_{\text{pressure defect}} \right] dA. \tag{4.19}$$

The pressure coefficient, C_p, is defined as

$$C_p = \frac{p_d(r) - p_\infty}{q_\infty}, \tag{4.20}$$

and the dynamic pressure, q_∞, is defined as

$$q_\infty = \frac{1}{2}\rho V_\infty^2. \tag{4.21}$$

Equation 4.19 is the main result of this subsection, which demonstrates that drag is generated both by defects in axial momentum and pressure in the exit plane of the device.

4.4.2 Drag Generating Axial Exhaust Flow Devices

For devices with purely axial exhaust flow (i.e., no swirl), the pressure drag term is zero, meaning the exit flowfield has straight and parallel streamlines and the exit static pressure

equals freestream static pressure everywhere in the exit flowfield. The exit velocity ratio, $V_{z,d}/V_\infty$, may be related to the total pressure change by invoking the Bernoulli equation upstream and downstream of the actuator disk, across which the total pressure changes:

$$\omega\left(r^*\right) = -\frac{\Delta p_t}{q_\infty} = \frac{p_{t,\infty} - p_{t,d}}{\frac{1}{2}\rho V_\infty^2} = \frac{\frac{1}{2}\rho V_\infty^2 - \frac{1}{2}\rho V_{z,d}^2}{\frac{1}{2}\rho V_\infty^2} = 1 - \left[\frac{V_{z,d}\left(r^*\right)}{V_\infty}\right]^2. \tag{4.22}$$

The sign convention for ω is taken to be consistent with the definition of a typical turbomachinery blade passage loss coefficient, such that a loss of total pressure means ω is positive. Equation 4.19 simplifies to

$$\begin{aligned} C_{D,axial} = \frac{F_{drag}}{\frac{1}{2}\rho_\infty V_\infty^2 A_f} &= \frac{1}{A_f}\int_{A_d}\left[2\frac{V_{z,d}\left(r\right)}{V_\infty}\left(1 - \frac{V_{z,d}\left(r\right)}{V_\infty}\right)\right] dA \\ &= \frac{1}{A_f}\int_{A_d} 2\left[\sqrt{1-\omega\left(r\right)} - \left(1-\omega\left(r\right)\right)\right] dA. \end{aligned} \tag{4.23}$$

Inspection of the integrand of Equation 4.23 reveals that its maximum value occurs for $V_{z,d}/V_\infty = 0.5$, or for $\omega = 0.75$. Thus this constant exit velocity ratio or loss coefficient results in the maximum drag coefficient, as shown for different exit area to actuator disk area ratios, A_d/A_f, in Figure 4-8. Increasing area ratio simply increases the drag linearly, by increasing throughflow. The effect of increasing exit area is theoretically the same with or without swirling flow. In the remainder of this thesis, it is assumed that $A_d/A_f = 1$ for simplicity. It may be assumed that opening the exit area is an option for increasing drag, e.g., with a variable area nozzle, though the flow may be limited by diffuser stall if the area ratio A_d/A_f becomes too large.

For $A_d/A_f = 1$, the maximum theoretical drag coefficient is 0.5. Further exit velocity reduction or greater loss coefficient beyond this theoretical maximum value reduces drag. As reduction in exit velocity is associated with reduced capture streamtube area, it suggests that spillage of additional mass flow around the duct may generate nacelle suction forces

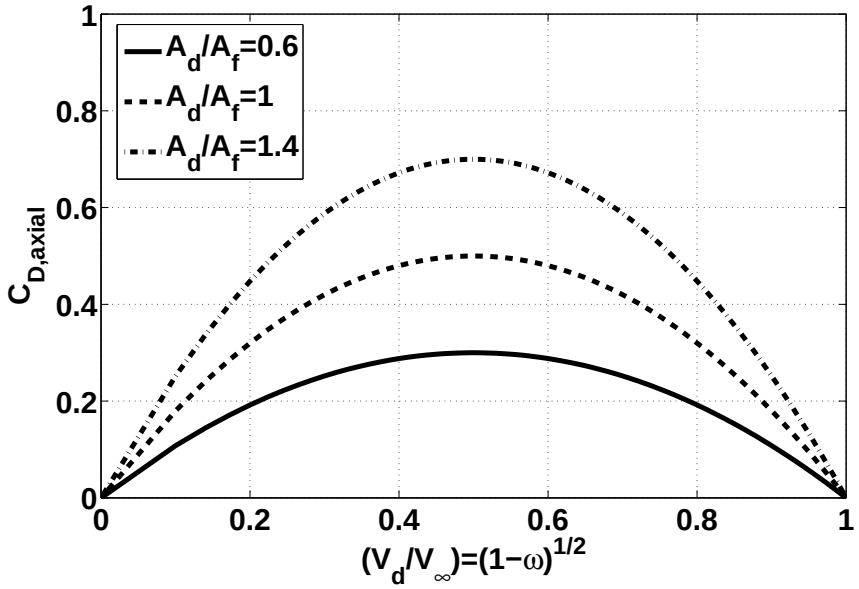

(a) Drag coefficient vs. velocity ratio.

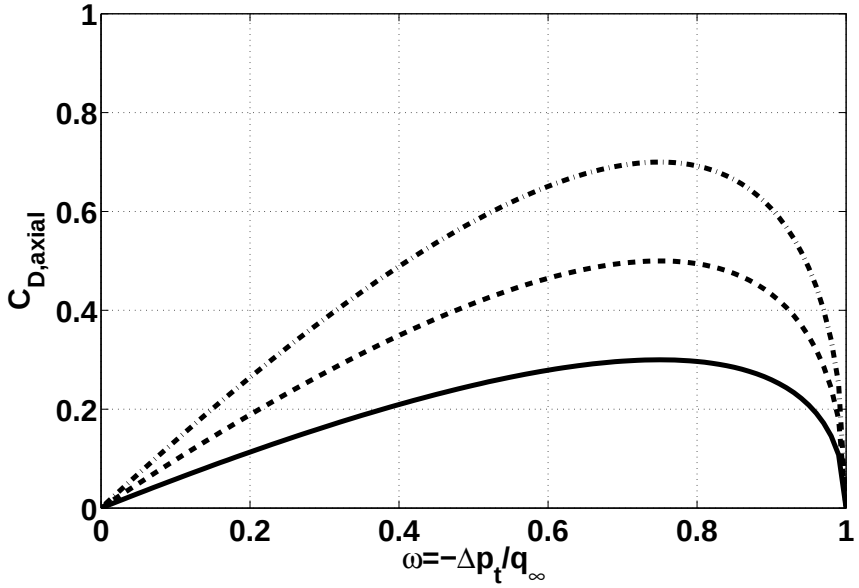

(b) Drag coefficient vs. total pressure reduction coefficient.

Figure 4-8: Drag coefficient as a function of throttling parameters $V_{z,d}/V_\infty$ and ω for purely axial exhaust flow for different area ratios. Peak drag coefficient equals 0.5 times area ratio, implying an exit area increase leads to higher maximum drag.

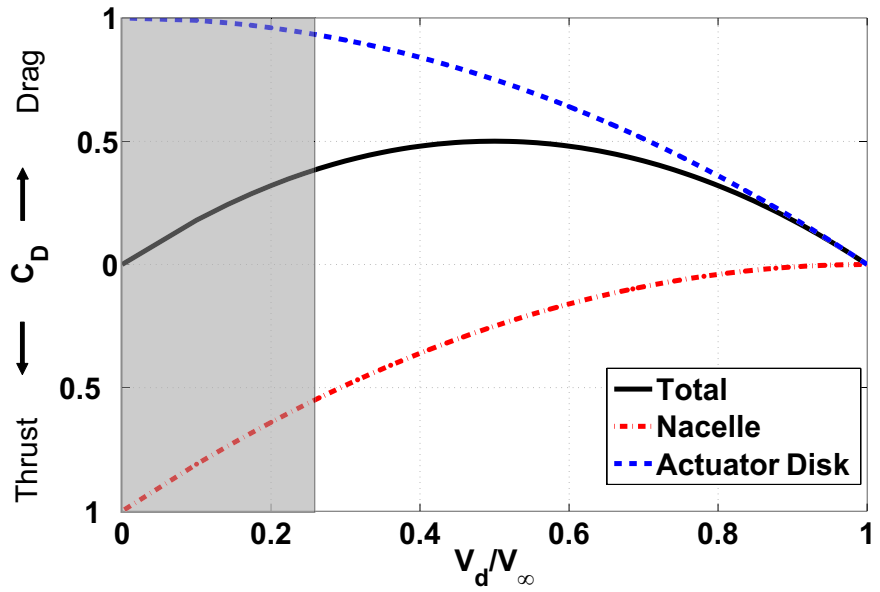

(a) Drag coefficient breakdown vs. velocity ratio.

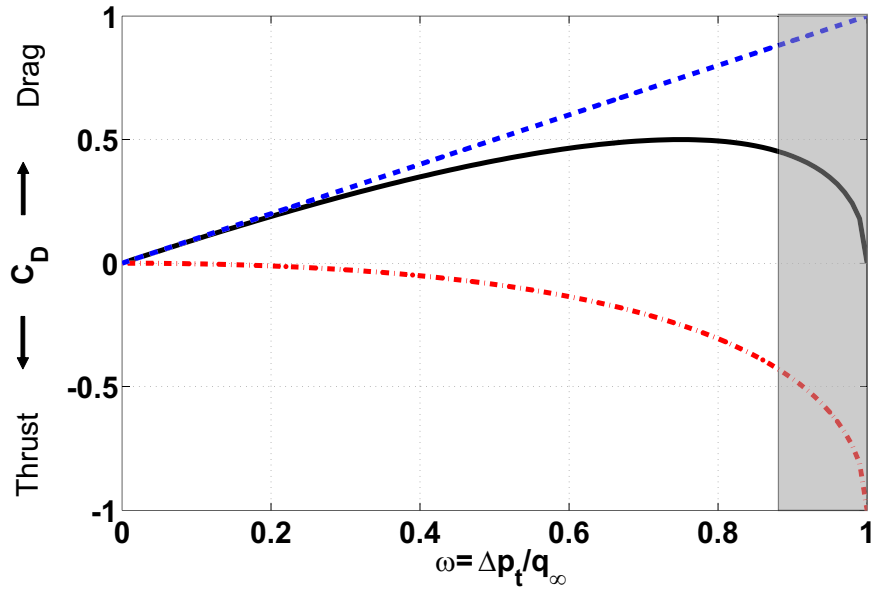

(b) Drag coefficient breakdown vs. total pressure reduction coefficient.

Figure 4-9: Drag coefficient breakdown for purely axial exhaust flow devices indicates that total drag is comprised of a drag force on the actuator disk and a thrust force on the nacelle. Shaded area indicates likely region of vortex shedding instability, as suggested by Figure 4-10.

that counteract the drag forces on the actuator disk, as discussed in chapter 2 of Greitzer et al. [27]. This nacelle suction force may be identified by subtracting out the actuator disk

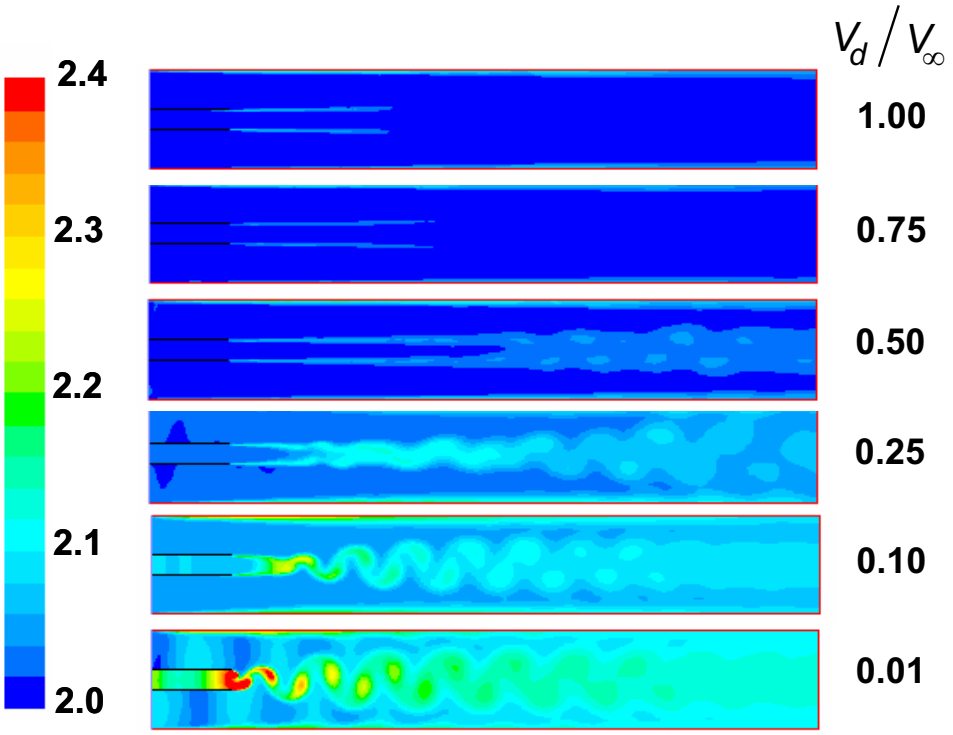

Figure 4-10: Instantaneous unsteady contours of dimensionless entropy, $T_{t,\infty}s/V_\infty^2$, on 2D CFD of deficit flow with varying velocity ratio at device scale Reynolds number. Nozzle height is 2.16 meters. Computations indicate that vortex shedding instability develops at velocity ratios $\lesssim 0.25$.

drag coefficient, $C_{D,a.d.}$, from the total drag, $C_{D,axial}$,

$$C_{D,nacelle} = C_{D,axial} - C_{D,a.d.} = C_{D,axial} - \omega. \tag{4.24}$$

For the case of $A_d/A_f = 1$, the three decomposed drag coefficients $C_{D,nacelle}$, $C_{D,a.d}$, and $C_{D,axial}$ are presented in Figure 4-9. The figure demonstrates that the nacelle force is always negative[5], i.e., in the direction of thrust, with magnitude increasing rapidly with increased loss coefficient or reduced exit velocity ratio.

In the limit of unity loss coefficient or zero velocity ratio, the model predicts zero total drag, i.e., an equal balance between the actuator disk drag force and the nacelle thrust

[5]The reader is reminded of assumption 4 in Section 4.4.1, which states that the spilled flow remains attached at the inlet. Violation of this requirement changes the validity of the model, due to flow separation and unsteadiness that is assumed deleterious to the low noise goals of the device.

force. This result is not physical, however, because zero velocity ratio corresponds to zero throughflow, suggesting the onset of device-scale unsteady bluff body effects. This suggests that the model is not valid below a critical velocity ratio, i.e. above a certain loss coefficient. Unsteady computational fluid dynamics (CFD) solutions of a two dimensional, planar nozzle flow with various velocity ratios presented in Figure 4-10 suggests that the critical velocity ratio is about 0.25. The result is qualitatively and quantitatively similar to flow studies on bluff body flows with and without supercritical base bleed [4, 78, 79, 96]. Contours of entropy generation demonstrate that below this value bluff body effects generate large-scale unsteady vortex shedding. This is a stability limit that constrains the validity of the model (shown by the shaded area in Figure 4-9), and is assumed undesirable from a noise generation point of view. The exit velocity ratio is also a mass flow capture fraction, which suggests that excessively low throughflows should be avoided for acoustical reasons.

4.4.3 Swirling Flow Dynamics

The model for a purely axial flow device suggests that the theoretical maximum drag coefficient is limited to a value of 0.5 for $A_d/A_f = 1$. Attention is now turned to swirling flows, which are shown to theoretically outperform axial exhaust flows within the assumed stable flow limits. This section provides a brief overview of swirling flow dynamics, while the next section extends the drag model to swirling flows with a prescribed exit circulation distribution.

Swirling flows have features that are significantly different from flows without swirl. All real swirling flows are vortical structures[6], that originate in the boundary layers of the surfaces over which the working fluid moves. These surfaces shed vortex lines in a manner consistent with the features of the flow. Behind a bluff body at high Reynolds number, vortex lines originate as closed rings that lose their orientation relatively rapidly due to random stretching from a highly turbulent wake. On a delta wing at high angle of attack,

[6]The mathematical concept of an irrotational swirling flow is called a free vortex, for which circumferential velocity is inversely proportional to radius. This flow exhibits a numerical singularity on the centerline which is physically never realized due to the effect of viscosity.

flow separation occurs near the wing apex, resulting in the rolling up of two highly coherent streamwise vortices that persist for many characteristic lengths downstream. In the case of the swirl tube, the vortex lines are generated in the boundary layers of swirl vanes and the nacelle end walls. Aft of the vanes these lines become aligned by the bulk fluid motion so as to develop a strong streamwise component of vorticity at the duct exit.

Swirling flows have a more complex description than non-swirling flows because the equations of motion are non-linear and coupled in such a way to make simple analytical models mathematically challenging. A key feature of highly swirling flows is strong radial pressure gradients. In addition, axial and circumferential velocity components are usually highly coupled, as energy conservation in the absence of lost work constrains the balance of kinetic energy components ($u_z^2/2, u_\theta^2/2$) and flow work (p/ρ). The strong coupling means that vortex cores become increasingly sensitive to far-field variations in pressure with increasing swirl. Because of this sensitivity, excessive swirl leads to the vortex breakdown phenomenon, a feature that is manifested as an abrupt change in flow properties. At high Reynolds number this includes unsteadiness, turbulence, and rapid diffusion of primary vorticity. New insight into the underlying physics of vortex breakdown is not a primary goal of this thesis. Instead, vortex breakdown is taken here to be a known phenomenon, studied extensively in experiment, theory, and computation, that is important because it will set a limitation on swirl tube performance. The effect of this limitation is a major unknown to be quantified in Chapter 5.

Many of the dominant effects of swirling flow are inertial in nature [27]. Hence, the equations of inviscid, incompressible, axisymmetric flow are the starting point to examine some of the critical aspects of swirling flow dynamics. Axisymmetry suggests that the natural coordinate system be cylindrical, and defined by the radial, circumferential, and axial components, (r, θ, d). By neglecting the viscous terms, the flow is described as pressure driven. The continuity equation, and the axial, circumferential, and radial momentum equations are respectively given as:

$$\frac{1}{r}\frac{\partial}{\partial r}\left(ru_r\right) + \frac{\partial}{\partial z}\left(u_z\right) = 0 \tag{4.25}$$

$$\frac{\partial u_z}{\partial t} + u_r\frac{\partial u_z}{\partial r} + u_z\frac{\partial u_z}{\partial z} = -\frac{1}{\rho}\frac{\partial p}{\partial z} \tag{4.26}$$

$$\frac{\partial}{\partial t}\left(ru_\theta\right) + u_r\frac{\partial}{\partial r}\left(ru_\theta\right) + u_z\frac{\partial}{\partial z}\left(ru_\theta\right) = 0 \tag{4.27}$$

$$\frac{\partial u_r}{\partial t} + u_r\frac{\partial u_r}{\partial r} + u_z\frac{\partial u_r}{\partial z} = -\frac{1}{\rho}\frac{\partial p}{\partial r} + \frac{\left(ru_\theta\right)^2}{r^3} \tag{4.28}$$

The circumferential momentum balance, Equation 4.27, states that the quantity (ru_θ) is constant following a fluid particle[7]. Changes in radius thus lead to changes in circumferential velocity in a pressure driven flow. This concept is important in understanding the dynamics of the flow with respect to effective area changes within a swirling streamtube.

The radial momentum balance, Equation 4.28, has two terms on the right hand side, a radial pressure gradient that acts as a real force on a fluid particle, and an apparent force term that comes from the centripetal acceleration of the fluid particle. This apparent centrifugal force can be viewed as a radial gravitational field of strength $1/r^3$ acting on an apparent density of strength $\left(ru_\theta\right)^2$, where the density analogy is based on the observation that (ru_θ) following a fluid particle is constant [27]. In the absence of radial velocity the flow is said to be cylindrical, or in simple radial equilibrium, satisfying:

$$\frac{\partial p}{\partial r} = \frac{\rho u_\theta^2}{r}. \tag{4.29}$$

The sign of the right hand side of Equation 4.29 is always positive, meaning that pressure gradients are always radially outward in a swirling flow. For most natural and man made unconfined swirling flows, the atmosphere or free stream acts as a mechanical sink that sets

[7]This is another statement of Kelvin's theorem for an incompressible, inviscid flow with conservative body forces, which states $D\Gamma/Dt = 0$, where $\Gamma = \oint_C \vec{u}\cdot d\ell$ is defined as the circulation around a closed contour C. For convenience C may be taken as a circle of radius r about the centerline.

a pressure boundary condition on the outer regions of the flow. Hence, swirling flows have sub-atmospheric pressures. The pressure drag generated by the swirl tube is later shown to be the dominant drag mechanism for the device.

Vortex Breakdown

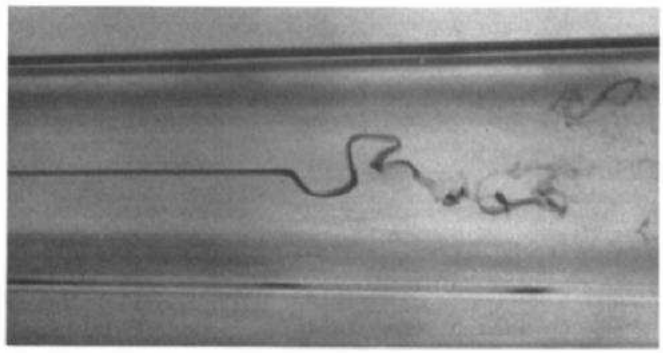

(a) Spiral type.

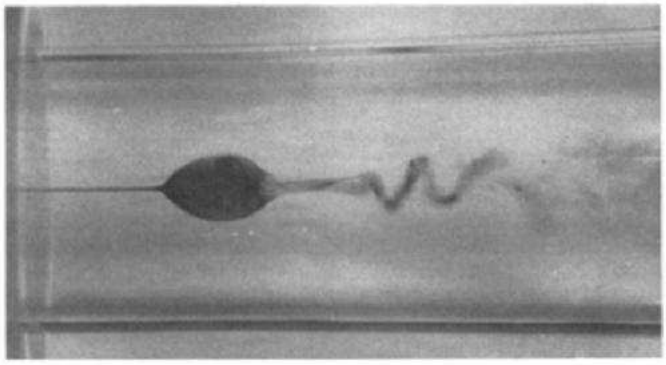

(b) Bubble type.

Figure 4-11: Types of vortex breakdown, adopted from Leibovich [48].

Vortex breakdown, or vortex burst, is a phenomenon that occurs in swirling flows that exceed a critical swirl threshold. It is characterized by a transition from a small, tightly-bound vortex with high velocities to a larger, more-diffuse vortex with lower velocities. For laminar flows three major types of vortex breakdown have been classified in the literature: 1)

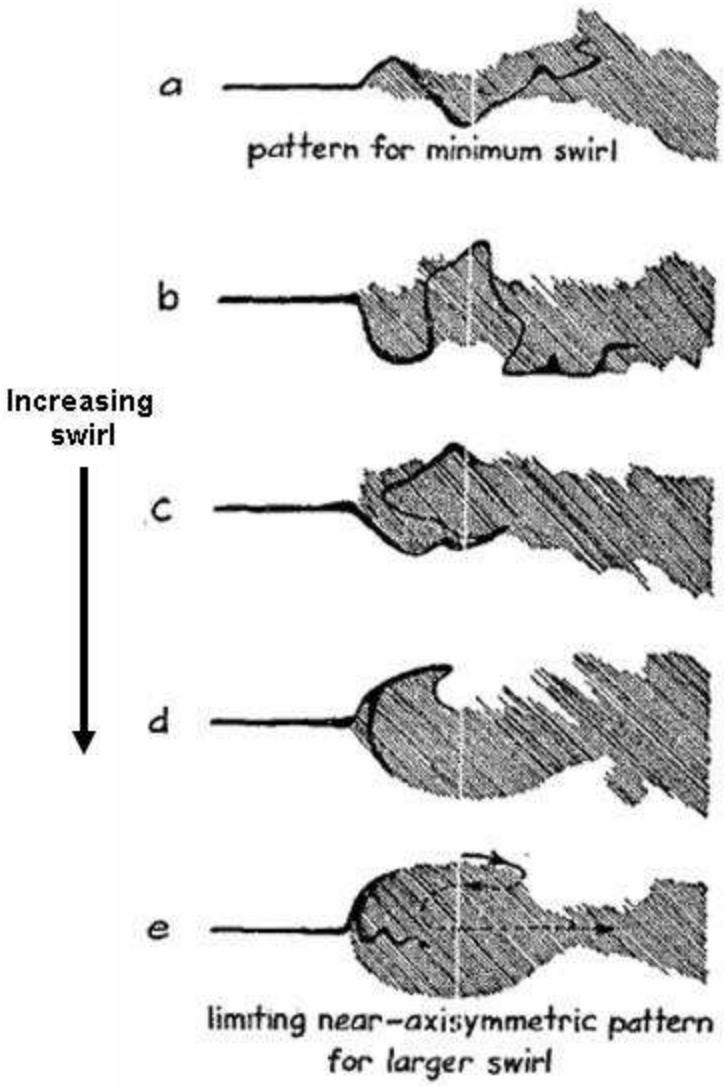

Figure 4-12: Types of vortex breakdown from low to high swirl, adopted from Hall [28] based on the photographs of Sarpkaya [74].

double helix, 2) spiral, and 3) axisymmetric, or bubble-type, though other minor variations have also been noted [64]. Double helix-type breakdown occurs at the lowest swirl velocities, spiral-type at higher swirl velocities, and bubble-type at the highest velocities. Figure 4-11 is adopted from Leibovich [48], and shows flow visualizations of spiral- and bubble-type vortex breakdown. These visualizations are generated in a vortex tube, i.e. a weakly diffusing

tube that creates an adverse pressure gradient in the streamwise direction. It is the adverse pressure gradient that triggers the sensitivity in the vortex core mentioned earlier that leads to the breakdown.

Figure 4-12, adopted from Hall [28], and based on the photographs of Sarpkaya [74] suggests that the spiral breakdown evolves into the bubble breakdown with increasing swirl. As the swirl tube is a high Reynolds number device, the bubble-type breakdown is expected to characterize the flow field when critical swirl is exceeded. The bubble-type vortex breakdown is seen at the highest swirl levels, and increasing swirl moves the breakdown further upstream [16]. For the swirl tube, a separation bubble near the duct exit may create an effective blockage that reduces the throughflow and hence reduces the vane loadings and the drag. It is also observed that the separation bubble is not closed at its rear, and is usually characterized by increased unsteadiness and turbulence. As the size of the bubble is expected to be at the size of the device for excessive swirl, this is viewed as potentially detrimental to swirl tube acoustics.

Numerous physical explanations of the vortex breakdown phenomenon exist in the literature. Vortex breakdown theory has been grouped into four major classes by Delery [16]: 1) quasi-cylindrical approach and analogy to boundary layer separation, 2) solution of axisymmetric Navier-Stokes equations, 3) concept of critical state, or wave theory, and 4) hydrodynamic instabilities. As it is not a primary aim of this thesis to shed new light on the fundamental nature of vortex breakdown, the reader is directed to important works and reviews given by Delery [16], Hall [28], Leibovich [48] and Sarpkaya [74] for further details on the phenomenon. A brief discussion of the concept of critical state is provided here to elucidate the conceptual explanation that is adopted in this thesis.

The concept of critical state As reviewed by Hall [28], this concept is first proposed by Squire [83] and is later modified by Benjamin [6] and others. Squire proposes that the conditions for the possible existence of standing waves is a sufficient criterion for breakdown because downstream disturbances can propagate upstream. Benjamin then suggests that Squire's critical state has an important but not exclusive role in explaining breakdown. His

own work explains breakdown as a "transition between two steady states of axisymmetric swirling flow, being much the same in principal as the hydraulic jump in open channel flow." The transition is said to occur between supercritical and subcritical states, where the former cannot support standing waves and the latter can. At a high level, their analyses [28] involve combining the governing equations into a single partial differential equation in terms of the circumferential component of a streamfunction, ψ_θ, the so-called Bragg-Hawthorne Equation [5] for incompressible flow,

$$\frac{\partial^2 \psi_\theta}{\partial r^2} - \frac{1}{r}\frac{\partial \psi_\theta}{\partial r} + \frac{\partial^2 \psi_\theta}{\partial z^2} = \frac{r^2}{\rho}\frac{dp_t}{d\psi_\theta} - K\frac{dK}{d\psi_\theta}, \tag{4.30}$$

where $u_r = -(1/r)\,\partial\psi_\theta/\partial z$, $u_z = (1/r)\,\partial\psi_\theta/\partial r$, $K = ru_\theta$, and p_t is the stagnation pressure. Stationary axisymmetric perturbations are then superimposed over a quasi-cylindrical flow, $\Psi(r,z)$, such that

$$\psi_\theta(r,z) = \Psi(r,z) + \epsilon F(r,z)e^{\gamma z}. \tag{4.31}$$

Eigensolutions of the equation are then examined to determine if at least one standing wave is supported. If at least one eigenvalue, γ^2, is negative, the criterion is met and the flow is said to be subcritical, allowing disturbances to propagate upstream and trigger vortex breakdown. Otherwise the flow is supercritical, indicating disturbances decay, and vortex breakdown does not occur.

A quasi one-dimensional model of waves on vortex cores presented by Darmofal et al. [15] for unconfined geometries suggests that the comparison of a convective speed and a wave speed may provide a stability criterion that is consistent with the onset of vortex breakdown. By assuming a Rankine vortex model of the swirling flow, a wave speed, c, is found to be proportional to the level of circulation in the vortex core:

$$c^2 = \frac{\Gamma_\infty^2}{8\pi A} = \frac{u_{\theta,max}^2}{2}. \tag{4.32}$$

Increasing swirl leads to increasing wave speed. This speed is compared to the assumed

uniform convective speed in the streamwise direction, u_z. A criticality condition,

$$\frac{c}{u_z} = \frac{u_{\theta,max}/\sqrt{2}}{u_z} > 1, \tag{4.33}$$

is derived when the wave speed exceeds the uniform convective speed, such that disturbances may propagate upstream. This leads to a critical swirl parameter, S_c, at the core radius:

$$S_c = \frac{u_{\theta,max}}{u_z} > \sqrt{2} \approx 1.41. \tag{4.34}$$

The result provided by the quasi-one-dimensional model is a useful estimate when compared to Benjamin's value of 1.2. Again, a strong analogy exists between the concept of waves on vortex cores and a compressible shock wave or a hydraulic jump. Stable flow is said to be supercritical, because perturbations are convected downstream with the flow, whereas a subcritical, high entropy solution develops beyond the critical swirl level.

Of greatest importance for the design of the swirl tube is the criterion for vortex breakdown. Delery's summary [16] on this indicates that the existence of breakdown is not always well posed, and the definition of a breakdown criterion can sometimes be ambiguous. However, the most important feature is the axial and swirl velocity distribution. The salient feature of axisymmetric swirling flows near the breakdown threshold is a swirl parameter, S_D, of 1.2, defined by Delery as

$$S_D = \frac{\Gamma_0}{V_\infty r_c}, \tag{4.35}$$

where r_c is the vortex core radius and Γ_0 is the circulation around a circle of radius r_c. This swirl parameter is the inverse of a Rossby number. The critical value of S_D of 1.2 is found to be fairly consistent across the theoretical approaches that predict the vortex breakdown criterion. The corresponding maximum flow angle is generally near 50°.

In this thesis the swirl parameter, S, will be treated as the metric to judge the onset of vortex breakdown:

$$S = \frac{u_\theta}{u_z}. \tag{4.36}$$

S is simply the tangent of the swirl angle. This definition of swirl parameter allows it to be plotted as a flowfield variable, and will be presented as such in the next chapter. It is worth noting that the value of S that corresponds to 50° swirl angle is also 1.2, suggesting S_c, S_D and S are approximately consistent parameters. In the next subsection it is assumed that the swirling flow stability limit occurs near a value of $S = 1.2$ at the Burger vortex core, or critical radius. In Chapter 5 high-fidelity computations and experimental verification will demonstrate that this assumption is quantitatively valid.

4.4.4 Drag Generating Swirling Exhaust Flow Devices

In this subsection the drag from a swirling exit flow is quantified by extending the control volume analysis to such flows. A swirl parameter near $S = 1.2$ is assumed to indicate the onset of vortex breakdown, setting the validity limit of the model. The radial coordinate, r, is first non-dimensionalized to r^* by the circular duct outer radius, r_d, i.e.,

$$r^* = \frac{r}{r_d}. \tag{4.37}$$

It is assumed that a total pressure change may occur at the actuator disk. For the case of a ram pressure driven swirl tube, this would imply a total pressure loss, (and mass flow throttling), whereas for a pumped swirl tube (defined in Section 4.3) the net total pressure would rise due to the fan stage work. The dimensionless total pressure change is given as

$$\omega\left(r^*\right) = \frac{p_{t,\infty} - p_{t,d}}{\frac{1}{2}\rho V_\infty^2} = -\frac{\Delta p_t\left(r^*\right)}{\frac{1}{2}\rho V_\infty^2}. \tag{4.38}$$

Simple radial equilibrium (see Equation 4.29) is invoked next. Under this assumption, Equation 4.28 simplifies to a dimensionless form in terms of the pressure coefficient,

$$\frac{dp}{dr} = \frac{\rho V_{\theta,d}^2}{r} \Longrightarrow \frac{dC_p}{dr^*} = \frac{2\left(V_{\theta,d}/V_\infty\right)^2}{r^*}. \tag{4.39}$$

The pressure coefficient at a radial location, r^* is found by integrating the above equation. Assuming that the circumferential velocity distribution is known, the pressure distribution becomes

$$C_p\left(r^*\right) = -\int_{r^*}^{1} \frac{2\left(V_{\theta,d}/V_\infty\right)^2}{\tilde{r}} d\tilde{r}, \tag{4.40}$$

where $\tilde{r}$ is the variable of integration. The atmospheric pressure boundary condition constrains C_p to equal zero at $r^* = 1$. The total pressure at any radial location in the downstream plane is defined as

$$p_{t,d} = p_d + \frac{1}{2}\rho V_{z,d}^2 + \frac{1}{2}\rho V_{\theta,d}^2 = p_{t,\infty} + \Delta p_t = p_\infty + \frac{1}{2}\rho V_\infty^2 + \Delta p_t. \tag{4.41}$$

Equation 4.41 can be manipulated to define the pressure coefficient at any radial location in terms of ω, and the axial and radial velocities, such that

$$C_p\left(r^*\right) = \frac{p_d - p_\infty}{\frac{1}{2}\rho V_\infty^2} = 1 - \omega\left(r^*\right) - \left(\frac{V_{\theta,d}}{V_\infty}\right)^2 - \left(\frac{V_{z,d}}{V_\infty}\right)^2. \tag{4.42}$$

Finally, by combining equations 4.40 and 4.42, the axial velocity may be written as:

$$\frac{V_{z,d}\left(r^*\right)}{V_\infty} = \sqrt{1 - \omega\left(r^*\right) - \left(\frac{V_{\theta,d}}{V_\infty}\right)^2 + \int_{r^*}^{1} \frac{2\left(V_{\theta,d}/V_\infty\right)^2}{\tilde{r}} d\tilde{r}}. \tag{4.43}$$

Hence in the steady, incompressible model of ducted swirling outflow, the total pressure change and swirl velocity profiles, $\Delta p_t\left(r\right)/q_\infty$ and $V_{\theta,d}\left(r\right)/V_\infty$, respectively, are sufficient to describe the entire behavior of the device including:

- The total drag coefficient, as well as contributions from the axial momentum flux drag and pressure drag terms.
- The total mass flow, and hence the spillage and the net nacelle forces.
- The exit velocity and pressure profiles, and the swirl parameter profile, and hence a first indication of stability margin.

Results

The exit circulation distribution in the preliminary analytical modeling is specified as a Burger vortex distribution [27]. This representation is typical of many naturally occurring vortices [16]:

$$\frac{rV_{\theta,d}}{r_d V_\infty} = \left(\frac{K_c}{r_d V_\infty}\right)\left[1 - exp\left(-1.26\frac{r^2}{r_{crit}^2}\right)\right] \tag{4.44}$$

The Burger vortex distribution is defined by two parameters, a circulation multiplier, $K_c^* = K_c/r_d V_\infty$ and a critical radius, $r_{crit}^* = r_{crit}/r_d$. Toward $r^* = 0$ the Burger vortex distribution becomes a forced vortex ($rv_\theta \sim r^2$), while at large radii the distribution approaches a free vortex ($rv_\theta \sim$ constant). The circulation distribution is smooth, with the transition from forced to free vortex occurring at the critical radius. The factor 1.26 appears in the equation to ensure that the maximum $V_{\theta,d}$ occurs at the critical radius.

The prescribed exit circulation distribution also defines the dimensionless circumferential velocity profile, and hence the pressure coefficient given by Equation 4.42. Once the total pressure change is prescribed as $\omega(r^*)$, Equations 4.40 and 4.42 may be combined to obtain the axial velocity. These known quantities may be substituted into Equation 4.19 to yield an explicit expression of the drag coefficient given by

$$C_D = \underbrace{\frac{1}{A_f}\int_A \left[2\sqrt{1-\omega\left(r^*\right)-\left(\frac{V_{\theta,d}}{V_\infty}\right)^2+\int_{r^*}^1 \frac{2\left(V_{\theta,d}/V_\infty\right)^2}{\tilde{r}}d\tilde{r}} \times\left(1-\sqrt{1-\omega\left(r^*\right)-\left(\frac{V_{\theta,d}}{V_\infty}\right)^2+\int_{r^*}^1 \frac{2\left(V_{\theta,d}/V_\infty\right)^2}{\tilde{r}}d\tilde{r}}\right)\right] dA}_{\text{axial momentum flux drag coefficient}} \tag{4.45}$$

$$+\underbrace{\frac{1}{A_f}\int_A\int_{r^*}^1 \frac{2\left(V_{\theta,d}/V_\infty\right)^2}{\tilde{r}}d\tilde{r}dA}_{\text{pressure drag coefficient}}$$

$$= C_{D,\text{ax. mom.}} + C_{D,\text{press.}}.$$

Exit Flow Field It is useful to first examine the general features of the exit flow for a particular swirl and total pressure change distribution. A simple ram pressure driven swirl tube with total pressure change resulting from typical airfoil cascade profile losses of $\omega = 0.08$ is considered. For $r^*_{crit} = 0.5$ and $K^*_c = 0.77$ the total drag coefficient, C_D, is found to be 0.80. Figure 4-13 shows dimensionless profiles of axial velocity, circumferential velocity, negative pressure coefficient and swirl parameter. Going from the outer radius toward the core the swirling flow is characterized by decreasing pressure, in this case about 3.5 times the freestream dynamic head on the duct centerline. Relative to freestream, the flow accelerates in the core due to the low pressure, but decelerates at the outer radius, i.e., it is jet-like ($V_z/V_\infty \sim 2$) on the core and wake-like ($V_z/V_\infty \sim 0.6$) at the outer radius. The prescribed circumferential velocity approaches a forced vortex on the centerline. The swirl parameter, $S = V_{\theta,d}/V_{z,d}$, has a local maximum of 1.48, and is 1.08 at the critical radius. From the vortex breakdown stability criteria given in Section 4.4.3, this flow is suggested to be near the stability limit of $S = 1.2$ at the critical radius.

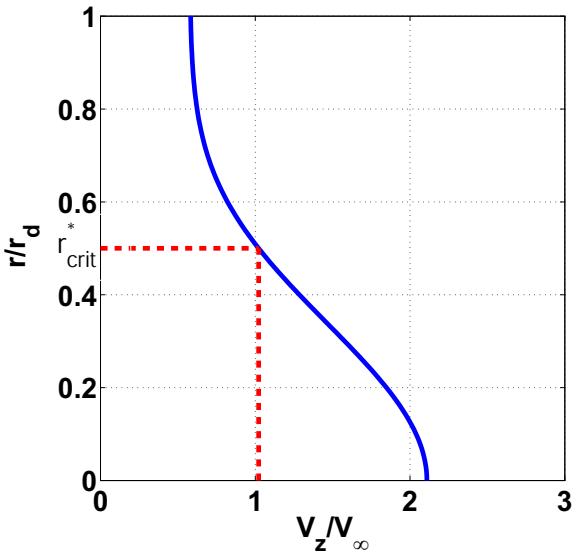

(a) Axial velocity

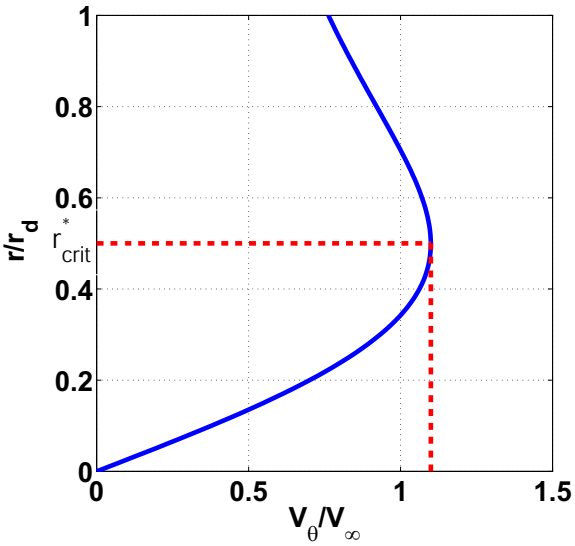

(b) Circumferential velocity

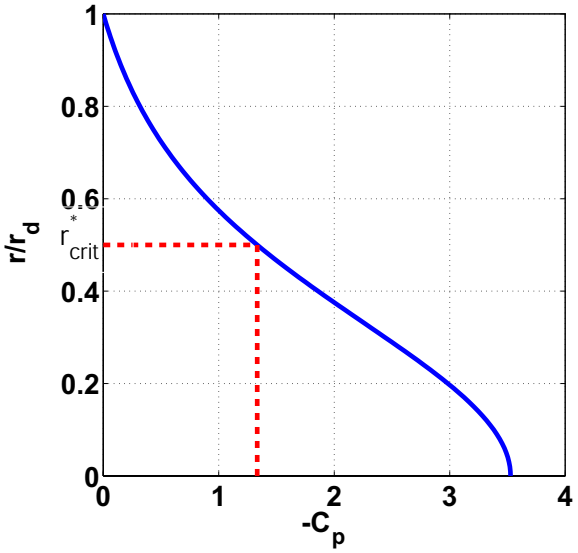

(c) Pressure defect

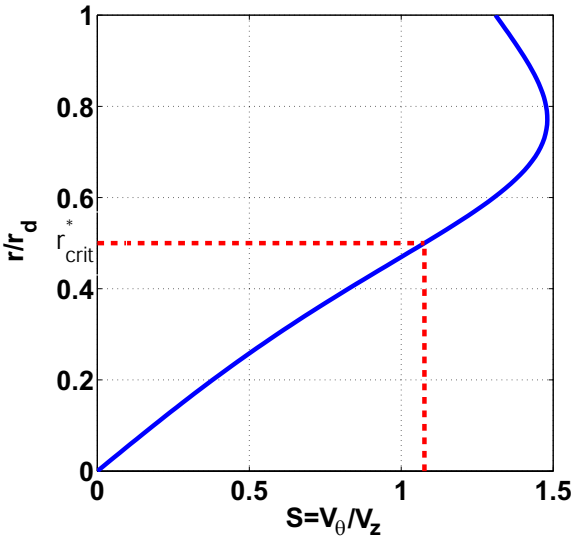

(d) Swirl parameter

Figure 4-13: Profiles of axial velocity, circumferential velocity, pressure coefficient, and swirl parameter for analytical swirl tube model with Burger vortex exit flow parameters of $\omega = -\Delta p_t/q_\infty = 0.08$, $r^*_{crit} = 0.50$, and $K^*_c = 0.77$, yielding drag coefficient of $C_D = 0.8$.

If the exit total pressure is known everywhere, it is possible to characterize the tradeoffs made between the static and dynamic pressure components along the profile through energy conservation arguments. On the centerline the circumferential velocity approaches zero since the flow resembles a forced vortex. Hence the total pressure is composed of the static pressure

and the axial component of dynamic pressure. This may be viewed as trading low pressure for high axial velocity. On the outer radius, the static pressure equals the freestream, such that along a streamline the circumferential dynamic pressure component is increased at the expense of the axial dynamic pressure component. Hence circumferential velocity is traded for axial velocity. One clear limit within the assumptions of the model then is that the circumferential velocity may not be increased to the extent that the axial velocity stagnates anywhere in the flow. For the Burger vortex circulation distribution of the current model the maximum value of the swirl multiplier, K_c^*, to avoid zero axial velocity on the outer radius is given by

$$(K_c^*)_{\max} = \frac{\sqrt{1+\omega}}{1 - exp\left[\frac{-1.26}{\left(r_{crit}^*\right)^2}\right]}. \tag{4.46}$$

Swirling flow dynamics suggests a tendency for stagnation and reverse flow to occur on the centerline in bubble-type vortex breakdown; the limitation to flow stagnation on the outer radius presented in Equation 4.46 at least qualitatively supports the notion that excessive swirl may lead to an instability and hence unsteady flow.

The parameterized design space of 1) a ram pressure driven, or throttled swirl tube, and 2) a fan driven, or pumped swirl tube are next explored to provide a more complete picture of the effects of loss and swirl distribution on drag generation. In addition, design recommendations are presented. The $C_D = 0.8$ Burger vortex design point with radial profiles presented Figure 4-13 is indicated in subsequent figures by a blue triangle.

Ram Pressure Driven Swirl Tube For the ram pressure driven swirl tube, total pressure loss coefficient is assumed to have a constant value of $\omega = 0.08$. Figure 4-14 presents iso-contours of drag coefficient overlayed by iso-contours of swirl parameter at $r = r_{crit}$ in the design space defined by the dimensionless Burger vortex parameters K_c^* and r_{crit}^*. The maximum swirl multiplier at each critical radius is given by Equation 4.46, and is demarcated by the heavy dashed blue line. Solutions to the right of this line violate the energy conservation constraint discussed earlier and thus do not exist.

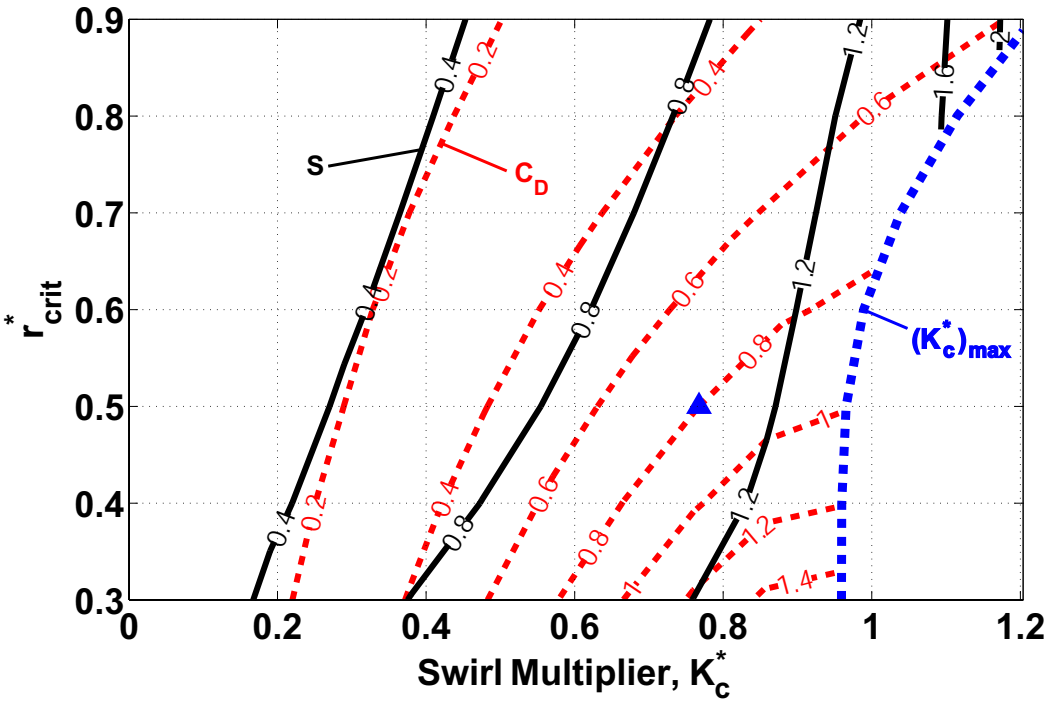

Figure 4-14: Contours of predicted total drag coefficient (C_D, dashed red) and swirl parameter at $r = r_{crit}$ (S, solid black) in (K_c^*, r_{crit}^*) space for ram pressure driven swirl tube having $\omega = 0.08$. Triangle indicates point with $C_D = 0.8$ and $r_{crit} = 0.5$, whose radial profiles are presented in Figure 4-13. Heavy, dashed blue line indicates $(K_c^*)_{\max}$ threshold.

The key design recommendation that emerges from the figure is that the highest drag is associated with a highly swirling vortex with small core size. Drag coefficient contours become closer together as K_c^* increases, indicating that the rate of change of drag with respect to maximum swirl level increases with swirl. Maximum C_D values also increase with decreasing r_{crit}^*, with values above 1 at $r_{crit}^* \lesssim 0.5$.

The highest levels of S at $r = r_{crit}$ are found to be just above 1.2, suggesting that the reverse flow limit derived from the axial/circumferential dynamic pressure balance arguments is qualitatively in accord with the vortex breakdown criteria mentioned in the previous subsection.

Figure 4-15 again presents iso-contours of drag coefficient overlayed by iso-contours of capture stream tube to duct exit area, A_{capt}/A_d. The vertical axis defined by $K_c^* = 0$ has a

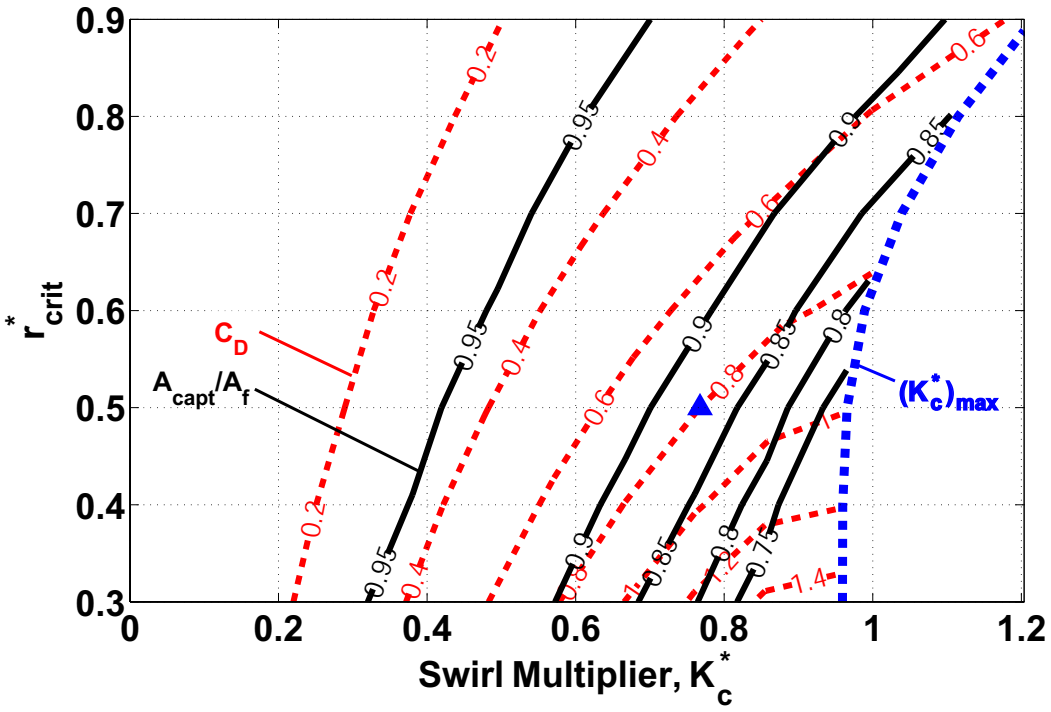

Figure 4-15: Contours of predicted total drag coefficient (C_D, dashed red) and capture streamtube to actuator disk area ratio (A_{capt}/A_f, solid black) in (K_c^*, r_{crit}^*) space for ram pressure driven swirl tube having $\omega = 0.08$. Triangle indicates point with $C_D = 0.8$ and $r_{crit} = 0.5$. Heavy, dashed blue line indicates $(K_c^*)_{\max}$ threshold.

value of A_{capt}/A_d of 0.96, meaning that the total pressure loss of $\omega = 0.08$ in the actuator disk without swirl reduces mass flow by four percent, per Equation 4.22. The A_{capt}/A_d contours indicate that mass flow decreases with increasing swirl, but the spilled mass flow from swirl alone is rather small for drag coefficients below about 0.4. For high drag, high swirl cases a throttling effect of ten to twenty percent mass flow reduction is seen relative to non-swirling flow. Thus, another recommendation for a ram pressure driven swirl tube is that good inlet design should incorporate a droop to avoid high incidence angle from this amount of spillage.

Figure 4-16 presents iso-contours of the two components of the total drag coefficient, namely, the pressure drag, $C_{D,\text{press.}}$, and the axial momentum flux drag, $C_{D,\text{ax. mom.}}$, in the (K_c^*, r_{crit}^*) space. The figure indicates that the pressure drag dominates the overall drag at high swirl. For example, in the $C_D = 0.8$ design point indicated by the blue triangle,

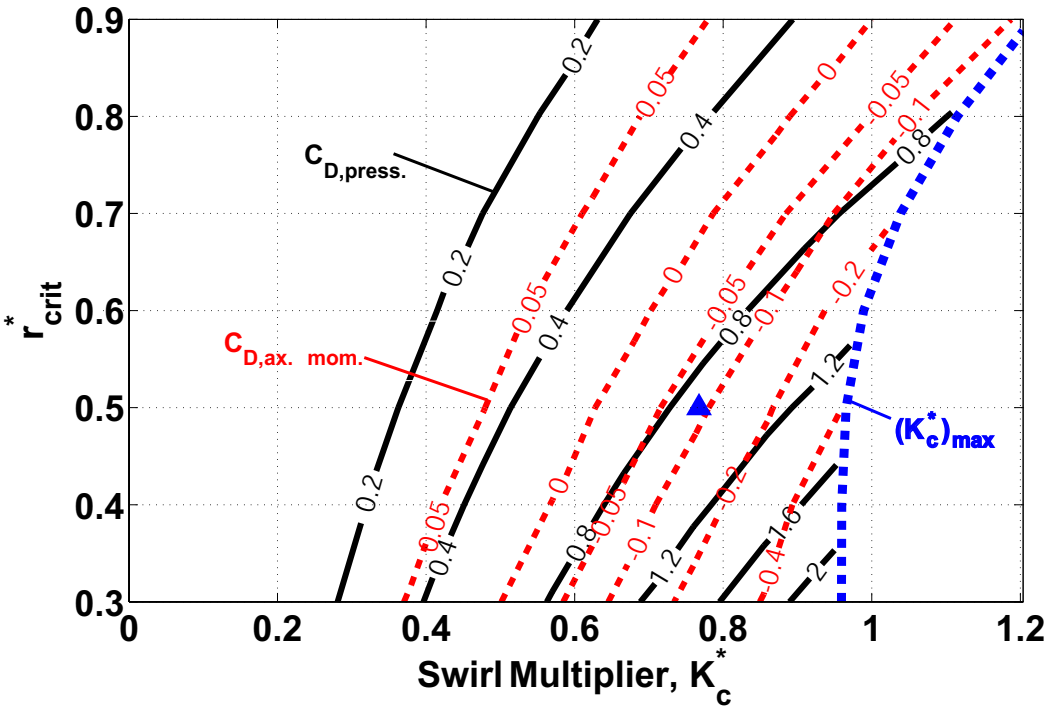

Figure 4-16: Contours of predicted drag coefficients from pressure defect ($C_{D,\text{press.}}$, solid black) and net axial momentum flux ($C_{D,\text{ax. mom.}}$, dashed red) in (K_c^*, r_{crit}^*) space for ram pressure driven swirl tube having $\omega = 0.08$. Triangle indicates point with $C_D = 0.8$ and $r_{crit} = 0.5$. Heavy, dashed blue line indicates $(K_c^*)_{\max}$ threshold.

pressure drag is an order of magnitude larger than momentum flux drag, rendering the latter essentially negligible[8]

At the fixed value of $r_{crit}^* = 0.5$, the effect of loss and swirl parameter on drag coefficient is presented in Figure 4-17. Iso-contours of C_D are normal to the vertical direction along the zero swirl line defined by $S = 0$, while at high swirl parameter levels these contours are roughly normal to the horizontal direction. The key implication is that for high levels of swirl, loss has a weak effect on the overall drag. Assuming a swirl parameter similarity associated with a physical set of swirl vanes[9], this figure suggests that loss goes from the

[8]The axial momentum flux drag actually has small negative values at high swirl, i.e., it theoretically produces a thrust component, because the axial momentum excess on the centerline is greater than the axial momentum defect at the outer radius.

[9]This is suggested in the pumped swirl tube computations of Section 5.5.1.

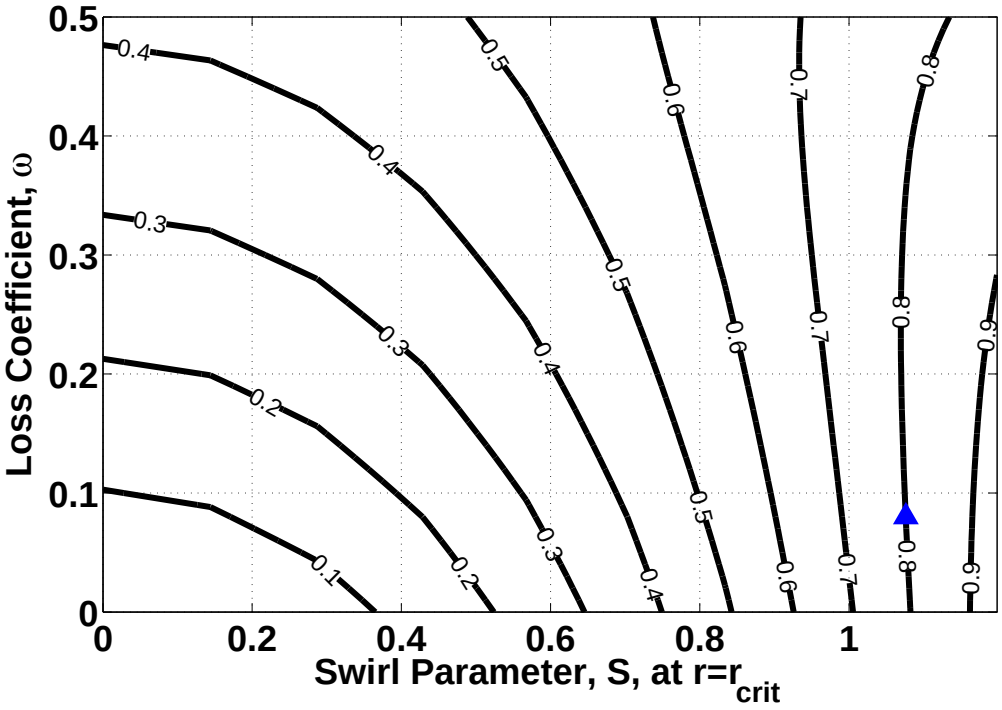

Figure 4-17: Contours of predicted total drag coefficient (C_D) in (S, ω) space for ram pressure driven swirl tube having $r/r_{crit} = 0.5$.

dominant drag mechanism at low swirl vane angles to a weak drag mechanism at high swirl vane angles. This drives the design recommendation that for high drag coefficient, greater emphasis should be placed on achieving the correct flow turning, with secondary emphasis placed on the accuracy of loss modeling.

Pumped vs. Throttled Swirl Tube Comparison The total pressure change $\Delta p_t/q_\infty$, is varied from positive (pumping) to negative (throttling) for fixed $r^*_{crit} = 0.5$, in the range of allowable swirl multiplier levels 0 to $(K_c)_{max}$. Figure 4-18 presents iso-contours of C_D and S (at $r = r_{crit}$). In the pumped regime, negative values of C_D correspond to net thrust. Fixed values of S may be associated with a fixed set of swirl vanes. Hence, along a fixed S iso-contour in the direction of pumping, C_D decreases due to the fan stage work input. However, for a given $\Delta p_t/q_\infty$, the difference in C_D between a fan stage with purely axial exit

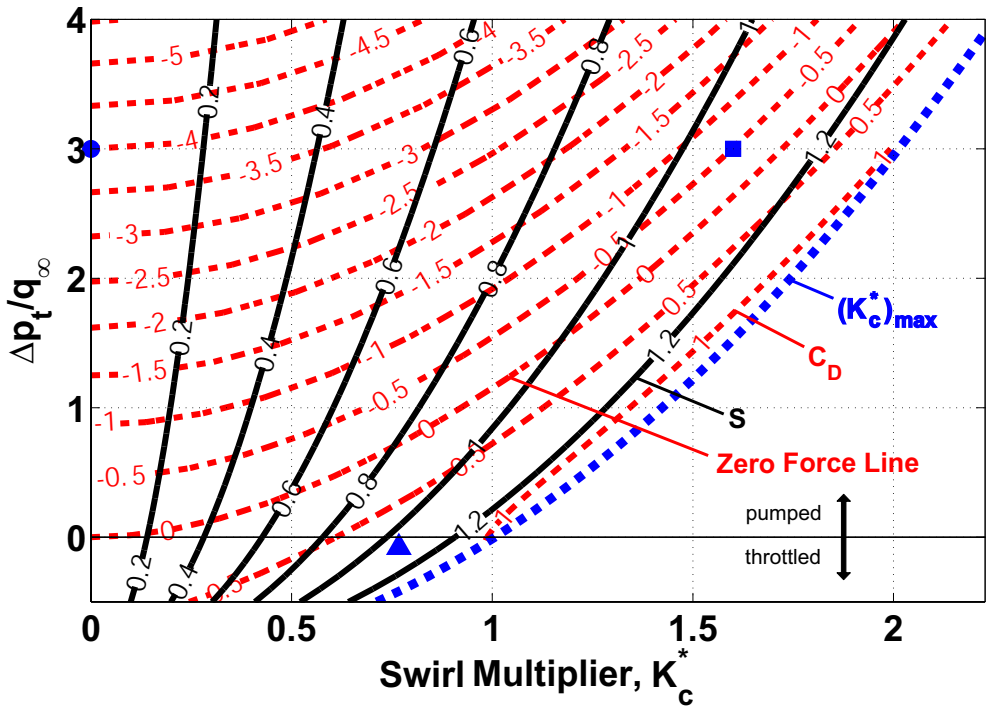

Figure 4-18: Contours of predicted total drag coefficient, C_D (dashed red), and swirl parameter, S (solid black), in $(K_c^*, \Delta p_t/q_\infty)$ space for pumped or throttled swirl tube with $r/r_{crit} = 0.5$. Dashed blue line indicates $(K_c^*)_{\max}$ threshold.

flow ($K_c^* = 0$) and a swirling outflow case at fixed S increases in the direction of increased pumping, suggesting that a pumped swirl tube generates greater effective drag through thrust reduction, relative to a stand alone, ram pressure driven swirl tube with similar critical swirl parameter (and hence, vane angle).

The three symbols in Figure 4-18 correspond to devices that illustrate this effect. A ducted fan stage with pressure rise of $\Delta p_t/q_\infty = 3$ having purely axial exhaust, shown by the circle, may operate in parallel with a stand alone, ram pressure driven swirl tube with $C_D = 0.8$, shown by the triangle. An alternate configuration is a pumped swirl tube having the same total pressure rise and the same swirl vanes, and is marked by the square. The device comparison is depicted in Figure 4-19. The difference in C_D between the two configurations suggests that a pumped swirl tube produces greater thrust reduction ($C_D = 3.5$) relative to

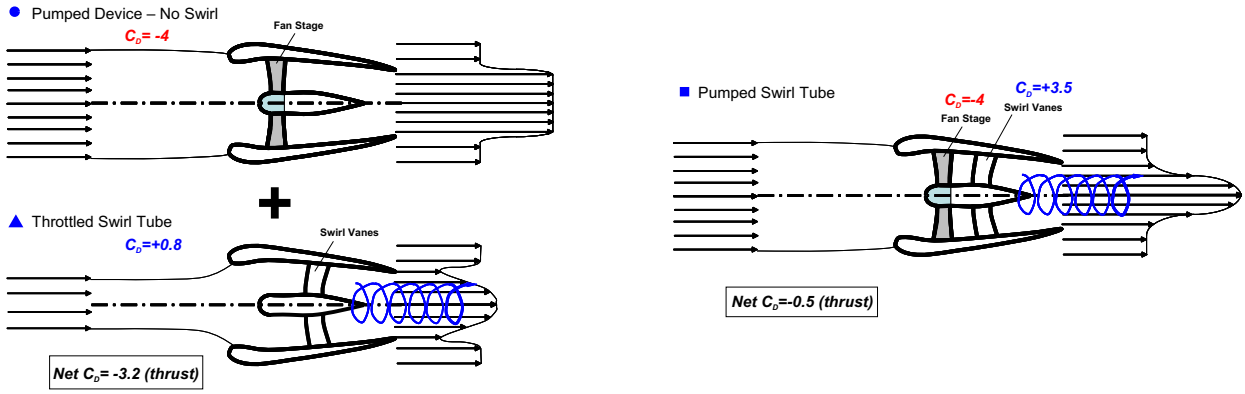

(a) Conventional fan engine plus stand alone, ram pressure driven swirl tube.

(b) Pumped swirl tube.

Figure 4-19: Comparison between conventional fan engine at approach idle plus stand alone, ram pressure driven swirl tube versus pumped swirl tube, for $\pi_{fan} = 1.06$, $M_\infty = 0.17$, $A_d/A_f = 1$, suggests that pumping of swirl vanes generates greater effective drag in the form of thrust reduction.

a ram pressure driven swirl tube ($C_D = 0.8$). Within the framework of the quiet approach requirements analysis that assumes approach thrust is fixed by the go-around maneuver requirement, thrust reduction is equivalent to drag generation. For a dimensionless total pressure rise[10] of $\Delta p_t/q_\infty = 3$, the drag coefficient difference between purely axial exhaust flow, $C_D = -4$, and the maximum swirling flow drag coefficient, $C_D = -0.5$, results in an equivalent drag coefficient of 3.5, about 4 times larger than a stand alone, ram pressure driven swirl tube with $C_D = 0.8$. This amount of effective drag would be sufficient to change the glideslope angle at constant approach velocity from 3° to 7°, resulting in 7.4 dB potential overall noise reduction if it were quiet.

The higher effective drag coefficient from pumping results from greater ingested mass flow, leading to greater vane loadings. Figure 4-20 presents the same total drag coefficient contours overlayed with iso-contours of captured steamtube area fraction, A_{capt}/A_f. At $\omega = \Delta p_t/q_\infty = 3$ the captured streamtube area is roughly twice that of a ram pressure

[10]The selected total pressure change across the fan stage of $\Delta p_t/q_\infty = 3$ corresponds to a fan stage pressure ratio of 1.06 at a flight Mach number of 0.17, typical of approach speeds for the SAX conceptual aircraft design described in Section 4.1.

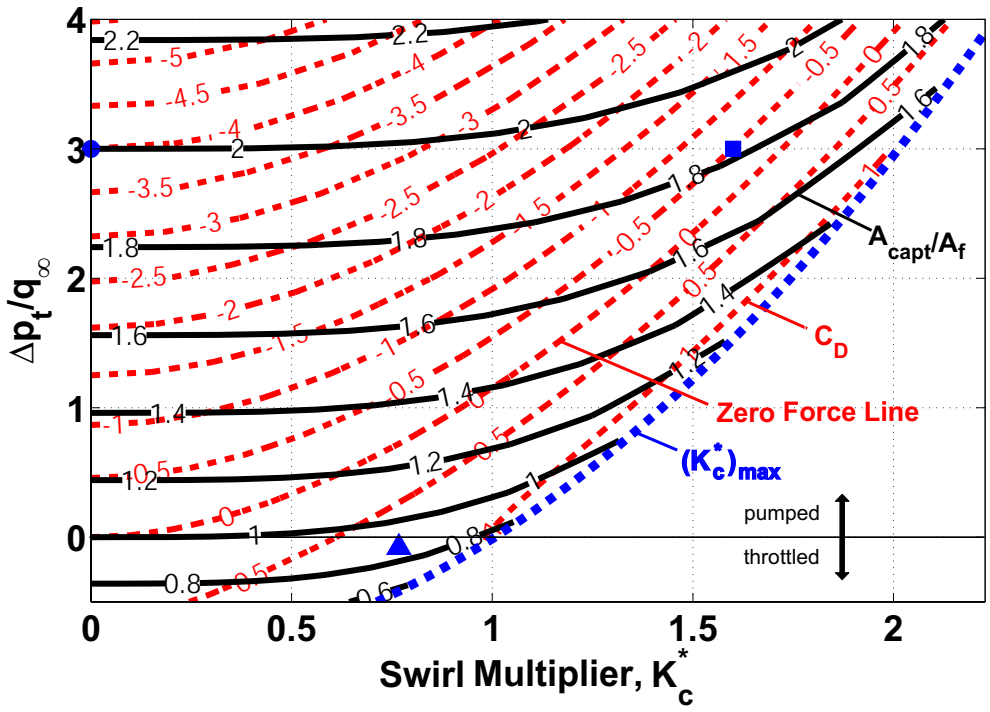

Figure 4-20: Contours of predicted total drag coefficient, C_D (dashed red), and capture streamtube to actuator disk area ratio, A_{capt}/A_f (solid black), in $(K_c^*, \Delta p_t/q_\infty)$ space for pumped or throttled swirl tube with $r/r_{crit} = 0.5$. Dashed blue line indicates $(K_c^*)_{\max}$ threshold.

driven value $\Delta p_t/q_\infty = -\omega = -0.08$. Capture steamtube ratio at fixed S (at $r = r_{crit}$) is a good general indicator of the ratio of flowfield velocities between two cases with different total pressure changes. Higher velocities in the pumped case suggest a noise increase relative to the ram pressure driven case, though a noise scaling law would have to be experimentally determined. As the effective drag benefits of a pumped swirl tube come with a noise penalty, it is recommended that these tradeoffs be quantified in future work.

The iso-contours of A_{capt}/A_f also indicate that for high swirl a given $\Delta p_t/q_\infty$ has the ten to twenty percent throttling effect relative to axial exhaust flow, as mentioned earlier. For a fan driven system, this may affect operability of the turbomachinery. This suggests that a wide operating range fan design for approach, or a variable area nozzle may be practical technologies for propulsion system integration.

4.5 Chapter Summary

This chapter introduced the idea of a novel quiet drag device called a swirl tube. The motivation provided here leads to the aerodynamic design and aerodynamic and acoustic validation presented in the next chapter. The swirl tube idea is developed using mission requirements analysis and parametric control volume modeling.

As the CMI Silent Aircraft Initiative has the goal of designing an aircraft that is functionally silent outside a typical airport perimeter, a step reduction in noise is needed relative to conventional aircraft. On approach, an aerodynamically and acoustically clean airframe is required. In addition operational changes such as slower and steeper approach profiles are required. This identifies the need for quiet drag, i.e., a departure from the strong correlation between drag and noise of conventional devices such as flaps, slats, or landing gear. Preliminary modeling indicates that:

1. Quiet drag requirements for the SAX conceptual aircraft to realize several decibels noise reduction are comparable to the clean airframe drag. More generally, steepening a conventional glideslope from 3° to 6° requires quiet drag roughly equal to the component of weight in the direction of the conventional glideslope.

2. Bluff body drag coefficients based on propulsion system fan area (C_D about 1.0) are capable of steepening a conventional glideslope from 3° to 4° at fixed approach speed, potentially resulting in 2.5 dB noise reduction. Overall noise reduction of 5 or more dB may be realizable through a combination of quiet drag coupled with quiet high-lift devices that enable slow and steep flight.

A preliminary drag model has been developed for a ducted device with purely axial and swirling exit flows, assuming steady, incompressible inflow and outflow. The model assumes an axisymmetric actuator disk with area equal to the duct exit ($A_d/A_f = 1$) imparts a change in total pressure and swirl. For ram pressure driven devices with throttling, i.e., net total pressure loss, the modeling results suggest:

1. A maximum drag coefficient of 0.5 is theoretically possible for a device with uniform axial outflow at an exit to freestream velocity ratio, $V_{z,d}/V_\infty$, of 0.5, equivalent to a non-dimensional total pressure change, $-\Delta p_t/q_\infty = \omega$=0.75.

2. A swirl tube generates maximum drag coefficients greater than 0.8, a nearly two-fold increase versus a purely axial outflow device.

3. The exit flow features of a typical swirl tube with high drag coefficient may include: i) axial velocity excess ($2V_\infty$) on the centerline, ii) axial velocity defect ($0.6V_\infty$) at the outer radius, and iii) high pressure defect at the centerline ($3.5q_\infty$).

4. The vortex breakdown instability is likely to set the limitation to maximum swirl tube capability, near a swirl parameter of 1.2, or 50° exit flow angle. Hence a recommended design would be close to but not in excess of this swirl parameter limit.

5. Loss of total pressure throttles the swirl tube mass flow. Loss increases drag at low swirl, but has a weak effect on overall drag at high swirl. Design for high drag should place greater emphasis on proper flow turning, with loss prediction being a secondary consideration.

6. Stable swirling flow without additional losses reduces mass flow ten to twenty percent at maximum drag relative to purely axial flow. A good swirl tube design should account for this level of spillage by incorporating a droop in the inlet leading edge.

Scenarios with a net total pressure rise are also generated to simulate the interaction of a swirl generator with an upstream fan stage. For a pumped swirl tube, the model suggests that:

1. Swirl generation downstream of a fan stage generates high effective drag by reducing the maximum thrust capability more than the drag produced by a separate, ram pressure driven swirl tube. For a typical approach idle setting this may be several times the ram pressure driven swirl tube drag.

2. The pumped swirl tube ingests greater mass flow than the ram pressure driven swirl tube, suggesting that exit velocities will be higher and noise possibly scales to some appropriate velocity ratio power law.

3. The throttling effect of swirl relative to axial exit flow suggests that a wide operating range fan design or a variable area nozzle may be beneficial for propulsion system integration.

Chapter 5

Swirl Tube: A Novel Turbomachinery Concept for Mission 2

Chapter 4 introduces the concept of the swirl tube, a quiet drag device that generates a ducted swirling outflow to enable slow and steep approach profiles for a functionally quiet aircraft. A parametric study using a control volume analysis and a survey of swirling flow dynamics suggests that high drag coefficients ($C_D \gtrsim 0.8$) may be achieved with stable, highly swirling flows. This chapter presents the details of the aerodynamic design, and computational and experimental validation of the swirl tube aerodynamics and acoustics. A ram pressure driven swirl tube is found to be a viable quiet drag device at full-scale, generating a scaled drag coefficient near 0.8 with noise signature well below the goals of a functionally quiet aircraft. A successful design for high drag and low noise requires a stable, swirling exit flow with maximum swirl angle near 50°. The vortex breakdown phenomenon is found to acoustically and aerodynamically limit swirl tube performance, by generating a device-scale, unsteady separation bubble near the duct exit. Important aspects of the system integration of a swirl tube with an airframe/propulsion system are explored at the end of the chapter. Swirl generated downstream of a fan stage at approach idle setting, a so-called pumped swirl tube, is found to produce large thrust reductions, relative to the drag of a ram pressure driven device, suggesting a potential opportunity for additional quiet drag.

The increased mass flow and exit velocities that result from fan stage work require future acoustic validation of this configuration.

5.1 Objectives

Two major hypotheses are tested in this research. The first hypothesis is that a swirl tube can generate high drag coefficient ($\gtrsim 0.8$) based on throughflow area, with exhaust flow fields that contain no large-scale unsteadiness. The second hypothesis is that the flow fields associated with the stable swirling exhaust flow are viable, quiet alternatives to high-drag control surfaces (flaps, slats, spoilers) and landing gear, enabling their use on a quiet aircraft. Testing these hypotheses requires meeting the following objectives:

1. Defining and quantifying the relationship between swirling flow, drag, and noise.
2. Quantifying the required swirling exit flow fields of the device.
3. Describing the limitations imposed on the device by the vortex breakdown phenomenon.
4. Characterizing swirl tube noise signature, identifying noise mechanisms and establishing acoustic power scaling laws.
5. Identifying the system integration issues and challenges associated with the implementation of a swirl tube on a quiet aircraft.

5.2 Technical Approach

A technical roadmap of swirl tube research is presented in Figure 5-1. The objectives of this research are met through aerodynamic design and aerodynamic and aeroacoustic experimental validation of swirl tubes with different swirl angle distributions. The final step is to identify technical challenges associated with the implementation of swirl tubes into

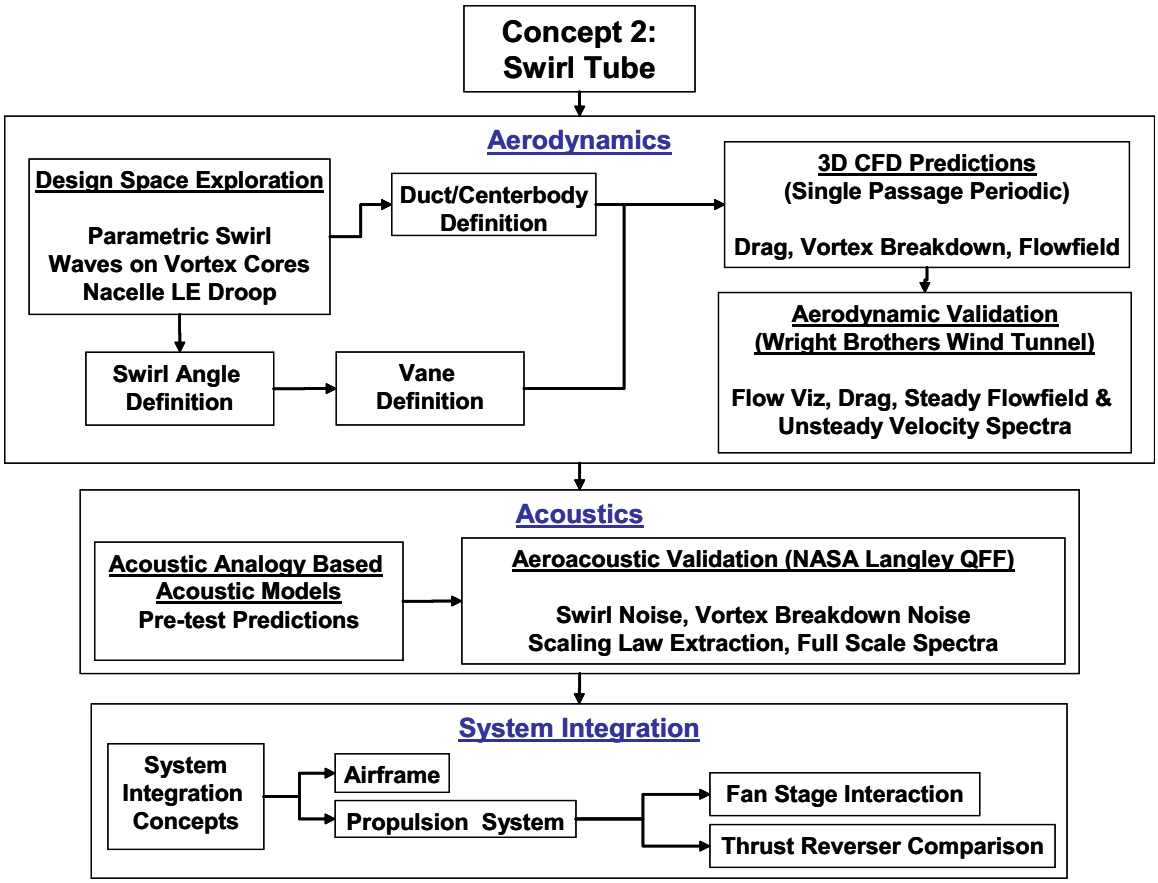

Figure 5-1: Swirl tube technical roadmap.

the airframe/engine system. The technical approach is executed sequentially in remaining sections, as described here.

Swirl tube aerodynamics are discussed in Section 5.3. Section 5.3.1 begins with a sweep of the design space of a duct/centerbody geometry with parametrically defined internal swirl distribution, using an inviscid, axisymmetric throughflow analysis tool, MTFLOW. MTFLOW output provides the first definition of the ducted swirl vane exit angles and exit flow fields. Candidate vane exit angle distributions are selected from a family of swirl distributions for various drag coefficients. Sectional vane design methods in Section 5.3.2 then define the three-dimensional blade geometry, for which single-passage periodic CFD computations are performed using Fluent, as discussed in Section 5.3.3. The CFD computations include the internal and external flow fields, and are intended to predict the drag coefficient and

give a description of the flow fields. The CFD computations also account for the viscous nature of the vortex core, which MTFLOW does not. The Fluent computations identify the critical conditions for the onset of the vortex breakdown instability. Finally, model-scale aerodynamic tests at the MIT Wright Brothers Wind Tunnel (WBWT) conducted by the author and Mobed [61] are described in Section 5.3.4. The goals of these tests are to 1) experimentally validate the aerodynamic design and 2) identify potential noise source mechanisms that arise from unsteadiness in the flow field. The experimental validation is done through drag measurements, flow field mapping and flow visualization. Unsteady velocity signals measured from hot-wire anemometers indicate potential broadband acoustic source regions.

Swirl tube acoustics are discussed in Section 5.4. To the author's knowledge, the noise signature of the flow field emanating from such a device has not previously been reported. A major research challenge is to determine the swirl tube sound generation mechanisms and scaling laws. A brief description of modeling efforts to estimate the noise from the swirling flow are provided in Section 5.4.1. These noise models rely on CFD postprocessing, combining jet noise concepts from Lighthill's acoustic analogy [49, 50] with Tam et al.'s [88, 89] adjoint Greens function solutions of the linearized Euler equations. Acoustic validation tests at the NASA Langley Quiet Flow Facility are subsequently discussed in Section 5.4.2. Noise spectra from swirl tubes with different swirl distributions are presented, with an emphasis on comparison between stable swirling flow and vortex breakdown. Acoustic power scaling laws are also deduced, as well as geometric scaling for aircraft application, demonstrating the viability of the swirl tube for quiet drag on approach. In addition, the acoustic experiments ultimately demonstrate that the aforementioned theoretical models fall short of capturing the correct swirl tube noise sources or levels, indicating that more effort should be spent on this type of noise modeling in future.

In Section 5.5 high-level system integration issues are presented. Swirl tube integration into a propulsion system bypass or mixing duct is challenging because the downstream resistance offered by swirl vanes affects the fan stage operating point. CFD computations

of swirl vanes downstream of an idealized fan stage (a so-called pumped swirl tube) are presented in Section 5.5.1. These computations demonstrate that pumping increases the mass flow through the swirl vanes, resulting in greater thrust reduction than a ram pressure driven swirl tube. The computations also highlight the importance of a low approach idle setting on overall quiet approach feasibility. The effect of swirl vanes downstream of a fan stage on the fan operating point is also discussed. In Section 5.5.2 the effectiveness of a quiet drag device is compared to a thrust reverser during the landing roll. Although not mandated by aviation authorities, thrust reversers are shown to provide the most stopping capability on a slippery runway. Hence, a recommendation is made to incorporate the swirl tube device concept into the thrust reverser mechanism if a propulsion system-integrated configuration is chosen.

5.3 Swirl Tube Aerodynamics

In Section 4.4 an analytical ducted drag generation model using a Burger vortex exit swirl distribution and vortex breakdown limits from swirling flow dynamics supports the hypothesis that a drag generating swirling exhaust flow device may generate high drag coefficients ($\gtrsim 0.8$), about twice the theoretical maximum of a drag generating axial exhaust flow throttling device. In this section this hypothesis is confirmed through aerodynamic design and computational and experimental validation of a swirl tube.

Conceptually, the design process begins in Section 5.3.1 with a sweep of the design space using streamline curvature methods in an inviscid, axisymmetric flow solver. Important gas path-design effects such as loss and blockage are also studied. A family of vane designs are then generated in Section 5.3.2 and computationally modeled with CFD in Section 5.3.3. The CFD includes viscous effects in the core and establishes the flow fields for the stable cases. CFD also identifies the vortex breakdown threshold. In Section 5.3.4, wind tunnel testing, including flow visualization, hot-wire anemometry, and drag measurement by force balance is used to validate the swirl tube design process and hypothesized drag capability.

5.3.1 Two Dimensional Axisymmetric Computations

The swirl tube drag capability is modeled with an axisymmetric flow solver, MTFLOW [20], within a design space of parametrically defined circulation distributions. Swirl vanes are treated as actuator disks [34] of finite axial extent contained within a nacelle/centerbody geometry. The output of MTFLOW contains the internal and external streamline trajectories in the meridional (axial-radial) plane. Swirling flow streamline exit angles may be extracted as a function of radius, providing the first step to three-dimensional vane design.

Computational Methods

MTFLOW is a collection of programs that allows for the viscous/inviscid analysis and design of axisymmetric bodies, and is an extension of the Euler equations-based methods using intrinsic streamline grids that are described by Drela [19]. It includes effects of swirl, heat addition, loss and blockage. The flow solver is given the duct and centerbody geometry, and allows for a discontinuity of blockage, entropy (loss), circulation (rv_θ) plus a prescribed rotational speed (to allow for shaft work transfer), and additional stagnation enthalpy due to heat transfer or heat release, along the streamlines that pass through the swirl generating stators (the actuator disk). As the swirl tube is adiabatic with no rotating parts, heat transfer and work transfer are neglected. The maximum allowable swirl limit is found to correspond to the development of waves on the vortex core, signifying the onset of the vortex breakdown instability.

A duct and centerbody geometry are first designed assuming swirl vanes with a hub to tip ratio, r_H/r_f, of 0.25. This is chosen to be consistent with preliminary fan designs for the SAX BWB aircraft described in Section 4.1. The dimensionless duct geometry is shown in Figure 5-2, with the actuator disk outer radius[1], r_f having the reference value of unity. The actuator disk is defined in the region from $z/r_f = -0.23$ to $z/r_f = 0.23$. In this region, the duct and center body form a constant cross-section annulus with outer radius 1 and hub to tip ratio 0.25. The forward portion of the centerbody is designed as a 2.5 : 1 ellipse, and

[1] As the swirl tube idea is motivated by the available throughflow area of an engine duct, the subscript f references the fan face.

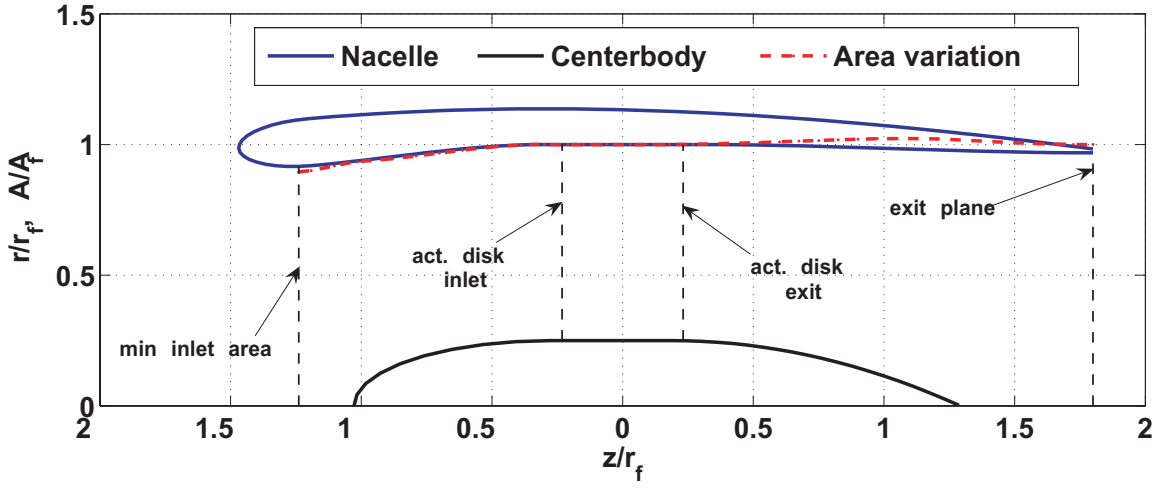

Figure 5-2: Nacelle and centerbody geometry. Dotted red line shows cross-sectional area variation normalized to annulus area at $z/r_f = 0$ (actuator disk position).

the aft centerbody is designed to come to a sharp point at $z/r_f = 1.29$, and is faired to the constant radius hub section using a polynomial spline. The nacelle geometry is a drooped airfoil with a chord length equal to $\sim 160\%$ of the actuator disk outer diameter and maximum thickness to chord ratio of $\approx 6\%$. The nacelle leading edge is a $3:1$ ellipse with a 5° droop. This droop is selected by visually examining the streamlines of a similar, undrooped elliptical leading edge for a representative swirl generation case in order to minimize high angles of attack on the nacelle leading edge due to spillage. The nacelle trailing edge is designed to have an approximate thickness-to-chord of 0.5%. The exit area of the duct is chosen to be equal to the actuator disk annular area. Therefore the exit diameter of the duct is smaller than the actuator disk annulus outer diameter by the factor $\sqrt{15/16}$.

The duct cross-sectional area variation, normalized to the actuator disk cross-sectional area, is also shown as a dashed red line in Figure 5-2. One may infer from the CV analysis of Section 4.4.1 that increasing the nozzle exit area increases the theoretical maximum drag capability (Maximum C_D also increases, because it is defined in terms of A_f, not A_d). As this effect is already well understood, a $1:1$ area ratio between the actuator disk and the duct exit is selected for simplicity. The minimum inlet area is shown to be $\approx 90\%$ of the

annulus area. The area ratio between the minimum inlet area and the actuator disk is based on an assumed cruise design Mach number at the actuator disk face of 0.66 and a Mach number at the minimun inlet area of 0.85, to match a typical aircraft engine inlet geometry. A gradual area change in the inlet diffuser section is selected to prevent flow separation.

The duct geometry is read by MTFLOW, with an actuator disk definition of the swirl profile and uniform total pressure loss equaling 4% of the freestream dynamic pressure between the axial stations $z/r_f = -0.23$ and $z/r_f = 0.23$. In addition, a prescribed blockage of 6% is chosen to model the vane thickness. The loss and blockage levels are selected to be typical of turbomachinery cascades. The axial coordinate $z/r_f = 0$ represents the stacking location of the vane airfoil sections, and it is from this location that the flow domain is dimensioned. The flow domain is defined two nacelle chord lengths upstream of $z = 0$ and three nacelle chord lengths downstream of $z = 0$. The outermost radial bound of the domain is two nacelle chords from the centerline ($r = 0$).

In exploring the design space, the swirl distribution in the annular actuator disk is based on a circular Burger vortex-like circulation (rv_θ) distribution. The Burger vortex is a realistic representation of a stable vortex found in nature [27], because it has a smooth and continuous rv_θ distribution, approaches a forced vortex ($rv_\theta \propto r^2$) in the core, and approaches a free vortex ($rv_\theta \propto$ constant) away from the core[2]. The two dimensionless parameters that define the Burger vortex are maximum swirl level, $K_c^* = K_c/r_f V_\infty$, and critical radius, $r_{crit}^* = r_{crit}/r_f$. As the quantity rV_θ is convected along streamlines in steady, axisymmetric, inviscid swirling flow[3], and the duct flow evolves from annular to circular as the centerbody ends, it is advantageous to prescribe the changes in circulation across the annular actuator disk as a function of streamline coordinate, ψ, in MTFLOW [20]. The Burger vortex-like circulation (rv_θ) distribution is thus mapped from radial to stream function coordinates under the assumption of a circular Burger vortex with uniform axial velocity,

$$\frac{\psi}{\psi_{crit}} = \left(\frac{r}{r_{crit}}\right)^2. \tag{5.1}$$

[2]See Equation 4.44.
[3]See Section 4.4.3.

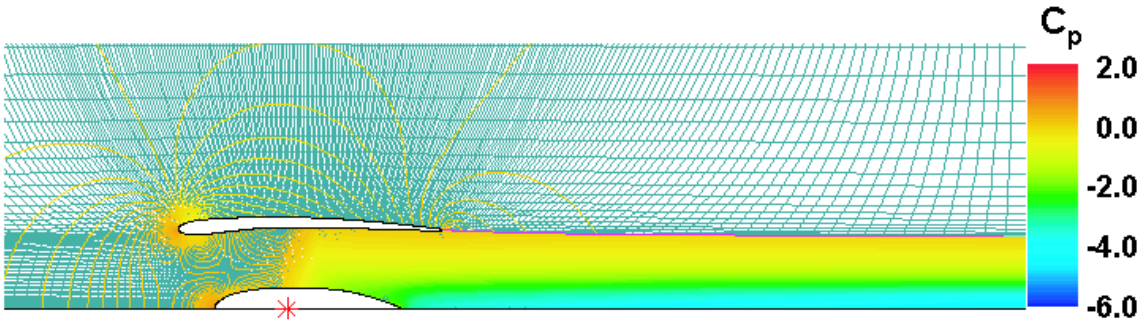

(a) Supercritical (converged) case: Pressure coefficient distribution for $K_c^* = 0.77$, $r_{crit}^* = 0.7$, $C_D = 0.80$.

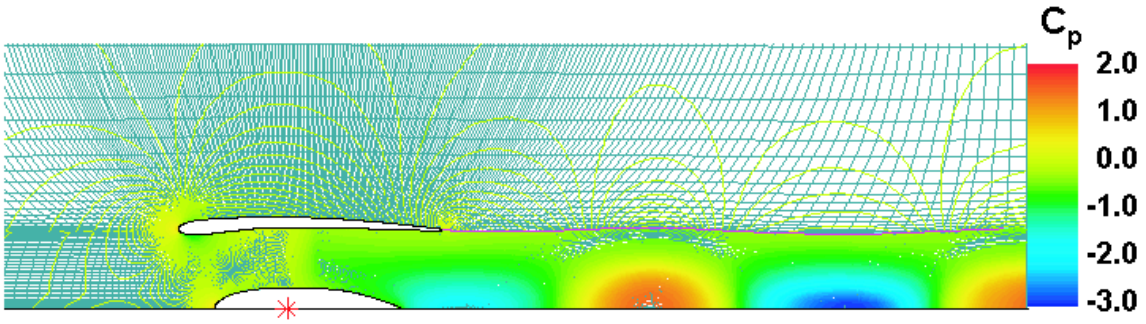

(b) Subcritical (unconverged) case: Pressure coefficient distribution showing standing wave-like behavior along centerline for $K_c^* = 1.10$, $r_{crit}^* = 0.7$. Standing wave is indicative of vortex breakdown.

Figure 5-3: MTFlow pressure coefficient (C_p) distributions for supercritical and subcritical (vortex breakdown) swirling flow.

In other words, the steamfunction coordinate ψ is an indication of the mass flux contained within the streamtube of radius r, assuming uniform axial velocity. The Burger vortex-like circulation distribution is thus defined as

$$\frac{rV_\theta}{r_f V_\infty} = K_c^* \left[1 - exp\left(-1.26\frac{\psi}{\psi_{crit}}\right)\right]. \tag{5.2}$$

Convergence and Stability

MTFLOW generates an initial streamline grid through the domain, based on the geometry and the prescribed actuator disk parameters. The code then iteratively adjusts the streamlines, along which the value of rv_θ is prescribed, until all governing equations are satisfied

within a prescribed convergence criterion. Converged solutions show an increasing pressure defect with increasing swirl. Figure 5-3(a) shows the pressure coefficient distribution of a converged solution at the parameter values of $K_c^* = 0.77$ and $r_{crit}^* = 0.7$, with predicted drag coefficient of 0.80.

For a fixed $r_{crit}^* = 0.7$, solutions become unstable at some critical value of maximum swirl level. This observation is consistent with the vortex breakdown instability shown to occur at a critical value of swirl parameter in many classic swirling flows [6, 15, 16, 30]. Standing waves on the vortex core are found to develop during the iterations, as depicted in Figure 5-3(b) for the parameters $K_c^* = 1.10$ and $r_{crit}^* = 0.7$. The concept of critical state for vortex breakdown was presented in Section 4.4.3 as the condition where standing waves are supported. In MTFLOW, solutions do not converge at the onset of these cases; hence, non-convergence in MTFLOW is associated with the vortex breakdown instability.

Results

Figure 5-4 presents MTFLOW generated iso-contours of total drag coefficient (C_D) and duct exit swirl parameter (S) at $\psi = \psi_{crit}$, plotted in the design space of the non-dimensional maximum circulation and vortex core radius, K_c^* and $r_{crit}^* = \sqrt{\psi_{crit}^*}$, respectively. These iso-contours are shown for converged cases only, i.e., the blank area to the right of the heavy dashed blue line corresponds to unconverged solutions that are associated with the vortex breakdown instability. At the highest swirl levels, MTFLOW finds converged cases with $C_D > 1$.

Comparing Figure 5-4 to the analytically derived results of Figure 4-14 suggests that the preliminary analytical models capture the C_D and S iso-contour trends. For low levels of drag ($C_D \sim 0.2$) and swirl parameter ($S \sim 0.4$), the values of constant C_D and S roughly match, while at higher values they do not. This is because as swirl level increases, the uniform axial velocity assumption employed in the MTFLOW swirl distribution expression (Equation 5.2) becomes increasingly weaker. The low pressure, non-swirling region on the centerline creates a high axial velocity (trading low static pressure for high axial dynamic pressure), while

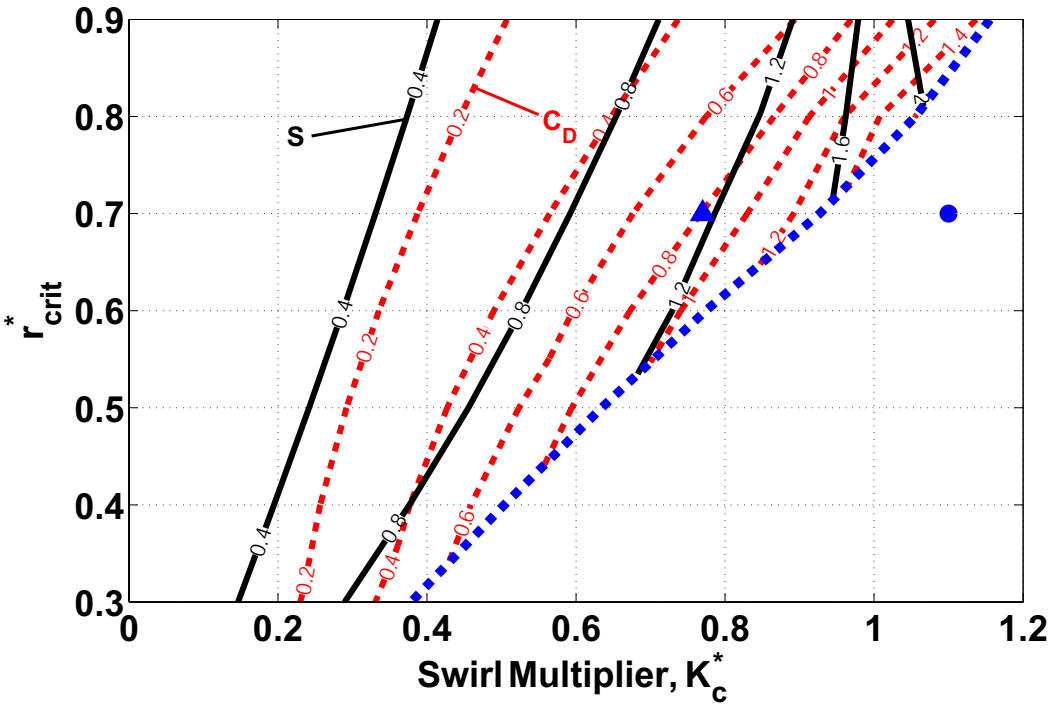

Figure 5-4: Contours of MTFLOW computed total drag coefficient (C_D, dashed red) and duct exit swirl parameter at $\psi = \psi_{crit}$ (S, solid black) in (K_c^*, r_{crit}^*) space for ram pressure driven swirl tube having $\omega = 0.08$. Triangular and circular symbols represent converged $(K_c^* = 0.77, r_{crit}^* = 0.7)$ and unconverged $(K_c^* = 1.10, r_{crit}^* = 0.7)$ cases shown in Figure 5-3. Dashed blue line demarcates boundary between converged and unconverged solutions.

the highly swirling flow on the outermost radius has nearly atmospheric pressure and low axial velocity (trading low axial dynamic pressure for high swirling dynamic pressure). This causes streamlines to become bunched toward the centerline, effectively reducing the core radius. The radial shift of the core relative to the prescribed value of r_{crit}^* is an artifact of the uniform axial velocity assumption, and is the likely reason that unconverged solutions appear at values of S well below 1.2 for lower values of r_{crit}^*. In addition, the minimum achievable vortex core radius in real swirling flows is limited by viscous effects that are neglected in MTFLOW. On the other hand, for high values of r_{crit}^* MTFLOW admits solutions with values of S well above 1.2, beyond the regime of observed vortex breakdown onset [16]. As the goal of the entire endeavor is to design a family of swirl tubes of increasing flow angle

that spans stable and vortex breakdown flowfields, these mitigating factors suggest that an intermediate critical radius whose solutions span the assumed vortex breakdown indicator of $S = 1.2$ represents a sound design choice. A parametrically designed family of vanes of intermediate radius, $r^*_{crit} = 0.7$ (ψ^*_{crit}=0.49), is thus presented in the next subsection for various drag coefficients. The moderate critical radius of 0.7 is recommended as a compromise between excessive turning at the outer edge near the nozzle shear layer for large r^*_{crit}, and excessive core vorticity for a small r^*_{crit} which may compare poorly to a real swirling flow that has large viscous dissipation in the core.

Effect of Prescribed Actuator Disk Loss and Blockage

The effects of prescribed actuator disk loss and blockage are studied on a constant vane exit angle basis in order to understand their implications on the accuracy of the drag predictions. Low levels of loss and blockage consistent with turbomachinery ($\lesssim$ 12%) are considered, because the device concept consists of a ducted cascade of swirl vanes. The key findings are:

- Loss is found to have a second-order effect ($\lesssim$ 10%) on the drag levels.
- Local blockage in the actuator disk increases the exit swirl parameter and hence drives the flow toward vortex breakdown.

For the purposes of a swirl vane design methodology, changes in effective loss and blockage provide a means to explain small discrepancies between measured and predicted drag as discussed in Section 5.3.4. During a first design iteration it is recommended to place greater emphasis on achieving sufficient flow turning. If a second design iteration is required the values of loss and blockage may be adjusted to provide greater accuracy to the predicted levels. A summary of the loss and blockage computational experiments is provided below.

Loss. Loss is increased by a factor of three, from the baseline case of 4% to 12% of freestream dynamic head. It is found that increasing the loss the can theoretically increase or decrease the drag, depending on whether the drag is dominated by a defect in

axial momentum or pressure, as given by Equation 4.19. This observation is consistent with the analytical result presented in Figure 4-17 in Section 4.4.4. For the baseline case of $C_D = 0.40$, a three-fold increase in the loss results in an increase in drag to $C_D = 0.44$. For the baseline case of $C_D = 1.10$ the opposite is true – a three-fold increase in loss results in a drag reduction to $C_D = 1.06$. The physical mechanism present can be explained as follows: increasing the loss reduces the mass flow and also the flux of axial momentum through the swirl tube. Since turning angle is held fixed between cases, this results in a reduced swirl velocity magnitude and reduced pressure defect (from Equation 4.39). At low turning angles ($\lesssim 35°$), the reduction in axial momentum flux drag from an increase in actuator disk loss is greater than the reduction in pressure drag, resulting in greater overall drag. At the highest turning angle near the critical vortex breakdown swirl parameter ($\gtrsim 50°$), the axial momentum flux drag is the weaker term compared to the pressure drag and hence a small increase in loss can result in lower overall drag.

Blockage. Blockage is increased by two-fold from 6% to 12%, holding swirl vane angle fixed for a low drag case. The resulting baseline drag coefficient of $C_D = 0.40$ is found to increase to $C_D = 0.47$. Blockage creates an area constriction in the vane passages. Since the duct exit area remains unchanged, negligible change in mass flow is found. Hence the duct exit axial velocity is also relatively unchanged. The axial and circumferential velocity through the actuator disk must thus increase to satisfy mass conservation. The increase in circumferential velocity at fixed radii implies an increase in rv_θ, which is a quantity that is convected along the streamlines (from Kelvin's theorem, Section 4.4.3). Finally, this results in higher values of rv_θ at the duct exit, compared to the relatively unchanged axial velocity at the same station. The observed increase in drag coefficient also corresponds to an increase in swirl parameter. The design implication of this for high swirl vane angles is that an increase in effective blockage may trigger vortex breakdown. Therefore, vane angle setting should compensate for blockage effects, with higher blockage values requiring lower blade angles in order to achieve a given exit flow field.

$C_{D,MTFLOW}$	α_{max}
0.40	34°
0.60	41°
0.80	47°
1.00	53°
1.10	57°
1.31	64°

Table 5.1: Maximum vane turning angle (rounded to nearest degree) associated with drag coefficient computed by MTFLOW.

5.3.2 3D Vane Design Methodology

The output of the design space exploration in the previous subsection provides flow angles at the actuator disk exit station for various swirl distributions. Vane exit angles are thus obtained for MTFLOW computed drag coefficients of 0.40, 0.60, 0.80, 1.00, 1.10, and 1.31, the latter two being very close to the vortex breakdown condition based on MTFLOW convergence behavior. Vane inlet angles are assumed to be 0°. All geometries are based on the selected critical radius value of 0.7, i.e., $\psi^*_{crit} = (0.7)^2 = 0.49$, from Equation 5.2. Table 5.1 shows the maximum vane turning angles associated with these designs.

As swirl tube vane passages are accelerating the flow, the 3D vane design methodology is conceptually similar to the design of turbine stators, and consists of designing airfoil sections at constant spanwise stations between the leading and trailing edge radii of each of the MTFLOW streamlines. An example of a typical airfoil section is shown in Figure 5-5. Cubic Bezier splines, defined by four control points, define the pressure side of each spanwise section, using a fixed set of parameters[4]. Circles are located along the pressure side points to create an envelope that defines the suction side. The circle size is decreased to tailor

[4]Two control points set the pressure side leading and trailing edge. Since inlet and exit angles are known, tangents can be extended from each point. Each tangent has one additional control point along it, defined by the fraction of the distance from the leading (or trailing) edge point to the intersection point of the two tangents. These fractional values are fixed at 60% and 80% from the leading and trailing edges, respectively, for all vane sections.

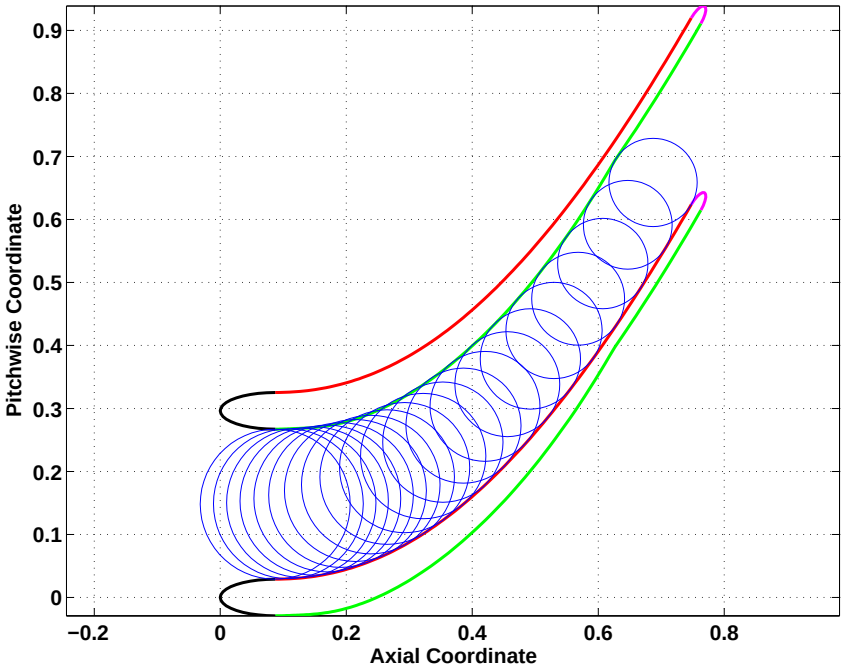

Figure 5-5: Example of sectional vane design for inlet (upstream) angle, θ_u, of 0°, exit (downstream) angle, θ_d, of 60° and solidity, σ, of 3. The pressure side (red), is defined using a Bezier spline. Suction side (green) is defined by the area distribution of circles. Leading (black) and trailing (magenta) edges are 3:1 half-ellipses.

the area of the passage to have a favorable pressure gradient[5], minimizing the risk of flow separation. The leading and trailing edges of the blade are designed as $3:1$ half-ellipses. Figure 5-6 shows the result of stacking up the radial sections into a 3D vane.

A linear solidity function defines the blade chord length from hub to tip, on the basis of twenty vanes. A count of twenty vanes is chosen to satisfy the solidity requirement and ensure that the axial extent of the vanes fits within the constant cross-section annular region

[5]A smooth area distribution for all vane geometries was found by trial and error to be:

$$\frac{A}{A_u} = 1 + \eta\left(1 + \cos \pi t^n\right)\left(\frac{\cos\theta_u}{\cos\theta_d} - 1\right) \tag{5.3}$$

where A_u is the inlet (upstream) area, $\eta = 0.35$, $n = 1.2$, and t is the Bezier spline parameter for the pressure side, ranging from 0 at the leading edge to 1 at the trailing edge. t varies approximately linearly with the axial coordinate of the pressure side.

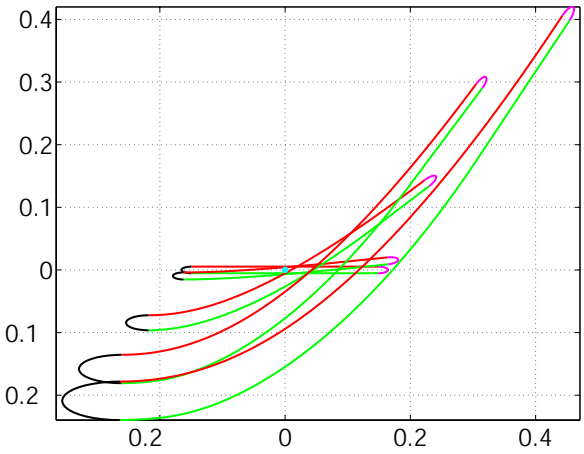

(a) Vane airfoil sections geometries at five radial stations. $(0, 0)$ is stacking location.

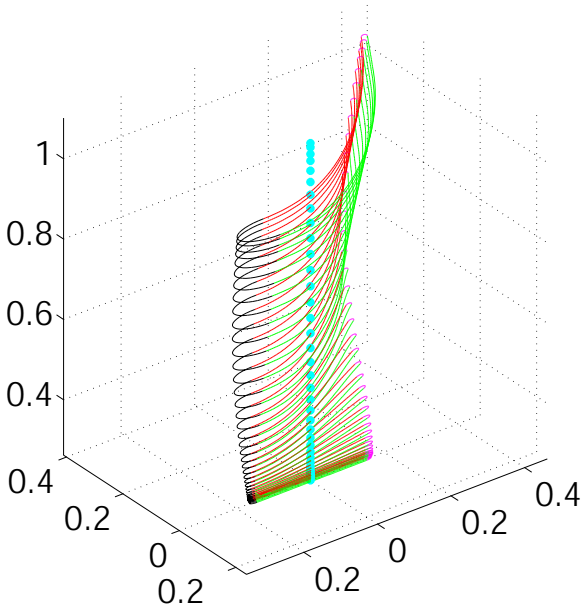

(b) Airfoil sections stacked to generate three-dimensional vane design. Stacking line is indicated by cyan circles.

Figure 5-6: Examples of sectional vane design.

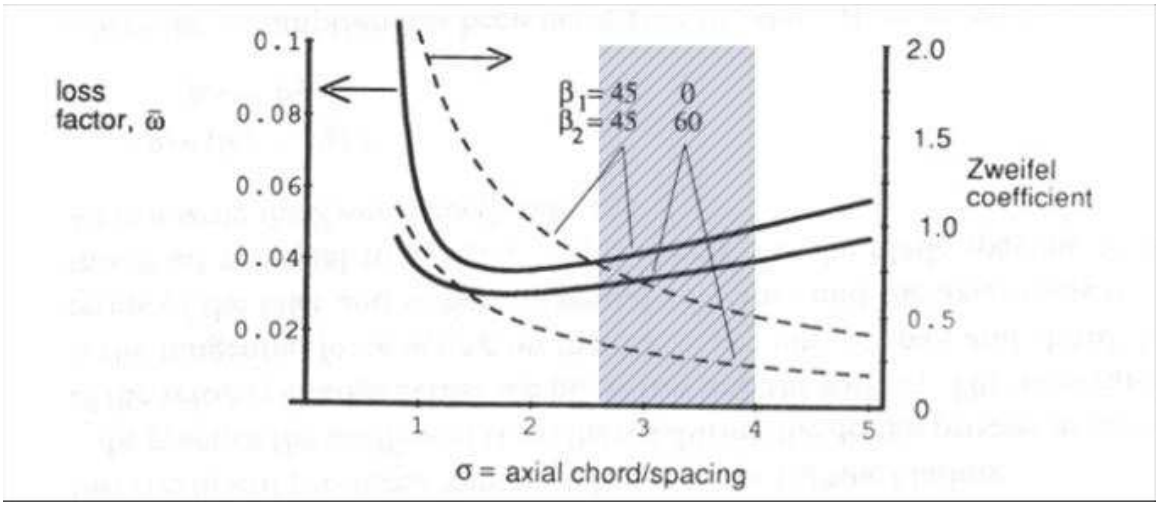

Figure 5-7: Loss factor and Zweifel coefficient as a function of axial chord to spacing for two types of turbine vanes. Design range is shaded. The plot suggests that a turbine vane with inlet and exit angles of 0° and 60°, respectively, and axial chord-to-spacing ratios of 2.6 to 4 has sufficient Zweifel coefficient and reasonably low losses. Figure adopted from Kerrebrock [47]

of the duct described in Section 5.3.1. Solidity is defined as vane chord divided by spacing. The solidity varies monotonically from 3 at the tip to 4 at the hub. The axial chord divided by spacing varies from 2.6 at the tip to 4 at the hub. As depicted in Figure 5-7 adopted from Kerrebrock [47], the solidity range suggests low profile losses, as well as low Zweifel coefficient [98], i.e., blade loading. Low loadings ensure that the flow is properly turned within the vane passage, with minimal deviation.

5.3.3 Three Dimensional CFD Computations

The swirl vane and nacelle/centerbody design completes the geometric definition of the various swirl tubes. A preliminary indication of swirl tube drag coefficient is obtained from MTFLOW assuming an inviscid, axisymmetric flowfield. As the vortex core region of the swirling exhaust flow is affected by viscosity and is turbulent at high Reynolds numbers, higher fidelity modeling is warranted to improve the predicted drag and flowfield ahead of experiments. Engine-scale, single passage periodic, steady CFD computations are performed using Fluent for the subset of swirl tubes in Table 5.1 with maximum local vane angles of 34°, 47°, 53°, 57°, and 64°. The objectives of the CFD computations are to: 1) predict which swirl vane angles result in vortex breakdown, 2) compare the 3D single passage periodic flow fields to MTFLOW to validate the preliminary scan of the design space, 3) define the exit flow fields with the effect of viscosity included, and 4) provide a higher fidelity drag estimate for the stable cases.

Computational Method

The standard Reynolds Averaged Navier-Stokes (RANS) $k-\epsilon$ turbulence model is employed in Fluent to capture the effect of turbulent mixing in regions of high shear. Each case is run to between 10,000 and 20,000 iterations to ensure low ($\lesssim 10^{-4}$), decaying residuals in converged cases (stable flow), and numerically stable (unchanging) residuals in unconverged cases (vortex breakdown). It is found that the cases with 34°, 47°, and 53° swirl vane angle converge, while the cases with 57° and 64° swirl vane angle do not converge due to formation

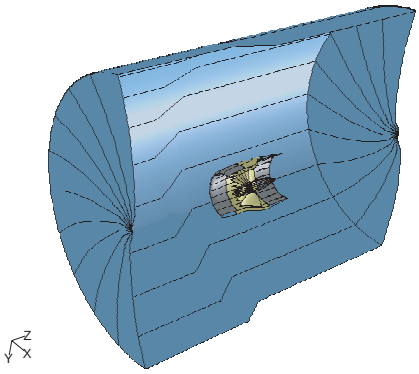

(a) Swirl tube (gray and gold) and outer domain pressure far-field boundaries (blue) shown.

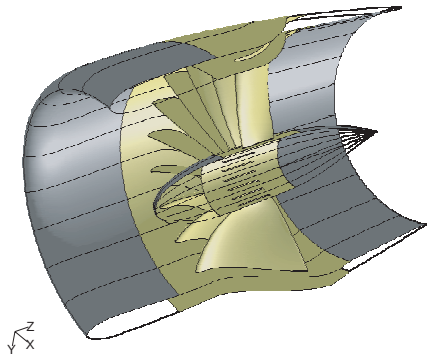

(b) Zoomed-in view of Figure 5-8(a) showing one-half of swirl tube wall geometry (nacelle in gray, vanes in gold).

Figure 5-8: Typical CFD domain replicated to show ten periodic passages.

of a centerline separation bubble indicative of vortex breakdown.

A full-scale geometry is selected to simulate high Reynolds numbers seen in practical use. The outer diameter of the swirl vanes is set to 2.16 meters, comparable to the preliminary fan diameter of the CMI SAX conceptual aircraft powerplant or a large commercial fan engine on a conventional civil airliner.

Computational domains are single passage periodic based on twenty vanes (wedges of 18°), and include the internal and external flow field, to capture the forces on the vanes and the nacelle forces that arise from spillage. The first computational domain generated for the case with 34° vane angle extends roughly 4.5 nacelle lengths upstream and downstream of the vane stacking station ($z = 0$). The outer domain is located roughly 2 nacelle lengths from the centerline. All computational grids have approximately 1.2 million cells. As flow profile non-uniformities and centerline gradients increase with swirl angle, it is found that a substantial increase in axial grid resolution is required to ensure convergence. In order to keep the total number of grid cells approximately constant, the downstream domains of all cases except the 34° swirl vane angle are reduced to be the same as the MTFLOW computational domain, namely, 2 nacelle chords lengths upstream and 3 nacelle chords downstream of the

vane stacking station. The outer domain is also located 2 nacelle chords from the centerline. Figure 5-8(a) shows the smaller domain bounds used for all swirl tube cases except 34°, and Figure 5-8(b) presents an enlarged view of one-half of a typical swirl tube to give the reader an indication of the relative dimensions of the nacelle/centerbody and swirl vanes. The axial direction is indicated by the z-axis. The half-geometries are generated by nine periodic replications of the CFD domain, as indicated by the solid black lines.

The upstream, downstream, and outer radial boundary conditions are set to pressure far-field in Fluent, with Mach number equal to 0.17 and the freestream direction set to positive z. Ambient density is based on a representative approach altitude. Rotationally periodic boundaries are 18° apart and are bounded by the three pressure far-field boundaries. Although the domain extends to the centerline, a specific centerline boundary condition is not required. The surfaces of the swirl vane, the nacelle and the centerbody are modeled as adiabatic walls.

Flowfield Comparison Between Stable (47° Swirl Angle) and Vortex Breakdown (57° Swirl Angle) Cases

Figures 5-9 through 5-11 present flow field comparisons between the 47° and 57° swirl vane angle cases. The figures compare Mach number (M), swirl parameter (S), and pressure coefficient (C_p), respectively. The Mach number comparison demonstrates that vortex breakdown occurs between the swirl vane angles of 47° and 57°. Numerically, the breakdown manifests itself as a separation bubble on the centerline very close to the duct exits. As these are steady single passage periodic computations based on 20 vanes, one would only expect the three-dimensionality of the unsteady breakdown flow field to be captured qualitatively. The CFD computations give an idea of the size and extent of the separation bubble. The swirl parameter comparison of Figure 5-10 suggests that the critical swirl parameter for vortex breakdown is close to 1.2, consistent with other studies on the vortex breakdown phenomenon [6, 16] and results shown in Figure 5-4 for $r_{crit}/r_f = 0.7$. The pressure coefficient distribution, C_p, suggests that the maximum pressure defect is roughly 3.5 times the

freestream dynamic head. In the exit flow field the pressure defect gradually decreases in the streamwise direction for the stable case of 47° swirl vanes, while a more abrupt reduction of C_p defect occurs at the separation bubble – analogous to the abrupt change across a hydraulic jump or a one-dimensional compressible shock wave undergoing transition from super- to sub-critical state.

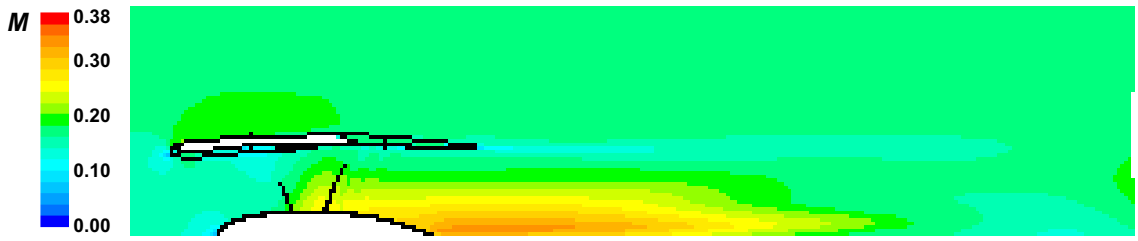

(a) 47° swirl vanes.

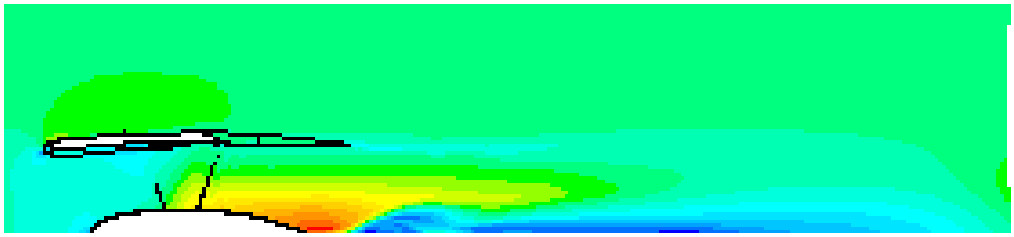

(b) 57° swirl vanes.

Figure 5-9: Mach number on periodic boundary of CFD cases.

Figure 5-12 shows the pressure coefficient distribution over the swirl tube surfaces for the 47° swirl angle case. No adverse pressure gradient occurs along the vanes in the streamwise direction, suggesting the vane design methodology is sound. It is also apparent that the stagnation point occurs at the drooped nacelle leading edge, validating the selection of droop angle and inlet design. A downstream plane located at 0.5 nozzle exit diameters downstream of the trailing edge shows the radial extent of the pressure defect in the swirling flow.

Overall, the flow field and surface pressure comparisons indicate that:

- the flow regime transitions from stable, steady swirling flow to unsteady vortex breakdown between swirl vane angles of 47° and 57°.
- the vortex breakdown separation bubble occurs near the duct exit, suggesting adverse

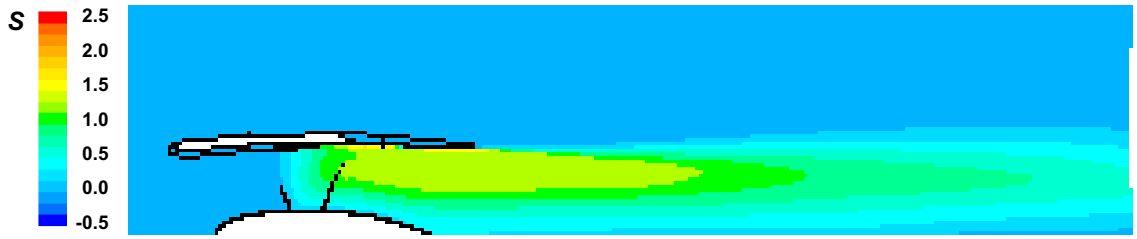

(a) 47° swirl vanes.

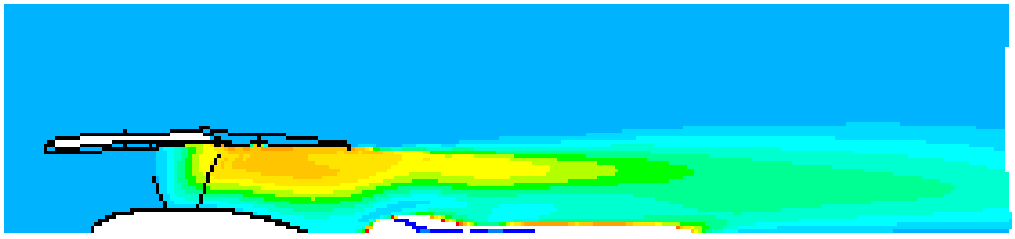

(b) 57° swirl vanes.

Figure 5-10: Swirl parameter on periodic boundary of CFD cases.

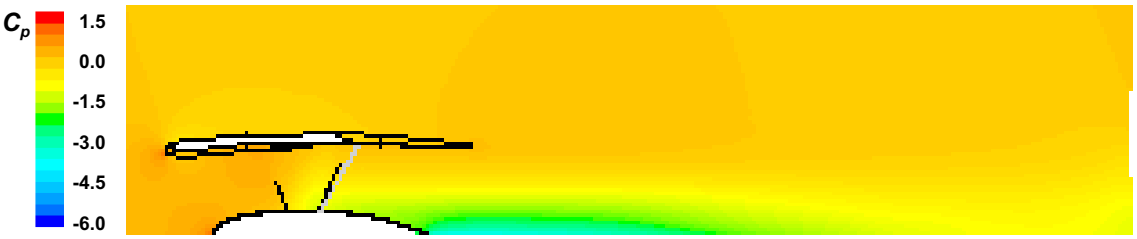

(a) 47° swirl vanes.

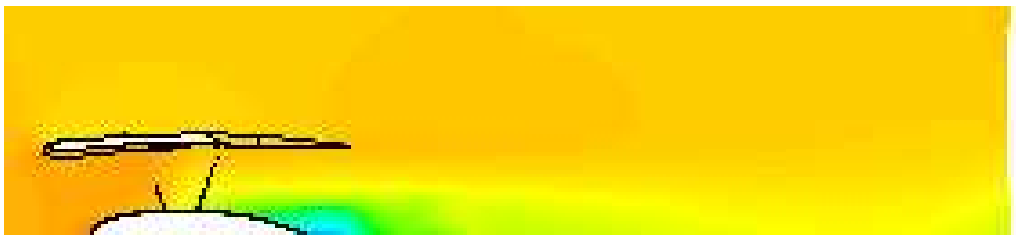

(b) 57° swirl vanes.

Figure 5-11: Pressure coefficient on periodic boundary of CFD cases.

acoustic implications from increased unsteadiness in the vicinity of solid surfaces and edges.

- the computations confirm that the swirl parameter of about 1.2 is a good indicator of vortex breakdown for this type of flow.

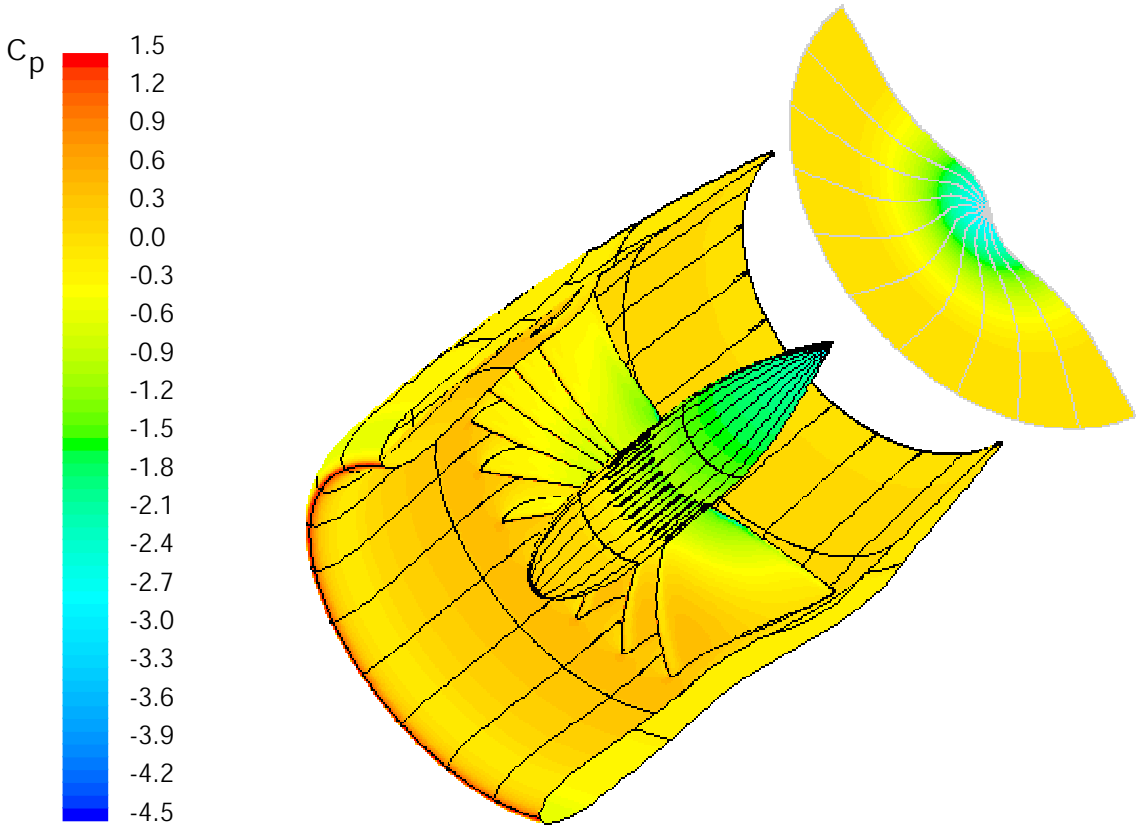

Figure 5-12: Pressure coefficient, C_p, on surfaces of swirl tube with 47° vane angle show low pressure at vane hub and aft centerbody. Radial extent of pressure defect is seen in plane 0.5 duct diameters downstream of exit. Maximum pressure defect in downstream plane is $C_p \approx -3.5$.

- the maximum pressure defect of 3.5 dynamic heads for the 47° and 57° swirl vane angle cases suggests that the maximum achievable drag occurs near these swirl angles, and that the 47° design will be most favorable in terms of drag and acoustics.

Comparison to MTFLOW

CFD computed radial profiles of Mach number, pressure coefficient, swirl angle, and (rv_θ) are compared in Figure 5-13 at the duct exit for the swirl tube with 47° vanes. The inviscid, axisymmetric flow approximation employed in the MTFLOW cases agrees well with CFD for each of the radial profiles, validating the preliminary design methodology using MTFLOW.

Expected discrepancies occur near the outer radius and the centerline, because CFD captures the viscous effects at the endwall boundary layer and the vortex core. One erroneous numerical feature that turns out to have little effect on the overall flow field is the finite swirl angle on the centerline in the CFD solution. As this occurs at $r^* \lesssim 0.1$, pressure forces in

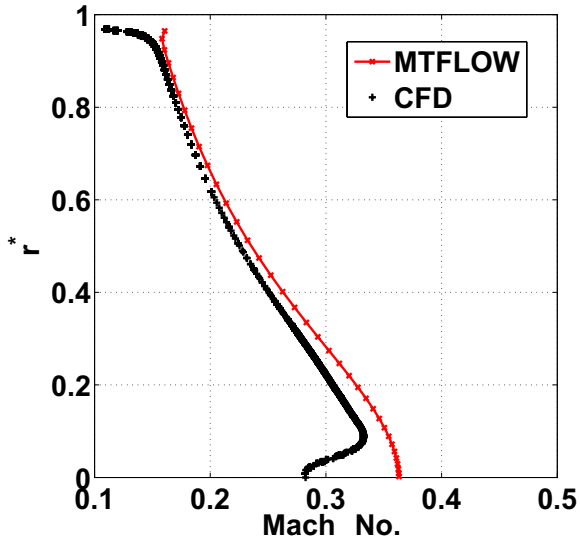

(a) Mach number radial profile.

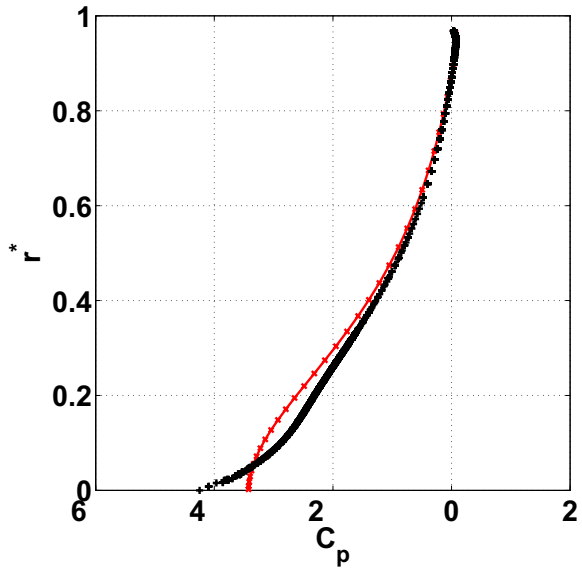

(b) Pressure coefficient radial profile.

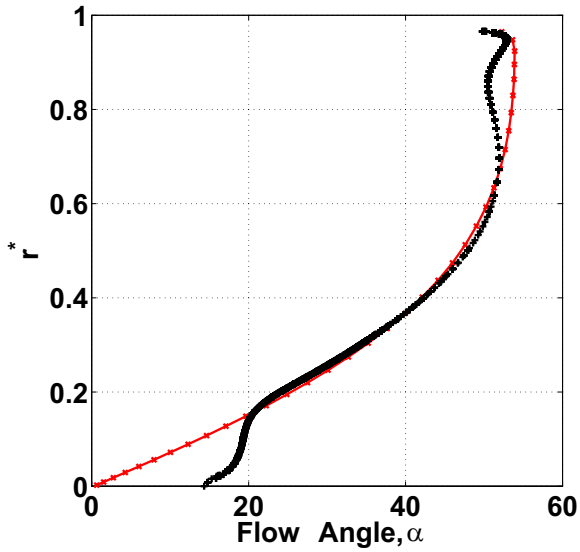

(c) Swirl angle radial profile.

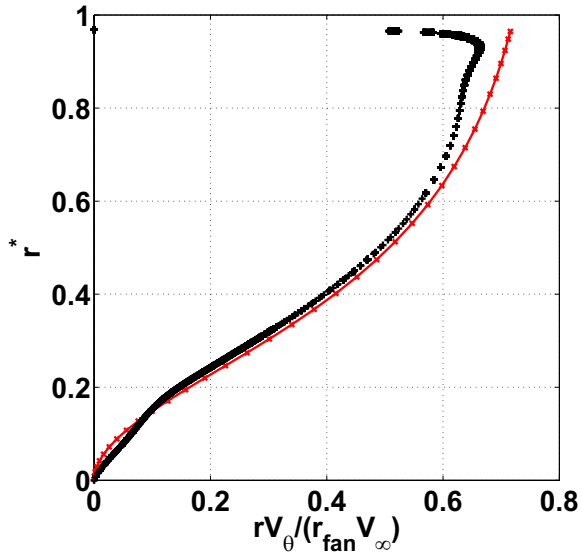

(d) Circulation radial profile.

Figure 5-13: MTFlow vs CFD comparisons for case with 47° swirl vanes.

	MTFLOW	CFD				
α_{max}	C_D	C_D	$C_{D,\text{press.}}$	$C_{D,\text{visc.}}$	Vortex Breakdown	Convergence
34°	0.40	0.39	0.32	0.07	No	Yes
47°	0.80	0.75	0.68	0.07	No	Yes
53°	1.00	0.84	0.77	0.07	No	Yes
57°	1.10	0.89	0.82	0.07	Yes	No
64°	1.31	0.94	0.38	0.06	Yes	No

Table 5.2: MTFLOW vs. CFD drag coefficient comparison. Total drag coefficient is given by C_D. Pressure and viscous drag coefficients are given as $C_{D,\text{press.}}$ and $C_{D,\text{visc.}}$, respectively.

this region only act over $\lesssim 1\%$ of the duct area, and have little effect on the CFD-predicted drag.

Table 5.2 compares the computed drag coefficient from MTFLOW to the CFD. For stable cases, there is some drag coefficient discrepancy between the two methods, because the MTFLOW computations do not include viscous drag components, whereas the CFD does. In general, the MTFLOW drag estimates are higher than the CFD. This is not unreasonable, as examination of the exit profile of C_p in Fig 5-13 shows a greater pressure defect in the MTFLOW cases on the annulus between 5 and 30 percent exhaust duct radius. The CFD computations do show greater pressure defect at the core below 5 percent exhaust duct radius, but this acts over a relatively small area (35 times smaller than the aforementioned annulus). As vortex breakdown is inherently unsteady, the steady CFD drag predictions are not quantitatively meaningful for the two highest swirl vane angle cases.

In summary, MTFLOW is a useful preliminary design tool that captures the pressure-driven regions of the swirling flow field accurately, and provides streamline exit angles for three-dimensional vane design. CFD provides the best preliminary estimate of vortex breakdown onset, and suggests qualitatively the extent of the vortex breakdown separation bubble. CFD also gives the most accurate pre-test prediction of drag levels and exit flow fields, accounting for viscous and turbulence effects. This completes the aerodynamic design of the various swirl tubes and leads to wind tunnel validation testing presented in the next section.

5.3.4 Model Scale Wind Tunnel Testing

Scale-model aerodynamic tests are next performed in the MIT Wright Brothers Wind Tunnel (WBWT). The primary test objective is to validate the aerodynamic design. This requires 1) flow visualization to identify swirl angles at which vortex breakdown occurs, 2) measurement of exit flow field velocity profiles using hot-wire anemometry, and 3) measurement of drag using a load cell and comparison to CFD computed values. Measured drag may also be inferred by integration of steady velocity profiles obtained through hot-wire anemometry (for the stable flow cases).

A second test objective is to determine potential noise sources, to guide the subsequent acoustic tests. This is accomplished by taking unsteady hot-wire measurements in the swirling flow downstream of the duct exit and identifying regions of unsteadiness that may correspond to potential quadrupole noise sources, i.e., ones that arise from turbulence in open flows [18, 49, 50].

The full test matrix consisting of smoke and oil flow visualization, drag measurements, and steady and unsteady hot-wire measurements in the flow field downstream of the nozzle exit is shown in Table 5.3. A selected subset of the results is shown in this thesis. Details of the entire test, including a facility description, are provided in Mobed [61].

Test Article

A picture of the swirl tube mounted in the WBWT is shown in Figure 5-14. The outer diameter of the model swirl vanes is 7.036 inches (0.179 meters), i.e., at 12:1 scale relative to the full-scale CFD diameter of 2.16 meters. Nacelle and centerbody parts are fabricated from aluminum, and plastic swirl vane sub-assemblies have been fabricated using stereo lithography (SLA). The SLA parts are designed as a one-piece annular cascade of 20 vanes with integral inner (hub) and outer (nacelle) walls. The outer walls have forward and aft flanges to smoothly mate in a modular fashion with the forward and aft nacelle parts. This vaned disk enables easy interchanging of different swirl tube geometries. The swirl tube is mounted on an airfoil shaped pylon designed to transmit loads to a force and moment

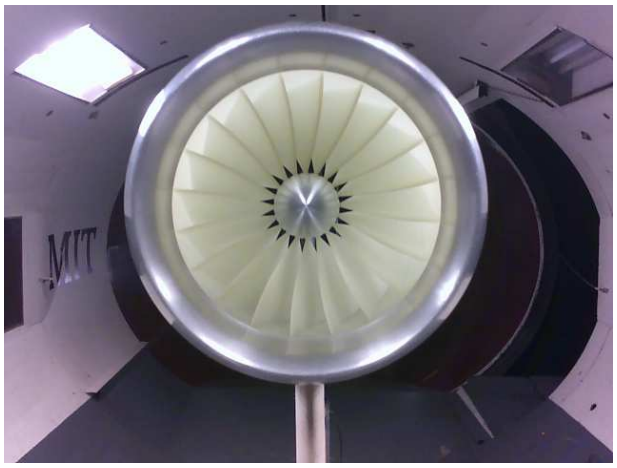

(a) Forward looking aft view of MIT Swirl Tube.

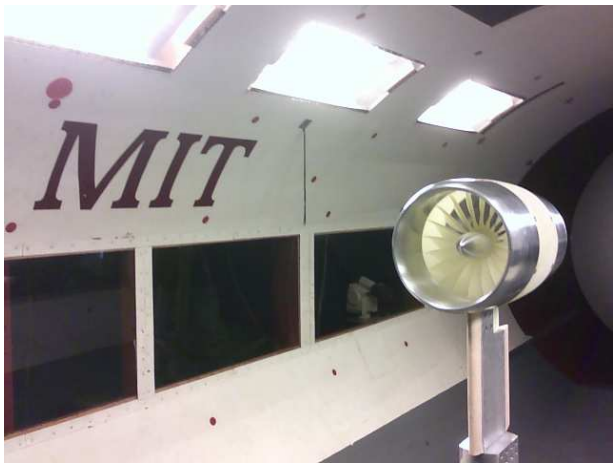

(b) Swirl tube in WBWT.

Figure 5-14: WBWT wind tunnel experimental set-up.

balance located underneath the wind tunnel floor. Boundary layers are tripped by applying tape with forward facing serrations near the leading edges of the vanes, inner and outer nacelle, and pylon, to ensure fully turbulent flow, as expected in full-scale device operation. Details of the mechanical design are found in Mobed [61].

	$M = 0.06$	$M = 0.06$	$M = 0.03 - 0.17$	$M = 0.03$	$M = 0.11$
Configuration	Steady Velocity (Hot-wire)	Unsteady Velocity (Hot-wire)	Drag (Load Cell)	Smoke Visualization	Surface Oil Visualization
Pylon Only			×		
Empty Nacelle			×		
0° Blisk			×		
34° Blisk	×	×	×	×	×
41° Blisk			×	×	
47° Blisk	×	×	×	×	×
53° Blisk			×		
57° Blisk	×	×	×	×	×
64° Blisk	×	×	×	×	×

Table 5.3: WBWT test matrix.

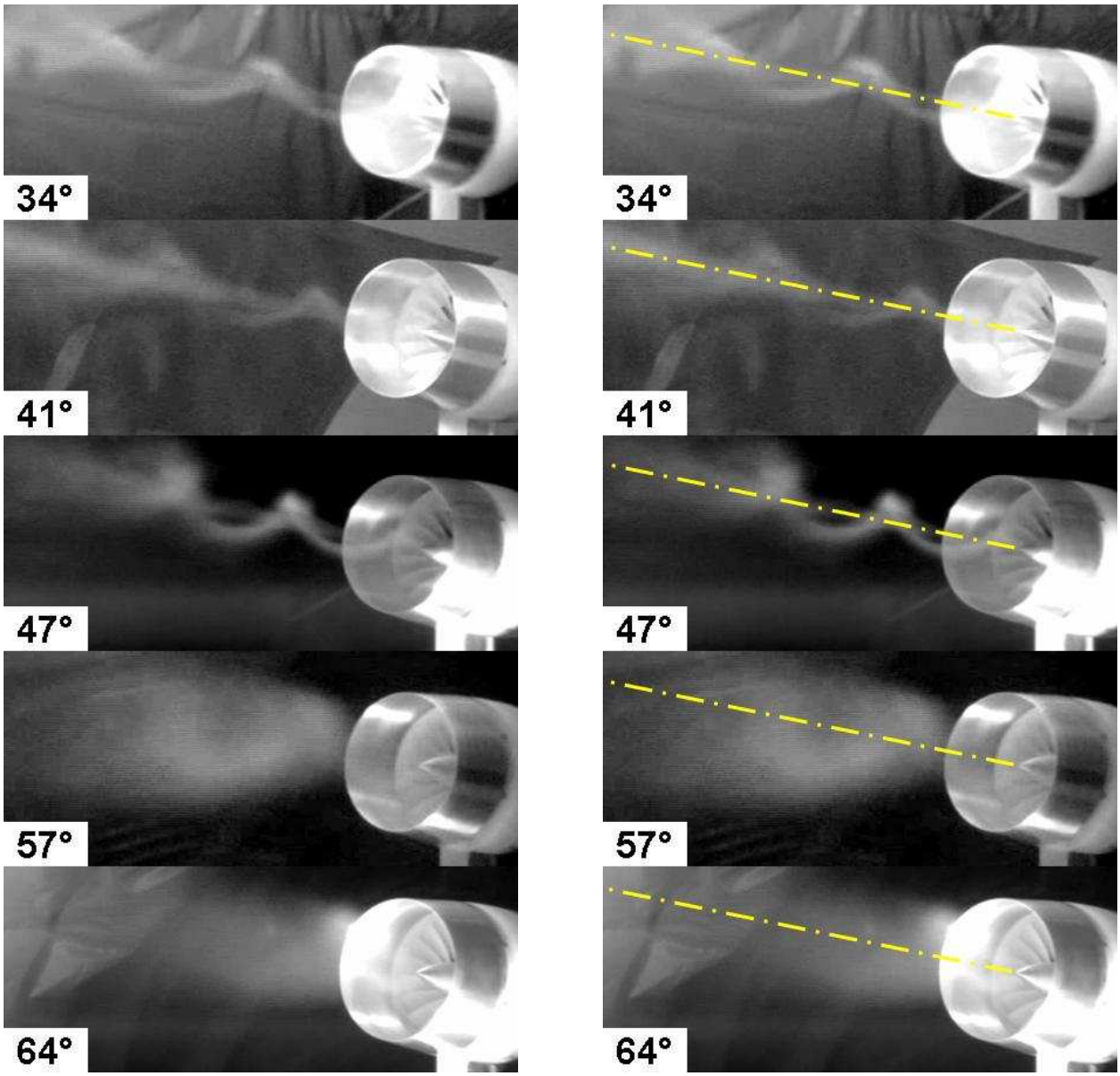

(a) Smoke visualization.

(b) Identical image as (a) with centerlines superimposed to indicate core axial smoke streak.

Figure 5-15: Flow visualization close to the centerline axis identifies a coherent vortex core within a steady swirling flow for the stable flow cases (34°, 41°, and 47° swirl vanes) and a large unsteady core for the cases with vortex breakdown (57° and 64° swirl vanes).

Flow Visualization

Instantaneous flow visualization images acquired at 30 frames per second for swirl tube vane angles of 34°, 41°, 47°, 57°, and 64° are presented in Figs. 5-15 and 5-16. Smoke is injected

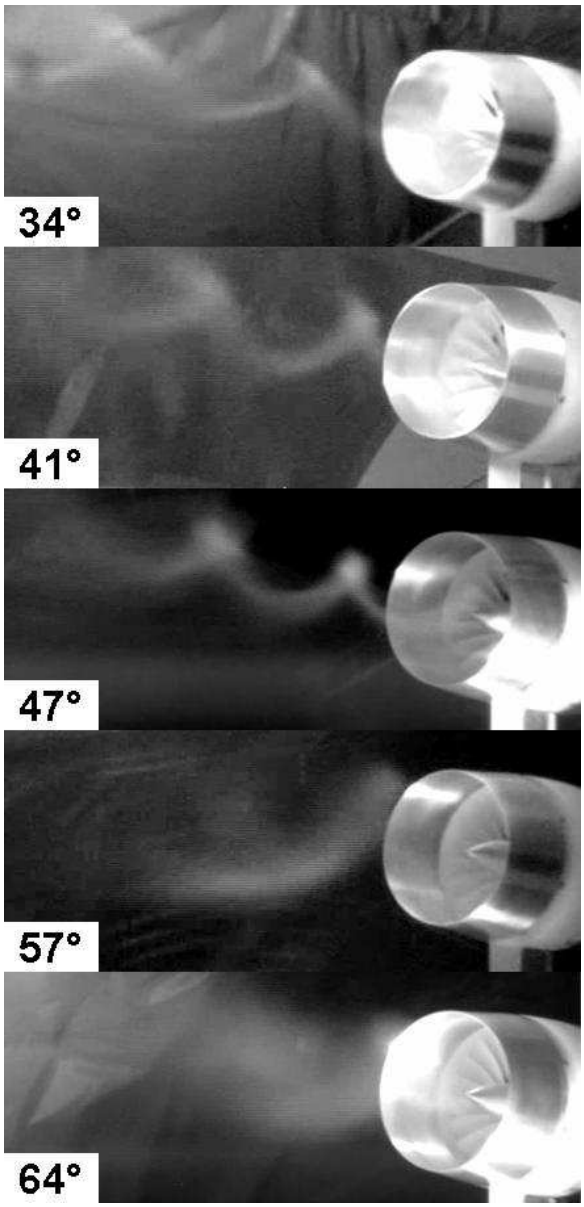

(a) Smoke visualization.

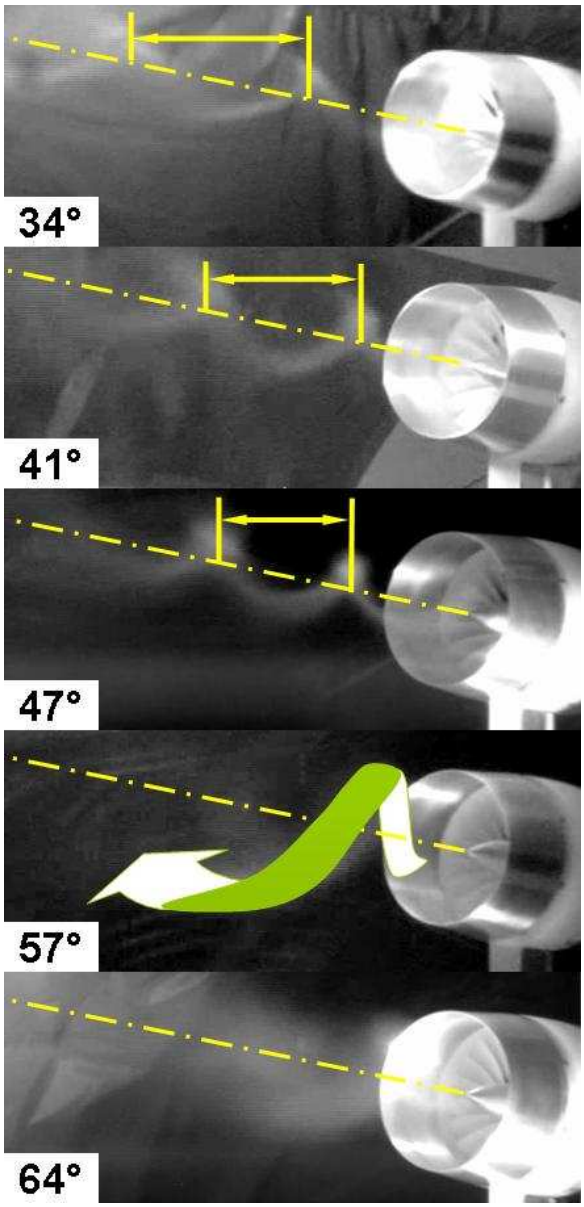

(b) Identical image as (a) with wavelength estimate for pre-breakdown cases indicative of flow angle and graphic representation of outer swirling flow for vortex breakdown cases.

Figure 5-16: Flow visualization at the outer radius identifies a tightly spiraling, steady swirling flow for stable cases (34°, 41°, and 47° swirl vanes) and indirectly infers an outer coherent swirling flow for vortex breakdown cases (57° and 64° swirl vanes).

via a hand-held heated wand that vaporizes liquid glycol upstream of the swirl tube. As flow is essentially incompressible ($M_\infty \leq 0.17$) and weakly Reynolds number dependent at

all test points, dynamic similarity allows selection of a low freestream velocity ($\sim$ 20 m/s) to minimize turbulent diffusion of the smoke streakline. By moving the smoke injection location radially, the dynamics of the swirling flow both near the vortex core and in the outer annular areas are revealed. The two figures show instantaneous smoke streaklines in the core region and at outer radial locations, respectively.

In the core region the smoke streaklines for the 34°, 41°, and 47° swirl vane cases clearly show a straight line of smoke on the axis of symmetry, surrounded by a tightly coiling helical smoke trail around the core. From this one can infer that the core in these stable cases is a coherent, tightly swirling flow structure. The fact that the line of smoke appears straight at the centerline stems from the fact that the Burger vortex-like rv_θ distribution selected to generate the vane exit angles has zero turning at the hub, such that the low momentum fluid that is in the boundary layers of the centerbody and vanes near the hub exits the swirl vanes axially. The vanes are designed to turn the flow significantly just a short distance away from the hub, such that the helical smoke streakline wraps itself tightly around this core. The flow visualization for cases with 57° and 64° swirl vanes clearly shows a device-scale, cloud-like smoke pattern just downstream of the exit, indicative of bubble-type vortex breakdown[6], in good agreement with CFD predictions presented earlier in Figure 5-9.

Smoke visualization at the outer radial locations in Figure 5-16 reveals the outer flow dynamics. For example, the wavelength of the helical coil formed by the streaklines in the stable cases becomes shorter as the swirl angle increases, as expected. The instantaneous picture of the 57° case shows what appears to be coherent outer swirling flow around the burst vortex. Although it is difficult to visualize in the instantaneous images presented in the thesis, it becomes apparent when viewing the image series at 30 frames per second. The graphic in the right column of the 57° swirl vane case qualitatively describes the streakline shape of the coherent outer swirling flow.

The flow visualizations confirm that the steady, single passage periodic domain CFD captures the onset of vortex breakdown. In the next section experimentally measured velocity profiles from the swirling exhaust flow are compared to CFD to quantitatively assess the

[6]see Section 4.4.3

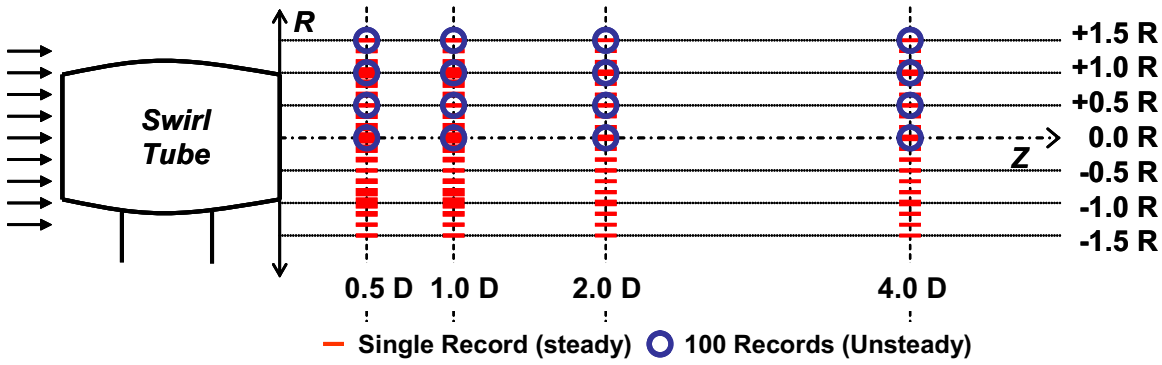

Figure 5-17: Hot-wire traverse locations for steady and unsteady measurements. All measurements are taken in the vertical plane that passes through the swirl tube centerline.

accuracy of the predictions.

Hot-wire Anemometry

Steady and unsteady velocity measurements are made in the vertical plane passing through the swirl tube centerline using hot-wire probes at locations depicted in Figure 5-17. Unsteady axial and circumferential velocity signals are obtained by orienting the probe's wire perpendicular to these respective directions, under the assumption of zero radial velocity component, i.e., simple radial equilibrium. Each time record is sampled at 40 kHz with a total of 16,384 points, resulting in a sampling time of $25\mu s$ and an overall record length of 0.4096 seconds. For steady measurements, the average value of single records are computed along radial traverses at axial stations of 0.5, 1.0, 2.0, and 4.0 nozzle diameters downstream of the nozzle exit. For unsteady measurements, the power spectra of 100 consecutive records are computed at 0.0, 0.5, 1.0 and 1.5 nozzle radii at the same axial stations. All hot-wire measurements are made at a freestream Mach number of 0.06. Further details of the hot-wire experimental procedure are provided in Mobed [61].

Steady Velocity Measurements. Figs. 5-18 to 5-20 compare CFD predicted and experimentally measured values of dimensionless axial and circumferential velocity, along with computed swirl angle, for the 34°, 47°, and 57° swirl vane cases, respectively, at axial sta-

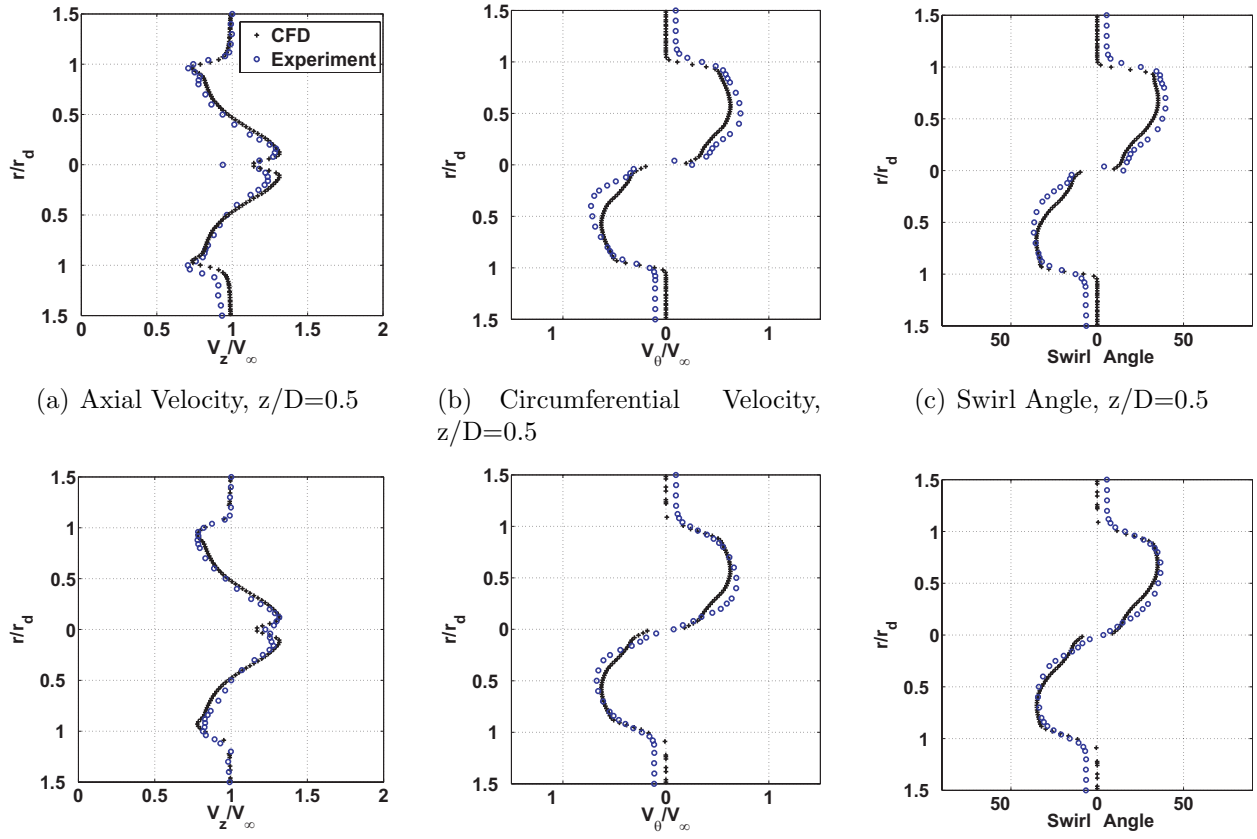

(a) Axial Velocity, z/D=0.5

(b) Circumferential Velocity, z/D=0.5

(c) Swirl Angle, z/D=0.5

(d) Axial Velocity, z/D=2.0

(e) Circumferential Velocity, z/D=2.0

(f) Swirl Angle, z/D=2.0

Figure 5-18: Axial velocity, circumferential velocity, and computed swirl parameter (S) vs. radial location for case with 34° swirl vanes. Top row, $z/D = 0.5$, bottom row $z/D = 1.0$.

tions $z/D = 0.5$ (top row) and 1.0 (bottom row). The experimental measurements for the stable cases (34° and 47°) show good agreement with CFD. The size and shape of the viscous core are well captured. The computed swirl angle measurements are favorable, though slight overturning of several degrees appears to be a feature of the stable cases at $z/D = 0.5$. Maximum stable duct exit swirl angles of about 50° are achieved in the 47° swirl vane case.

In the 47° swirl vane angle case, the location of the vortex center appears to be below the geometric centerline at $z/D = 0.5$, and slightly above the geometric centerline at $z/D = 1.0$. When compared to the 34° and 57° swirl vane cases this asymmetry is striking. It is not clear whether this is due to a slight error in the radial positioning of the hot-wire probe or a physically displaced vortex center. A possible conjecture is that the flow is near the onset

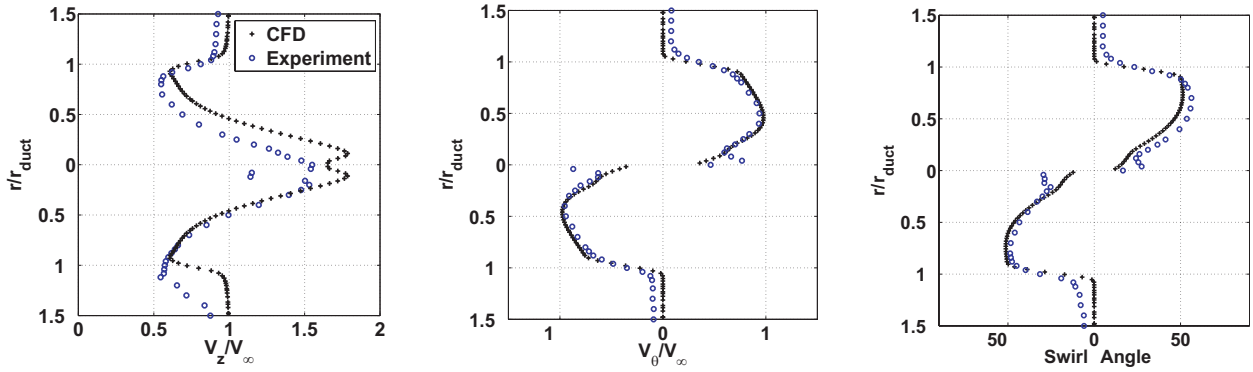

(a) Axial Velocity, z/D=0.5

(b) Circumferential Velocity, z/D=0.5

(c) Swirl Angle, z/D=0.5

(d) Axial Velocity, z/D=2.0

(e) Circumferential Velocity, z/D=2.0

(f) Swirl Angle, z/D=2.0

Figure 5-19: Axial velocity, circumferential velocity, and computed swirl parameter (S) vs. radial location for case with 47° swirl vanes. Top row, $z/D = 0.5$, bottom row $z/D = 1.0$.

of the vortex breakdown instability, where a standing wave, or perhaps a minor precession of the vortex core offsets its center of rotation from the axis of symmetry, as depicted by the laminar spiral vortex breakdown images in Figure 4-11. This conjecture warrants further investigation because the acoustic spectrum of the 47° swirl vane case presented in Section 5.4.2 has a shape that may be indicative of the flow regime cross-over between stable, swirling flow and vortex breakdown.

The 57° swirl vane angle case suggests that there is coherent swirling flow at the outer radial locations, at indicated by the qualitatively well captured axial and circumferential velocity profiles between 0.75 and 1.0 radii at both axial stations. At lower radii, there is disagreement, indicative of the size and presence of a vortex breakdown separation bubble,

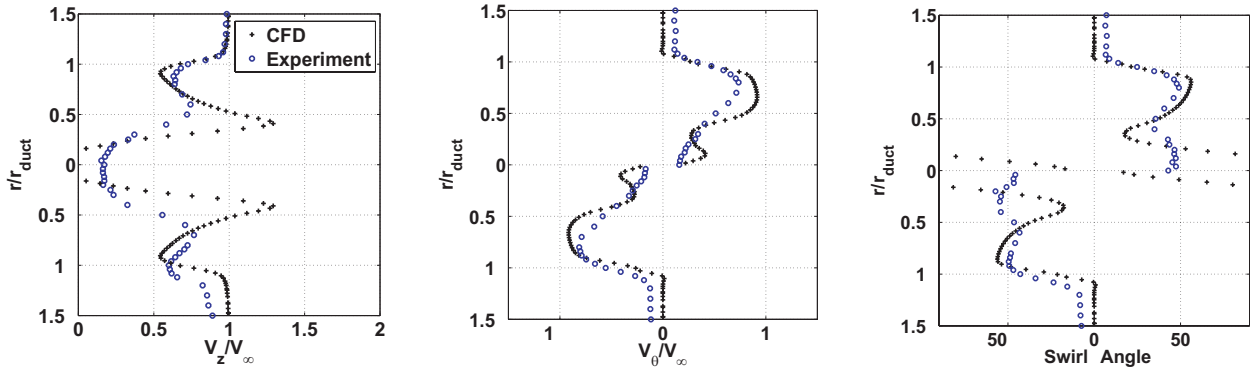

(a) Axial Velocity, z/D=0.5

(b) Circumferential Velocity, z/D=0.5

(c) Swirl Angle, z/D=0.5

(d) Axial Velocity, z/D=2.0

(e) Circumferential Velocity, z/D=2.0

(f) Swirl Angle, z/D=2.0

Figure 5-20: Axial velocity, circumferential velocity, and computed swirl parameter (S) vs. radial location for case with 57° swirl vanes. Top row, $z/D = 0.5$, bottom row $z/D = 1.0$.

and consistent with flow visualization in Figs. 5-15 and 5-16. This disagreement stems from the fact that the flow in the separation bubble is highly unsteady and does not satisfy simple radial equilibrium, making the hot-wire probe unable to identify the mean flow direction below $r/r_d \sim 0.75$.

Taken in toto, the steady hot-wire measurements quantitatively validate that CFD computations accurately describe the stable flowfield in the near exhaust ($z/D \lesssim 1.0$), and qualitatively confirm the nature of the bubble-type vortex breakdown.

Power Spectra of Unsteady Velocity Components. Figure 5-21 presents power spectra of the unsteady axial and tangential velocity components one diameter downstream of

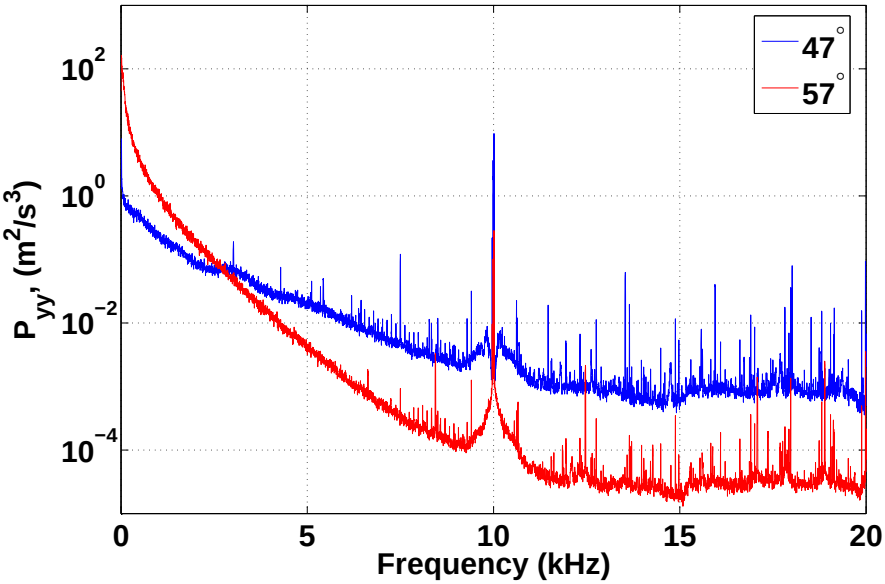

(a) P_{yy} of unsteady axial velocity, V_z

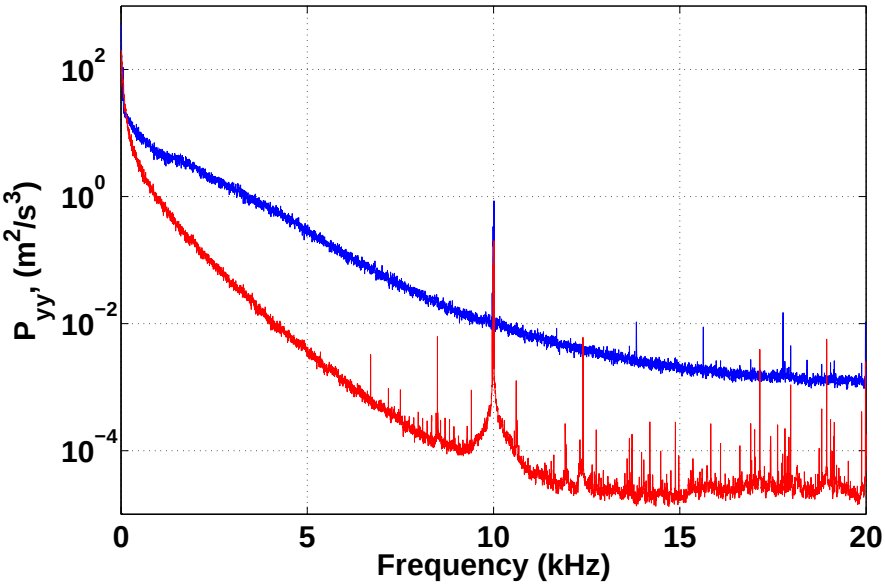

(b) P_{yy} of unsteady circumferential velocity, V_θ

Figure 5-21: Power spectra of unsteady axial and tangential velocity in core region, $r^* = 0$, at axial location one diameter downstream of nozzle exit, $z/D = 1.0$. Data is presented at constant bandwidth of 2.44 Hz.

the duct, $z/D = 1.0$, in the core region of the flow, i.e., the swirl tube centerline, $r^* = 0$. Similar power spectra in the shear layer region, i.e., $r^* = 1$, are presented in Figure 5-22.

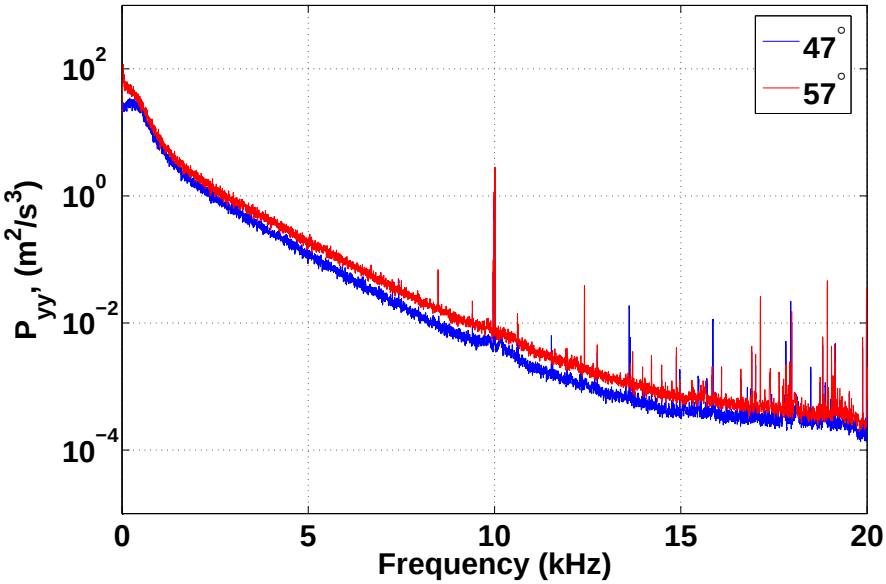

(a) Axial velocity, V_z^2

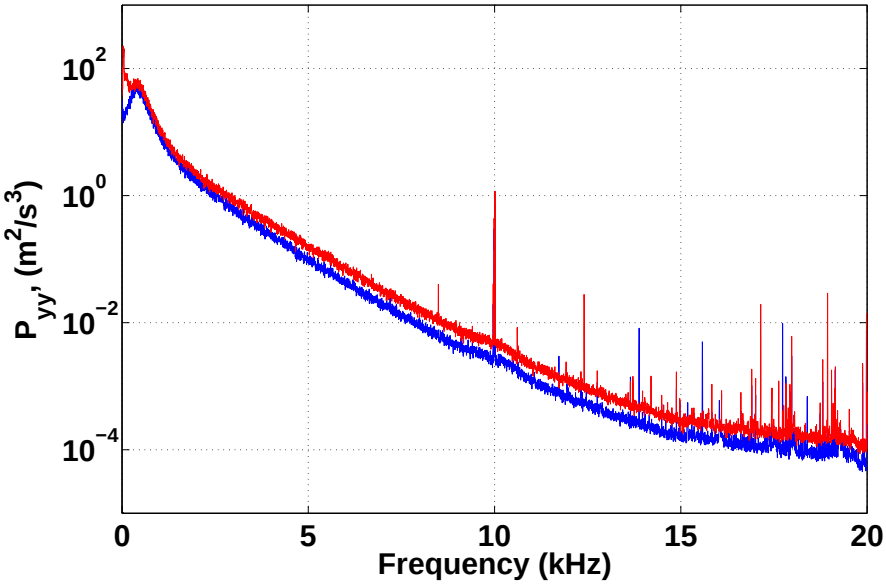

(b) Circumferential velocity, V_θ^2

Figure 5-22: Power spectra of unsteady axial and tangential velocity in shear layer region, $r^* = 1$, at axial location one diameter downstream of nozzle exit, $z/D = 1.0$.

As the downstream location is far from the surfaces of the swirl tube, the power spectra are suggested to provide guidance about the presence of possible quadrupole noise sources,

i.e., ones arising from turbulence in open flow. The wind tunnel is set to a freestream Mach number, M_∞, of 0.06 during the data acquisitions[7]. Power spectra of both velocity components are included because there is no a priori knowledge of whether the turbulence has any preferred direction. The spectra are presented in linear narrowband format at a constant bandwidth of 2.44 Hz.

At frequencies below 10 kHz, velocity power spectra are generally broadband in nature. At 10kHz a spike appears in all cases and at both radial locations and axial locations. This spike is likely to be spurious electrical noise, as it does not match any expected Strouhal numbers (based on device length scales) or measurement apparatus natural frequencies. At frequencies above 10 kHz, many of the spectra appear to have additional sharp tones. These are also likely to be spurious, as acoustic spectra presented in Section 5.4.2 at similar Strouhal number suggest primarily broadband acoustic sources at high frequencies.

The spectra between the stable flow and vortex breakdown cases compare differently in the core (Figure 5-21) and shear layer (Figure 5-22) regions. On the core the stable swirling flow case (47° swirl vanes) has levels of spectral energy that are generally at least one order of magnitude greater than corresponding spectra of the vortex breakdown case (57° swirl vanes). The tangential velocity power spectrum of the 47° swirl vane case suggests greater acoustic energy than the corresponding 57° swirl vane case spectrum at all frequencies. The axial velocity power spectrum of the 47° swirl vane case suggests lower acoustic energy at low frequency, but greater acoustic energy at high frequency. Spectral comparisons at axial stations $z/D = 0.5$ and $z/D = 2.0$ are in accord with these observations. This suggest the possible presence of a more pronounced quadrupole source on the core in the case of the stable swirling flow versus the vortex breakdown flow, especially at the highest frequencies.

In the shear layer the level of spectral energy is similar between the two cases, though slightly stronger for the case with 57° swirl vane angle. Although the velocity profile varies between cases, the shear layer power spectra do not vary greatly, suggesting that the shear

[7]As a reference to the reader, a Strouhal number of unity based on this velocity (near room temperature) and swirl tube exit diameter is close to 100 Hz. In Section 5.4.2 most acoustic spectra are presented for $M_\infty = 0.17$, implying a unity Strouhal number close to 300 Hz.

layer noise may be similar to other known shear layer flows. Overall, the spectra suggest that the core region may have a unique noise signature in the case of the stable, swirling flow, and that the acoustic differences in shear layer region may be less pronounced between the two flows.

It should be noted that overall noise levels are difficult to judge based on the spectra. As will be shown in Section 5.4.2, the vortex breakdown flow noise is much louder ($\sim$ 15 dB) than the stable flow noise, but concentrated at the duct exit (hence not quadrupole in nature), where unsteady data is not taken. Two hypotheses (that will be confirmed in Section 5.4.2) may be drawn from the unsteady spectral comparisons:

1. The noise spectra are largely broadband in nature.

2. The stable, 47° swirl vane angle case is likely to have increased quadrupole noise sources in the core region, relative to the 57° swirl vane angle case with vortex breakdown.

Drag Measurements

Drag is experimentally measured in WBWT for comparison to converged CFD predictions for stable exit flows, and to quantify the swirl tube drag capabilities for stable and vortex breakdown exit flows. The experimentally measured drag coefficient represents an average value of drag coefficients taken at various freestream Mach numbers between $M = 0.06$ and $M = 0.17$. The three key results from the measurements are:

1. Experimentally measured drag coefficient is found to be higher than CFD predicted drag[8] by up to 0.08, but can be plausibly explained by small differences in flow turning observed in the steady velocity profiles taken with hot-wire anemometry.

2. A maximum stable flow model-scale drag coefficient of 0.83 is measured for the 47° swirl vane angle case, demonstrating high drag coefficient ($\gtrsim$ 0.8) for steady swirling outflows. Full-scale drag coefficient estimate based on a Reynolds number correction

[8]Only CFD predictions from converged, stable flow cases are compared to measured cases without vortex breakdown, i.e., 34° and 47° swirl vanes.

	Experiment (model-scale)				CFD (corrected to model-scale)		
Case	C_D	$C_{D,\text{visc.}}$	$C_{D,\text{press.}}$	$C_{D,\text{int.}}$	C_D	$C_{D,\text{visc.}}$	$C_{D,\text{press.}}$
Pylon Only	0.42						
Empty Nacelle	0.08						
0°	0.14	0.14	0.00				
34°	0.52	0.14	0.38	0.48	0.44	0.12	0.32
47°	0.83	0.14	0.69	0.81	0.80	0.12	0.68
53°	0.85	0.14	0.71	V.B.	0.89	0.12	0.77
57°	0.82	0.14	0.68	V.B.	0.94	0.12	0.82
64°	0.76	0.14	0.62	V.B.	0.98	0.10	0.88

Table 5.4: Table of measured and CFD computed drag coefficients for model-scale geometry. All C_D values are referenced to the axially projected swirl vane annulus area. CFD values of viscous drag coefficient, $C_{D,\text{visc.}}$, are corrected to model-scale using Reynolds number correction of Equation 5.4. Pylon drag is shown for reference only, and is subtracted out of all other cases.

suggest drag coefficients of 0.78 and 0.79 for vane outer diameters of 2.16 and 1.20 meters[9], respectively.

3. Maximum drag coefficient occurs near the flow regime change from stable swirling flow to vortex breakdown.

Table 5.4 compares CFD predicted drag coefficients with those obtained experimentally at WBWT. All numbers correspond to model-scale geometry. Direct swirl tube drag measurement is made with the force and moment balance. Pylon alone drag is first measured and then subtracted from the drag of each of the swirl tube test articles, including an empty nacelle and the case with 20 straight vanes (0° turning). The swirl tube experimental drag from the force balance is given by C_D. The measured drag coefficient of the case with 20 straight vanes is estimated to equal the experimental viscous drag coefficient, $C_{D,\text{visc.}}$, for all of the swirl tube cases, as it has similar surface area. The difference between C_D and $C_{D,\text{visc.}}$ is thus assumed to equal the experimental pressure drag, $C_{D,\text{press.}}$

[9] 2.16 meters corresponds to the CFD computations based on the fan diameter of an early variant of the SAX powerplant. 1.20 meters corresponds to the final SAX powerplant fan diameter, and is used for full-scale noise spectral extrapolation in Section 5.4.2

For the stable 34° and 47° swirl vane cases, total drag coefficient is also independently estimated by integration[10] of the hot-wire axial and circumferential velocity profiles at $z/D = 1.0$, assuming the flow satisfies simple radial equilibrium ($v_r = 0$). It is given in the table by $C_{D,\text{int.}}$. Pressure defect integration is a two-step procedure involving a pressure coefficient profile computation followed by pressure drag coefficient computations, as given by the equations of Section 4.4.1. The drag estimate from measured velocity profile integration of the stable cases is consistent to within 0.04 of the drag coefficient values measured on the force and moment balance. The CFD drag coefficient is calculated by force integration over the swirl tube vane, nacelle and centerbody surfaces (C_D). The total drag is made up of a viscous and pressure component, $C_{D,\text{visc.}}$ and $C_{D,\text{press.}}$, respectively, obtained from shear and normal force integration over these surfaces. As CFD is performed at full-scale (12:1 relative to the model), a Reynolds number correction is applied to the viscous drag component based upon turbulent flat plate skin friction coefficient, [77], which is inversely proportional to the 1/5th power,

$$C_f \propto \text{Re}^{1/5} \tag{5.4}$$

The correction suggests that the CFD viscous drag coefficient increases from 0.07 to 0.12 at model-scale.

Figure 5-23 presents measured C_D as a function of swirl vane angle, and compares CFD predicted values for converged, stable flow cases. The figure and Table 5.4 indicate that a higher drag coefficient is measured in the experiment relative to the CFD, for the experimental cases that do not undergo vortex breakdown ($\leq 47°$ swirl vane angle). The drag coefficient measurement error is conservatively estimated at 0.03, based upon the maximum difference between individual drag coefficient measurements at different Mach numbers and the average drag coefficient, for all cases. The discrepancy in drag coefficient is suggested to occur from the slight overturning measured in the steady hot-wire traverses. Overturning is

[10]The station $z/D = 1.0$ is chosen for the integration because it displays good symmetry above and below the centerline ($r/r_{duct} = 0$). Absolute values of V_z/V_∞ and V_θ/V_∞ can then be averaged between the upper and lower profiles. In addition, because the hot-wire probe erroneously measures finite circumferential velocity outside the swirling flow region due to probe vibration, the decision is made to set $V_z/V_\infty = 1$ and $V_\theta/V_\infty = 0$ above $r/r_{duct} = 1.2$.

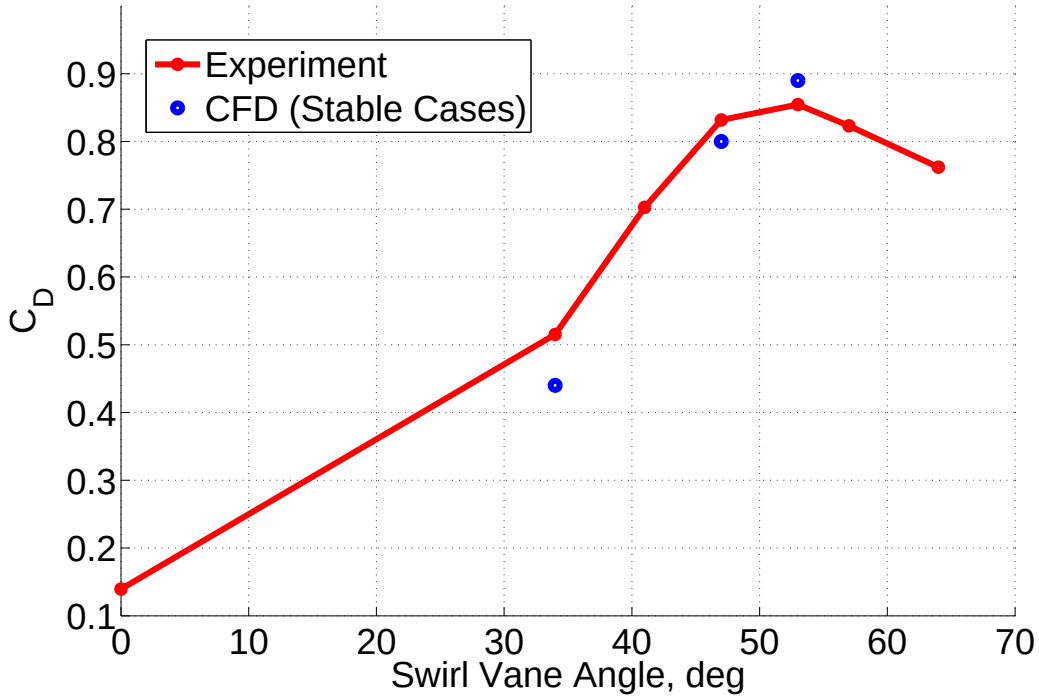

Figure 5-23: Model-scale drag coefficient vs. swirl vane angle shows measured drag coefficient of 0.83 for highest stable flow swirl vane angle (47°). CFD drag coefficient adjusted for model-scale is shown for converged, stable flow cases (34°, 47°, and 53° swirl vane angles).

likely to stem from small differences in the effective loss and blockage between experiment and CFD. For example, slightly lower axial velocity and slightly higher swirl parameters are consistent with increased loss and increased blockage, as discussed in Section 5.3.1.

Experimentally measured drag coefficients validate the hypothesis that the swirl tube can produce a high drag coefficient ($\gtrsim 0.8$) based on through flow area with stable exit flow. In the 47° case, a maximum model-scale drag coefficient of 0.83 is measured. A Reynolds number scale adjustment of the measured model drag coefficient using Equation 5.4 suggests full-scale drag coefficients of 0.78 and 0.79 for vane outer diameters of 2.16 and 1.20 meters, the latter of which is presented for full-scale acoustics spectra in Section 5.4.2.

Finally, the peak measured drag coefficient demonstrates that drag capability drops off at high swirl vane angles ($\gtrsim$ 57°) that correspond to vortex breakdown cases. The likely

cause of this is the flow blockage effect caused by the unsteady separation bubble. A key insight from the experiments is that the optimum drag corresponds to flow that is near the transition to vortex breakdown.

WBWT Test Summary

To conclude this section on the wind tunnel tests, it is worth restating important results that have been found from the experiments:

- The swirl tube is capable of generating a high drag coefficients of 0.83 at model-scale and 0.79 at full-scale (6.7:1) when the flow is stable and has exit swirl angles close to 50°.

- Vortex breakdown is a limiting flow phenomenon that occurs at a critical swirl vane angle ($\gtrsim 57°$), and results in the formation of a device-scale separation bubble near the duct exit. Maximum drag is found to occur at a swirl vane angle near the vortex breakdown threshold, beyond which higher swirl vane angle results in lower drag.

- Swirl tube CFD computations are capable of capturing the stable, swirling flow fields, size of the viscous core, and vortex breakdown threshold. The experiments validate the aerodynamic design process.

5.4 Swirl Tube Acoustics

In this section the acoustics of the swirl tube are presented to confirm the hypothesis that outflows that are steady (i.e., stable) at device-scale have noise signatures that are quiet. The goal of the swirl tube concept is thus achieved by demonstrating that full-scale swirl tube noise signatures fall below the background noise of a well populated area in the vicinity of an airport.

Noise from the swirl tube represents a major research challenge because there are numerous potential noise sources that must be quantified. These sources include acoustic scattering

of turbulent structures past trailing edges (e.g., duct exit), vane wake self-noise, quadrupole sources associated with the turbulent structures in the swirling outflow, and noise from vortex breakdown in the vicinity of the duct exit. To the author's knowledge, the latter two, swirling quadrupole sources and vortex breakdown, are poorly understood at present. An attempt at modeling the quadrupole noise from a stable, swirling flow is thus presented in Section 5.4.1, as a prelude to acoustic tests at the NASA Langley Quiet Flow Facility (QFF), using concepts from Lighthill's acoustic analogy and other fine-scale turbulence based models. A CFD integration technique is proposed to predict the swirling flow noise spectra of the 34° and 47° cases at $M_\infty = 0.17$. Computed results indicate that these sources, as modeled, are quiet at most frequencies relative to the QFF facility background noise, and have a steep high frequency roll-off of over 5 dB per octave (when presented in third-octave bandwidths). Subsequent acoustic measurement at QFF show high signal-to-noise ratio, significant high frequency noise levels, and a more gradual roll-off, confirming that the assumed model is insufficient to describe the stable swirling flow noise and warrants further modeling work in future investigations.

Key results from the QFF acoustic tests are presented in Section 5.4.2. To address the research challenge of identifying the various aforementioned sources, a test matrix is devised to include all swirl tube geometries plus an empty nacelle and a case with straight vanes, to systematically identify noise from trailing edge scattering, vane generated turbulence, swirling outflow, and vortex breakdown. Noise from the test articles is measured at various Mach numbers and directivity angles, using an array of far-field microphones. Both auto-spectra and array-based post-processed noise data are presented. The noise-drag-swirl relationship confirms the hypothesis that a high-drag, low-noise configuration exists, and is characterized by a stable swirling outflow with exit swirl angles of about 50°. Measured individual microphone noise spectra show that the two classes of flow fields are acoustically distinct, with vortex breakdown noise as much as 15dB louder than stable swirling flow at the highest frequencies, confirming the hypothesis that stable, swirling flow is acoustically desirable because of no large scale unsteadiness. Mach number scaling and array processed

data suggest that the stable swirling flow has both dipole and quadrupole sources. Scaling to typical installed size on an aircraft shows that the swirl tube is successful at generating quiet drag, and is therefore a viable device for slow, steep approach applications.

5.4.1 Swirl Mixing Noise Models based on Lighthill's Acoustic Analogy

One of the major challenges in acoustics is prediction of noise generated by turbulence. Over the past half-century acousticians have applied theoretical models of turbulence generated quadrupole noise sources to the problem of high-speed jet noise prediction. In this section an attempt is made to apply aspects of some of these jet noise models to the problem of a stable, swirling turbulent flow exiting the swirl tube[11]. In light of this project, the idea is born to modify a validated noise source term for straight jets with attempted corrections for swirling sources, to obtain a preliminary estimate of swirling flow quadrupole noise. Concepts from Lighthill's acoustic analogy and Tam's fine-scale turbulence based noise prediction tool are combined to form a proposed source term that can be integrated to predict the stable, swirling flow noise at side directivity angles. The success of this idea lies in the suitability of the assumed source term. In Section 5.4.2 it is shown that this model is insufficient at describing the stable, swirling flow noise, because the primary quadrupole noise is empirically found to reside in the vortex core, whereas the present model predicts that at peak noise frequency the sources mainly reside in the shear layer that forms at the duct trailing edge.

Background

Sir James Lighthill's Acoustic Analogy is developed in two seminal papers in 1952 [49] and 1954 [50], to model aerodynamically generated sound. The essential idea presented by Lighthill is to rewrite the compressible equations of continuity and linear momentum, in the absence of mass (volume) sources or external forces, respectively. The final form isolates a

[11] As the theory of noise generation from vortex breakdown near the exit of a duct has not received much attention to the author's knowledge, it's treatment in this thesis remains strictly empirical. The first quantifications of noise signature and scaling laws associated with this source are presented in Section 5.4.2

wave propagation operator acting on the density fluctuation on the left hand side (LHS). All other terms are brought to the right hand side (RHS) as analogs to acoustic sources:

$$\frac{\partial^2 \rho'}{\partial t^2} - a_\infty^2 \nabla^2 \rho' = \frac{\partial^2 T_{ij}}{\partial x_i \partial x_j} \tag{5.5}$$

In Equation 5.5, ρ' is the density fluctuation, a_∞ is the ambient sound speed, and the Lighthill stress tensor, T_{ij}, is defined by

$$T_{ij} = \rho v_i v_j + \left(p' - a_\infty^2 \rho'\right) \delta_{i,j} - \tau_{ij}, \tag{5.6}$$

where v_i is the velocity, p' is the pressure fluctuation, and τ_{ij} is the viscous stress tensor. Also, δ_{ij} is the Kronecker delta. The double divergence operator on the RHS indicates that the source term is a so-called quadrupole. For subsonic, non-combusting flows, the Lighthill stress tensor is dominated by the Reynolds stress term, $\rho v_i v_j$ [24]. Through dimensional arguments one arrives at the classic theoretical scaling for jet noise which states that at low subsonic Mach numbers the acoustic power, P, scales as the eighth power of the jet velocity (or Mach number),

$$P \propto \overline{\rho'^2} \sim \rho_0^2 M^8 \frac{D^2}{|x|^2}. \tag{5.7}$$

In the above equation, ρ_0 is the mean density, M is the jet Mach number, D is the jet diameter and x is the distance from the observer to the compact jet source. It should be noted that when apparent mass (volume) sources and external forces are included in the continuity and momentum equations, respectively, the RHS also includes the so-called monopole and dipole sources, which can arise from flow mechanisms other than turbulence in open flows. For example, the unsteady forces that act on compact rigid bodies such as rotating blades in turbulent flow resemble an external force on the flow that produces dipole noise. Within acoustic analogy theory, monopole and dipole source acoustic power scales with the fourth and sixth power, respectively [18].

Jet-noise prediction from acoustic analogy theory is one method of jet noise modeling.

The primary challenge is adequate representation of the acoustic source term, which is dependent on the flow itself. As time-accurate direct numerical simulation (DNS) of turbulent flows are computationally prohibitive, adequate representation comes from modeling techniques that describe the turbulent flow in a time-averaged sense. Numerous authors have constructed approximate source terms using experimental measurements of statistical turbulence (Reynolds stress terms) [25, 63, 69]. This approach is an attractive method for a first model of noise from a swirling flow. As the swirl tube outflow has a different flow structure than free shear flows like an axial jet, the accuracy of the predicted noise will depend in part on whether the fine-scale turbulence source terms, and and their assumed model constants, are applicable to this flow.

Fine-Scale Turbulence Jet Noise: Tam's Model. A notable exception to the acoustic analogy approach is Tam's use of adjoint Greens function methods on the linearized Euler equations [88, 89] to predict fine-scale turbulence noise from jets. Fine-scale and large-scale turbulence are identified by Tam et al. [91] and Tam [87] as two distinct mechanisms for which similarity spectra may be generated for all axisymmetric jets. Fine-scale turbulence noise radiates fairly uniformly at side directivity angles relative to the jet axis, but decays at aft angles, i.e., in the so-called cone of silence. Noise from large-scale structures dominates at these aft angles. Semi-empirical fine-scale turbulence jet noise prediction models are developed in several papers with good agreement to experiment [89, 90, 92].

The approach begins with the Greens function formulation of the linearized Euler equations. The difficulty in solving a distributed noise source problem for an observer at a fixed point in space is recognized to be computationally expensive, because a separate Greens functions must be generated for every possible spatial unit forcing in the source region. Using integration by parts, Tam et al. [88] identify the adjoint operator of the governing linearized equations, enabling the source and observer to be switched; in this way, a computation with single unit forcing at the observer location provides the adjoint Greens function of the pressure in the entire spatial domain. By weighting this kernel function with an appropriate source term, constructed from Reynolds Averaged Navier-Stokes (RANS) CFD output of

the jet, the spectral density and sound spectrum can be computed in eqs. 5.8 and 5.9 as

$$S\left(\vec{x},\omega\right)=4\pi\left(\frac{\pi}{\ln 2}\right)^{3/2}\times\iiint_{\text{Vol}}\frac{\hat{q}_s^2\ell_s^3}{c_0^2\tau_s}\frac{\exp\left[\frac{\omega^2\ell_s^2}{\bar{u}^2(4\ln 2)}\right]}{\left[1+\omega^2\tau_s^2\left(1-\frac{\bar{u}}{a_\infty}\cos\theta\right)^2\right]}\left|p_a\left(\vec{x}_2,\vec{x},\omega\right)\right|d\vec{x}_2 \quad (5.8)$$

and

$$SPL\left(f\right)=10\log\left[\frac{4\pi S\left(\vec{x},\omega\right)}{p_{\text{ref}}^2}\right]+10\log\left(\Delta f_{Hz}\right). \quad (5.9)$$

The terms ℓ_s, τ_s, and $\hat{q}_s^2/c_0^2$ are defined from the RANS CFD as $c_\ell\left(k^{3/2}/\epsilon\right)$, $c_\tau\left(k/\epsilon\right)$, and $A^2\left(\frac{2}{3}\bar{\rho}k\right)^2$, respectively. The constants c_ℓ, c_τ, and A have been empirically found to be 0.256, 0.233, and 0.755, respectively [89]. The radian frequency, ω, is equal to $2\pi f$.

At side directivity angles, mean flow effects are negligible, so that a far-field approximation to the magnitude of the adjoint Greens function of pressure can be exactly derived by solving a Helmholtz equation, as shown by Morris and Farrasat [63] and given in Equation 5.10:

$$\text{(at } 90^\circ\text{)}\ \ \left|p_a\left(\vec{x}_2,\vec{x},\omega\right)\right|^2=\frac{\omega^2}{64\pi^4c_0^4x^2}. \quad (5.10)$$

For jets at side directivity angles, then, RANS CFD computations may be used to compute the fine-scale jet noise spectra by integration of the source term with the adjoint Greens function in Equation 5.10. Morris et al. have also shown that similar results can be obtained from acoustic analogy derived source terms [63].

The accuracy of the implementation is first verified for an axisymmetric jet using the Tam et al. [89] and Morris et al. [63] source terms, before implementing a modification for the helical source motion due to swirl. Figure 5-24 compares the CFD computed one-third octave band noise spectra to empirical correlations, for a one meter diameter axisymmetric jet with axial exhaust, referenced to an observer distance of one meter and side directivity angle (90°). The four plots suggest that both Tam et al.'s and Morris et al.'s approaches

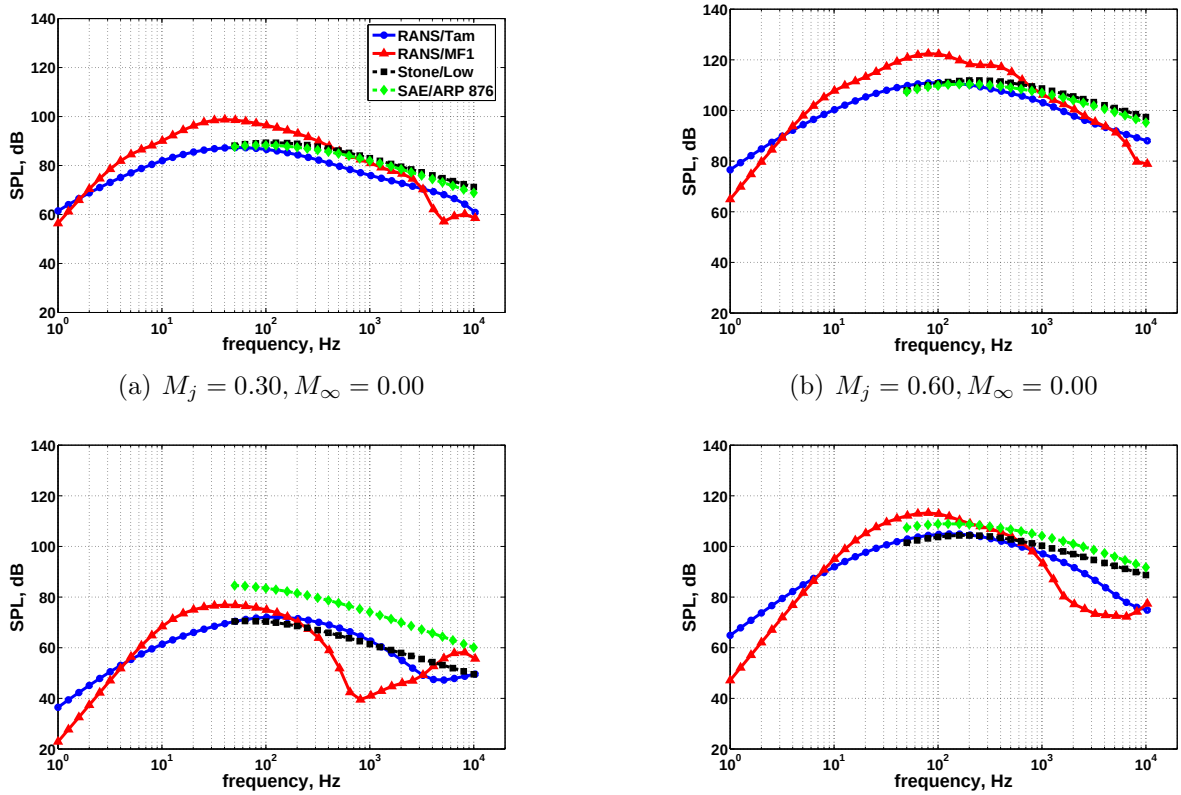

(a) $M_j = 0.30, M_\infty = 0.00$

(b) $M_j = 0.60, M_\infty = 0.00$

(c) $M_j = 0.30, M_\infty = 0.17$

(d) $M_j = 0.60, M_\infty = 0.17$

Figure 5-24: Comparison between computed jet noise spectra using Tam's fine scale turbulence noise source, Morris-Farassat source term, and Stone and SAE round single jet empirical models. Jet diameter is 1 meter. Spectra scaled to $r = 1$ m, for an observer angle of $\theta = 90°$.

produce reasonable results (within about 5 dB) for straight jets at different Mach numbers and different freestream velocities, when compared to the Stone jet noise model [85] or the Society of Automotive Engineers (SAE) Aerospace Recommended Practice (ARP) for single jets [82]. The predicted spectra from the straight jet CFD computations use the $k - \epsilon$ turbulence model with model constants as recommended by Thies and Tam [95]. The level of agreement in the figure suggests that use of these constants is reasonable for a first attempt at the swirl tube outflow noise prediction.

Swirling Sources - Tanna's Model. Tanna [94] analytically models the noise amplification due to the helical motion of sources present in swirling flows. In the next subsection this

amplification factor is combined with Tam's source term to create a noise source integrand for a swirling flow. For a randomly oriented, harmonically varying point quadrupole of radian frequency ν, he predicts the amplification of the mean square value of the fluctuating pressure $\langle p'^2 \rangle$ to be related to the quadrupole strength $\langle T \rangle$ as

$$\frac{\langle p'^2 \rangle}{\langle T \rangle} = \frac{\nu^2}{\left(4\pi c_0^2 r\right)^2 \left(1 - M_z \cos\psi\right)^5} \left[F_1\left(\alpha'\right) + \left(\frac{\Omega}{\nu}\right)^2 F_2\left(\alpha'\right) + \left(\frac{\Omega}{\nu}\right)^4 F_3\left(\alpha'\right) \right], \tag{5.11}$$

with α' defined in terms of the observer angle ψ and the Mach numbers components in the tangential (M_θ) and axial (M_z) directions as

$$\alpha' = \frac{M_\theta \sin\psi}{1 - M_z \cos\psi}. \tag{5.12}$$

The angle ψ is measured from the positive axial direction, z, to the line connecting the observer and the swirling source. The functions F_1, F_2, and F_3 are defined as:

$$F_1\left(\alpha'\right) = \frac{8 + 24\alpha'^2 + 3\alpha'^4}{8\left(1 - \alpha'^2\right)^{9/2}}, \tag{5.13}$$

$$F_2\left(\alpha'\right) = \frac{120\alpha'^2 + 60\alpha'^4 - 165\alpha'^6 - 15\alpha'^8}{16\left(1 - \alpha'^2\right)^{13/2}}, \tag{5.14}$$

and

$$F_3\left(\alpha'\right) = \frac{64\alpha'^2 + 464\alpha'^4 - 648\alpha'^6 - 325\alpha'^8 + 418\alpha'^{10} + 27\alpha'^{12}}{128\left(1 - \alpha'^2\right)^{17/2}}. \tag{5.15}$$

Assuming the point acoustic stress T_{ij} is known, Tanna's relation can be applied to include the effect of helical motion of the source. At the side directivity angle of $\psi = 90°$, the term α' equals M_θ. Hence this factor is a strong function of tangential Mach number at side directivity angles. Since all Mach numbers are relatively low on approach, Tanna's factor turns out to be weak in altering the assumed source strength.

Modeling Approach

In the present model, the major simplifying assumption used with Tanna's relation, Equation 5.11, is that the source strength T_{ij} between a helically (e.g., swirling exhaust flow) and axially convecting (e.g., straight jet) source is unchanged. In this case one may compare the ratio of $\langle p'^2 \rangle$ values between a helically and axially ($M_\theta = 0 \Rightarrow \alpha' = 0$) moving source at $\psi = 90°$ to obtain an amplification correction,

$$\frac{\langle p'^2 \rangle_{\text{Helical}}}{\langle p'^2 \rangle_{M_\theta=0}} = F_1(\alpha') + \left(\frac{\Omega}{\nu}\right)^2 F_2(\alpha') + \left(\frac{\Omega}{\nu}\right)^4 F_3(\alpha') \tag{5.16}$$

The Tam spectral density integral (Equation 5.8) and the so-called Tanna amplification correction (Equation 5.16) are multiplied together to create the swirling flow spectral density integral. This expression is a significant simplification to the theory, but represents a first attempt to assess the swirling flow noise by linking it to the turbulent kinetic energy, turbulence dissipation rate and swirling flow kinematics, obtained from RANS CFD.

Results

Axisymmetric CFD computations on the swirl tube nacelle aft-geometry with a long domain ($> 10D$ downstream) are performed with the swirling flow profiles of the 34° and 47° swirl vane CFD cases of Section 5.3.3 prescribed as inlet boundary conditions. Figure 5-25 presents a comparison of NASA Langley Quiet Flow Facility (QFF) background spectra and noise spectra of a model-scale swirling flow at 1 meter observer distance. The 47° swirl vane case flowfield is ~ 10 dB louder than the 34° swirl vane case flowfield, consistent with the higher Mach numbers in the former case. However, the predictions indicate that this type of noise source may be rather quiet, making detection in a facility such as QFF challenging. A field plot of the noise source integrand obtained from the product of equations. 5.8 and 5.16 is shown in Fig 5-26 for the case of 47° swirl vanes. The figure suggests that the fine-scale turbulence, or quadrupole, noise source is concentrated in the shear layer region. It is shown in the next subsection, that the model does not capture the dominant quadrupole noise sources in the vortex core. An improved model of the swirl tube quadrupole noise may

require relaxing the assumption of randomly oriented quadrupoles that are are unchanged between axial and helical motion, as well as a careful assessment at the RANS CFD modeling constants. In addition, the measured noise signature is shown to have significant sources due to scattering near the nozzle exit, which is not accounted for by the preliminary modeling and must be included to improve the overall predictions.

5.4.2 Model Scale Acoustic Testing

Test Facility

Model-scale acoustic tests have been performed at NASA Langley's Quiet Flow Facility (QFF) in Hampton, VA. The QFF is a state of the art anechoic free jet wind tunnel facility

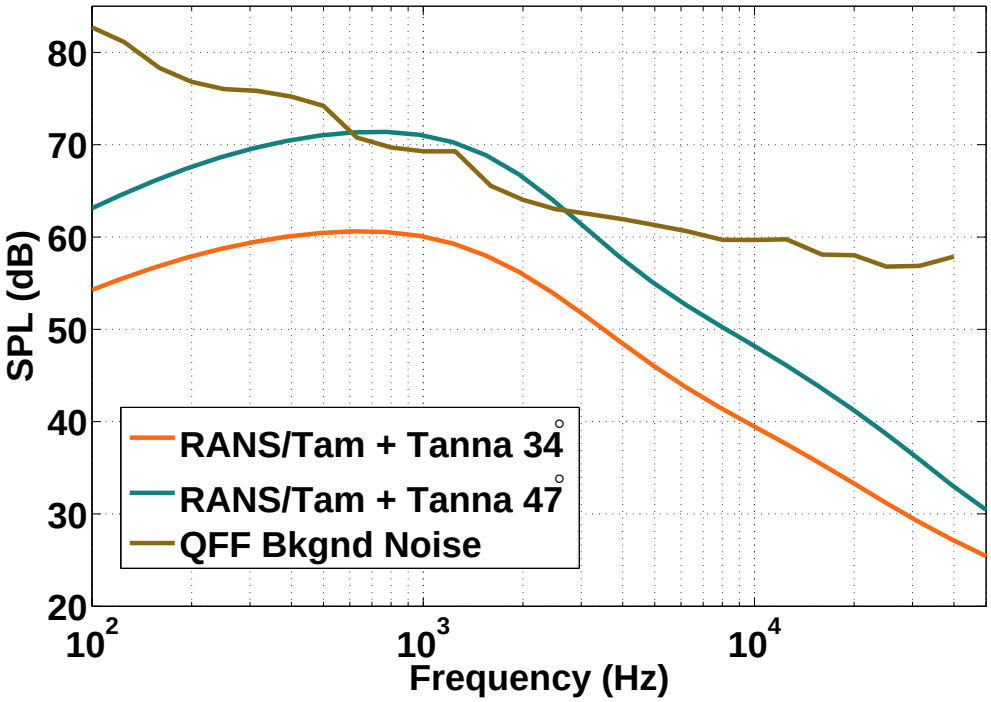

Figure 5-25: Hybrid Tam + Tanna model prediction of stable swirling flow noise using 2D CFD computation of swirl tube aft geometry. QFF facility background included for reference. One-third octave band spectra corrected to 1 meter observer distance at 90° observer location.

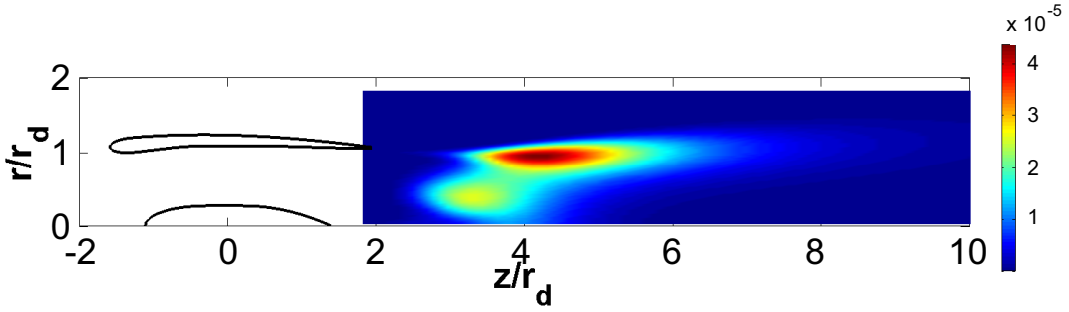

Figure 5-26: Spectral density integrand (at predicted peak noise frequency) for two-dimensional CFD of swirl tube exit flowfield for case of 47° swirl vanes. Freestream Mach number is set to 0.17. Axis units are in meters, based on full-scale CFD geometry of 2.16 m swirl vane outer diameter.

that has been used to make seminal measurements of self-noise from airfoils [7], leading edge slat noise [57, 58], flap-edge noise [9, 56], and tip-vortex noise [8], in addition to other model components such as rods of varying cross-section [42] to simulate landing gear components. The facility test chamber, pictured in Figure 5-27, has a vertical 2 ft. x 3 ft. free jet nozzle housed within a 9.1 meter x 6.1 meter x 7.6 meter anechoic chamber. Sound absorbing foam wedges line all sides of the chamber to prevent reflections. Additional details of the facility are contained in Hubbard et al. [39].

Acoustic pressure time-histories are acquired using six fixed-pole microphones and an array of 41 microphones covered with a cloth wind screen, a so-called Medium Aperture Directional Array (MADA), that can be rotated in a polar arc. The array polar arc variation is depicted in Figure 5-28. The radial distance from the test article center to the center of the MADA is 1.524 meters (5 feet). The MADA setting employed in the swirl tube acoustic tests ranges from $-124°$ to $-56°$ from vertical, with $-90°$ being the side directivity angle that is presented in this results portion of this section. The six pole microphones are located at a radial distance of 1.995 meters (6.54 feet), and have forward, aft and side directivity locations relative to the test article on the near and far sides of the tunnel. Results from pole microphones are not presented in this thesis. Additional information on the swirl tube

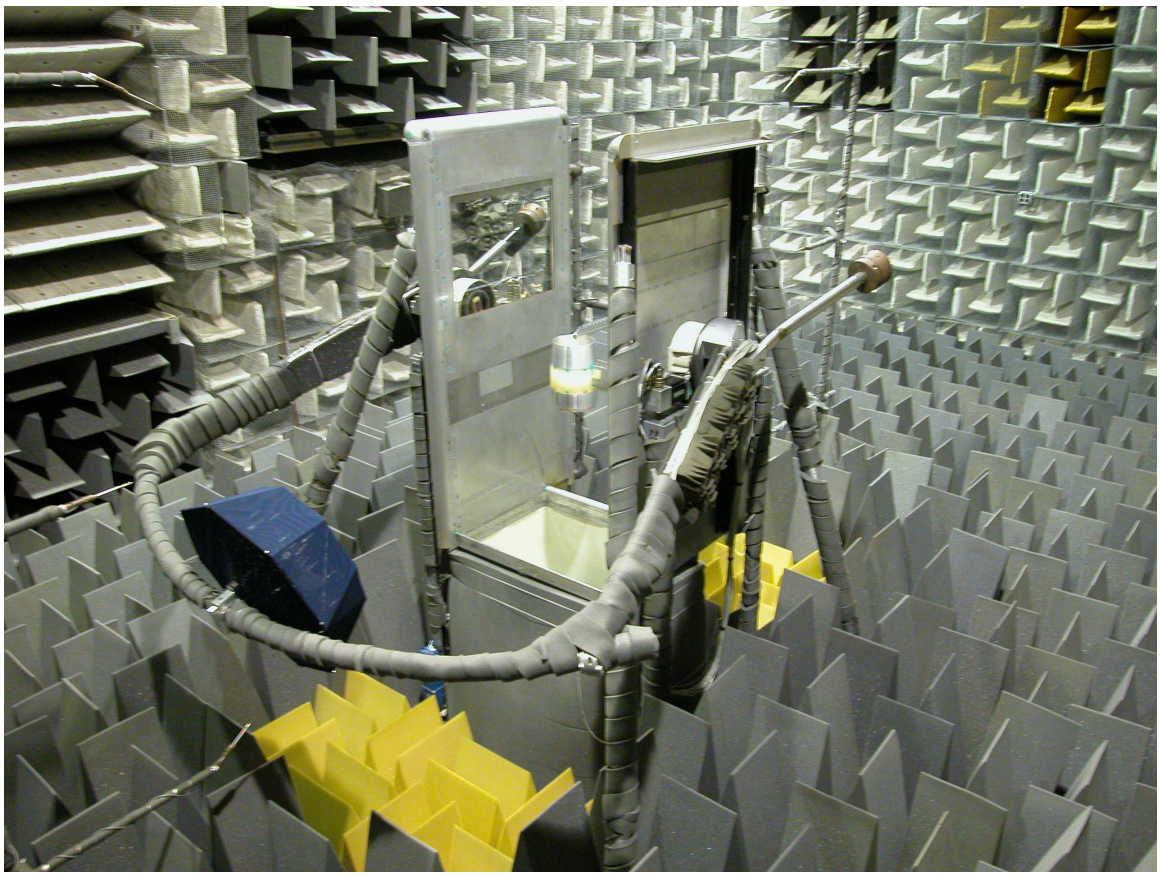

(a) QFF showing anechoic treatment, microphone array boom, and tunnel open jet and side walls.

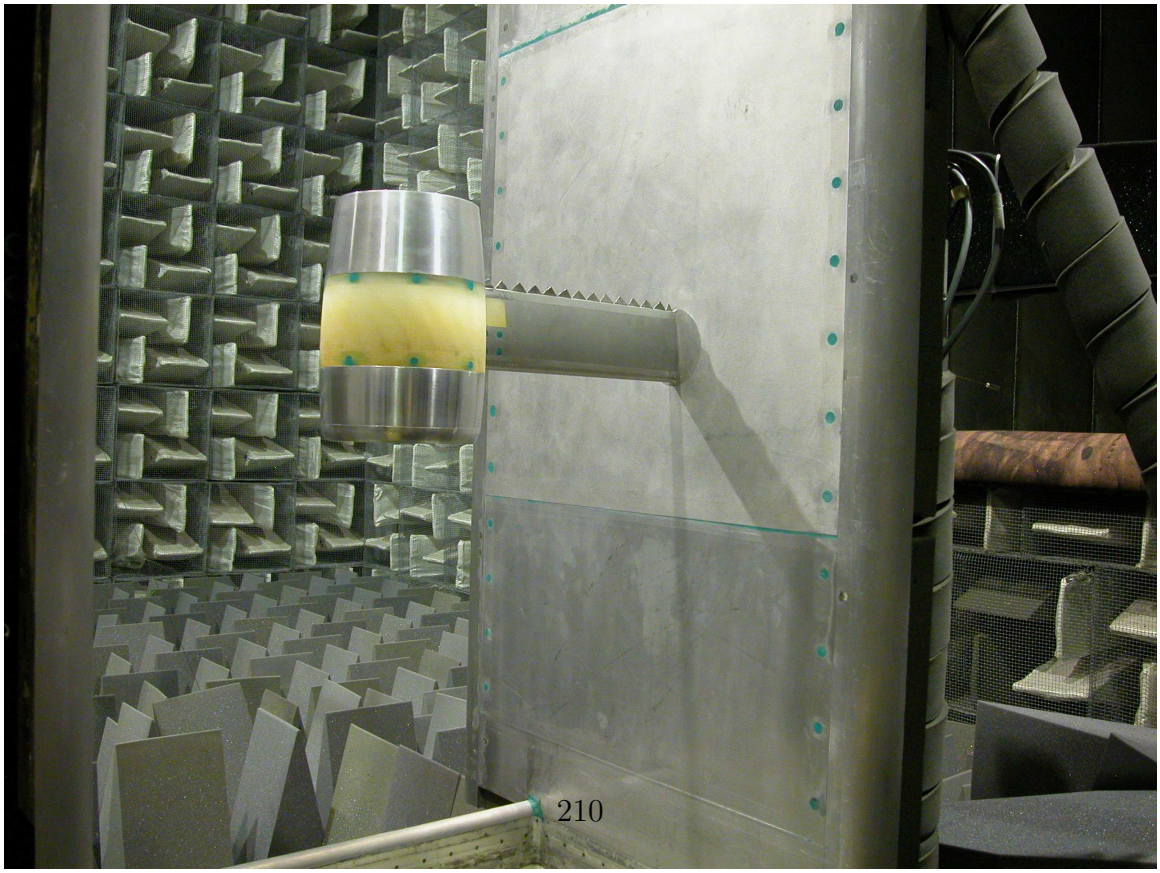

(b) Typical swirl tube QFF installation.

Figure 5-27: Photographs of NASA LaRC QFF setup.

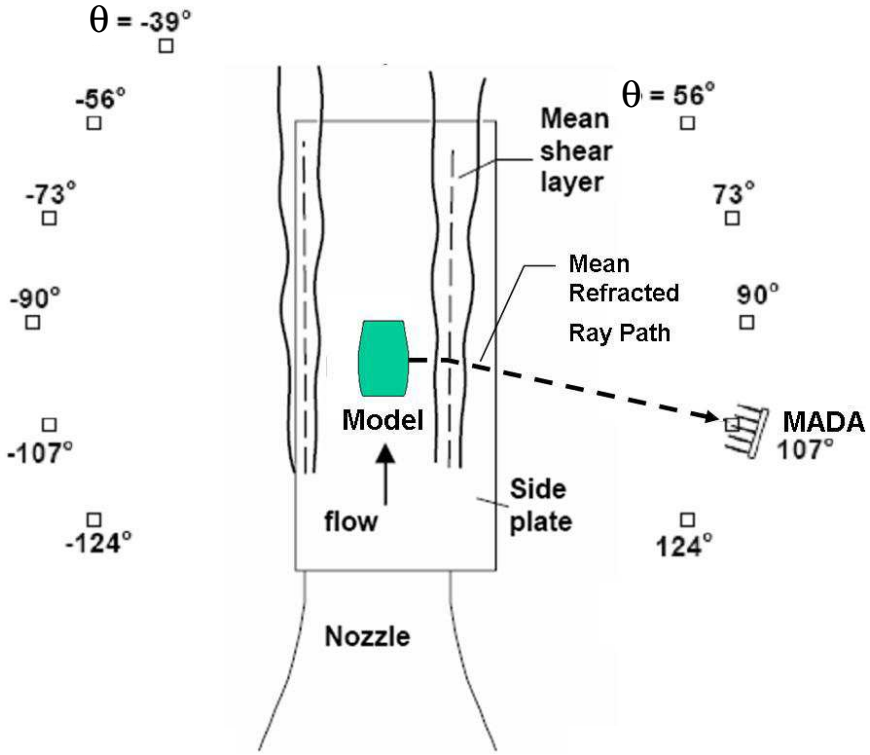

Figure 5-28: QFF directional array polar arc variation capabilities, adopted from [9]. Medium Aperture Directional Array (MADA) is depicted relative to the free jet with swirl tube model installed. Vertical free jet flow is from bottom to top. In this thesis, all data are presented with array in $\theta = -90°$ position.

acoustic tests can be found in Mobed [61].

As airfoil noise tends to be rather quiet relative to background noise in most anechoic facilities, the QFF has also been a leader in the development of diagnostic postprocessing techniques to identify sound sources, including coherent power output methods [41] and phased array techniques [40]. The most advanced phased array technique currently developed is the Deconvolution Approach for the Mapping of Acoustic Sources (DAMAS) [10, 11, 12]. This technique removes much of the uncertainty associated with array based techniques by removing beamforming characteristics from output presentations. DAMAS iteratively solves a unique system of linear equations which accounts for reciprocal influence at different

locations over the survey regions. This technique has been validated using archival data from high-lift airframe component sources and calibration sources. Previously validated sources, however, have not been quadrupoles distributed in space. In the swirl tube acoustic tests, a hypothesized noise mechanism is turbulence associated with the swirling outflow, a potential quadrupole source. A key goal for the DAMAS technique, is to identify sources that are spatially distributed in the swirling flow-field. Results presented at the end of this section indicate that the DAMAS technique has successfully identified such sources, confirming its versatility in analyzing complex aeroacoustic devices with multiple noise mechanisms.

Test Program

An extensive test program has been conducted, the details of which are documented in Mobed [61]. Important configurations that are described here include variations of swirl tubes with vane angles of 34°, 41°, 47°, 53°, 57°, and 64°. As the 47° and 57° swirl vane angle cases are extensively compared between CFD and wind tunnel tests, and shown to straddle the flow regime transition between stable flow and vortex breakdown barrier, additional comparison of these cases is shown in the next subsections. In addition, reference cases of a pylon alone, an empty nacelle and a swirl tube with 20 straight vanes (0° vanes) have also been tested to isolate the noise signatures associated with pylon and nacelle trailing edge scattering and vane self-noise.

Test Objectives

The working hypothesis of the swirl tube device concept is that stable, highly swirling flows can produce high levels of drag for relatively low levels of noise. Objectives that must be met in order to confirm this hypothesis are:

1. Quantification of the far-field sound pressure level (SPL) of a full-scale swirl tube.
2. Comparison of the spectral shapes of different swirl tube cases.
3. Identification of the spatial location of the sources (and hence the noise mechanisms).

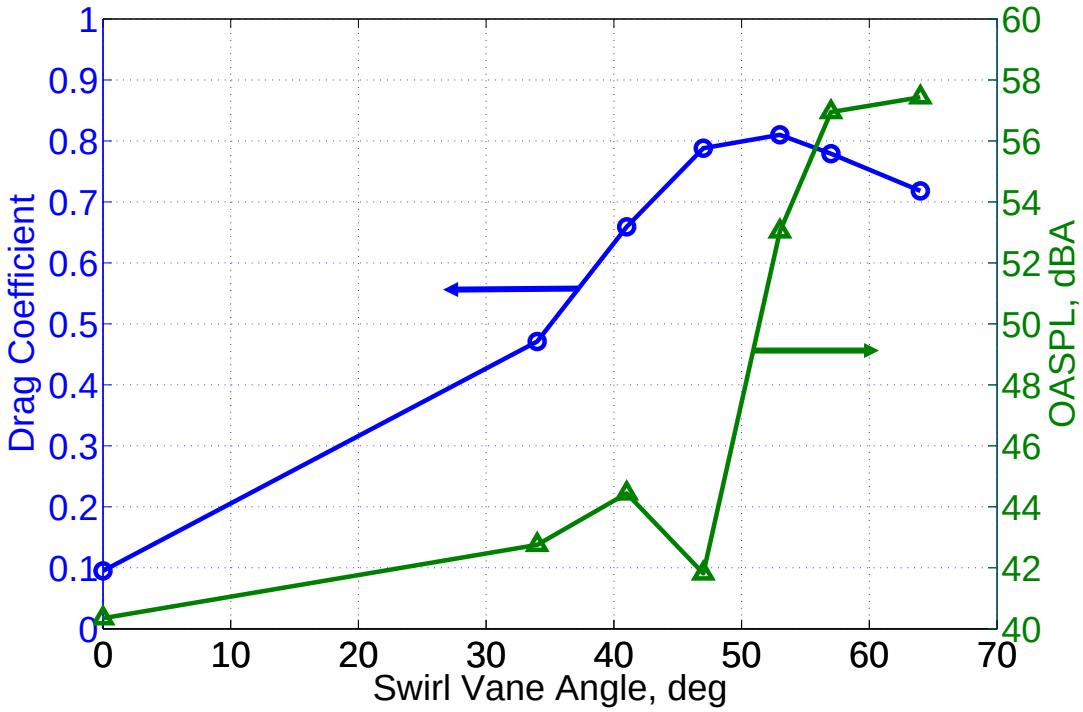

Figure 5-29: Full-scale (1.2 m diameter) drag coefficient (C_D) and overall sound pressure level (OASPL) vs. swirl angle suggests that a high-drag, low-noise configuration exists at swirl vane angle of 47°. Freestream Mach number for OASPL is 0.17. Observer location is 120 m from the source, at sideline angle of $\theta = -90°$ (see Figure 5-28).

4. Establishment of the scaling laws, as a function of Mach number, for the acoustic power of the various sources.

The data used to satisfy the objectives are 1) far-field noise spectra and 2) DAMAS source noise maps for the two types of flows: stable, and vortex breakdown.

Results

The results in this subsection are shown at a freestream Mach number of 0.17, consistent with typical CMI SAX approach speeds[12] of 60 m/s, and at a side directivity angle of $\theta = -90°$, unless otherwise indicated.

[12]See Table 4.2.

The Noise vs. Drag vs. Swirl Relationship. The primary conclusion that emerges from the acoustic test is that the ram pressure driven swirl tube concept is capable of achieving a high drag coefficient (about 0.8) with low noise. Figure 5-29 presents the full-scale[13] drag coefficient and A-weighted, overall sound pressure level (OASPL) as a function of swirl vane angle. The plot demonstrates that the high full-scale drag coefficient of 0.79 found in the stable 47° swirl vane case also corresponds to an A-weighted OASPL of 42 dBA, about 20 dBA quieter than a well-populated urban area in the vicinity of an airport, and comparable to a quiet library [38]. All of the stable flow cases, from 0° straight vanes to 47° swirl vanes have similar OASPLs, making this noise-to-drag characteristic different from the one-to-one relationship of conventional drag devices such as flaps, slats, spoilers, and struts (e.g., landing gear). This result suggests that the swirl tube concept has the potential to be a key enabler for quiet approach profiles for future aircraft. For swirl tube design, stable, highly swirling flow with maximum exit swirl angle close to 50° is the critical feature required to achieve low noise and drag coefficient above 0.8.

Stable Outflow (47° Swirl Vanes) vs. Vortex Breakdown (57° Swirl Vanes). Figure 5-30 compares the narrowband (17.44 Hz bandwidth) and third-octave autospectra of the 47° and 57° swirl vane angle cases at side directivity angle, as measured by a single array microphone 1.524 meters from the center of the swirl tube circular duct exit. Empty tunnel background noise is also presented, and indicates that the data is acquired with excellent signal-to-noise ratio over the majority of the frequency range ($\gtrsim$ 1 kHz). Both swirl tube spectra are broadband in nature, with no strong tones present, consistent with power spectra of unsteady velocity obtained with hot-wires in the Wright Brothers Wind Tunnel (see Section 5.3.4). The vortex breakdown spectrum appears purely additive, relative to the stable flow spectrum. The plots also indicate that noise from vortex breakdown near the duct exit has a white-noise-like spectral shape that is flat in narrowband presentation and upward sloping in third-octave presentation. Vortex breakdown increases noise substantially

[13]Here, full-scale is taken to be 1.2 meters swirl vane diameter (6.7 times the model-scale diameter) and 120 meters observer distance, consistent with an approach profile of 3° at a distance of 2290 meters from touchdown.

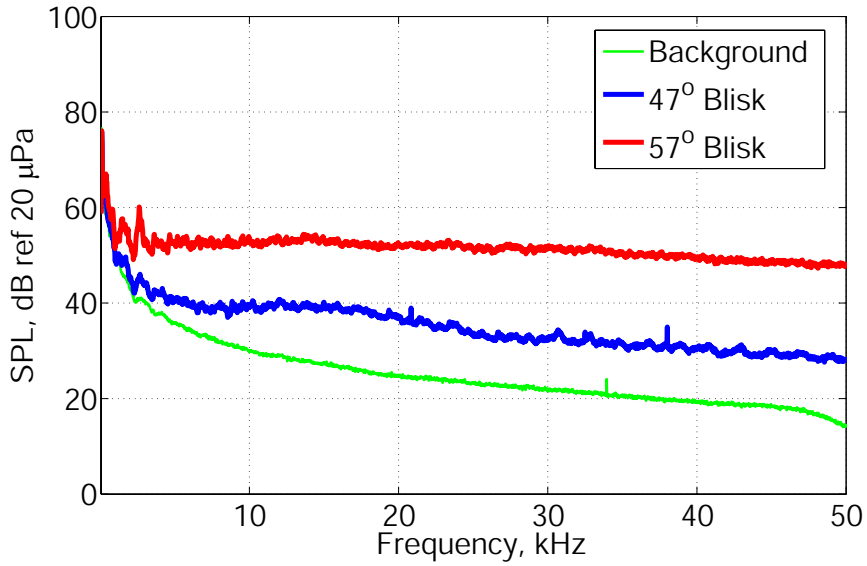

(a) 17.44 Hz Constant Bandwidth.

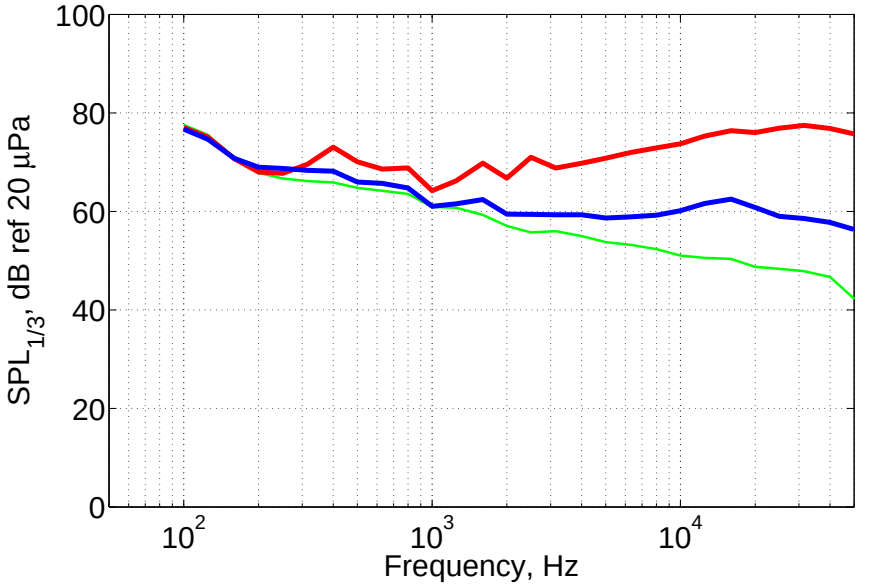

(b) Third-octave band.

Figure 5-30: Model-scale spectra at 47° and 57°, Mach=0.17, $\theta = -90°$.

at nearly all frequencies. The level of the increase is about 15 dB at the higher frequencies; hence, crossing the vortex breakdown threshold is deleterious for noise as well as drag coefficient.

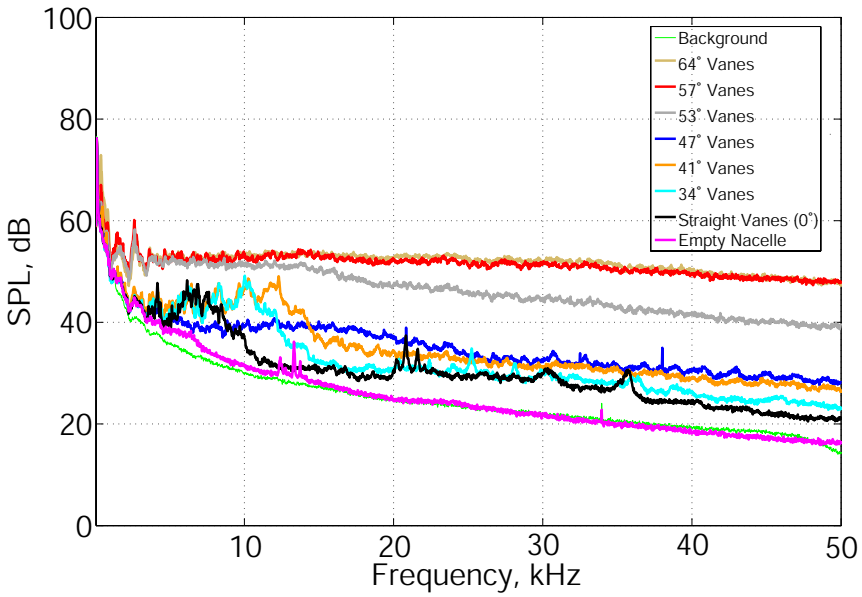

(a) 0 to 50 kHz range, 17.44 Hz Constant Bandwidth.

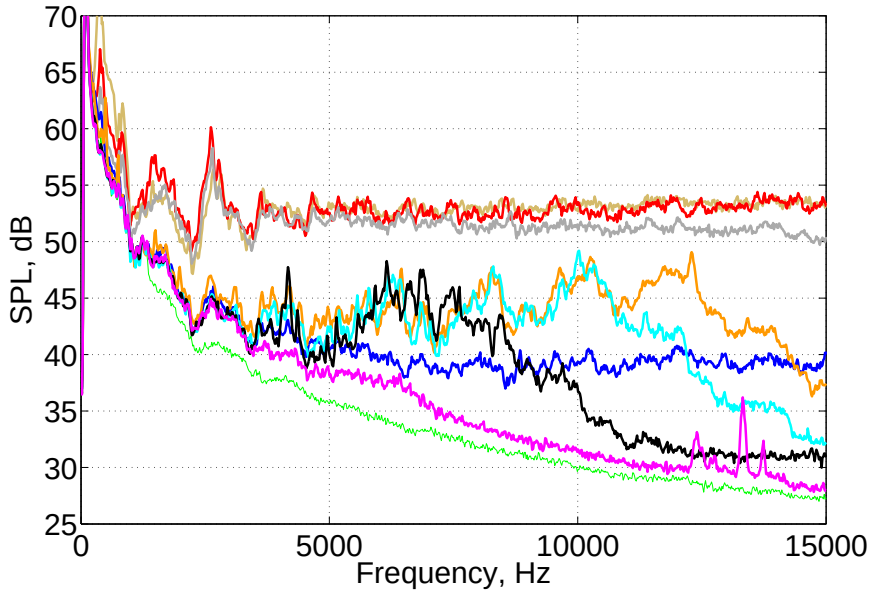

(b) Magnified view of (a), 0 to 15 kHz range, 17.44 Hz Constant Bandwidth.

Figure 5-31: Overall spectral comparison of all swirl tube configurations, constant 17.44 Hz bandwidth, Mach=0.17, $\theta = -90°$.

Comparison of Autospectra (All Swirl Vane Angles). Figure 5-31 presents a narrowband comparison of autospectra of swirl tubes with vane angles of 34°, 41°, 47°, 53°, 57°, and 64°. The upper figure presents the entire frequency range to 50 kHz, while the lower

figure magnifies the lower frequency features up to 15 kHz with finer resolution on the SPL axis. For reference autospectra from an empty (vaneless) nacelle, a nacelle with straight vanes (0°) and tunnel background noise are also included. The spectra are all predominantly broadband in nature. Two families of noise spectra are clearly suggested: stable (0°, 34°, 41°, and 47° swirl vane angle) and vortex breakdown (53°, 57°, and 64° swirl vane angle). In addition, from an acoustic design point of view, it becomes apparent that the goal for the designer should be to design for an exit flow that is as close to the stability threshold as possible without exceeding it in order to achieve low noise and high drag.

Stable flow noise spectra ($\leq 47°$ swirl vane angle) appear to have a broadband spectral peak in the 5 to 20 kHz range. This feature appears jagged in the cases with 0°, 34° and 41° vanes, while it is broadly smeared for the 47° case, possibly suggesting the onset of a gradual transition away from this noise signature. The upper frequency range of this broadband feature increases with swirl angle. This suggests that increasing the swirl angle increases the frequency of acoustic events within a given flow volume. The fact that the straight vaned (0°) case autospectrum exhibits the basic noise signature of the autospectra of cases with non-zero swirl vane angle also implies that the vanes and aft centerbody are a necessary feature of the noise signature. In other words, the vane self-noise may generate the sources that are acoustically scattered past the vane trailing edges and sharp aft centerbody ($\overline{\rho'^2} \propto M^{5-6}$), and finally convected, axially or helically into the swirling exhaust flow where they may generate fine-scale turbulence noise ($\overline{\rho'^2} \propto M^{7-8}$).

Further consideration of the smearing of this feature in the 47° swirl vane case may be made in the context of aerodynamic experimental results presented in Section 5.3.4. Flow visualization indicates that the exit flow of the case with 47° swirl vanes is stable, but the steady axial velocity profile obtained through hot-wire anemometry at $z/D = 0.5$ and 1.0 indicates the possibility of a displaced vortex center. One possible conjecture is that this flowfield, while stable, may also have some unique features on its core, such as a standing wave, or the onset of a spiral-type vortex breakdown, that beneficially affects the noise signature by smearing the frequency content of the noise mechanism relative to it's lower

swirl counterparts.

A final observation of the stable flow spectra of vaned cases is that at high frequency there appears to be a rolling off of the sound pressure level with frequency. The slope of this roll-off appears to be gradual, but identical for all of the stable swirling flow cases.

Examination of vortex breakdown spectra ($\geq 53°$ swirl vane angle) suggests that a distinctly different class of dominant noise mechanism is present in these cases. At high frequency, the noise spectra do not roll off as steeply as the stable spectra. The 57° and 64° swirl vane case noise signatures are nearly identical, showing that the presence of the fully burst vortex is the dominant feature that overshadows details of the swirling flow, despite the fact that the measured drag coefficients are not identical (0.82 and 0.76, respectively). In this context, the case with 53° swirl vanes appears to have the elevated levels of the burst vortex noise signature, and the high frequency rolloff of the stable flow cases. This suggests that its flowfield is near the cross-over from the stable regime to vortex breakdown. The transition between 47° and 53° is stark in terms of sound pressure level, but similar in terms of shape, demonstrating that these cases bridge the two classes of flow.

The empty nacelle spectrum shows two broadband peaks near 2 and 3 kHz, consistent with trailing edge scattering of structures within the turbulent boundary layer of the nacelle and/or supporting pylon. The level of this feature in the stable flow, vaned cases is virtually identical to the empty nacelle. By contrast, the vortex breakdown spectra have two sharp broadband peaks at the same frequencies, but 5-10 dB louder. By conjecture, this may suggest that the presence of the unsteady vortex breakdown separation bubble in the vicinity of the duct and pylon trailing edges provides a mechanism to amplify the scattering.

Full Scale Noise Signature (47° vs. 57° Swirl Vanes). Measured swirl tube autospectra scaled to the size of the final CMI SAX aircraft conceptual design fan diameter, and to an observer distance typical of an approach profile, are presented in Fig 5-32. The full-scale spectra confirm that a swirl tube at practical geometric scale is quiet relative to the background noise of a typical urban area in the vicinity of an airport.

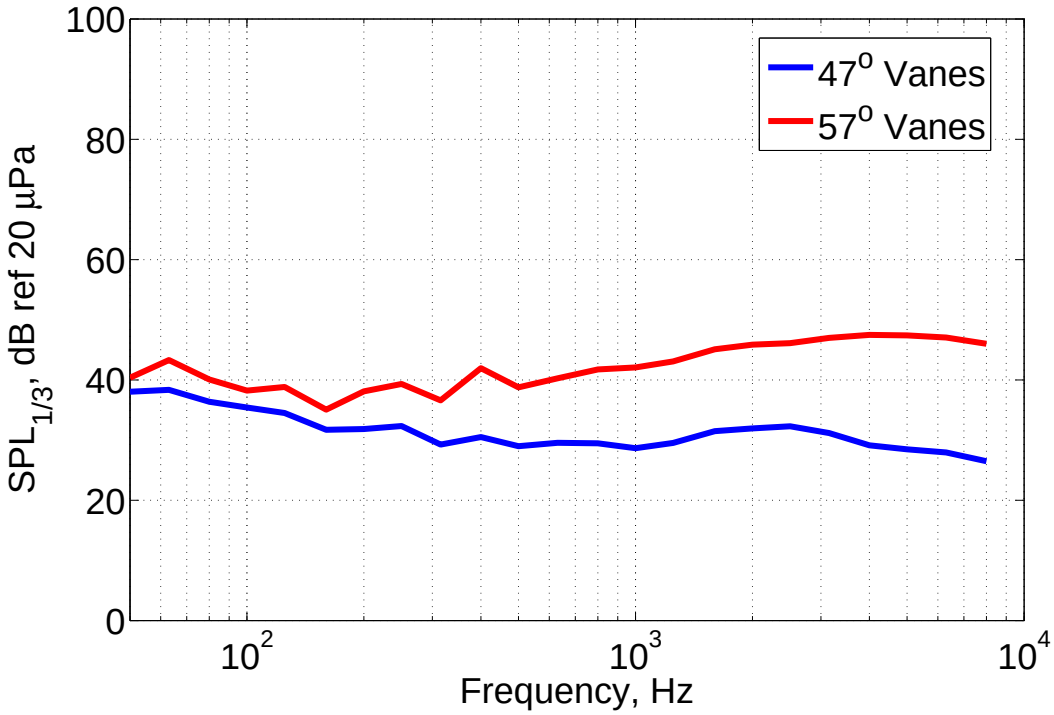

Figure 5-32: Full-scale third-octave band autospectra at 47° and 57°, Mach=0.17, $\theta = -90°$.

The QFF array microphone distance is 1.524 m, while full-scale observer distance[14] is estimated to be 120 m. The model-scale vane outer diameter is 0.18 m, while the full-scale diameter[15] is set at 1.2 m. The distance scale factor is thus 79 and the geometric scale factor is 6.7.

The scaled third-octave SPL shows that both swirl tubes are in fact quiet, although the 47° swirl tube is nearly inaudible in a typical urban environment, as 30 dB is comparable to a whisper. It should be noted that these spectra are for a single swirl tube, while a next generation quiet aircraft would likely require several swirl tubes (~ 4) to increase the glideslope angle by roughly one degree. Even with multiple swirl tubes, however, the overall noise would be well below any background noise levels in an airport environment.

[14]The full-scale observer distance corresponds to a point directly below an aircraft on a standard 3° glideslope that is 2290 meters away from touching down. Atmospheric attenuation is not included in the scaling.

[15]Note this differs from the "full" scale CFD geometric OD used in Section 5.3.3 which is 2.16 meters.

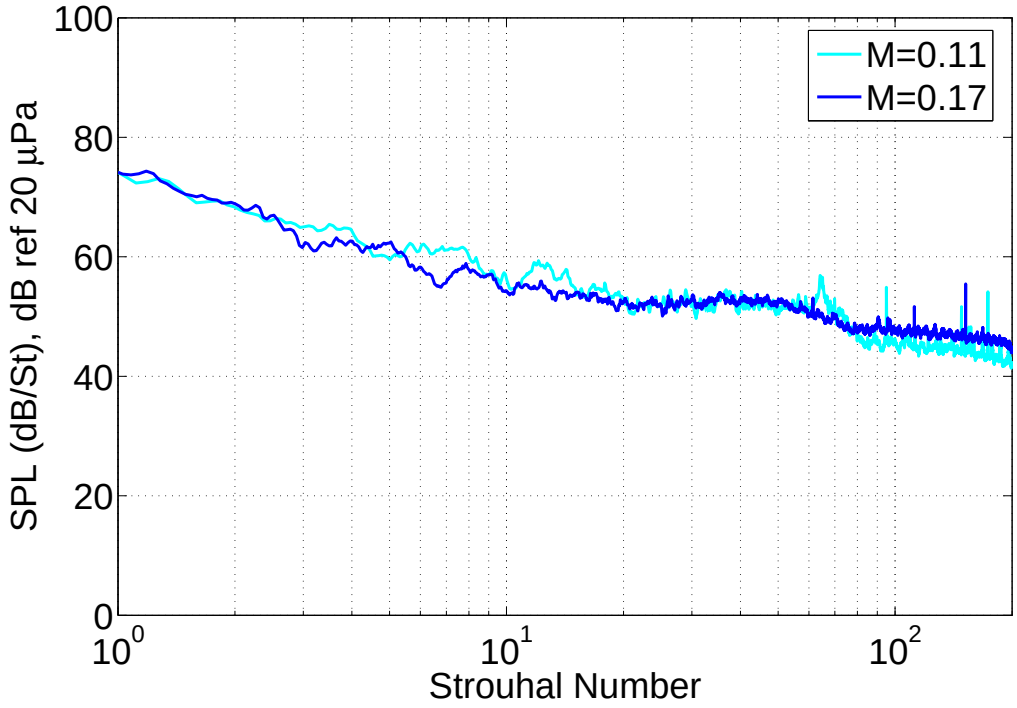

(a) n=6.5. Good collapse is suggested for $20 < St < 60$.

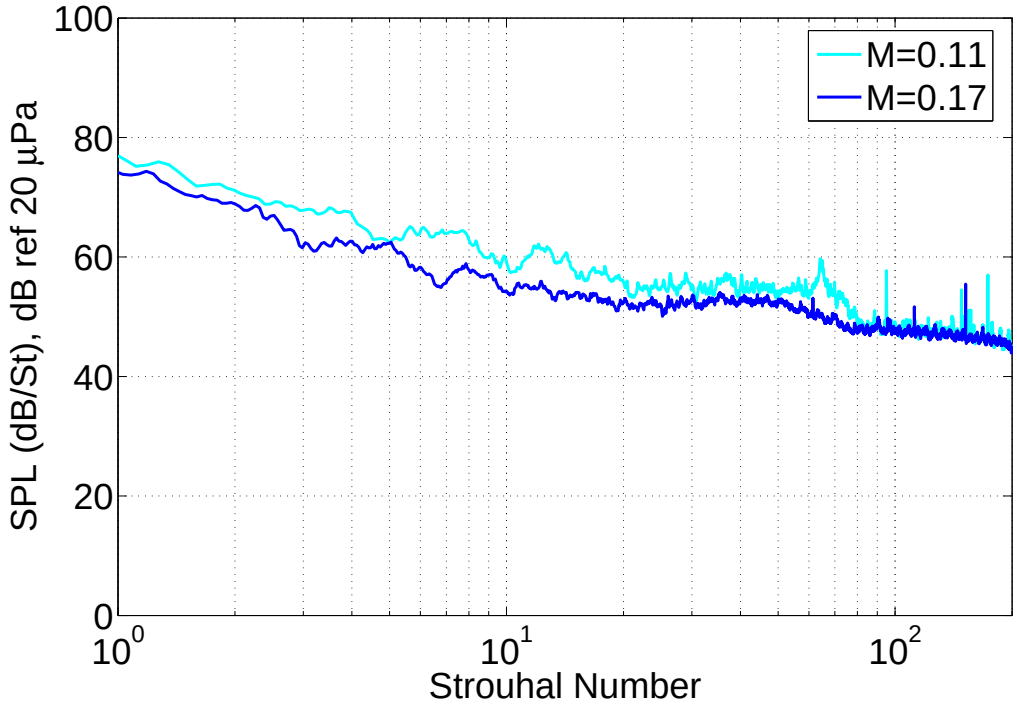

(b) n=8.0. Good collapse is suggested for $80 < St < 200$.

Figure 5-33: Mach number scaling of 47° spectra assuming different scaling exponents, n, per Equation 5.18. All spectra are presented non-dimensionally in a dB/St basis basis.

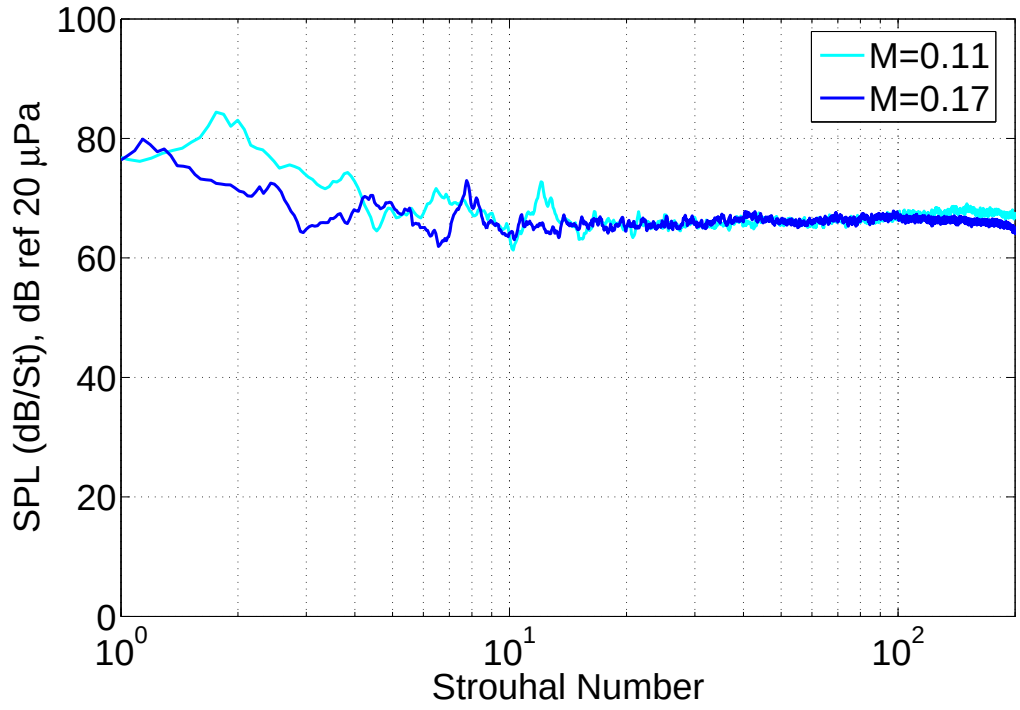

Figure 5-34: Mach number scaling of 57° spectra assuming $n = 7.5$ power law, per Equation 5.18. All spectra are presented non-dimensionally in a dB/St basis. Good collapse is suggested for $15 < St < 100$.

Mach Number Scaling (47° and 57° Swirl Vanes). A preliminary Mach number scaling of the 47° and 57° swirl vane autospectra at the −90° microphone array position is presented in Figs. 5-33 and 5-34, respectively. Results suggest that different power scaling laws are applicable to the stable and vortex breakdown exit flow fields. All spectra are non-dimensionally presented in a decibel per Strouhal bandwidth. The Strouhal number, St, is defined as

$$St = \frac{fD}{V_\infty}, \tag{5.17}$$

where f is the frequency in Hz, V_∞ is the freestream velocity in m/s, and D is the characteristic swirl tube diameter of 0.179 m. The reference Mach number condition is chosen to be 0.17, for which spectra are unaltered. At the lower Mach number condition of 0.11,

the spectra are scaled up to the reference Mach number by performing a deduced power law adjustment:

$$SPL_{Scaled} = SPL_{(M=0.11)} + 10nlog_{10}\left(\frac{M_{ref}}{0.11}\right) \tag{5.18}$$

It is worth recalling that acoustic analogy theory suggests that trailing edge scattering and dipole noise mechanisms scale with the powers 5 and 6, respectively, while quadrupole noise mechanisms scale with the power 8. In the case of the stable swirling flow emanating from the swirl tube with 47° vanes, the $n = 6.5$ deduced power law shows good collapse at Strouhal numbers in the range of 20 to 60, suggestive a scattering/dipole dominated noise mechanism, while the $n = 8.0$ deduced power law shows good collapse at Strouhal numbers in the range of 80 to 200, suggestive of a quadrupole noise mechanism. The spectra of the swirl tube with 57° vanes collapse tightly over the Strouhal number range of 15 to 100 for the deduced power of $n = 7.5$. Dipole noise is associated with unsteady forces from turbulent flow over compact bodies, while scattering noise occurs from the boundary condition imposed by a sharp trailing edge, suggesting that these sources are located in the vicinity of the swirl tube surfaces and edges, while quadrupole sources are caused by turbulence in an open flow, suggesting that these sources may reside in the swirling exhaust flow. It is shown in the next section that DAMAS integrated results support this observation for the stable swirling flow case.

DAMAS Source Mapping (47° vs. 57° Swirl Vanes). The power of DAMAS lies in the fact that its output provides a spatial source mapping of the mean square value of the fluctuating pressure, $< p'^2 >$, in dB, on a volumetric basis, at each grid point for each one-third octave band frequency. The total sound pressure level in any given frequency band is thus simply the $< p'^2 >$ summation of the values at all of the grid points. In this way, DAMAS is able to re-construct an entire auto-spectrum, as well as selectively integrate source regions in space to isolate different source spectra associated with localized mechanisms. Figure 5-35 depicts the three integration zones selected to evaluate potential

sources. Flow is from bottom to top, as pictured in Fig 5-27. Zone 1 is the aft region, enclosing the swirling flow field as well as the nacelle exit. Zone 2 is the forward region, enclosing the nacelle inlet. Zone 3 is the pylon region, enclosing the entire pylon that holds the swirl tube in the facility.

Figures 5-36 and 5-37 present source maps and one-third octave integrated spectra constructed from the DAMAS array post-processing program for the 47° and 57° swirl vane cases, respectively, at a M=0.17 sideline angle (−90°) test point. The computed DAMAS outputs show the localized spectra of the aft, fore, and pylon regions as circular, triangular, and square symbols, respectively, and the overall noise spectra as diamonds. Good agreement is found between the overall DAMAS computed noise spectra, and auto-spectra from two individual array microphones, presented as solid cyan and magenta lines. Background noise is also provided in green, for reference. In the bottom row of each figure, DAMAS source maps at 2.5, 16, and 31.5 kHz, corresponding to Strouhal numbers of about 8, 49, and 96,

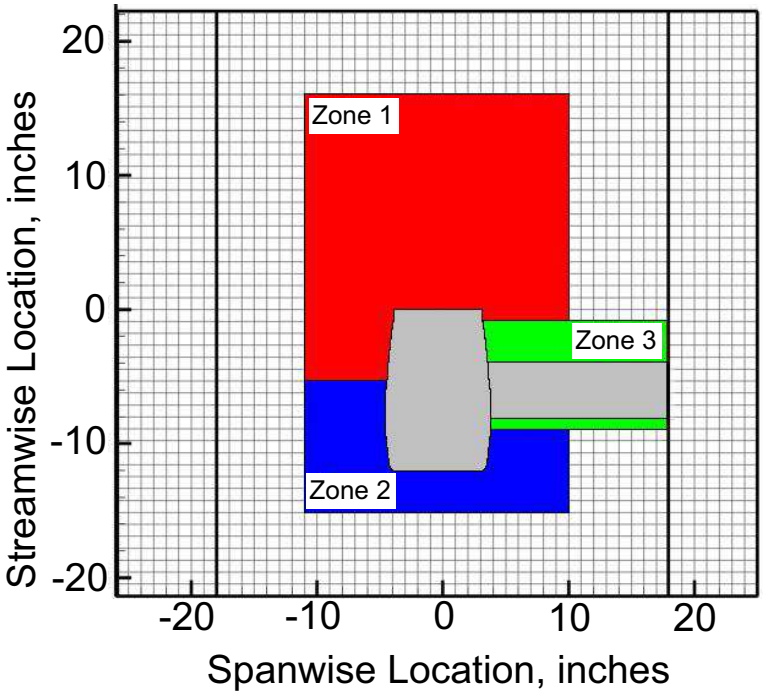

Figure 5-35: DAMAS integration zones. Zones 1, 2, and 3 correspond to aft, fore, and pylon regions, respectively.

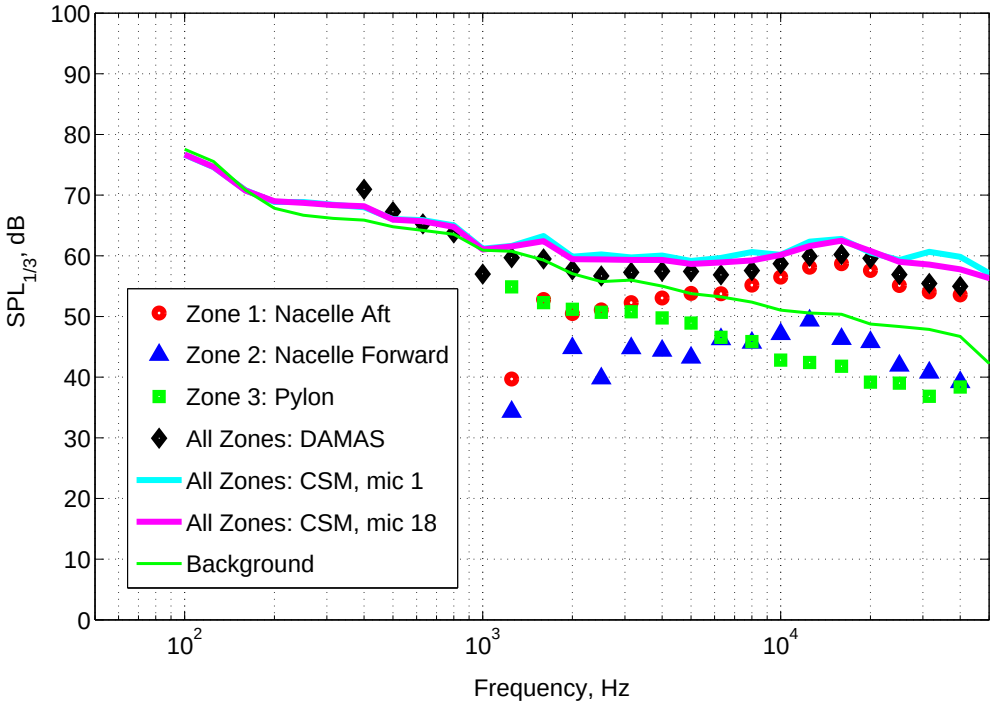

(a) 47° case DAMAS integrated spectra

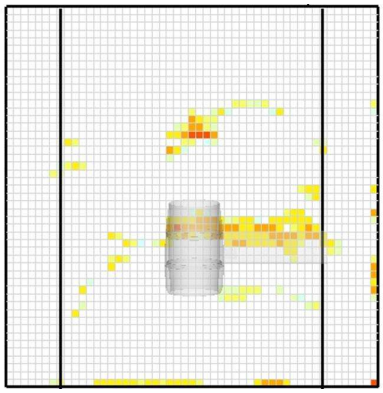

(b) Source map, 2.5 kHz ($St \approx 8$).

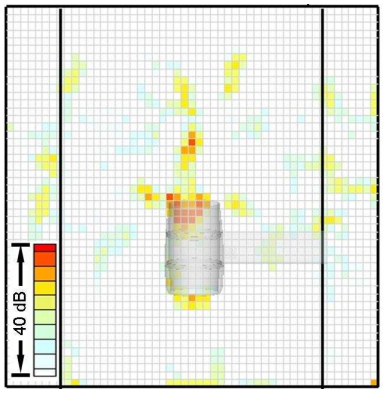

(c) Source map, 16 kHz ($St \approx 49$).

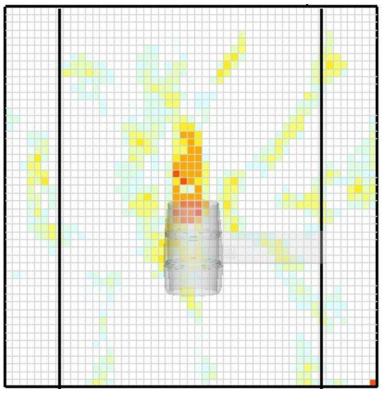

(d) Source map, 31.5 kHz ($St \approx 96$).

Figure 5-36: DAMAS zone-integrated spectra and source maps, 47° swirl vane angle case, $M = 0.17$, $\theta = -90°$.

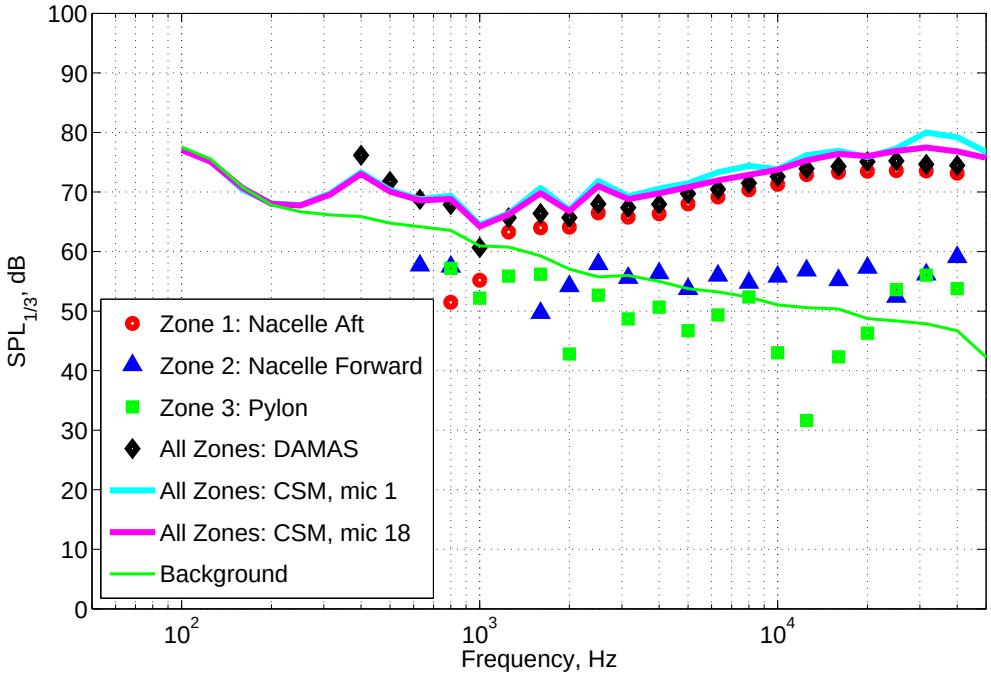

(a) 57° case DAMAS integrated spectra

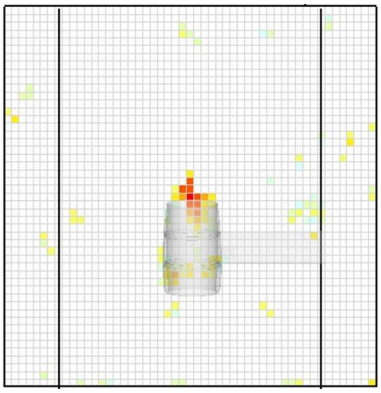

(b) Source map, 2.5 kHz ($St \approx 8$).

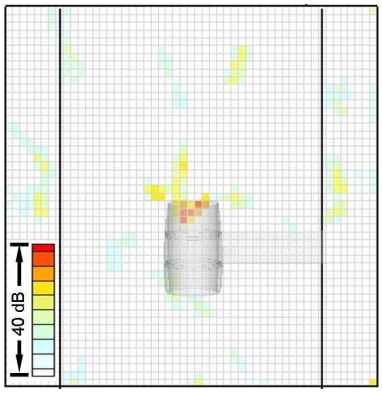

(c) Source map, 16 kHz ($St \approx 49$).

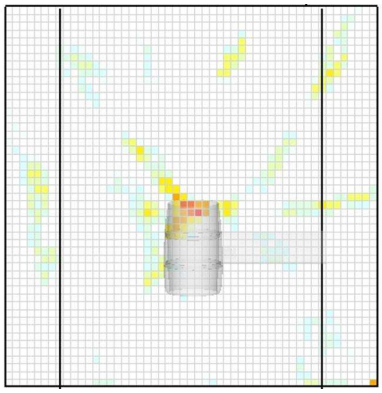

(d) Source map, 31.5 kHz ($St \approx 96$).

Figure 5-37: DAMAS zone-integrated spectra and source maps, 57° swirl vane angle case, $M = 0.17$, $\theta = -90°$.

respectively, indicate regions of high source intensity. It should be noted that each DAMAS source map presented here has its own scaling, giving the reader a idea of the source location but not the source level.

The integrated source spectra for the 47° swirl vane case in Figure 5-36 indicate a clear aft zone source dominance at frequencies above 3 kHz, while below this frequency both aft and pylon zones contribute to the noise signature. The DAMAS source maps at the bottom of the figure show that the aft zone has a volume source downstream of the duct trailing edge at all three selected frequencies. In the 2.5 kHz third octave band ($St \approx 8$) there is significant source activity at the pylon trailing edge, while in the 16 and 31.5 kHz third octave bands ($St \approx 49$ and 96, respectively) there is activity located near the duct exit and in the swirling outflow. The presence of noise sources both in the outflow region of the swirling flow and near trailing edges such as the duct and pylon are consistent with the earlier indication of the presence of both quadrupole sources and dipole sources shown in the Mach number scaling. Hence one may conclude that a high-drag generating, stable, swirling flow emanating from a ram pressure driven swirl tube has a complex source definition that is distributed both in space and near the device edges.

By contrast the 57° vortex breakdown case displays an aft dominant behavior at all selected frequencies, as shown by the integrated spectra and the source mapping of Figure 5-37. One must assume that the burst vortex (which behaves as a large unsteady flow blockage or body downstream of the duct exit) generates its own noise and is likely to affect the trailing edge noise of the pressure driven flow exiting the duct. The unsteadiness may provide a mechanism to amplify the scattering and/or dipole-like edge noise sources, in addition to creating its own quadrupole-like self-noise. In addition, the pylon trailing edge source is independent of the swirl tube fluid dynamics, and is hence present in both stable and vortex breakdown cases. As shown by the 2.5 kHz source map, however, the magnitude of the vortex breakdown noise source is loud enough to mask the distributed pylon trailing edge source that is clearly seen in the 47° swirl vane case of the previous figure. A clear picture emerges of the fundamental differences between the swirl tube with stable swirling flow and

with a burst vortex, where the former is quieter, with a combination of scattering/dipole-like duct edge sources that scale like the power 6.5, and distributed quadrupoles in the outflow that scale like the power 8. Vortex breakdown contains a concentrated source at the duct trailing edge that appears to scale with the power 7.5.

QFF Test Summary. To conclude this section on the acoustic tests, it is worth restating important results that have been found from the experiments:

- At the scale needed for commercial aircraft operation, and at a typical observer distance on approach, a ram pressure driven swirl tube can be designed to have a relatively quiet A-weighted OASPL of about 40 dBA, well below the background noise of a well populated area. Hence, it is a viable quiet drag device.

- Scaling laws imply that the noise from high-drag generating, stable swirling flow cases is dominated by scattering/dipole sources at the duct edge that may scale with the power 6.5 in the Strouhal number range of 20 to 60 based on swirl vane diameter and quadrupole sources in the swirling flow that may scale with the power 8.0 in the Strouhal number range of 80 to 200. Vortex breakdown noise is dominated by a source near the duct exit that may scale with the power 7.5 in the Strouhal number range of 15 to 100.

- Vortex breakdown introduces a dramatic increase in noise, with sources concentrated at the duct exit (and edges). At high frequencies, the vortex breakdown spectrum appears similar to white noise and is about 15 dB louder than a highly swirling, stable case. Hence, the goal for effective swirl tube design is to deliver a stable exit flow close to but not in excess of the vortex breakdown stability threshold in order to achieve high drag and low noise.

In the context of the swirl tube project timeframe, the above presentation represents a preliminary assessment of the noise levels, mechanisms and scaling laws. Future work should focus on a detailed decomposition of swirl tube noise spectra for all angles, with scaling laws extracted on a zonal basis using DAMAS.

5.5 Swirl Tube System Integration

The swirl tube has been shown to be an aerodynamically and aeroacoustically feasible quiet drag device when scaled to geometries of practical interest. Sections 5.3 and 5.4 have confirmed the hypothesis that a high-drag, low-noise design exists in the swirl tube design space.

In this section system integration issues are considered. As a propulsion system-integrated configuration requires interaction with a fan stage, so-called pumped swirl tube computations are presented in Section 5.5.1. These computations are an extension of the single passage periodic CFD computations presented in Section 5.3.3, that highlight the importance of low approach idle setting to achieving a slow, steep approach trajectory. Pumped swirl vanes are found to provide greater thrust reduction (equivalent to drag) than a parallel engine/swirl-tube configuration, due to larger mass flows, and hence, higher aerodynamic loadings on the vanes. In addition, downstream actuating vanes offer the potential to completely close, allowing integration with a thrust reverser system by serving as blocker doors on landing. The primary drawback to this configuration, however, is the high exit Mach numbers, for which the noise can only be estimated through simple scaling arguments.

Section 5.5.2 concludes this section and the chapter with a landing roll comparison between a conventional thrust reverser and a swirl tube. It is found that a thrust reverser is the only effective stopping device on a slippery runway (where brakes are ineffective). The thrust reverser benefits from ingesting a large mass flow of air, generating ram drag. As thrust reversers require blocker doors to redirect the ingested mass flow, it is recommended that a propulsion system-integrated quiet drag device serve a dual function of swirl vanes on approach and fully closed blocker doors during the landing roll.

5.5.1 Upstream Fan Stage Interaction

The extensive design and validation exercises in sections 5.3 and 5.4 describe the performance of a conventional swirl tube, i.e., driven by ram pressure. This subsection presents results from CFD experiments incorporating a uniform, step change in total pressure upstream of the swirl vanes to simulate a pumped swirl tube. This simple model of an upstream fan stage

allows a comparison between ram pressure driven and pumped swirl tube configurations.

To begin, a dimensionless thrust coefficient is defined for a ducted fan stage with purely axial exhaust flow:

$$C_T = \frac{T}{\frac{1}{2}\rho_\infty V_\infty^2 A_f} \tag{5.19}$$

The thrust, T, may be determined by compressible flow relations and a knowledge of the fan stage pressure ratio π and efficiency η, assuming flow is purely axial and expanded to ambient pressure through a duct with exit area A_d. The duct exhaust area, A_d, is set equal to the fan face area, A_f, consistent with the conventional swirl tube. The thrust coefficient is non-dimensionalized in the same manner as the swirl tube, such that C_T can directly be compared to measured values of drag coefficient, C_D.

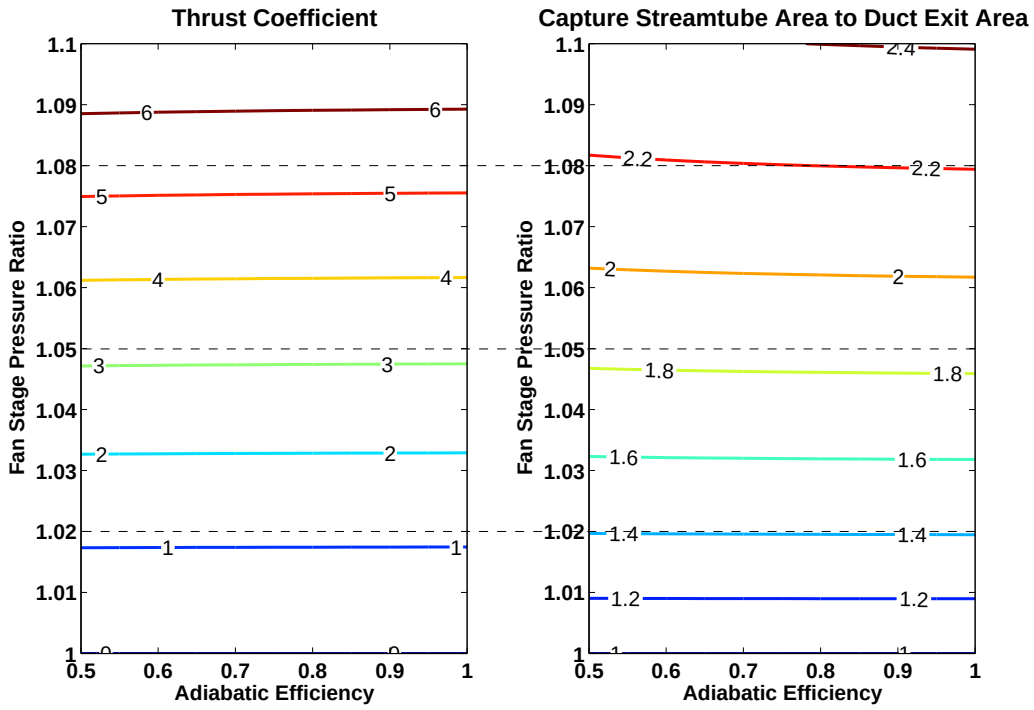

Figure 5-38: Iso-contours of the thrust coefficient (C_T) and captured streamtube area ratio, for various approach idle pressure ratios and assumed fan stage efficiencies. Approach Mach number is 0.17.

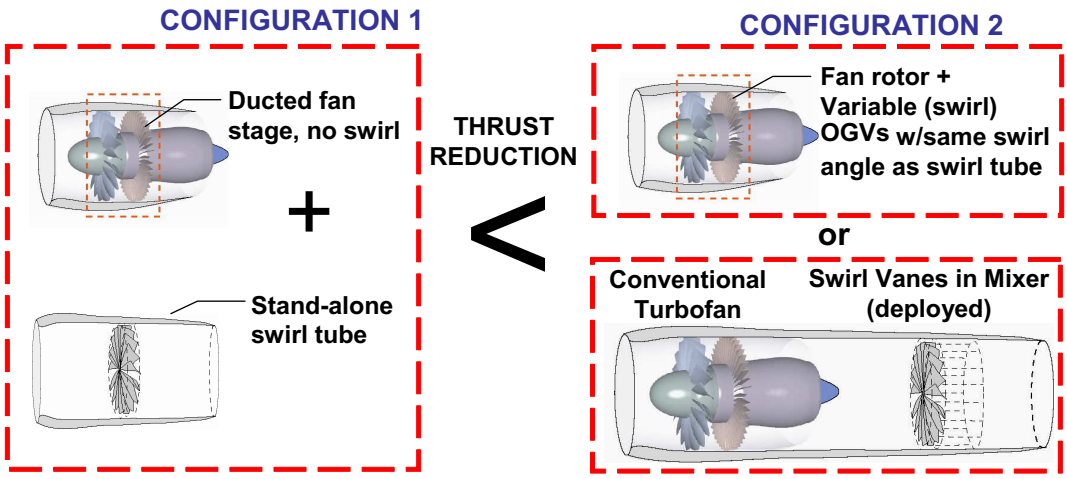

Figure 5-39: Thrust reduction comparison between engine and stand alone, ram pressure-driven swirl tube (configuration 1) versus propulsion system-integrated swirl vanes (pumped swirl tube, configuration 2).

Figure 5-38 depicts isocontours of C_T and capture streamtube area normalized to duct exhaust area, as a function of fan stage pressure ratio and efficiency, assuming a freestream Mach number of 0.17. The figure suggests that the forward thrust from an ideal fan stage cancels the drag from a stand alone ram pressure-driven swirl tube with $C_D = 1$ at a pressure ratio less than 1.02. Thus a very low approach idle setting would be needed in order for the system to produce net drag. Approach idle pressure ratios of $\lesssim 1.02$ may not be feasible from the go-around maneuver requirement that states that the engines must be able to return to full power rapidly enough to safely abort a landing during final approach. The figure also shows that both thrust coefficient and captured stream tube area increase nearly linearly with π in the range shown, because of increased mass and momentum flux. Fan stage efficiency has negligible effect because the temperature rise from lost work is small. The increased captured streamtube area leads to greater mass flow and dynamic pressures within the duct. Thus one should expect that swirl vanes downstream of a pumping stage will have higher loadings, and thus more effectively contribute to system drag (or thrust reduction) than ram pressure driven swirl vanes, as depicted in Figure 5-39.

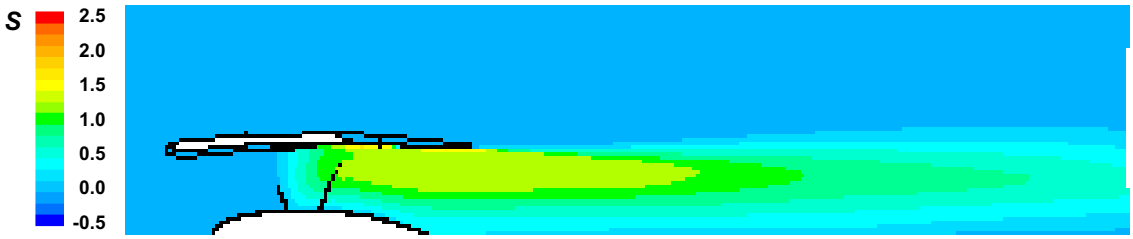

(a) Ram pressure driven swirl tube with 47° vanes.

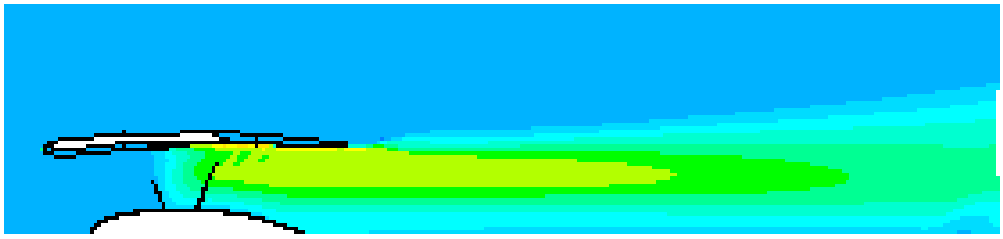

(b) Pumped swirl tube with 47° vanes.

Figure 5-40: Swirl parameter on periodic boundary of ram pressure driven and pumped swirl tube CFD cases, $\pi = 1.08$.

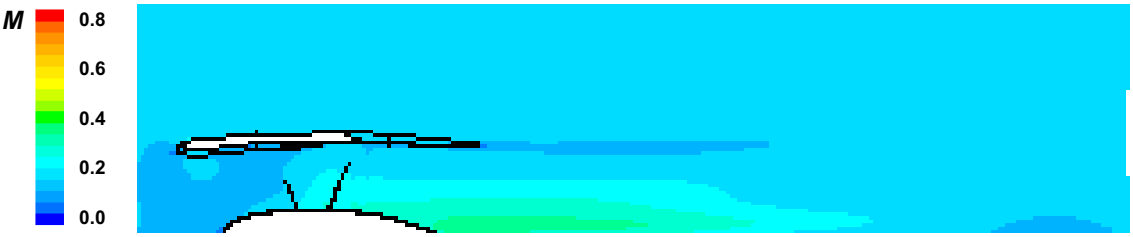

(a) Ram pressure driven swirl tube with 47° vanes.

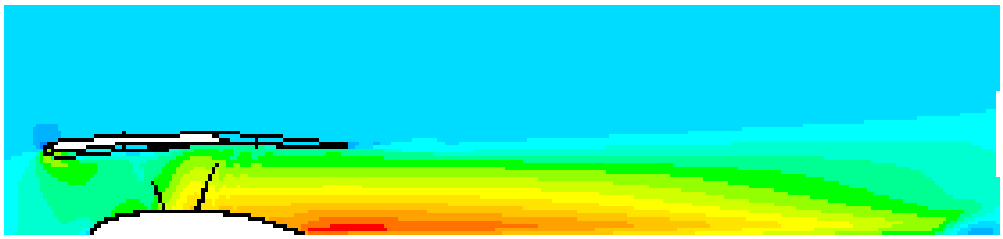

(b) Pumped swirl tube with 47° vanes.

Figure 5-41: Mach number on periodic boundary of ram pressure driven and pumped swirl tube CFD cases, $\pi = 1.08$.

Single passage periodic CFD computation are performed on the swirl tube cases discussed in Section 5.3.3 by placing a step change in total pressure at an interface zone upstream of the vanes. A 3 by 3 case matrix of pressure ratios (1.02, 1.05, and 1.08) and swirl vane angles

(34°, 47°, and 57°) are generated for freestream Mach number of 0.17. Swirl parameter and Mach number flow field comparisons between a conventional and a pumped swirl tube are presented in Figs. 5-40 and 5-41, respectively, at a pressure ratio of 1.08 and swirl vane angle of 47°. Figure 5-40 indicates a swirl parameter similarity between pumped and conventional swirl tubes, implying that vane geometry alone sets the stability criterion. In fact, it is found that vortex breakdown occurs in all of the pumped cases with 57° swirl vane angle. This suggests that vane aerodynamic design may be more a function of duct geometry than fan stage parameters.

Examination of the Mach number contours in Figure 5-41 indicates that exit velocities of a pumped swirl tube are jet-like rather than wake-like, because the fan stage ingests a much greater mass flow. On the centerline, Mach numbers approaching 0.8 are seen for the pumped case – roughly twice as high as the conventional case – suggesting that a pumped swirl tube would be noisier than a conventional one. Swirl parameter similarity suggests that a rough estimate of the noise increase may be made by assuming a power scaling exponent of 8 (for quadrupole-type sources) and applying this to the ratio of maximum Mach numbers ($\sim$ 2) to predict a 24 ($\approx 80 \log_{10} 2$) dB increase. Referring to the full-scale spectra in Figure 5-32 indicates that this may just begin compete with other noise sources on a quiet aircraft. Rigorous quantification of this will be essential to correctly sizing a propulsion system integrated quiet drag device in future.

Table 5.5 summarizes the CFD predicted drag results. The total drag coefficient of the pumped device is shown as C_D, and is computed by two methods: 1) a wall stress integration of all swirl tube surface plus an actuator disk force on the fan stage zone, estimated as the zone area times the step change in static pressure (which is assume equal to the prescribed total pressure change), and 2) a control volume integration on boundaries well upstream and downstream of the device. The total drag coefficients are found to agree to within 0.2 by these two methods, which is sufficient to draw general conclusions.

Actuator disk load in the thrust direction, given as $C_{D,a.d.}$, is assumed equal to the pressure rise times the disk area, and increases linearly with pressure ratio. Pressure and

Case		Wall Stress Integration				Control Volume Integration		
π	α_{max}	C_D	$C_{D,\text{press.}}$	$C_{D,\text{visc.}}$	$C_{D,a.d.}$	$C_{D,tot.,CV}$	$C_{D,mom.flux,CV}$	$C_{D,press.,CV}$
1.02	34°	−0.27	0.60	0.12	−0.99	−0.22	−0.51	0.29
1.02	47°	0.50	1.39	0.11	−1.00	0.57	−0.55	1.12
1.02	57°	0.87	1.76	0.10	−1.00	0.97	−0.16	1.13
1.05	34°	−1.54	0.78	0.19	−2.52	−1.42	−1.82	0.40
1.05	47°	−0.10	2.24	0.17	−2.52	0.00	−1.77	1.77
1.05	57°	0.58	2.95	0.15	−2.52	1.07	−0.55	1.62
1.08	34°	−2.90	0.87	0.26	−4.02	−2.69	−3.27	0.58
1.08	47°	−0.80	2.99	0.23	−4.02	−0.66	−3.11	2.45
1.08	57°	0.20	4.03	0.20	−4.02	0.20	−1.33	1.53

Table 5.5: Pumped swirl tube drag coefficient comparison and breakdown.

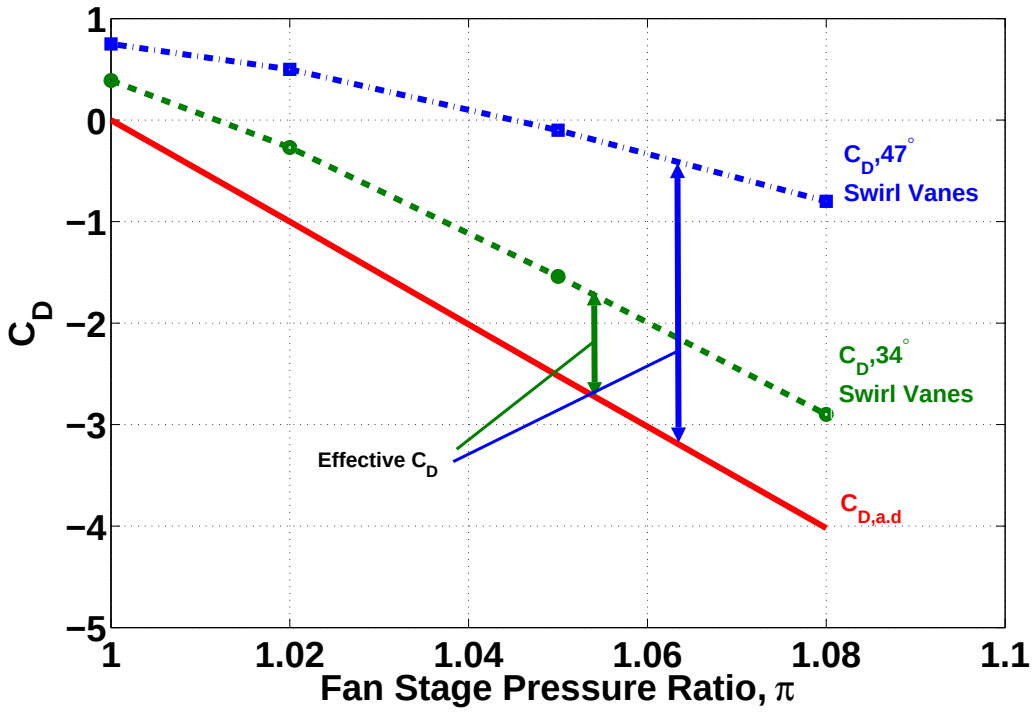

Figure 5-42: Graphical depiction showing that the effective drag coefficient from a pumped swirl tube is approximately the difference between the total drag coefficient and the actuator disk drag coefficient on the fan stage. Negative numbers indicate net forces in the thrust direction. Freestream Mach number is 0.17.

viscous forces on the duct and swirl vanes also increase with pressure ratio, as shown by $C_{D,\text{press.}}$ and $C_{D,\text{visc.}}$. As a system, swirl vanes downstream of a fan stage produce significantly more thrust reduction than a conventional swirl tube. For example, at $\pi = 1.08$, the 47° vanes produce effective drag coefficients, $C_{D,\text{press.}} + C_{D,\text{visc.}}$, of > 3, a factor of three greater than a ram pressure driven swirl tube. This is graphically depicted in Figure 5-42.

In summary, a fan-stage upstream of a ducted set of swirl vanes, a so-called pumped swirl tube, produces greater effective drag through thrust reduction than a stand alone ram pressure driven swirl tube. This occurs because the pumping increases the ingested mass flow and hence the swirl vane loadings. The mass flow increase also leads to greater exit velocities, implying a noise increase that must be quantified in the context of the airframe/propulsion system noise to determine if this configuration leads to effective quiet drag. The analysis also underscores the importance of a low propulsion system idle setting to achieving slower, steeper approach profiles to reduce noise. Assuming that approach idle setting is fixed by the go around requirement and can not be reduced, further examination of the pumped swirl tube configuration is recommended as a potential noise reduction method for next generation and conventional aircraft.

5.5.2 Comparison to Thrust Reverser

The drag capability of a swirl tube at approach velocities motivates the question of its effectiveness as a stopping device on landing, i.e., a thrust reverser replacement. The purpose of this subsection is to compare the performance of a quiet drag device such as the swirl tube to a conventional thrust reverser, during landing, to answer whether such a device can practically assist in the stopping of an aircraft on landing roll. The primary figure of merit is the landing roll distance for various stopping mechanisms under various runway conditions, as measured from a 50 foot obstacle that must be cleared per Federal Aviation Administration (FAA) regulations.

Three types of aircraft are modeled: a 737-700, 777-200ER, and the CMI SAX functionally silent aircraft. These three aircraft are selected due to their distinct powerplant bypass

ratios of about 5, 9, and > 15 during ground roll. A comparison is made between 1) brakes alone, 2) brake plus a quiet drag device, and 3) brakes plus a thrust reverser. The results of the study suggest that brakes alone can provide most of the stopping force on a dry or wet runway, while a quiet drag device and a thrust reverser have a secondary effect. On a slippery runway, i.e., an emergency situation when brakes are much less effective, the study suggests that a thrust reverser is a much better stopping mechanism than a quiet drag device, because a quiet drag device is not effective at low speeds. The majority of the effectiveness of the thrust reverser comes from its ability to ingest a large streamtube of air to generate ram drag. This leads to the recommendation to integrate variable vanes into a bypass or mixing duct, to provide pumped swirl tube drag on approach. These vanes could then swivel to a closed position on landing to serve the function of a thrust reverser blocker door.

Modeling Approach

The next subsection describes the various models employed in the stopping distance calculations.

Governing Equation. Newton's second law on the aircraft is given by,

$$m_{\text{landing}} \frac{dV}{dt} = k_0 + k_1 V + k_2 V^2, \tag{5.20}$$

where the right hand side represents the various stopping mechanism forces. The aircraft mass during landing is assumed constant during the event. The equation is solved using an ordinary differential equation (ODE) solver, to obtain the time history of the aircraft landing roll. The k coefficients are determined by the stopping mechanism models, as described below.

Airframe Drag and Quiet Drag. A constant airframe drag coefficient is assumed in this model. To this an additive quiet drag device coefficient is applied if one or multiple quiet drag devices such as swirl tubes are employed. The quiet drag coefficient is assumed to be

1.00 based on throughflow area for simplicity. Overall throughflow area is set equal to the total fan area of the propulsion system of each aircraft. Hence this type of drag is assumed to be proportional to the square of the velocity, and both types of drag contribute to the k_2 coefficient in Equation 5.20, i.e.,

$$\text{Airframe and/or Quiet Drag} \propto V^2.$$

Braking. Rolling resistance braking coefficients are selected based on values published by Raymer [70] and summarized in the Table 5.6, assuming the conservative scenario of worn brakes performing at the lowest range of the published values.

The braking coefficient times the aircraft weight gives the stopping force, which is an assumed constant that contributes to the k_0 coefficient in Equation 5.20, i.e.,

$$\text{Wheel Braking Force} \propto \text{Constant}.$$

Thrust Reverser. The thrust reverser is modeled as a device that has two drag generation mechanisms, ram drag and reverse stream thrust drag. The operating point is defined by an off-design gas turbine simulation model, GasTurb, for each engine type, to model the core, fan, or mixed nozzle temperature and pressure ratios. The engine geometric parameters then set the ingested mass flow and the ideal forward stream thrust that each engine stream generates. The ram drag is the ingested mass of the fan stage times the aircraft velocity. As thrust reverse is a high-power operating point where the pressure rise across the fan is

Scenario	$\mu_{braking}$
Brakes Off, Wheels Rollng	0.03
Brakes On, Dry Runway	0.30
Brakes On, Wet Runway	0.15
Brakes On, Slippery/Icy Runway	0.06

Table 5.6: Braking coefficient summary reproduced from Raymer [70], assuming the conservative scenario of worn brakes.

much larger than the ram pressure rise, the ingested mass flow, $\dot{m}$, based on static operation at the selected engine setting is assumed constant during the landing event. The ram drag then equals the product of $\dot{m}$ and the aircraft velocity. Since $\dot{m}$ is constant, it is equal to the k_1 coefficient in Equation 5.20 and

$$\text{Ram Drag} \propto V.$$

The thrust reverser efficiency, η_{tr}, is a factor that multiplies the ideal forward stream thrust as defined by Asbury et al. [3]. This product is the assumed reverse stream thrust for either a mixed or fan stream. η_{tr} is set at 31% for the mixed flow exhaust thrust of the CMI SAX functionally silent aircraft, and 54% of the separate flow fan stream exhaust thrust on the 737 and 777 aircraft, based on published values [3]. The core streams on the 737 and 777 are modeled to generate forward thrust. As all streams are assumed choked during thrust reverser operations, these thrust levels are assumed constant and contribute to the k_0 coefficient in Equation 5.20, i.e.,

$$\text{Forward or Reverse Stream Thrust Force} \propto \text{Constant}.$$

Assumed Event Sequences

Assumed event sequences, shown below, are modeled per correspondence with a senior captain at easyJet airlines [62].

Dry and Wet Runway. These are assumed to be routine procedures for the pilot-in-command.

1. The aircraft clears a 50 foot (15.24 meter) obstacle on a given glideslope angle and flares at 5 meters altitude.

2. At $t = 0$ seconds, the rear wheels touch down ($\mu_{\text{Rolling}} = 0.03$).

3. At $t = 3$ seconds, the nose wheel is flown down. The rear brakes are auto-locked such that μ_{braking}=0.15.

4. At $t = 5$ seconds, the thrust reverser, if available, is engaged. During the transient only ram drag is produced (to crudely average the spool up time with the steady state reverse stream thrust). Brakes are assumed pilot-locked ($\mu = 0.30$) below 100 knots (51.4 meters/second).

5. At $t = 11$ seconds, the thrust reverser, if available, reaches steady state. A standard reverser setting of 85% corrected engine speed (N_1) is assumed for SAX, while 70% corrected N_1 is assumed for the 737 and 777. The thrust reverser is turned off below 60 knots (30.9 meters/second), to avoid the risk of re-ingesting hot gases into the fan stream.

The same scenario applies to the wet runway except that the pilot locked braking coefficient is $\mu = 0.15$. If present, a quiet drag device such as a ram pressure driven swirl tube is assumed to provide drag during the entire event.

Slippery/Icy Runway. A slippery or icy runway is treated as an emergency scenario. It is assumed that the pilot has situational awareness of the slippery runway, and is therefore able to respond more rapidly than in a routine dry or wet runway scenario.

1. The aircraft clears a 50 foot (15.24 meter) obstacle on a given glideslope angle and flares at 5 meters altitude.

2. At $t = 0$ seconds, the rear wheels touch down ($\mu_{\text{Rolling}} = 0.03$).

3. At $t = 3$ seconds, the nose wheel is flown down. The rear brakes are pilot-locked such that μ_{braking}=0.06. The thrust reverser, if available, is rapidly engaged. During the transient only ram drag is produced (to crudely average the spool up time with the steady state reverse stream thrust).

4. At $t = 9$ seconds, the thrust reverser, if available, reaches steady state. Maximum reverse is applied as 85% corrected N_1 for all aircraft types. The thrust reverser is turned off below 20 knots (30.9 meters/second), trading the hot gas re-ingestion risk for a shortened stopping distance.

Again, if present, a quiet drag device such as a ram pressure driven swirl tube is assumed to provide drag during the entire event.

Runway Condition, Stopping Mechanism	**737-700A**	**777-200ER**	**SAX11**
Dry, Brakes Only	1144	1336	1399
Dry, Brakes + Swirl Tube ($C_D = 1.00$)	1120	1263	1304
Dry, Brakes + Thrust Rev.	1063	1181	1197
Wet, Brakes Only	1550	1734	1762
Wet, Brakes + Swirl Tube ($C_D = 1.00$)	1493	1655	1643
Wet, Brakes + Thrust Rev.	1362	1458	1450
Slippery, Brakes Only	3007	3393	3094
Slippery, Brakes + Swirl Tube ($C_D = 1.00$)	2767	3060	2710
Slippery, Brakes + Thrust Rev.	1543	1550	1541
Slippery, Brakes + Thrust Rev. (Ram Drag Only)	$----$	$----$	1976
Published Landing Field Length (Janes)	1418	1616	$----$

Table 5.7: Landing roll lengths in meters for various scenarios. Published values from Jane's [44] included for comparison.

Results and Discussion

The primary figure of merit is the landing roll distance for various stopping mechanisms. Table 5.7 presents the landing roll distances in meters for the three aircraft types considered in this study. From the table, the important finding of this study is that on dry and wet runways, braking alone absorbs the majority of the aircraft's touchdown kinetic energy, while on a slippery runway (an emergency scenario which is considered unsafe for normal operation), a thrust reverser is the most effective stopping device. This finding is consistent with data shown in Yetter [97].

In none of these conditions is a quiet drag device such as a ram pressure driven swirl tube effective at significantly reducing stopping distance. Thus, a stand alone swirl tube would

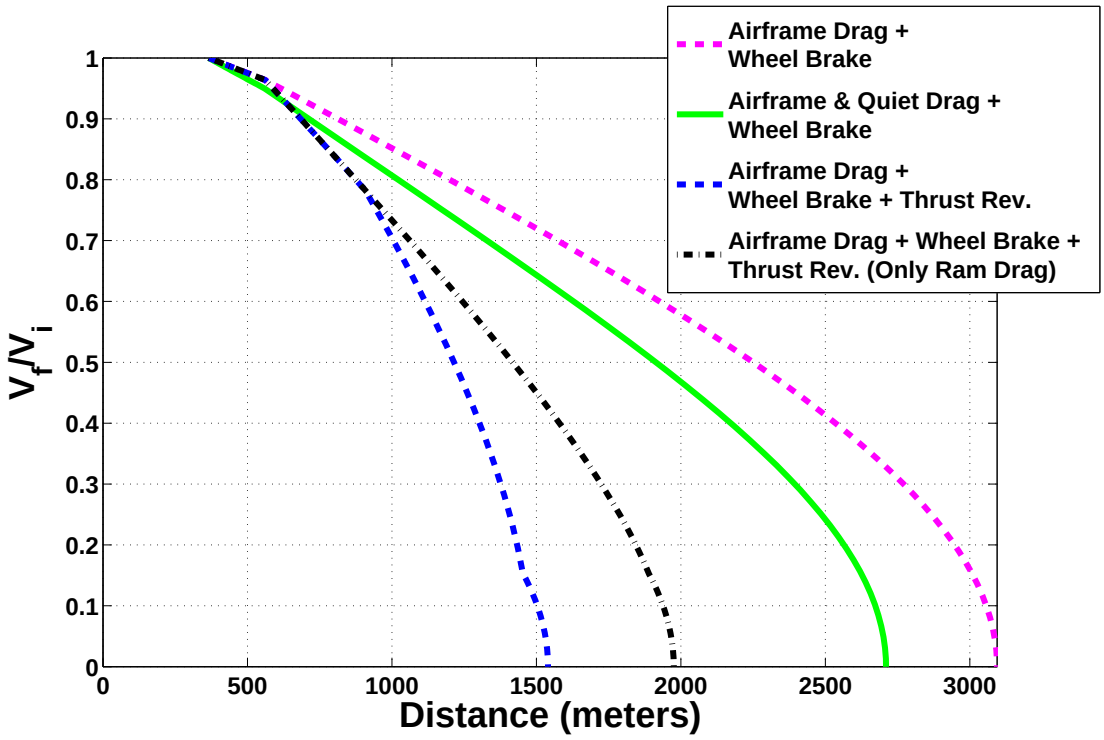

Figure 5-43: SAX landing roll velocity vs. distance.

not be an effective a thrust reverser replacement. However, it should be noted that thrust reversers are required by FAA regulations [97], and that airlines find them popular primarily because they reduce brake wear and allow for shorter taxi times between the runway and terminal.

In the case of a pumped swirl tube, achieved through deployable swirl vanes in a bypass duct downstream of a fan stage, it may be possible to actuate the vanes to a closed position on landing. This would serve the function of thrust reverser blocker doors. In this case the quiet drag device could be integrated into a thrust reverser package, possibly mitigating weight penalties associated with the actuating vanes. This concept is presented in Figure 4-6 as part of the earlier discussion on swirl tube configurations.

For the SAX BWB type aircraft with embedded, boundary layer ingesting (BLI) engines, installation issues are non-trivial. Figure 5-43 shows a plot of ground velocity divided by initial touchdown velocity versus landing distance measured from the 50 foot obstacle. Two

thrust reverser scenarios are shown, one with ram drag alone, requiring the ingested flow to be dumped radially outwards, and one with a mixed exhaust reverse stream thrust model. The computed stopping distances suggest that the CMI SAX embedded engine installation could have many of the benefits of a thrust reverser, while possibly saving weight by dumping flow radially only, by using the ram drag only option. This would require a nacelle door to open above the embedded engine to dump flow upwards (perhaps the only practical direction for an embedded engine). It is recommended that this integration scenario for a swirl tube/thrust reverser package be pursued in future designs of highly integrated airframe/propulsion systems such as the final SAX design.

5.6 Summary of Major Findings

The major findings and key messages from this chapter may be summarized as:

1. A ram pressure driven swirl tube is a viable quiet drag device, because it can generate high drag coefficient (0.83 measured at model-scale, estimated as 0.79 for full-scale, 1.2 meters diameter) with low noise signature. An A-weighted OASPL of 42 dBA on approach is estimated, suggesting the device noise falls well below the background noise of a well populated urban area.

2. A successful low-noise, high-drag swirl tube design achieves stable swirling flow as close to but not exceeding the vortex breakdown threshold. Maximum flow angles at the duct exit are close to 50°.

3. Vortex breakdown is the limiting aerodynamic and aeroacoustic physical phenomenon to swirl tube performance. Excessive swirl angle leads to breakdown, which reduces drag and increases noise by about 15 dB at high frequencies.

4. Scaling laws and DAMAS source maps indicate that the noise signature of the preferred swirl tube configuration (47°) has both scattering and/or dipole-like sources near the duct trailing edge and quadrupole-like volume sources in the swirling exhaust.

5. The swirl tube, as designed, generates greater effective drag when pumped by a fan stage, because its ingested mass flow and vane loadings increases. The increased exit velocity suggests a noise penalty. For the case of 47° swirl vanes, up to three times greater effective drag occurs, at an estimated noise penalty of 24 dB. This suggests a careful pumped swirl tube noise assessment as part of a system level noise assessment is needed in future work.

6. Swirl tubes are not as effective as thrust reversers for landing on a slippery runway. However, by actuating to a completely closed position, swirl vanes may be incorporated into a thrust reverser package by serving as blocker doors on landing.

Chapter 6

Summary and Conclusions of the Thesis

This chapter summarizes the research conducted and lists the contributions of the thesis. In proposing two novel turbomachinery concepts, new areas of research are opened to further exploration. This chapter also offers recommendations for future work to further the research presented in this thesis.

6.1 Compressor Cooling

6.1.1 Summary of Research

Compressor cooling is motivated by the thermal management challenges associated with low-to-high Mach number (0 to 4+) aircraft missions. The idea of heat extraction within the blade passages of an axial compressor is conceived to improve performance, operability, and durability of compressors, as well as improve the overall turbopropulsion cycle by combining the function of a compressor and a heat exchanger.

The effect of blade passage surface heat extraction on axial compressor performance is assessed with computational experiments and meanline modeling. At the blade passage level, cooling improves blade-to-blade aerodynamic performance by:

1. lessening the total pressure reduction across the blade passage.

2. increasing the flow turning.

3. reducing the exit Mach number and total temperature, a potentially favorable scenario for downstream blade rows.

The improvement in total pressure reduction from cooling is found to be comparable to the Rayleigh line predicted result at low subsonic inlet Mach numbers (0.4), and greater than this amount at high subsonic Mach numbers (0.8). Blade passage flow computations provide the basis for generic bulk performance rules for a cooled compressor preliminary design (meanline) framework. Single- and multi-stage compressor performance is modeled at on- and off-design conditions. Pressure ratio and efficiency maps reveal that cooling inside the blade passages of a compressor provides:

1. an increase in the overall pressure ratio (at a given corrected flow).

2. an increase in the maximum mass flow capability.

3. an increase in the efficiency, referenced to an adiabatic, reversible process.

4. rear stage choking relief at low corrected speed.

Results also suggest that, if available, a given amount of cooling is better in the front of the compressor than in the rear. This is primarily a thermodynamic effect resulting from the downstream stages compressing the colder air to a higher pressure ratio for a given amount of work. For an adiabatically designed eight-stage compressor with pressure ratio of 5, results suggest that heat extraction of 1% of inlet stagnation enthalpy flux in each of the first four blade rows improves pressure ratio and efficiency by 23% and 15%, respectively, at design corrected speed and mass flow. Choking mass flow is also found to improve by 5% at design corrected speed.

Three-dimensional computations on a state-of-the art transonic rotor (NASA Rotor 35) are shown to be in accord with the conclusions from the meanline analysis.

A preliminary heat transfer analysis reveals that the beneficial impact of blade passage heat extraction is limited by available surface area and temperature difference. This favors heat exchange in the rear stages of a compressor, and suggests the existence of an optimal cooling scheme.

Finally, the primary efficiency metric presented in this thesis for comparison between adiabatic and non-adiabatic compressors is referenced to an adiabatic, reversible process. An alternate efficiency definition referenced to a non-adiabatic, reversible process is also presented. The former efficiency metric is recommended for component-level comparisons, while the latter may be appropriate as part of a system level analysis.

6.1.2 Summary of Contributions

Contributions from the compressor cooling research, as presented in Chapter 1, are repeated here as a summary:

1. Assessment of the effects of heat extraction on blade passage performance metrics.

2. Development of a first-of-its-kind compressor meanline modeling framework with heat extraction to assess the on- and off-design behavior of a cooled axial compressor.

3. Explanation of the causality between performance implications of heat extraction in blade passage flows and the behavior of an axial compressor, including a CFD simulation of a three-dimensional rotor passage of practical interest.

4. Establishment of new efficiency metrics for compressors with heat extraction, substantiated by a bookkeeping of entropy generation from viscous and thermal dissipation.

6.1.3 Recommendations for Future Work

Unanswered questions regarding the feasibility of cooled compression turbopropulsion cycles focus on the design requirements of a cooled compressor, and overall system performance in terms of specific thrust capability, fuel burn and weight penalties. These tradeoffs must

be quantified in future work to determine whether the compressor cooling concept is worth pursuing on a high speed flight vehicle, or other high temperature application such as a modern turbofan with high overall pressure ratio. Several recommendations for future work may be proposed in light of what is learned in this thesis.

Meanline modeling demonstrates that a given amount of cooling is favorable in the front stages of a compressor, because the benefit is also felt by downstream stages. This competes with the finding that higher heat transfer rates are achievable in the rear of the device, due to higher temperatures and blade solidities. A study that warrants further consideration is the optimization of a cooling scheme given these competing effects. This could be performed at a component level, assuming some type of heat sink capability and heat exchange scheme. A further step would be to optimize a cooling schedule over the course of a low-to-high Mach number mission. This becomes a system level thermal management problem, that is mission specific. A side-by-side comparison between a compressor- or hybrid- cooled turbojet cycle and a pre-cooled turbojet cycle is a recommended first step.

At the blade-to-blade level, an experiment on a cooled cascade is warranted to study different heat exchange schemes, as well as the effect of blade parameters such as the solidity, pitch, and turning on non-adiabatic performance. An experimental design study would bring to light the different challenges and tradeoffs involved in meeting the aerodynamic and heat transfer requirements. If successful at the cascade level, a cooled stator experiment on a compressor rig would be a logical next step. In addition, a compressor cooling scheme could be incorporated into casing surfaces to extract heat from rotor passages. Heat extraction across rotor blades would be the final and most challenging aspect of a cooled compressor, for which unconventional turbomachinery heat exchanger concepts such as a multiphase thermosyphon heat pipe may be explored.

Another potential compressor cooling study, numerical or experimental, would be to use conventional axial compressor tip casing treatments, which can have cooling fin-like structures that increase available surface area, for rotor blade passage cooling. This concept may be an attractive application because these treatments are already in place in some

compressors to improve operability, but may provide additional surface area to increase the available heat transfer rates.

6.2 Swirl Tube

6.2.1 Summary of Research

The concept of quiet drag is found to be a key enabler for a next-generation functionally quiet aircraft on approach. Deployment of a quiet drag device in clean airframe configuration offers the potential to reduce aircraft source noise and noise propagation to the ground. A device that generates swirling outflow from a duct, such as an aircraft engine, is conceived to have high drag and low noise. The simplest configuration is a ram pressure driven duct with non-rotating swirl vanes, a so-called swirl tube. A swirl tube aerodynamic design is performed using first principles and CFD computations, and validated through wind tunnel aerodynamic and acoustic testing.

First principles preliminary modeling suggests a theoretical maximum drag coefficient near 1.0 based on throughflow area. An inviscid, axisymmetric streamline curvature flow solver provides swirl vane exit angles for a family of swirl tubes modeled as actuator disks inside a nacelle and centerbody geometry. Three dimensional vanes are then designed to provide the proper turning. CFD computations complete the aerodynamic design by predicting drag coefficients and the onset of the vortex breakdown phenomenon.

The swirl tube aerodynamic design is validated through model-scale wind tunnel experiments. Flow visualization indicates that vortex breakdown occurs between cases with 47° and 57° swirl vane angle. Steady velocity measurements obtained from hot-wire traverses show excellent agreement between CFD and experiment, in terms of axial and circumferential velocity profile, size and extent of viscous core, and computation of swirl angle. The steady velocity measurements also show good qualitative agreement with the outer swirling flow of the vortex breakdown cases, as well as the presence of breakdown in the core region. Drag measurements validate the hypothesis that high drag coefficients ($\gtrsim 0.8$) are achiev-

able, with the preferred design having 47° swirl vane angle with model-scale drag coefficient of 0.83.

Swirl tube acoustics are experimentally assessed at the NASA Langley Quiet Flow Facility (QFF), a state-of-the art anechoic wind tunnel. Noise signatures are found to be broadband for all swirl tubes, with a clear distinction between stable and vortex breakdown outflows. Stable flows have broadband spectra that roll off at higher frequencies, while vortex breakdown flowfield spectra closely resemble white noise at high frequencies. In addition, vortex breakdown flowfield spectra are $\sim$ 15 dB louder than stable flows, demonstrating that a high-drag, low-noise design exists for highly swirling flows that do not exceed the vortex breakdown instability limit. When extrapolated to geometries of practical interest, it is found that the noise from a swirl tube is significantly below the background noise of a well populated area, demonstrating the viability of the swirl tube as a quiet drag device.

Propulsion system integration of swirl vanes downstream of a fan-stage, a so-called pumped swirl tube is assessed using CFD. The effect of pumping is found to increase the mass flow through the duct, providing large effective drag in the form of thrust reduction. Higher exit velocities from pumping indicate the need to quantify the noise from a pumped swirl tube. Finally, a recommendation is put forth to integrate swirl vanes into a thrust reverser package, with the swirl vanes capable of actuating to a closed blocker door position.

6.2.2 Summary of Contributions

A swirl tube is a novel turbomachinery concept that is conceived and developed as a solution to the clean airframe approach challenge for a next-generation, functionally quiet aircraft. Research contributions identified in Chapter 1 are repeated here as a summary:

1. Successful demonstration of quiet drag coefficient of 0.8 with noise signature of 42 dBA from a full-scale swirl tube.

2. Quantification of the relationship between swirl angle, drag, and noise for a family of swirl tube designs.

3. Identification and quantification of acoustic sources associated with the swirling outflow of a ram pressure driven swirl tube.

4. Identification of the limitations imposed by the vortex breakdown phenomenon on swirl tube aerodynamic and acoustic performance.

5. Preliminary description of the propulsion-system integrated effect of a fan driven swirl drag device for slow, steep approaches to reduce aircraft approach noise.

6. Recommendation to integrate swirl vanes into a thrust reverser system to achieve the dual functionality of drag on approach and thrust reverser blocker doors during landing.

6.2.3 Recommendations for Future Work

This thesis presents a thorough assessment of the aerodynamic and acoustic performance of a ram pressure drive swirl tube. This technology concept may thus be considered ready for the next-level of feasibility study involving practical implementation challenges on an aircraft. Mechanical design challenges for future work include deployment schemes in conventional and drag generation modes. Location and design of ducting on an aircraft should be considered by an aircraft manufacturer. Weight penalties associated with a ram air driven swirl tube should also be quantified.

Additional drag potential is suggested by preliminary modeling and computations of a pumped swirl tube. The acoustics of a pumped swirl tube should thus become the primary focus of further research to determine if a high-drag, low-noise design space exists for such a device. Fundamental experiments on highly swirling jet-like flows driven by approach idle pressure ratios would determine the noise penalty associated with the increased velocities of a pumped swirl tube exhaust. If successful, implementation of swirl vanes into an aircraft engine could follow, with the additional mechanical feature of thrust reverser blocker door capability.

Several different studies that were performed during the noise tests at the NASA Langley QFF include the effect of aft centerbody shape and throughflow, inlet distortion, and angle of

attack. The data from these non-standard configurations should be dissected to shed further light on the fundamental aerodynamic mechanisms that set the swirl tube noise signature.

Another important acoustics question would be whether the noise from a swirl tube could be further reduced through acoustic treatments. If there are noise sources internal to the swirl tube, as suggested by the DAMAS source maps, this may open the door for further noise reduction in a ram pressure driven or pumped swirl tube. Liner design for swirling flow should be investigated in this context.

Bibliography

[1] Agarwal, A. and A. P. Dowling. The Calculation of Acoustic Shielding of Engine Noise by the Silent Aircraft Airframe. *AIAA-2005-2996, 11th AIAA/CEAS Aeroacoustics Conference, Monterrey, California, USA, May 23-25*, 2005.

[2] Anderson, J. D. *Introduction to Flight, 3rd Ed.* McGraw-Hill Publishing Company, New York, NY, 1989.

[3] Asbury, S.C and J.A. Yetter. Static Performance of Six Innovative Thrust Reverser Concepts for Subsonic Transport Applications. Technical Memorandum 210300, NASA, Langley, VA, 2000.

[4] Bearman, P.W. The Effect of Base Bleed on the Flow behind a Two-Dimensional Model with a Blunt Trailing Edge. *The Aeronautical Quarterly*, 1967.

[5] Bragg, S.L. and W.R. Hawthorne. Some Exact Solutions of the Flow through Annular Cascade Actuator Discs. *Journal of the Aeronautical Sciences*, 17, 1950.

[6] Brooke Benjamin, T. Theory of the Vortex Breakdown Phenomenon. *Journal of Fluid Mechanics*, 1962.

[7] Brooks, T.F. Airfoil Self-Noise and Prediction. Reference Publication 1218, NASA, Hampton, VA, 1989.

[8] Brooks, T.F. and M.A. Marcolini. Airfoil Tip Vortex Formation Noise. *AIAA Journal*, 1986.

[9] Brooks, T.F. and W.M. Humphreys Jr. Flap-edge Aeroacoustic Measurements and Prediction. *Journal of Sound and Vibration*, 2003.

[10] Brooks, T.F. and W.M. Humphreys Jr. Three-Dimensional Application of DAMAS Methodology for Aeroacoustic Noise Source Definition. *AIAA-2005-2960, 11th AIAA/CEAS Aeroacoustics Conference, Monterrey, California, USA, May 23-25*, 2005.

[11] Brooks, T.F. and W.M. Humphreys Jr. A Deconvolution Approach for the Mapping of Acoustic Sources (DAMAS) Determined from Phased Microphone Arrays. *Journal of Sound and Vibration*, 2006.

[12] Brooks, T.F. and W.M. Humphreys Jr. Extension of DAMAS Phased Array Processing for Spatial Coherence Determination (DAMAS-C). *AIAA-2006-2654, 12th AIAA/CEAS Aeroacoustics Conference, Cambridge, Massachusetts, USA, May 8-10*, 2006.

[13] Clarke, J.B., N.T. Ho, L. Ren, J.A. Brown, K.R. Elmer, K. Tong and J.K. Wat. Continuous Descent Approach: Design and Flight Test for Louisville International Airport. *AIAA Journal of Aircraft*, 2004.

[14] Cumpsty, N.A. *Compressor Aerodynamics*. Longman, Cambridge, UK, 1989.

[15] Darmofal, D.L., R. Khan, E.M. Greitzer and C.S. Tan. Vortex Core Behavior in Confined and Unconfined Geometries: A Quasi-One-Dimensional Model. *Journal of Fluid Mechanics*, 2003.

[16] Delery, J.M. Aspects of Vortex Breakdown. *Progress in Aerospace Sciences*, 1994.

[17] Diedrich, A., J. Hileman, D. Tan, K. Wilcox and Z. Spakovszky. Multidisciplinary Design and Optimization of the "Silent" Aircraft. *AIAA-2006-1323, 44th AIAA Aerospace Sciences Meeting and Exhibit, Reno, Nevada, Jan. 9-12, 2006*, 2006.

[18] Dowling, A.P. and J.E. Ffowcs Williams. *Sound and Sources of Sound*. Ellis Horwood Limited, Chichester, UK, 1983.

[19] Drela, M. Two-Dimensional Transonic Aerodynamic Design and Analyis Using the Euler Equations. Report 187, MIT Gas Turbine Laboratory, Cambridge, MA, 1986.

[20] Drela, M. A User's Guide to MTFLOW 1.2 - Multi-passage throughFLOW Design/Analysis Program. November 1997 1997.

[21] Engineering Sciences Data Unit. *ESDU 81009: Estimation of Windmilling Drag and Airflow of Turbo-jet and Turbo-fan Engines*, 1981.

[22] Federal Aviation Administration. Federal Aviation Regulations, Part 25 Section 125. *FAA Document*, August 2006.

[23] Fluent, Inc., Lebanon, NH. *Fluent 6.1 User's Guide*, 2003.

[24] Goldstein, M.E. *Aeroacoustics*. McGraw-Hill, New York, NY, 1976.

[25] Goldstein, M.E. Ninety Degree Acoustic Spectrum of a High-Speed Air Jet. *AIAA Journal*, 2005.

[26] Gong, Y., B.T. Sirakov, A.H. Epstein and C.S. Tan. Aerothermodynanics of microturbomachinery. *ASME GT2004-53877*, 2004.

[27] Greitzer, E.M, C.S. Tan and M.B. Graf. *Internal Flow Concepts and Applications*. Cambridge University Press, Cambridge, UK, 2004.

[28] Hall, M.G. Vortex Breakdown. *Annual Review of Fluid Mechanics*, 1972.

[29] Harada, K., N. Tanatsugu and T. Sato. Development Study of a Precooler for the Air-Turboramjet Expander-Cycle Engine. *Journal of Propulsion and Power*, 2001.

[30] Harvey, J.K. Some Observations of the Vortex Breakdown Phenomenon. *Journal of Fluid Mechanics*, 1962.

[31] Heiser, W.H. and D.T. Pratt. *Hypersonic Airbreathing Propulsion*. AIAA, Washington, DC, 1994.

[32] Hewitt, F.A. and M.C. Johnson. Propulsion System Performance and Integration for High Mach Air Breathing Flight. In S.N.B. Murthy and E.T. Curran, editors, *High Speed Flight Propulsion Systems*, volume 137. AIAA, 1991.

[33] Hileman, J., Z. Spakovszky, M. Drela and M. Sargeant. Aerodynamic and Aeroacoustic Three-Dimensional Design for a "Silent" Aircraft. *AIAA-2006-241, 44th AIAA Aerospace Sciences Meeting and Exhibit, Reno, Nevada, Jan. 9-12*, 2006.

[34] Horlock, J.H. *Acutator Disk Theory.* McGraw-Hill, London, UK, 1978.

[35] Howe, M.S. A Review of the Theory of Trailing Edge Noise. *Journal of Sound and Vibration*, 1978.

[36] http://www.boeing.com.

[37] http://www.princeton.edu/∼stengel/MAE331.html.

[38] http://www.sengpielaudio.com/TableOfSoundPressureLevels.htm.

[39] Hubbard, H.H. and J.C. Manning. Aeroacoustic Research Facilities at NASA Langley Research Center: Description and Operational Characteristics. Technical Memorandum TM-84585, NASA, Hampton, VA, 1983.

[40] Humphreys, W.M., T.F. Brooks, W.H. Hunter, and K.R. Meadows. Design and Use of Microphone Directional Arrays for Aeroacoustic Measurements. *AIAA-1998-0471, 36th Aerospace Sciences Meeting and Exhibit, Reno, Nevada, USA, January 12-15*, 1998.

[41] Hutcheson, F.V. and T.F. Brooks. Measurement of Trailing Edge Noise Using Directional Array and Coherent Output Power Methods. *AIAA-2002-2472, 8th AIAA/CEAS Aeroacoustics Conference, Breckenridge, Colorado, USA, June 17-19*, 2002.

[42] Hutcheson, F.V. and T.F. Brooks. Noise Radiation from Single and Multiple Rod Configurations. *AIAA-2006-2629, 12th AIAA/CEAS Aeroacoustics Conference, Cambridge, Massachusetts, USA, May 8-10*, 2002.

[43] Isomura, K. and J. Omi. A Comparative Study of an ATREX Engine and a Turbo Jet Engine. *AIAA/ASME/SAE/ASEE 37th Joint Propulsion Conference*, 2001.

[44] Jane's Information Group, Coulsdon, Surrey, UK. *Jane's All the World's Aircraft*, 2005.

[45] Jenkins, D.R. *Space Shuttle: The History of the National Space Transportation System*. Dennis R. Jenkins, Cape Canaveral, FL, 2002.

[46] Johnson, J.E. Variable Cycle Engine Developments. In Murthy, S.N.B. and E.T. Curran, editor, *Developments in High-Speed-Vehicle Propulsion Systems*, volume 165. AIAA, 1995.

[47] Kerrebrock, J.L. *Aircraft Engines and Gas Turbines, 2nd Ed.* MIT Press, Cambridge, MA, 1992.

[48] Leibovich, S. The Structure of Vortex Breakdown. *Annual Review of Fluid Mechanics*, 1978.

[49] Lighthill, M.J. On Sound Generated Aerodynamically. I. General Theory. *Proceedings of the Royal Society of London A*, 1952.

[50] Lighthill, M.J. On Sound Generated Aerodynamically. II. Turbulence as a Source of Sound. *Proceedings of the Royal Society of London A*, 1953.

[51] Lilley, G.M. The Prediction of Airframe Noise and Comparison With Experiment. *Journal of Sound and Vibration*, 2001.

[52] Lockard, D.P. and G.M. Lilley. The Airframe Noise Reduction Challenge. Reference Publication 213013, NASA, Hampton, VA, 2004.

[53] Manneville, A. Propulsion System Concepts for Silent Aircraft. Master's thesis, MIT, May 2004.

[54] Manneville, A., D. Pilczer and Z. S. Spakovszky. Preliminary Evaluation of Noise Reduction Approaches for a Functionally Silent Aircraft. *AIAA Journal of Aircraft*, 2006.

[55] Manneville, A., D. Pilczer and Z. Spakovszky. Noise Reduction Assessments and Preliminary Design Implications for a Functionally-Silent Aircraft. *AIAA-2004-2925, 10th AIAA/CEAS Aeroacoustics Conference, Manchester, United Kingdom, May 10-12*, 2004.

[56] Meadows, K.R., T.F. Brooks, W.M. Humphreys Jr., W.W. Hunter, and C.H. Gerhold. Aeroacoustic Measurements of a Wing-Flap Configuration. *AIAA-1997-1595, 3rd AIAA/CEAS Aeroacoustics Conference, Atlanta, Georgia, USA, May*, 1997.

[57] Mendoza, J.M., T.F. Brooks, and W.M. Humphreys Jr. Aeroacoustic Measurements of a Leading Edge Slat Configuration. *International Journal of Aeroacoustics*, 1(3):241–274, 2002.

[58] Mendoza, J.M., T.F. Brooks, and W.M. Humphreys Jr. Aeroacoustic Measurements of a Wing-Slat Model. *AIAA-2002-2604, 8th AIAA/CEAS Aeroacoustics Conference, Breckenridge, Colorado, USA, June 17-19*, 2002.

[59] Miele, A. *Flight Mechanics, Volume 1: Theory of Flight Paths*. Addison-Wesley Publishing Company, Reading, MA, 1962.

[60] Mizobata, K., H. Kimura, H. Sugiyama, T. Sato and H. Kobayashi. Conceptual Design of Flight Demonstrator Vehicles for the ATREX Engine. *AIAA/NAL-NASDA-ISAS 12th International Space Planes and Hypersonic Systems and Technologies Conference, Norfolk, VA*, 2003.

[61] Mobed, D. Aero-Acoustics of Swirling Flows for Drag Applications. Master's thesis, MIT, December 2006.

[62] Moody, S. Personal communication, 2005.

[63] Morris, P.J., and F. Farassat. Acoustic Analogy and Alternative Theories for Jet Noise Prediction. *AIAA Journal*, 2002.

[64] Panton, R.L. *Incompressible Flow*. John Wiley and Sons, New York, NY, 1984.

[65] Pilczer, D. Noise Reduction Assessments and Preliminary Design Implications for a Functionally Silent Aircraft. Master's thesis, MIT, June 2003.

[66] Powell, T.H. and M.R. Glickstein. Precooled Turbojet Engine Cycle For High Mach Number Applications. *AIAA/SAE/ASME/ASEE 24th Joint Propulsion Conference*, 1988.

[67] Quayle, A. Personal communication, 2006.

[68] Quayle, A., A. Dowling, H. Babinsky, and W. Graham. Landing Gear for a Silent Aircraft. *AIAA-2007-231, 45th Aerospace Sciences Meeting and Exhibit, Reno, Nevada, USA, To Be Presented: January 8-11*, 2007.

[69] Raizada, N. and P.J. Morris. Prediction of Noise from High Speed Subsonic Jets Using and Acoustic Analogy. *AIAA-2006-2596, 12th AIAA/CEAS Aeroacoustics Conference, Cambridge, Massachusetts, USA, May 8-10*, 2006.

[70] Raymer, D.P. *Aircraft Design: A Conceptual Approach*. AIAA Education Series, Reston, VA, 1999.

[71] Reid, L. and R.D. Moore. Performance of Single-Stage Axial-Flow Transonic Compressor With Rotor and Stator Aspect Ratios of 1.19 and 1.26, Respectively, and With Design Pressure Ratio of 1.82. Technical Paper 1338, NASA, Cleveland, OH, 1978.

[72] Reynolds, T.G., L. Ren, J.B. Clarke, A.S. Burke and M. Green. History, Development and Analysis of Noise Abatement Arrival Procedures for UK Airports. *AIAA-2005-7395, AIAA 5th Aviation, Technology, Integration and Operations Conference, Arlingont, Virginia, USA, September 26-28*, 2005.

[73] Rudakov, A.S. and V.V. Balepin. Propulsion Systems with Air Precooling for Aerospaceplane. *SAE Paper 911182*, 1991.

[74] Sarpkaya, T. On Stationary and Travelling Vortex Breakdown. *Journal of Fluid Mechanics*, 1971.

[75] Sato, T., N. Tanatsugu, H. Hatta, K. Goto, H. Kobayashi, J. Omi and J. Tomike. Development Study of the ATREX Engine for TSTO Spaceplane. *AIAA/NAL-NASDA-ISAS 10th International Space Planes and Hypersonic Systems and Technologies Conference, Kyoto, Japan*, 2001.

[76] Sawai, S., T. Sato, H. Kobayashi, N. Tanatsugu and H. Ohtsuka. Flight Test Plan for ATREX Engine Development. *AIAA/NAL-NASDA-ISAS 12th International Space Planes and Hypersonic Systems and Technologies Conference, Norfolk, VA*, 2003.

[77] Schlichting, A.H. *Boundary Layer Theory*. McGraw Hill, New York, 1987.

[78] Schumm, M., E. Berger and P.A. Monkewitz. Self-excited Oscillations in the Wake of Two-dimensional Bluff Bodies and Their Control. *Journal of Fluid Mechanics*, 1994.

[79] Sevilla, A. and C. Martínez-Bazán. Vortex Shedding in High Reynolds Number Axisymmetric Bluff-body Wakes: Local Linear Instability and Global Bleed Control. *Physics of Fluids*, 2004.

[80] Shapiro, A.H. *The Dynamics and Thermodynamics of Compressible Fluid Flow*. Ronald Press, New York, 1953.

[81] Smith, M.J.T. *Aircraft Noise*. Cambridge University Press, Cambridge, UK, 1989.

[82] Society of Automotive Engineers. *SAE ARP876D: Gas Turbine Jet Exhaust Noise Prediction*, 1994.

[83] Squire, H.B. Analysis of the 'Vortex Breakdown' Phenomenon. Report 102, Imperial College, London, Aeronautics Department, 1960.

[84] Sreenath, A.V. Studies of Turbojet Engines for Hypersonic Propulsion. Technical report, McGill University, Department of Mechanical Engineering, 1961.

[85] Stone, J.R., D.E. Groesbeck and C.L. Zola. Conventional Profile Coaxial Jet Noise Prediction. *AIAA Journal*, 1983.

[86] Taguchi, H., T. Sato, H. Kobayashi, T. Kojima, K. Okai, K. Fujita, T. Ohta. Design Study on a Small Pre-Cooled Turbojet Engine for Flight Experiments. *AIAA/NAL-NASDA-ISAS 13th International Space Planes and Hypersonic Systems and Technologies Conference*, 2005.

[87] Tam, C.K.W. Jet Noise: Since 1952. *Theoretical and Computational Fluid Dynamics*, 1998.

[88] Tam, C.K.W. and L. Auriault. Mean Flow Refraction Effects on Sound Radiated from Localized Sources in a Jet. *Journal of Fluid Mechanics*, 1998.

[89] Tam, C.K.W. and L. Auriault. Jet Mixing Noise from Fine-Scale Turbulence. *AIAA Journal*, 1999.

[90] Tam, C.K.W., and N. Pastouchenko. Noise from the Fine Scale Turbulence of Nonaxisymmetric Jets. *AIAA-2001-2187, 7th AIAA/CEAS Aeroacoustics Conference, Maastricht, Netherlands, May 28-30*, 2001.

[91] Tam, C.K.W., M. Golebiowski, and J.M. Seiner. On the Two Components of Turbulent Mixing Noise from Supersonic Jets. *AIAA Paper 96-1716*, 1996.

[92] Tam, C.K.W., N. Pastouchenko and K. Vishwanathan. Fine-Scale Turbulence Noise from Hot Jets. *AIAA Journal*, 2005.

[93] Tanatsugu, N., T. Sato, V. Balepin, Y. Naruo, T. Mizutani, T. Kashiwagi, K. Hamabe, J. Tomike and R. Minami. Development Study on ATREX Engine. *Acta Astronautica*, 41(12), 1997.

[94] Tanna, H.K. On the Effect of Motion of Sources on Subsonic Jet Noise. *Journal of Sound and Vibration*, 1973.

[95] Thies, A.T. and C.K.W. Tam. Computation of Turbulent Axisymmetric and Nonaxisymmetric Jet Flows Using the K-epsilon Model. *AIAA Journal*, 1996.

[96] Wood, C.J. Visualization of an Incompressible Wake with Base Bleed. *Journal of Fluid Mechanics*, 1967.

[97] Yetter, J.A. Why Do Airlines Want and Use Thrust Reversers? Technical Memorandum 109158, NASA, Langley, VA, 1995.

[98] Zweifel, O. The Spacing of Turbomachine Blading, Especially with Large Angular Deflection. *Brown Boveri Review*, 32(12), 1945.